[redacted]

MARTIN MARIETTA ENERGY SYSTEMS LIBRARIES
3 4456 0349670 4

ORNL-1762
Progress

AEC RESEARCH AND DEVELOPMENT REPORT

CENTRAL RESEARCH LIBRARY
DOCUMENT COLLECTION

DECLASSIFIED
CLASSIFICATION CHANGED TO:
BY AUTHORITY OF:
BY:

SOLID STATE DIVISION

SEMIANNUAL PROGRESS REPORT

FOR PERIOD ENDING AUGUST 30, 1954

CENTRAL RESEARCH LIBRARY
DOCUMENT COLLECTION
LIBRARY LOAN COPY
DO NOT TRANSFER TO ANOTHER PERSON
If you wish someone else to see this document, send in name with document and the library will arrange a loan.

OAK RIDGE NATIONAL LABORATORY • U.S. ATOMIC ENERGY COMMISSION

OAK RIDGE NATIONAL LABORATORY
OPERATED BY
CARBIDE AND CARBON CHEMICALS COMPANY
A DIVISION OF UNION CARBIDE AND CARBON CORPORATION
UCC
POST OFFICE BOX P
OAK RIDGE, TENNESSEE

[redacted]

ORNL 1762
Errata

Copy No. 4

SOLID STATE DIVISION SEMIANNUAL PROGRESS REPORT FOR PERIOD ENDING AUGUST 30, 1954

ERRATA

p 52, column 1, Eq. 1

for $x_i = y_i + \ldots$, *read* $\dot{x}_i = y_i + \ldots$,

p 89, Table 11, heading of last double column

for Paramagnetic Centers of $\frac{1}{2}$ Spin *read* Paramagnetic Centers of Spin $\frac{1}{2}$

p 89, Table 11

the last two values in the last column, 6.1×10^{19} and 8.5×10^{19}, should appear in the next-to-last column to indicate that they were calculated from the value A $(= n\beta^2/\rho k)$

p 90, Table 12, column 1

quartz density should be 2.66 g/cm^3 instead of 3.58 g/cm^3

[redacted]

ORNL-1762

This document consists of 131 pages
Copy 4 of 162 copies. Series A.

Contract No. W-7405-eng-26

SOLID STATE DIVISION

SEMIANNUAL PROGRESS REPORT

For Period Ending August 30, 1954

D. S. Billington, Director
J. H. Crawford, Jr., Assistant Director

Edited by
J. T. Howe

DECLASSIFIED
CLASSIFICATION CHANGED TO:
BY AUTHORITY OF: E. J. Murphy 1-31-61
BY: B. O. Williams 6-8-61

DATE ISSUED

DEC 16 1954

OAK RIDGE NATIONAL LABORATORY
Operated by
CARBIDE AND CARBON CHEMICALS COMPANY
A Division of Union Carbide and Carbon Corporation
Post Office Box P
Oak Ridge, Tennessee

[redacted]

MARTIN MARIETTA ENERGY SYSTEMS LIBRARIES

3 4456 0349670 4

[redacted]

INTERNAL DISTRIBUTION

1. C. E. Center
2. Biology Library
3. Health Physics Library
4-6. Central Research Library
7. Reactor Experimental Engineering Library
8-11. Laboratory Records Department
12. Laboratory Records, ORNL R.C.
13. C. E. Larson
14. L. B. Emlet (K-25)
15. J. P. Murray (Y-12)
16. A. M. Weinberg
17. E. H. Taylor
18. E. J. Murphy
19. E. D. Shipley
20. D. S. Billington
21. F. C. VonderLage
22. W. H. Jordan
23. J. A. Swartout
24. S. C. Lind
25. F. L. Culler
26. A. H. Snell
27. A. Hollaender
28. M. T. Kelley
29. G. H. Clewett
30. K. Z. Morgan
31. T. A. Lincoln
32. A. S. Householder
33. C. S. Harrill
34. C. E. Winters
35. D. W. Cardwell
36. E. M. King
37. C. P. Keim
38. L. K. Jetter
39. E. J. Boyle
40. W. D. Manly
41. C. D. Susano
42. B. S. Borie
43. R. J. Gray
44. J. H. Frye, Jr.
45. E. E. Stansbury
46. G. P. Smith
47. J. E. Cunningham
48. E. C. Miller
49. A. F. Cohen
50. J. O. Betterton, Jr.
51. R. B. [redacted]
52. T. H. Blewitt
53. J. H. Crawford, Jr.
54. W. E. Brundage
55. O. Sisman
56. G. W. Keilholtz
57. J. T. Howe
58. R. H. Kernohan
59. S. E. Dismuke
60. J. C. Wilson
61. W. J. Sturm
62. M. T. Robinson
63. J. W. Cleland
64. K. Lark-Horovitz (consultant)
65. M. C. Wittels
66. R. A. Weeks
67. W. W. Parkinson
68. C. D. Bopp
69. C. D. Baumann
70. J. B. Trice
71. J. G. Morgan
72. G. E. Klein
73. R. G. Berggren
74. D. K. Holmes
75. D. K. Stevens
76. A. J. Miller
77. R. S. Livingston
78. R. J. Jones
79. D. D. Cowen
80. P. M. Reyling
81. G. C. Williams
82. D. Binder
83. M. J. Feldman
84. C. C. Webster
85. J. M. Warde
86. W. O. Harms
87. W. R. Willis
88. F. Seitz (consultant)
89. E. P. Wigner (consultant)
90. R. L. Sproull (consultant)
91. R. W. Johnson
92. H. G. MacPherson
93. G. E. Boyd
94. J. L. Gabbard
95. R. A. Charpie
96. M. J. Skinner
97. W. E. Browning
98. ORNL Document Reference Library, Y-12

[redacted]

[redacted]

EXTERNAL DISTRIBUTION

99. ANP Project Office, Fort Worth (R. N. Little)
100-107. Argonne National Laboratory
108-110. Atomic Energy Commission, Washington
111-114. Brookhaven National Laboratory
115. Division of Research and Medicine, AEC, ORO
116-118. Knolls Atomic Power Laboratory
119-120. General Electric Company, Richland
121. Hanford Operations Office
122-125. Los Alamos Scientific Laboratory
126-127. New York Operations Office
128. Patent Branch, Washington
129-143. Technical Information Service, Oak Ridge
144-145. University of California Radiation Laboratory, Berkeley
146-147. University of California Radiation Laboratory, Livermore
148. Massachusetts Institute of Technology (Kaufmann)
149. Battelle Memorial Institute
150-152. North American Aviation, Inc.
153. Westinghouse Electric Corporation
154. Savannah River Operations Office, Augusta
155-158. Phillips Petroleum Company
159. Materials Laboratory (WADC) 1 copy – Helen Akerd
160. Directorate of Research (WADC) 1 copy – Helen Akerd
161. National Advisory Committee for Aeronautics, Cleveland (Solid State Division, Lewis Flight Propulsion Laboratory)
162. General Electric Company (ANPD)

[redacted]

[redacted]

Reports previously issued in this series are:

ORNL-1025	Period Ending January 31, 1951
ORNL-1095	Period Ending April 30, 1951
ORNL-1128	Period Ending July 31, 1951
ORNL-1214	Period Ending October 31, 1951
ORNL-1261	Period Ending January 31, 1952
ORNL-1301	Period Ending May 10, 1952
ORNL-1359	Period Ending August 10, 1952
ORNL-1429	Period Ending November 10, 1952
ORNL-1506	Period Ending February 10, 1953
ORNL-1606	Period Ending August 31, 1953
ORNL-1677	Period Ending February 28, 1954

[redacted]

[redacted]

CONTENTS

PUBLICATIONS vii

PART I

SUMMARY 3

RADIATION METALLURGY 7
- Creep and Stress Corrosion 7
- Phillips Petroleum Company MTR Tensile Specimens 9
- Uranium-Aluminum Alloys 9
- Impact Tests 9
- Fatigue Tests 10
- Strain Gages 10
- Hot Metallography 11
- Fission-Fragment Annealing Studies 12
- High-Temperature, Short-Time-Grain-Growth Characteristics of Inconel 12
- Use of Ultrasonic Cleaning in the Hot Cell 14
- Simplified Adaptation of Metallography Polishing Unit for Remote Operation 16
- Cell Extension 17

NUCLEAR MEASUREMENTS 20
- BNL Neutron Spectrum – Radiation Damage Study 20
- MTR Neutron-Flux Spectra – Radiation Damage Study 20

ENGINEERING PROPERTIES 21
- LITR Fluoride-Fuel Loop 21
- ORNL Graphite Reactor Sodium-Inconel Loop 24
- Effects of Radiation on Thorium-Uranium Alloy Fuel Plates 34

FUSED SALTS 39
- Temperature as a Variable in Static-Corrosion Tests 39
- MTR Static-Corrosion Tests 39
- Facilities for Handling Radioactive Materials 41
- Remotely Operated Tube-Slitting Machine 41
- Analysis of Irradiated Fluoride Fuels for Uranium 43
- High-Temperature Check-Valve Tests 44
- Bench Test of Miniature In-Pile Loop 44
- Life Tests on a Remote RPM Meter, Bearings, and Small Electric Motor Under Irradiation 45
- Design Calculations for a Miniature Circulating Loop 48
- Fused-Salt Filling Apparatus 49
- Removal of Xe^{135} from Fluoride Fuels 50
- Calculation of Concentrations of Fission Products in Fluoride Fuels 50
- Fission-Product Corrosion Study 52
- Assay of U(III)-U(IV) Systems by Magnetic Means 53
- C_7F_{16}-UF_6 Irradiation 54

PART II

SUMMARY 61

SOLID STATE REACTIONS 65
- Neutron Irradiation of Indium Antimonide 65

[redacted]

[redacted]

Energy Levels in n-Type Germanium Irradiated at Room Temperature 71
Mobility in Bombarded n-Type Germanium 75
Radiation Effects on Lead-Wire Insulation 76
Bombardment of Rectifiers 78
Radiation Effects in Ionic Crystals 79
Magnetic Susceptibility Studies 81
Degeneracy and Effective Mass in Germanium 85
Irradiation Effects in Zircon Single Crystals 85
Unirradiated and Irradiated Piezo Quartz 86

ENGINEERING PROPERTIES 90
Properties of Reactor-Irradiated Ceramics 90
X-Ray Diffraction Patterns of Irradiated Elastomers 91
Radiation Effects on Plasticized Polyvinyl Chloride 91
Calculation of the Dynamic Young's Modulus and the Viscous Modulus from the Resonance Curves 93

CRYSTAL PHYSICS 97
Work-Hardening in Copper Crystals 97

SPECIAL PROJECTS 111
Neutron Irradiation of LiF 111
Paramagnetic Resonance in Irradiated Materials 112
Dielectric Constant and Loss Tangent of Irradiated Plastics at Microwave Frequencies 113
Thermal Conductivity of Dielectrics at Low Temperatures 115
Thermal- and Electrical-Conductivity Studies 115
A Rocking-Curve Adapter for the Norelco Wide-Range Diffractometer 117
Shielding for an X-Ray Diffractometer 120

[redacted]

[redacted]

PUBLICATIONS

Publications of the Solid State Division during the past six months were:

M. C. Wittels, "Radiation Damage Studies of Some Refractory Crystals," Gordon Research Conference on Solid State Reactions in Ceramics (July 15, 1954).

O. Sisman, "The Effects of High Energy Radiation on Plastics and Elastomers," Gordon Research Conference on Radiation Chemistry (July 6, 1954).

J. W. Cleland and J. H. Crawford, Jr., "Radiation Effects in Indium Antimonide," *Phys. Rev.* **93**, 894 (1954).

T. H. Blewitt, R. R. Coltman, Jr., and J. K. Redman, "Structural Defects in Copper and the Electrical Resistivity Minimum," *Phys. Rev.* **93**, 891 (1954).

W. J. Sturm and R. J. Jones, "Application of Thermocouples to Target Temperature Measurement in the Internal Beam of a Cyclotron," *Rev. Sci. Instr.* **25**, 392 (1954).

M. T. Robinson, *Release of Xenon from Fluoride Fuels: Proposal for an Experimental Program*, ORNL CF-54-6-4 (June 2, 1954).

M. T. Robinson, *Removal of Xe-135 from Fused Fluoride Fuels*, ORNL CF-54-8-51 (Aug. 9, 1954).

[redacted]

Part I

[redacted] PROJECTS

SOLID STATE DIVISION SEMIANNUAL PROGRESS REPORT

SUMMARY

RADIATION METALLURGY

Creep and Stress Corrosion. A design has been developed for an in-pile stress-corrosion apparatus. Fission heat is conducted through the stressed specimen to an annulus filled with sodium which conducts the heat away without constraining the stressed specimen. A temperature gradient of 500 to 800°F per inch is necessary to meet space requirements and to prevent sodium distillation out of the annulus. Temperature excursions of as much as 100°F/sec were experienced during simulated heat transfer tests. A creep apparatus that seems to meet requirements is now being bench-tested. Further tests on the compatibility of sodium with component materials at test temperatures are required before the apparatus can be operated in the LITR.

Phillips Petroleum Company MTR Tensile Specimens. A number of mechanical and physical properties have been measured for irradiated tensile specimens of 2S aluminum, 356 aluminum, QMV beryllium, and type 347 stainless steel. The 2S aluminum and the stainless steel showed yield points after irradiation.

Uranium-Aluminum Alloys. Tensile tests were begun on flat sheet specimens of aluminum containing 30% natural uranium, 5% enriched uranium, and 15% enriched uranium. The specimens had been irradiated for an integrated flux of 10^{20} neutrons/cm^2. The yield strength of the irradiated 5% and 15% enriched uranium specimens was increased by a factor of 2 to 3 over that of unirradiated specimens. There were moderate increases in tensile strength and large decreases in the elongation of the irradiated specimens.

Impact Tests. Machining procedures have been developed for notching impact specimens uniformly, but methods for economical quantity production are still to be achieved. Impact and tensile specimens of a number of stainless steels are now being irradiated in an LB piece in the MTR, and impact specimens of type 321 stainless steel are being irradiated at 100°C in hole HB-3 of the MTR. Irradiations will be performed at higher temperatures later.

Fatigue Tests. Cantilever sheet fatigue specimens are ready for irradiation in the MTR, but attempts to produce satisfactory subsize rotating-beam fatigue specimens have not yet met with success.

Strain Gages. A search is being made for a bonded-wire strain gage that will be reliable under radiation. Karma wire was found to have a temperature range of zero temperature coefficient of resistivity which can be made to occur at higher temperatures by using slower cooling rates during heat treatment. It is possible that a heat treatment will be found that will permit use of the wire during irradiations at high temperatures.

On paper-bonded strain gages the paper disintegrated during irradiation. Tests are not complete on bakelite-bonded gages.

Hot Metallography. Metallographic specimens of corrosion capsules, Pratt & Whitney solid-type fuel sandwiches, G-E fuel elements, and HRE corrosion samples were prepared and examined.

Fission-Fragment Annealing Studies. A study is being made of the effects of annealing on irradiated fuel plates of the Pratt & Whitney sandwich type with a type 347 stainless steel–UO_2 core. A portion of the neutron damage appeared to anneal out, even though full anneal temperature for stainless steel has not yet been reached. There seems to be no reduction in the fission-fragment damage.

High-Temperature, Short-Time-Grain-Growth Characteristics of Inconel. Static-corrosion Inconel capsules occasionally exhibit small areas of grain growth accompanied by enhanced corrosion. It is thought that these large grains may be caused by local hot spots of short duration in the fuel. It was found that carbide solubility was definitely dependent on the temperature and that large grains could be produced in an extremely short time.

Use of Ultrasonic Cleaning in the Hot Cell. Experiments with a mockup of an ultrasonic cleaning device have shown that the apparatus can be used for hot-cell work, provided two transducers are mounted at right angles and the samples are rotated during cleaning.

Simplified Adaptation of Metallographic Polishing Unit for Remote Operation. The remotely controlled metallographic polishing unit has been redesigned so that adaptation of a standard polishing unit for remote operation will be less expensive and so that maintenance will be easier. Four units of the new design will be mounted in the hot cell.

Cell Extension. An extension has been designed for the metallographic cell to accommodate a Tukon hardness tester, a stereomacroperiscope, and a removable research metallograph. A Bausch and Lomb metallograph will be mounted in the chemical area and will be used without its bellows as a microscope for optical inspection of etched specimens prior to photography.

NUCLEAR MEASUREMENTS

BNL Neutron Spectrum – Radiation Damage Study. The neutron-flux energy distribution was measured in hole E-25 of the Brookhaven Reactor so that the flux intensity might be correlated with radiation damage measured in lubricants and organic compounds by California Research Corporation.

MTR Neutron-Flux Spectra – Radiation Damage Study. Neutron-flux traverses are being made with fission probes in hole HB-3 of the MTR. After measurements have been completed on the empty hole, a beryllium moderator will be introduced and the new energy distribution will be measured. Materials will then be irradiated in the moderated and unmoderated neutron spectra in an effort to correlate the spectra with the radiation damage.

ENGINEERING PROPERTIES

LITR Fluoride-Fuel Loop. A loop containing enriched fluoride fuel was installed in hole HB-2 of the LITR, but development of a leak before the reactor was started made it necessary to remove the loop and cut it up to recover the fuel.

A second loop is being built which will have improved fuel and cooling circuits and revised piping at the reactor face so that connections may be made more rapidly. The loop will be filled and test-operated with a fluoride mixture containing no uranium; then, after being drained, it will be filled with fluoride fuel. This loop is scheduled for insertion in the LITR in December.

A special entrance door has been installed in the hot cell to permit the loop to be inserted in the cell after it is withdrawn from its shield, and special remotely controlled handling tools have been developed for cutting the samples and for inspecting the loop parts.

ORNL Graphite Reactor Sodium-Inconel Loop. Samples for metallographic examination were cut from various locations of the irradiated sodium-Inconel loop and from control tubing saved for comparison. Carbide precipitate was found at the grain boundaries of all samples, although it was not apparent prior to operation in the U-bend section, where the failure occurred; outer-surface grain boundaries also showed evidence of incipient fusion in this sample. It is thought that electrical arcing occurred when the heaters failed and that the arcing produced local overheating. Some decarburization occurred in other parts of the loop, both in the radiation field and out of it; otherwise, there was no perceptible corrosion effect on the Inconel by the sodium stream.

Effects of Radiation on Thorium-Uranium Alloy Fuel Plates. A study was made of the effects of radiation on thorium-uranium fuel plates clad with 52S aluminum and bonded with a 1.3% Si-Al barrier material.

After irradiation, the outline of the core was clearly visible, possibly because of selective corrosion. Measurements made of the clad plates showed no significant changes in dimensions. Radiographs were made of the cores after irradiation by placing the cores on a sheet of ordinary Lucite and leaving them overnight. No changes in core dimensions were detected. Density measurements made on both the clad plates and stripped cores indicated that the irradiated samples were about 1% less dense than the control sample. Chemical analysis of the clad material indicated that very little diffusion had occurred during rolling and irradiation of the plates. Bond strength of the clad material to the core was quite good. Metallographic examination of the clad-core interface showed no intermetallic phase. The irradiated cores had increased in hardness about 70%; the clad showed little hardness change.

FUSED SALTS

Temperature as a Variable in Static-Corrosion Tests. There has been no correlation of the corrosion found in past capsule tests with reactor power generation, time in the reactor, or salt composition. The temperature histories of the capsules that exhibited deepest penetrations

showed either that these capsules had been exposed to a high temperature for a long time or, as indicated by the temperature pattern along the capsule, that at least two of the three thermocouple readings were in error.

MTR Static-Corrosion Tests. Analysis of NaF-ZrF_4-UF_4 in three Inconel capsules irradiated at 1620°F in the MTR showed that there was even distribution of U, Fe, Cr, and Ni within the salt but that the salt had picked up considerable Fe and some Cr. Efforts are being made to reduce the possibility of contamination from steel tools used in sampling. The Inconel showed 2 to 5 mils penetration for capsules irradiated 300 hr and 20 mils for the capsule irradiated 777 hr.

A series of capsules containing NaF-ZrF_4 based on both UF_3 and UF_4 was irradiated in the MTR to study the effect of fission on static corrosion at 1500°F. Because of the limited solubility of UF_3 in NaF-ZrF_4 mixtures, the concentration of uranium was kept low in the UF_4 mixtures also. One UF_3 capsule and one UF_4 capsule have been examined after irradiation. Little corrosion was evident in the UF_3 capsule. There was intergranular-void formation in the UF_4 capsule to a depth of 1 to 2 mils.

Facilities for Handling Radioactive Materials. Two lead transfer casks and two lead storage vaults have been built for transfer and storage of the fluoride-fuel samples after they have been put in solution for chemical analysis. A metal table with a motor-driven pulley permits easy insertion and removal of the transfer shields to and from the hot cells.

Remotely Operated Tube-Slitting Machine. A tube-slitting machine has been developed for taking longitudinal sections through static-corrosion capsules. The capsule is gripped in such a position that one surface of a cut-off wheel lies in the plane of a diameter of the capsule. Various sizes of capsules and tubes may be slit longitudinally by using different gripping adapters.

Analysis of Irradiated Fluoride Fuels for Uranium. In the technique used for sampling fluoride fuel solutions, there is a possibility of contaminating the sample with particles from the drills used in coring, with hot-cell dirt, and with rubber particles etc. from the manipulator grips. Because the size of the samples formerly taken was small and because the precision of weighing was only ±4%, there has been an uncertainty in the uranium analyses of as high as ±5% or more. Efforts have been made to improve sampling techniques and handling procedures, and a marked improvement has been noted.

High-Temperature Check-Valve Tests. A check-valve pump would have the advantage of being a completely sealed, compact unit and would therefore be very desirable for use on a miniature in-pile loop containing a fluoride fuel. Consequently, a bench-test rig was built to test check-valve operation in a liquid fluoride-fuel atmosphere. The test rig consisted of two tanks connected by two tubes. Liquid salt was forced back and forth between the tanks and through check valves located in each connecting tube. Check balls were made of Inconel, stainless steel, and Stellite 25. The stainless steel balls gave the best results but even their length of operation was no more than 2 hr. Other valves stuck in both open and closed positions during operation and failed completely in less than 30 min.

Bench Test of Miniature In-Pile Loop. A bench test was made of the miniature molten-salt pump. Salt was pumped at 1500°F at a flow of 3.5 fps and a pressure drop of 11 psi. These values confirm previous calibrations made with water and prove that the pump is capable of meeting design specifications for the in-pile model.

Life Tests on a Remote RPM Meter, Bearings, and Small Electric Motor Under Irradiation. Components to be used in the LITR dynamic-loop experiment were tested in hole 53 of the ORNL Graphite Reactor. Approximately the same flux can be obtained at the center of the graphite reactor as will be experienced by the motor and rpm meter in their location above the upper grid of the LITR. Some of the insulating materials were replaced with ones known to hold up better under irradiation. Bearings were packed with special grease supplied by California Research Corporation for use under irradiation.

The first test resulted in overheating of the motor and failure at 100 hr. Postirradiation examination disclosed a cocked, upper bearing plate.

The motor used in test No. 2 operated for as long as it would be expected to under normal conditions. Postirradiation inspection showed that deterioration of the plastic commutator-segment spacers had caused the segments to loosen. The bearing grease and the rpm meter proved to be satisfactory.

A motor is now being constructed for high-temperature service.

Design Calculations for Miniature Circulating Loop. Calculations are being made of fuel temperatures for various conditions of fuel and air flow in a proposed air-cooled loop that is being considered for operation with its tip in the region of maximum thermal flux of hole C-48 in the LITR.

Fused-Salt Filling Apparatus. Improvements have been made in the methods and apparatus used for filling experimental equipment with high-purity molten fluoride fuels. Purified helium gas provides an inert atmosphere and is used to move the liquid fuel, which is kept molten by furnaces and electrical heaters and is measured by electrical-probe level detectors. Connections are made with Swagelok fittings. Flow of the salt is halted by application of a wet asbestos sponge to the transfer line, which is then heated locally and pinched off and welded.

Removal of Xe^{135} from Fluoride Fuels. A program has been initiated to study the purging of Xe^{135} from fluoride fuels under conditions expected to be present in the aircraft reactor. The purge gas will be helium, which will be monitored for Xe^{135} as the gas leaves a capsule of fluoride fuel in position HB-3 of the LITR.

Calculation of Concentrations of Fission Products in Fluoride Fuels. Fission products may either accelerate or inhibit corrosive attack on fluoride-fuel containers. There are chemical reactions resulting from differences of oxidation state between fission products and the original uranium. Rough calculations indicate that fission products produced from fluoride fuels at the beginning of an irradiation tend to contain an excess of oxidizing agent; the amount of oxidizing agent decreases with irradiation time until there is a tendency toward a reducing condition. Further calculations will be made on the electronic analog computer.

Fission-Product Corrosion Study. Solid fluoride-fuel bars of composition 41 will be irradiated for four weeks in the C-46 facility of the LITR in order to obtain a high concentration of fission products. The bars will be transferred to a new capsule upon removal from the reactor and will be held at 1500°F for two weeks. The fuel and its container will then be sampled and studied in the standard manner. Checks will also be made of the corrosion produced by placing unirradiated fuel in irradiated capsules.

Assay of U(III)-U(IV) Systems by Magnetic Means. A theoretical investigation was made of the possibility of analyzing for U(III) and U(IV) by making use of the paramagnetic properties of the two ions. The magnetic moments of the two are, however, too closely similar to be distinguished. It was therefore concluded that no practical scheme of assaying for U(III) and U(IV) in the presence of each other can be based on the magnetic properties of the two ions.

C_7F_{16}-UF_6 Irradiation. A mixture of C_7F_{16}-UF_6 is being considered for use in simulating liquid fuels in dynamic-shielding experiments. Two nickel capsules were irradiated in the ORNL Graphite Reactor. Gas pressure evolved was measured to be between 50 and 100 psia; the pressure in the control capsule was measured to be about 4 psia, the vapor pressure of the liquid. The gas contained CF_4, C_2F_6, C_7F_{16}, and other fluorocarbons, but no UF_6 could be detected.

RADIATION METALLURGY

CREEP AND STRESS CORROSION

W. W. Davis J. C. Wilson
J. C. Zukas N. E. Hinkle

The necessity for in-pile stress-corrosion experiments was discussed in an earlier report;[1] development of a suitable apparatus has been slowed by difficulty in securing constant heat-transfer rates from the fuel to a heat sink where the fission heat can be removed. In the design in Fig. 1, fission heat is conducted from the fuel through the stressed specimen wall to a sodium-filled annulus. The sodium acts as an efficient heat conductor that exerts no constraint upon the deformation of the specimen tube as it creeps under applied stress. Part of the fission heat is removed by gaseous convection at the outer surface of the sodium-containing chamber and part by conduction through a metal ring to a water jacket. Simpler designs in which the sodium was contained in a constant-diameter annulus did not permit good temperature control. The temperature gradient that resulted from simulated fission heat input at the bottom and from heat abstraction at the top caused heated sodium to rise discontinuously in the annulus, and temperature excursions of 100°F in 1 sec were not uncommon. A substantial temperature gradient (500 to 800°F per inch) is needed to meet headroom requirements in the experimental hole and to prevent sodium distillation out of the annulus.

In an attempt to control the severe temperature fluctuations, several designs of sodium annulus were tried; baffles, spirals, and ratios of outside-to-inside sodium-annulus diameters were varied, but these changes did not result in a successful control of the fluctuations. The apparatus shown in Fig. 1 appears to operate satisfactorily, but more operating time must be accumulated before it will be certain that sodium distillation, in sufficient quantities to cause trouble, is not taking place.

In Fig. 1 a tubular Inconel specimen (A) containing 0.2 g of fuel No. 44, fixed to base (B), is eccentrically loaded through a lever arm by a weight (W) and produces a stress pattern across the horizontal cross section which varies from a maximum tensile stress through zero at the neutral axis to a maximum compressive stress. Surrounding the specimen is a sodium coolant chamber (C) with baffles (D) and (E) which reduce the magnitude of the thermal convection currents and allow closer control of the specimen temperature. A furnace (F) helps to maintain the temperature at 1500°F throughout the test. Two thermocouple wells (G) project into the sodium chamber to a position near the walls of the specimen at the neutral axis. A double-walled, concentric, sodium fill line, with only the outer tube welded to the chamber, and a vacuum exhaust tube complete the apparatus. All surfaces in contact with the fuel and sodium are made of Inconel.

The assembly is hydrogen-fired for 1 hr at 1750°F, filled with fuel, and welded in a dry box under purified helium. The other parts of the container are welded into subassemblies, hydrogen-fired, then welded together, with helium backing up the welds. The lever arm and weight are adjusted and spot-welded onto the specimen, and the chamber covers are welded into place. Before the rig is filled with sodium, it is filled with NaK and heated to 1000°F to remove any oxide remaining on the metal surfaces. The rig is then washed with butyl alcohol, which reacts with the NaK and leaves the surfaces clean and ready to be filled with sodium.

The sodium, as supplied by C. D. Coughlen, is metered out into a tube that has first been cleaned with NaK, sealed with Swagelok fittings, and provided with a helium valve. A micrometallic filter sealed into the line removes any oxides of sodium that may be formed when the connection to the test rig is made. Once the connection is made, the apparatus is evacuated and the sodium is melted and forced into the chamber by helium pressure through the valve. A combination of high surface tension and back pressure made the filling of the chamber somewhat more difficult without this procedure. For the bench tests, in which sticks of sodium were used, the filled chamber was heated while a vacuum was pulled on the system, and a rise in pressure was noted at about 525°F, presumably from dissociation of sodium hydride. It remains to be seen if such a procedure is necessary to ensure the purity of the sodium now available. The dry-box work is completed by cutting the outer fill tube, removing the inner (contaminated) tube, and crimping and welding both the fill and exhaust tubes.

[1] W. W. Davis, J. C. Zukas, and J. C. Wilson, *Solid State Semiann. Prog. Rep. Feb. 28, 1954*, ORNL-1677, p 7.

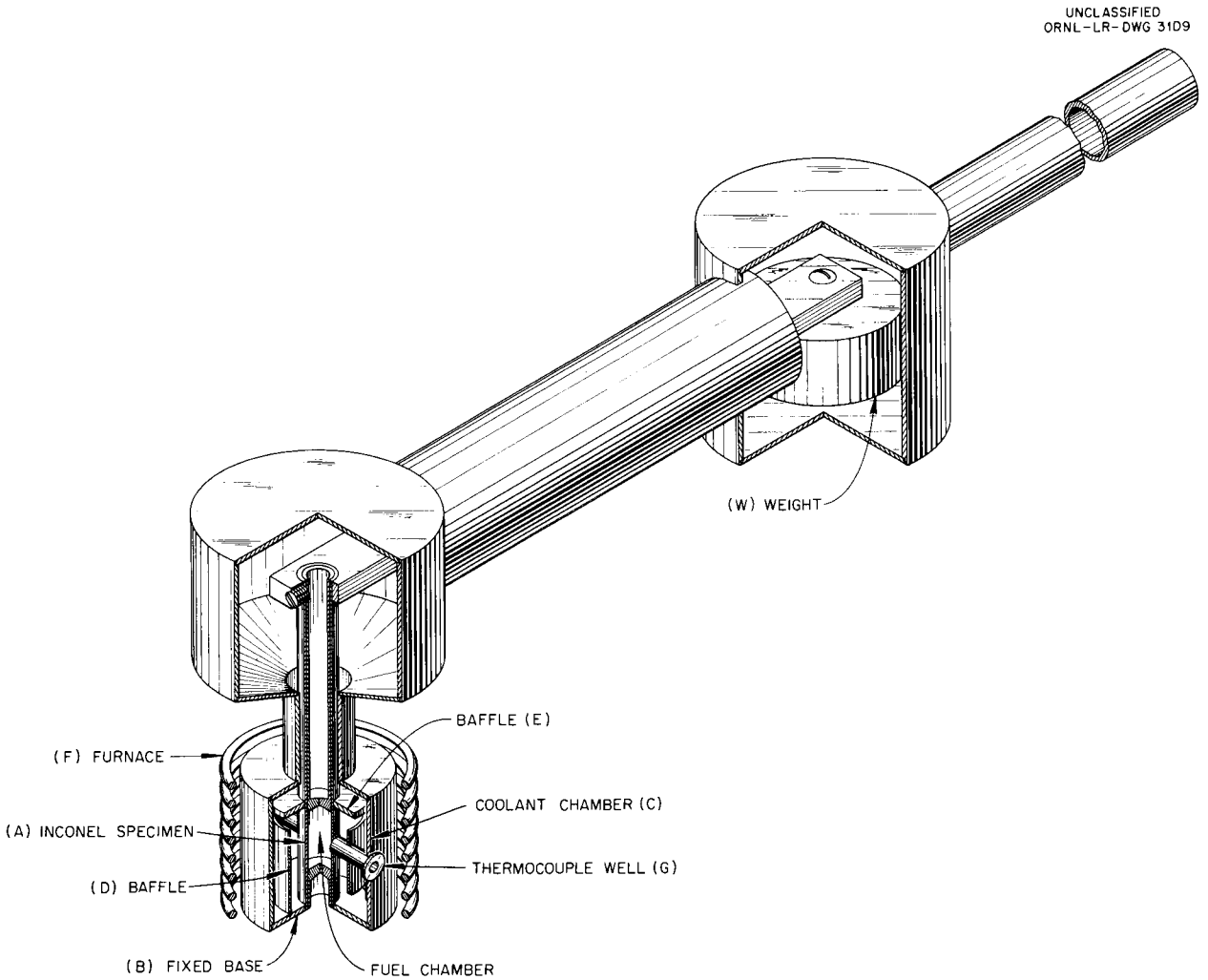

Fig. 1. Stress-Corrosion Apparatus.

The entire assembly is welded into a stainless steel water jacket furnished with Kovar seals and a capillary tube through which helium flows throughout the test. A probe beneath the weight cuts off the current to the furnace at a predetermined deflection of the lever arm and indicates the time required for a given degree of deformation. A gravity "tilt" indicator aids in plumbing the specimen in the exposure can. A base plate with a conical cup furnishes a well for the sodium in case of rupture during operation. A suitable safety system is being developed; a few modifications are contingent upon the results of the next bench test.

Approval by the LITR Experiment Review Committee is being withheld until additional tests are made on the compatibility of sodium with the various component materials it might contact if a rupture occurred at the test temperature. Several tests aimed at a qualitative determination of the speed of reaction and the heat generated by such reactions should be completed within a short time.

After an irradiation period of from two to six weeks in hole HB-3 of the LITR and a suitable decay period, the specimen is to be sectioned by the Remote Metallography Group and examined for stress-corrosion effects.

Bench tests on the specimen tube alone are under way with the outside surface in air. The inside of the tubes contain either air, helium, or salt No. 30. An atmosphere chamber has been built for testing

four specimens simultaneously in vacuum or any desired atmosphere. One 200-hr test has been completed on barren salt No. 30 at 1500°F and about 1500 psi. No stress dependence of corrosion was found; another specimen was operated for 400 hr but has not yet been examined. A melting and overturning technique for removing salt from the section that is to be examined metallographically has been successful; this will greatly simplify handling of irradiated capsules.

Apparatus for multiple tests of nickel and copper in vacuum and various atmospheres is being constructed. The MTR tensile creep test is scheduled for irradiation in September. The apparatus is being rewelded because shop-testing had destroyed part of the device.

PHILLIPS PETROLEUM COMPANY MTR TENSILE SPECIMENS

R. W. Hall[2] J. C. Wilson

Two sets of tensile specimens of 2S aluminum, 356 aluminum, QMV beryllium, and type 347 stainless steel irradiated to 3.5×10^{20} and 1×10^{21} neutrons/cm^2 (fast, >1 Mev) have been tested for hardness, density, length, diameter, yield and ultimate tensile strengths, elongation, and reduction of area. The results have been sent to R. L. Doan at the MTR. Both the 2S aluminum and type 347 stainless steel exhibited yield points in the irradiated condition; a yield phenomenon had been observed earlier in irradiated copper single crystals.[3] Remote operation of the Instron tensile machine was accomplished for the first time during these tests, and the hot-cell extensometer used in conjunction with the machine has operated satisfactorily on a variety of specimens.

URANIUM-ALUMINUM ALLOYS

W. W. Davis J. C. Wilson

Tensile tests were begun on a series of Hanford-irradiated aluminum alloys containing 30% natural uranium, 5% enriched uranium, and 15% enriched uranium. The enrichment was 93.5% in both enriched specimens. Thin, narrow, sheet specimens approximately 0.120×0.08 in. in cross section necessitated modification of the tensile-machine gripping arrangement so that no compressive or bending stresses would be introduced during closing of the grips. The irradiation temperature and integrated thermal flux were estimated to be 150°C and 10^{20} neutrons/cm^2 for the 6-month irradiation.

In the 5% alloy the yield strength increased from 15,300 psi before irradiation to 34,900 psi after irradiation, and the ultimate strength increased from 34,900 to 39,100 psi. For the 15% material the yield stress went from 21,700 to 58,600 psi, and the irradiated specimen broke at the latter stress. The ultimate strength of the control specimen was 25,300 psi and the elongation was 5%; the elongation on the irradiated specimen was about 0.3%. Several other specimens irradiated from 3 to 12 months are available for subsequent tests to determine the extent to which the damage may be annealed out. From the surface appearance of the specimens it is believed that the control (unirradiated) specimens were not so well annealed as the irradiated specimens; therefore it appeared likely that the strength values for the control specimens are too high for a fair comparison to be made between them and the irradiated material.

IMPACT TESTS

R. G. Berggren J. C. Wilson

Machining procedures for notching stainless steel impact specimens have been developed and have been used to prepare a number of specimens. These procedures are not yet satisfactory from the standpoint of economy of manpower, and further study is being given the specimen-fabrication problem.

Impact and tensile-test specimens of types 301, 302, 302B, 304L, 305, 321, and 347 stainless steel are at the MTR site for irradiation in an LB piece as soon as space is available.

Impact test specimens of type 321 stainless steel are currently being irradiated in hole HB-3 of the MTR. An irradiation plug for use in a horizontal beam hole of the MTR has been designed and is being fabricated. The irradiation temperature in this plug will be about 100°C. Data obtained from operation of this plug will be used in the design of a plug for irradiations at temperatures up to 300°C.

A number of irradiated steels are on hand, but impact tests have been delayed because of other test work in the hot cells.

[2] On loan from NACA, Cleveland.

[3] Unpublished data by T. H. Blewitt, ORNL.

FATIGUE TESTS

R. G. Berggren

Cantilever sheet fatigue specimens of type 301 stainless steel are at the MTR site for irradiation in an LB piece as soon as space becomes available.

Tests of subsize rotating-beam fatigue specimens have not been completely satisfactory; consequently, a study of the method of testing is being made.

STRAIN GAGES

J. C. Wilson

In an attempt to find suitable alloys for bonded-wire strain gages for use under irradiation, Karma wire (essentially 80% Ni and 20% Cr with iron and aluminum additions), Advance wire (constantan, composed of 45% Ni and 55% Cr), and paper and bakelite SR-4 gages were irradiated at 230°F for six weeks in hole HB-3 of the LITR.

Figure 2 shows the effect of neutron bombardment at 230°F on 0.001-in. Karma wire in three conditions: cold-drawn, annealed, and "special." Because of the high initial resistivity of the wire in the latter condition, it is believed that an ordering heat treatment had been given the metal. The behavior of the "special" wire under irradiation suggests that, at the onset of bombardment, disordering takes place as demonstrated earlier[4,5] by low-temperature irradiation of ordered Cu_3Au. After about 50 hr apparently enough lattice defects are produced by bombardment to cause enhanced diffusion and an accelerated rate of ordering results.

[4] S. Siegel and D. S. Billington, *Effect of Reactor Radiation on Metals*, TID-66, p 59 (Jan. 1949).

[5] T. H. Blewitt and R. R. Coltman, *Solid State Semiann. Prog. Rep. Feb. 28, 1954*, ORNL-1677, p 61.

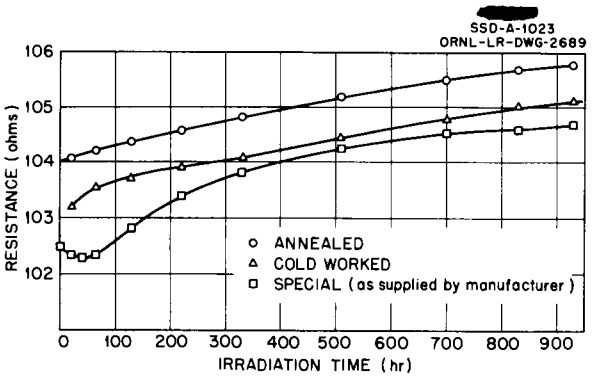

Fig. 2. Effect of Irradiation at 230°F in Hole HB-3 of the LITR on the Electrical Resistance of 0.001-in. Karma Wire in Three Conditions of Heat Treatment.

A sample from a second lot of Karma wire (0.005-in.-dia) was heated and cooled at various rates to determine the effect of the rate of heating or cooling on resistivity and temperature coefficient of resistivity. It may be seen from the curves in Fig. 3 that the temperature coefficient of resistivity is a function of temperature and the cooling rate. Apparently, a temperature range of nearly zero temperature coefficient of resistivity characterizes the slowly cooled material; the range is at higher temperatures for the slower cooling rates. This behavior might be utilized to advantage in strain gages for the HRE, where operation at about 600°F is desired. The most slowly cooled wire (curve 6 in Fig. 3) has a zero temperature coefficient of resistivity in this range, whereas the wire in the normally supplied condition (curve 1, slightly ordered) has a definite positive coefficient. Irradiations at higher temperatures will be made because of the possibility of finding a heat treatment that will condition the wire so that, at a given operating temperature, neutron bombardment will have little effect on its resistivity. If a proper treatment is found, wires such as Karma or Evanohm can be utilized for in-pile strain gages. The most substantial advantage of these wires is, of course, their high resistivity, which enables smaller gages (or higher resistivity gages) to be manufactured.

A paper-bonded SR-4 gage (type A-1) was included in the above irradiation; the paper disintegrated during the test and left the gage wire free. Advance wire is used in this type of gage. It is believed that the resistivity did not change appreciably, because the resistance of the gage assumed a constant value throughout the early stages of the test, passed through a brief period of increase, and then leveled out for the remainder of the test. It is suspected that the brief change in the resistance value was brought about by the stress being increased as the wire was freed of its paper support.

Two bakelite-bonded type SR-4 strain gages (type AB-1) mounted back-to-back on a dead-weight-loaded strip of steel were calibrated before irradiation. Postirradiation measurements have not been made with the specimen under load. The bakelite appeared to be somewhat blackened, but the gages were still bonded to the metal. During irradiation the resistance of the gages decreased about 0.2%.

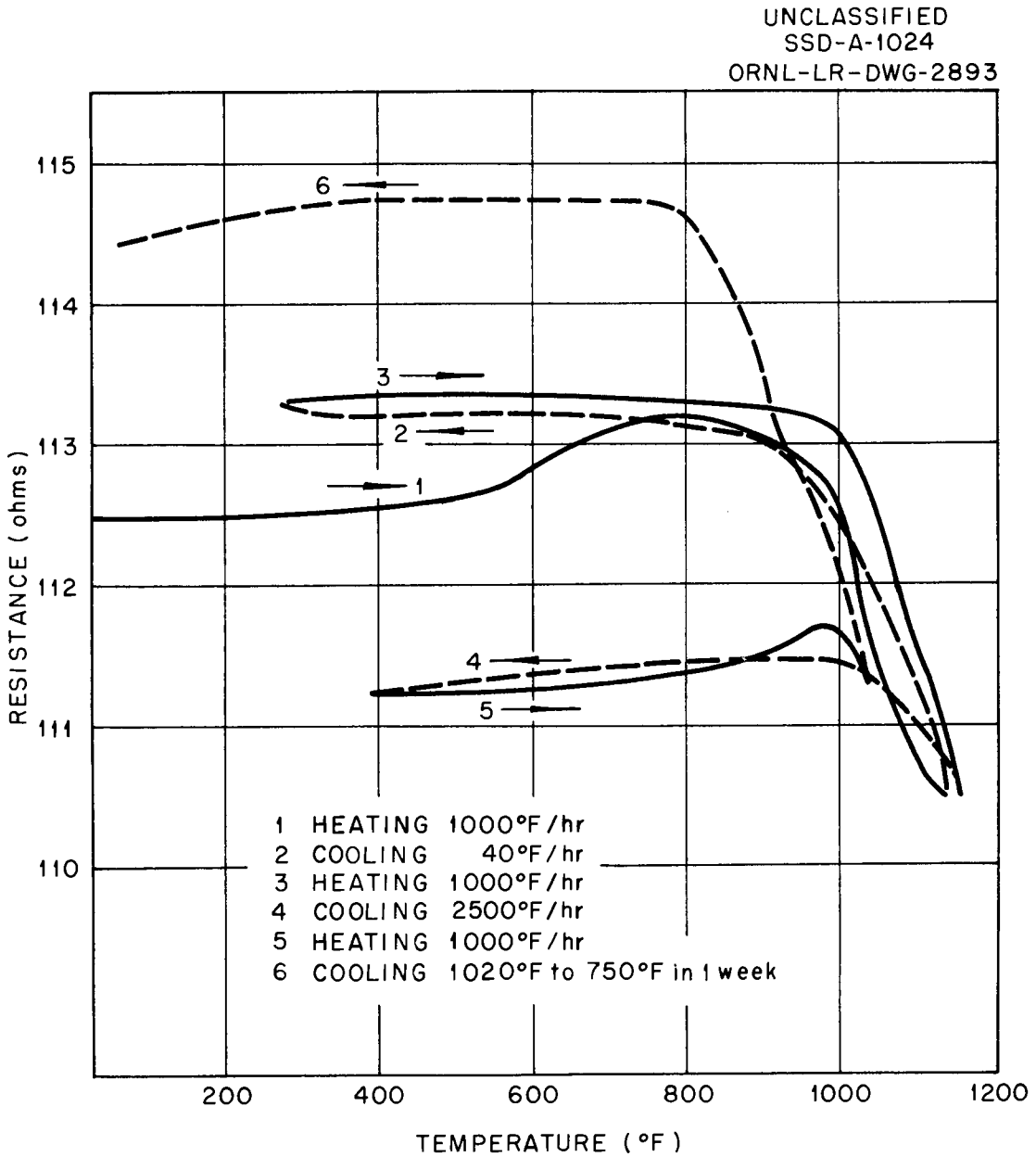

Fig. 3. Resistance vs Temperature Curves for 0.0005-in. Karma Wire.

HOT METALLOGRAPHY

M. J. Feldman W. Parsley
A. E. Richt R. N. Ramsey

Examination of six additional static-corrosion capsules irradiated in the MTR has been completed. Analysis of the examination is now in process. Of the six capsules examined, four were a continuation of the No. 30 salt corrosion tests and the other two were the initial capsules of the UF_3 salt series. All six samples were examined in longitudinal section.

Work has continued on the examination of the solid-type fuel sandwiches of interest to the Pratt & Whitney Aircraft Division. In addition to the two experiments mentioned in the previous semiannual report,[6] six other specimens have been examined.

[6] A. E. Richt, E. Schwartz, and M. J. Feldman, *Solid State Semiann. Prog. Rep. Feb. 28, 1954*, ORNL-1677, p 9.

The results on three of them (capsules 1-4, 1-6, 1-7) have been published.[7] A report covering the other three capsules (1-5, 1-8, 1-9) is in preparation. Points of major importance from results on the eight capsules processed to date are: bending of the stainless-matrix samples results in greater resistance to cracking and core-clad separation than bending of the iron-matrix samples; bending of the larger UO_2 particle size core results in better resistance to cracking than bending of the smaller particle size core; and irradiation of the small particle size core results in a greater increase in hardness than irradiation of the larger particle size core.

Work on solid-type fuel elements for the GE-ANP group has continued. Examination of two nichrome V wire fuel elements has been completed.[8,9] Examination of two single-plate fuel elements[10] and of one two-stage multiple-fuel-plate test assembly[11] has also been completed. Work will continue on both wire and multiple-plate elements.

Metallographic analysis of specimens from the HRE is also being carried on. Examination of six corrosion-test coupons has been completed.[12] Examination of various components of the reactor is now in progress, with work on a section of the core inlet line and a section of the core vessel now completed.[13] Work will continue on the project as required.

FISSION-FRAGMENT ANNEALING STUDIES

M. J. Feldman W. Parsley

Because of interest in the possibility of the removal of the radiation damage to fuel plates by annealing, a preliminary study was undertaken. The eight samples in Pratt & Whitney capsule 1-9 (four were small particle size, <3-μ UO_2, and four were large particle size, 15- to 44-μ UO_2) were selected for the study. Each sample was examined after it had been given one of the following treatments: (1) irradiation, no anneal; (2) irradiation followed by 900°F anneal for 24 hr; (3) irradiation followed by 1100°F anneal for 24 hr; and (4) irradiation followed by 1400°F anneal for 24 hr. A graph showing the results of this preliminary study is given in Fig. 4. The conclusion drawn from this initial study is that a portion of the neutron damage to the samples has been annealed out. Since the full annealing temperature for type 347 stainless steel is about 1800°F (for complete removal of the effects of cold work), a complete anneal for neutron damage at 1400°F was not expected. For the core, where the major portion of the damage is by fission fragments, it is felt that the curve shows a reduction in hardness because of a partial anneal of the neutron damage and no reduction in the fragment damage. An attempt will be made to determine the anneal necessary to remove all the neutron damage from this type of material and, if possible, the fission-fragment annealing temperatures.

HIGH-TEMPERATURE, SHORT-TIME-GRAIN-GROWTH CHARACTERISTICS OF INCONEL

M. J. Feldman A. E. Richt
W. Parsley

As an aid in the analysis of the static-corrosion capsules, a study was made of the high-temperature, short-time-grain-growth characteristics of the Inconel stock used for the tests. Information is available in the literature on the usual times and temperatures for Inconel grain growth, but because of the nature of the experiment, with its possibilities of local short-time hot spots in the fuel, this study was initiated. Figure 5 is a graph of the data obtained. Of major interest were the definite temperature dependence of the carbide solubility and the extremely short times (relative to the corrosion-test times) at which large grains could be produced. Details of the experiment have been published.[14]

[7] M. J. Feldman *et al.*, *Metallographic Analysis of Pratt and Whitney Capsules 1-4, 1-6, and 1-7*, ORNL CF-54-5-41 (May 5, 1954).

[8] M. J. Feldman *et al.*, *Metallographical Analysis of G. E. Wire Fuel Element No. 1*, ORNL CF-54-4-8 (April 1, 1954).

[9] M. J. Feldman, W. B. Parsley, R. N. Ramsey, and A. E. Richt, *Metallographical Analysis of G. E. Wire Fuel Element No. 2*, ORNL CF-54-9-142 (Sept. 22, 1954).

[10] A. E. Richt and R. N. Ramsey, *Metallographical Analysis of Single Plate Fuel Elements GE-ANP 3B and 3C*, ORNL CF-54-3-42 (March 9, 1954).

[11] M. J. Feldman *et al.*, *Metallographic Analysis of Two-Stage MTR Test Specimen GE-ANP-1B*, ORNL CF-54-7-77 (July 9, 1954).

[12] M. J. Feldman, W. B. Parsley, R. N. Ramsey, and A. E. Richt, *Metallographic Analysis of HRE Coupons and Coupon Holder, Report No. 1*, ORNL CF-54-7-110 (July 22, 1954).

[13] M. J. Feldman, W. B. Parsley, R. N. Ramsey, and A. E. Richt, *Metallographic Analysis of HRE Core and Fuel Inlet Line*, ORNL CF-54-8-216 (Aug. 16, 1954).

[14] M. J. Feldman, W. B. Parsley, R. N. Ramsey, and A. E. Richt, *Short Time—High Temperature Grain Growth Characteristic of Inconel*, ORNL CF-54-6-70 (June 8, 1954).

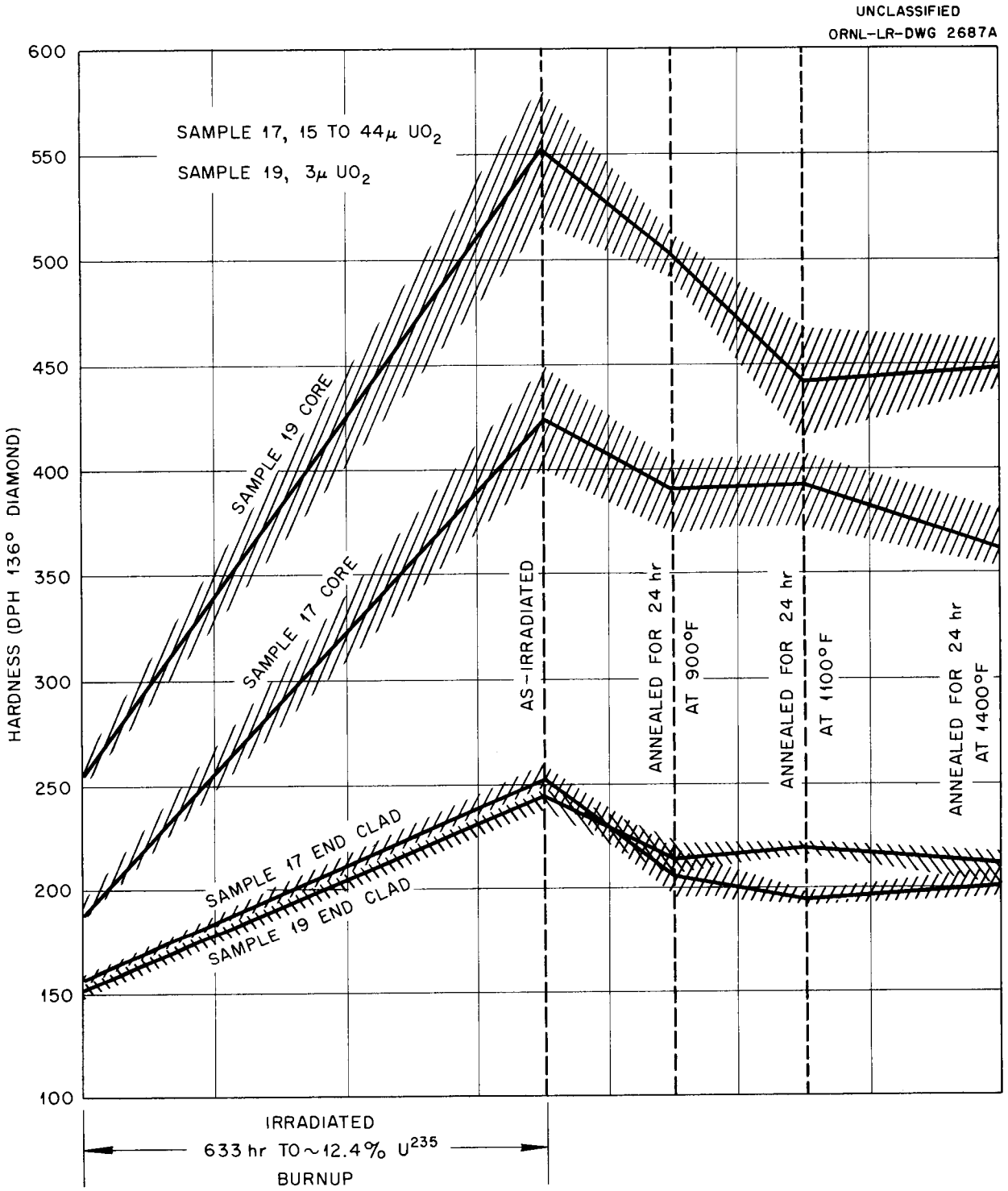

Fig. 4. Preliminary Annealing Study of Stainless Steel–UO_2 Fuel Plates in Pratt & Whitney Capsules.

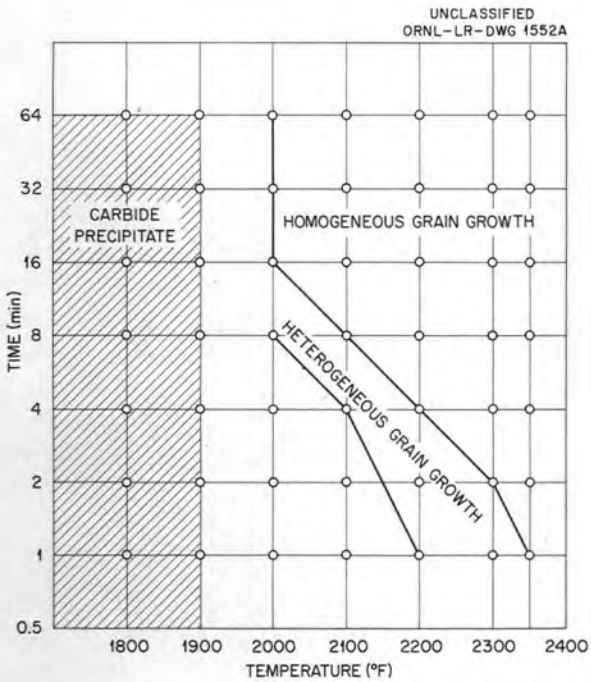

Fig. 5. Grain Growth Characteristics of Inconel.

USE OF ULTRASONIC CLEANING IN THE HOT CELL

M. J. Feldman M. G. Willey

Because of the complex mechanical nature of the present specimen cleaner[15] and its high cost of replacement and repair, the feasibility of adapting ultrasonic cleaning[16] in the hot cell was investigated.

Testing of specimens which had been subjected to conditions that duplicate the operations in the hot cell was done in the mockup shown in Fig. 6. The significant information gained from this mockup was a realization of the need for two transducers at right angles and for rotating the sample while it is in the high-intensity cleaning field. From this information a design for a working cleaner was derived; a sketch of the present model is shown in Fig. 7. Figure 8 is a diagram of the entire system to be utilized in hot-cell operation.

[15] M. J. Feldman and R. U. Acton, *Solid State Quar. Prog. Rep. Nov. 10, 1952*, ORNL-1429, p 22.

[16] M. J. Feldman, "Ultrasonic Cleaning in the Hot Cell," presented at the Brookhaven Hot Lab Meeting, May 1954, and to be published in *Nucleonics*.

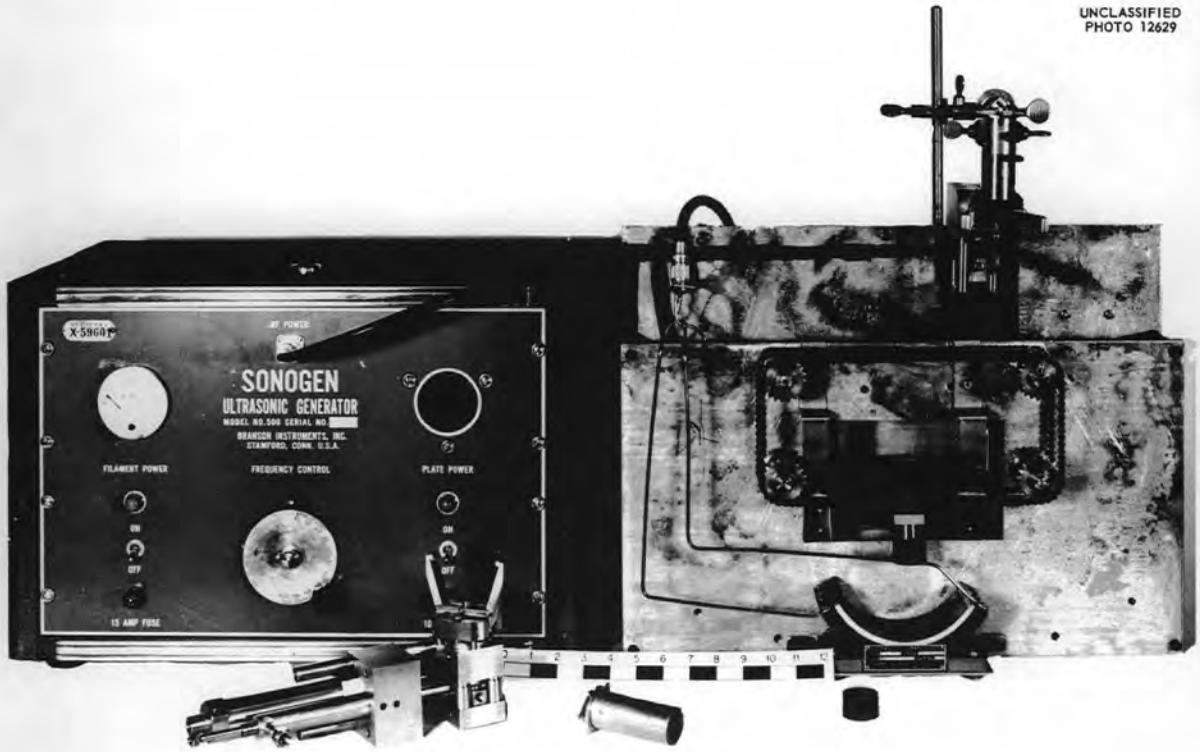

Fig. 6. Test Apparatus for Ultrasonic Specimen Cleaner.

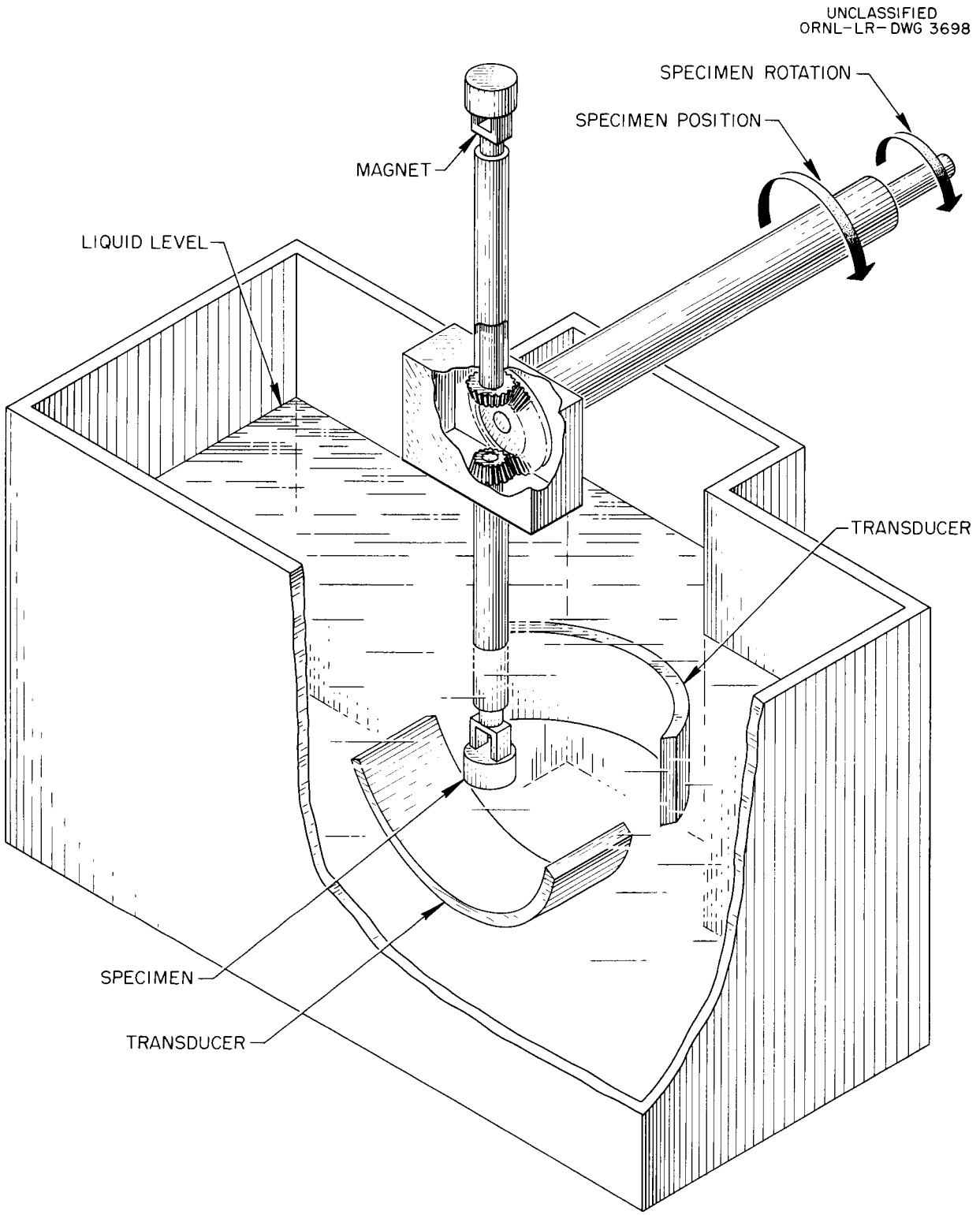

Fig. 7. Proposed Ultrasonic Specimen-Cleaning Unit.

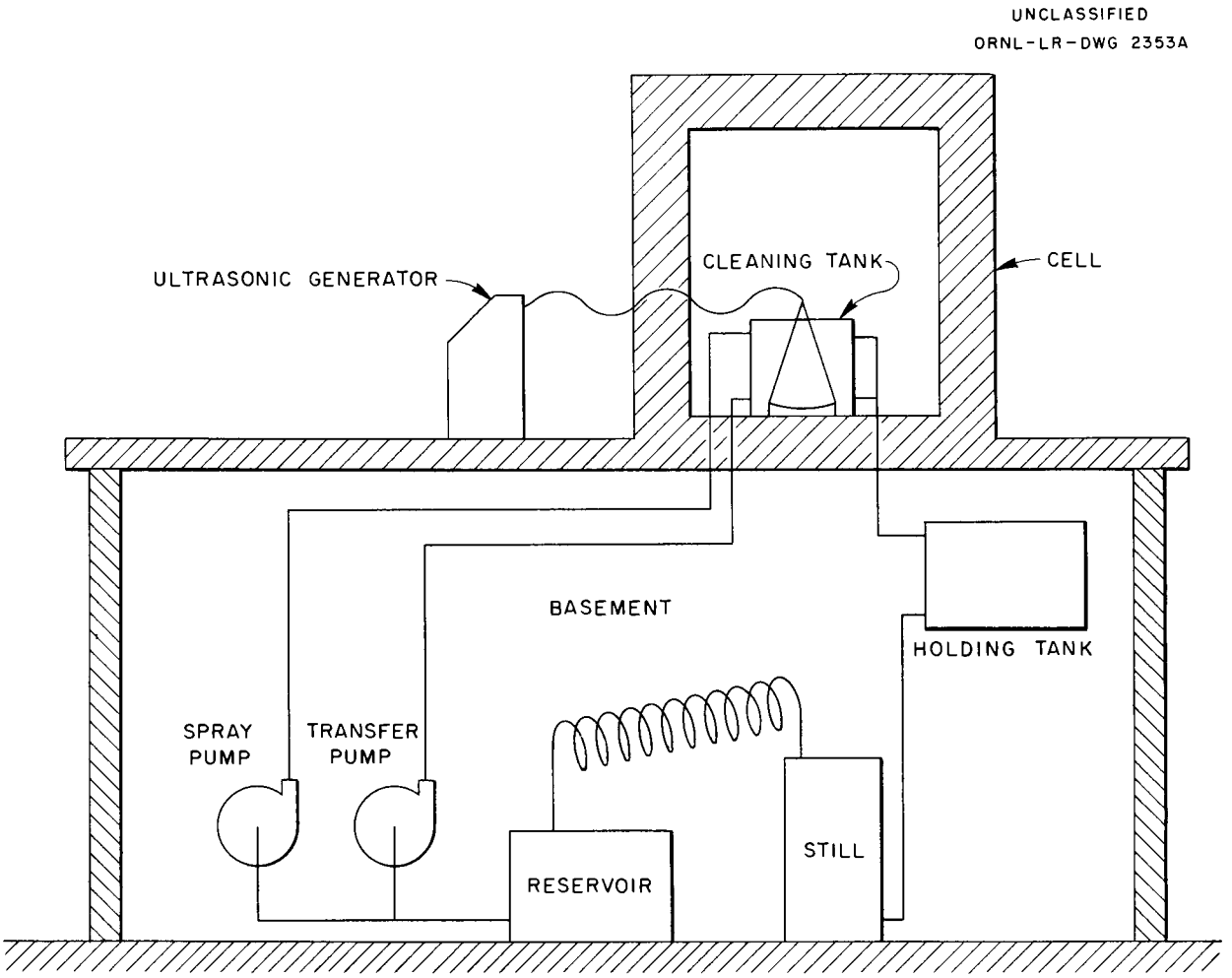

Fig. 8. Ultrasonic Cleaning-Block Diagram.

SIMPLIFIED ADAPTATION OF METALLOGRAPHIC POLISHING UNIT FOR REMOTE OPERATION

M. J. Feldman W. Parsley

Operation with the remote polishing unit, as described in an earlier report,[15] has been successful enough to warrant utilization of the same basic design in plans for the expansion of the hot-cell facility. In the original design of the polishing units great care was taken to ensure perfect parallelism of the many parts. To do this, bearings were replaced and a new bowl was cast and machined. Also, in the original model the turret drive was linked directly to the polishing-plate drive by means of a gear train.

When it was requested that the present facility be expanded, thought was given to a more simple and less expensive means of adapting the polishing units for remote operation. The first step was to replace the inset gear train used for driving the polishing turret with an exterior-mounted motor. There were two reasons for this change: maintenance on the gear train or shaft was difficult because it entailed disassembly of the entire unit, and the machining cost in making and installing the inset gear train was higher than the cost of an additional motor. The second step in adapting the polishing units for remote operation was to utilize the existing ceramic-covered cast bowl. The unit was completely disassembled, and all mating surfaces were ground true to the motor shaft. An advantage of this method is that the parallelism of the turret (and the samples) to the polishing plate is not affected by the manner in which the units are mounted to the table. The upper rounded edge

Fig. 9. Remotely Controlled Specimen-Polishing Unit.

of the bowl was ground flat to accommodate the cover plate, and then the ground surface was checked with a gage attached to the polishing disk. Figure 9 shows the external motor drive on one of of the original remote units. The adaptation of a table unit for remote operation is shown in Fig. 10, and, in more detail, in the operating and disassembled conditions in Figs. 11 and 12.

Material and labor costs for the conversion were approximately $50 and $600, respectively; the motor cost about $35. The new units can be installed in the cell for less than $1000 each; the units now in use cost about $6000 each. Present plans call for the installation of four new units flush-mounted on a stainless plate in the hot cell.

CELL EXTENSION

M. J. Feldman R. Hawkins[17]

The basic ideas on the extension to the metallographic cell are shown in Fig. 13. The extension will be constructed of 1-in. steel plate laminated to a 6-in. thickness. The cell will be separated

[17]Pratt & Whitney Aircraft Division.

Fig. 10. Metallographic Specimen Polishing Table Adapted for Hot-Cell Use.

Fig. 11. Details of Assembled Polishing Head on Metallographic Specimen-Polishing Table.

Fig. 12. Disassembled Polishing Head on Metallographic Specimen-Polishing Table.

into two areas, one for optical equipment and the other for chemical operations such as etching.

The cell is so designed as to incorporate the stage of the research metallograph inside the cell and yet leave the entire metallograph as an easily removable unit. Also included in the design is a section of the floor in the chemical cell which can be lowered so that fresh solutions can be introduced from the outside. The Tukon hardness tester is positioned in the cell so that the optical system can be brought to the front face of the cell by means of a right-angle extension to the standard microscope. The base of the hardness tester extends through the cell floor and will be encased in a lead-brick chimney. The Bausch & Lomb GBILS metallograph now being used for photography will have its bellows removed and will be placed in the chemical area. The photographic ocular will be extended to project through the wall, and the unit will be used to examine etched samples prior to photography. Also incorporated in the optical section of the extension is the stereomacroperiscope, which will be used for survey and macrophotography.

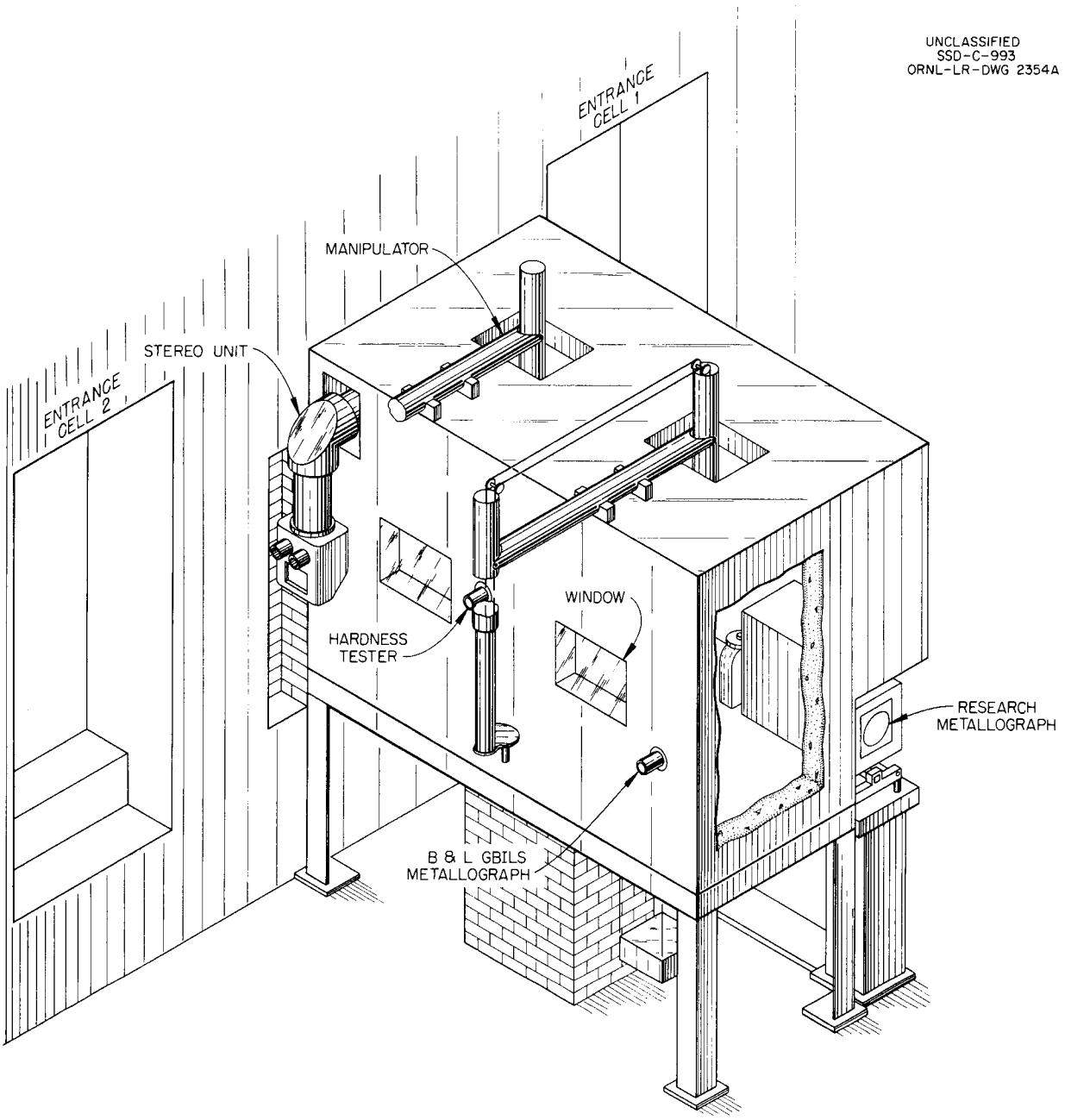

Fig. 13. Metallographic-Cell Extension.

NUCLEAR MEASUREMENTS

BNL NEUTRON SPECTRUM – RADIATION DAMAGE STUDY

J. B. Trice
P. M. Uthe
N. Shiells[1]
J. G. Carroll[1]
R. Bolt[1]
V. Walsh[2]

A series of measurements were made in hole E-25 of the Brookhaven Reactor to determine neutron-flux energy distributions. The project was a cooperative effort with California Research Corporation and Brookhaven National Laboratory. Information obtained from these measurements is to be used for correlating neutron-flux intensity and energy distribution with radiation damage to certain lubricants and organic compounds that have been irradiated in E-25 and examined by CRC.

Data for the irradiated samples have been coded for the ORACLE by the Mathematics Panel so that the large number of arithmetical computations usually required by a threshold-detector experiment can be performed in a shorter period of time than is usual.

[1]California Research Corporation.

[2]Brookhaven National Laboratory.

[3]General Electric Company.

[4]J. B. Trice and P. M. Uthe, *Solid State Semiann. Prog. Rep. Feb. 28, 1954*, ORNL-1677, p 14.

MTR NEUTRON-FLUX SPECTRA – RADIATION DAMAGE STUDY

P. M. Uthe
T. L. Trent
J. B. Trice
J. Moteff[3]

Fission probes having different fissionable materials are being used to make neutron-flux traverses in facility HB-3 of the MTR. Fissionable material used included U^{238}, U^{236}, Np^{237}, and Th^{232}, whose fission threshold energies span the energy region between ½ and 2 Mev. The data from these traverses will be used with the results from activations in HB-3 of other, nonfissionable, threshold detectors that are in the process of being irradiated.

After measurements have been completed in HB-3 with the hole empty, several inches of beryllium will be introduced into the hole in such a way as to change the energy distribution of the transmitted neutrons.

The new energy distribution will then be measured; afterward, certain materials will be irradiated in both moderated and unmoderated neutron spectra, and an attempt will be made to correlate spectra and radiation damage.[4]

ENGINEERING PROPERTIES

[redacted]

LITR FLUORIDE-FUEL LOOP

W. E. Brundage
C. D. Baumann
F. M. Blacksher
R. M. Carroll
J. R. Duckworth
C. Ellis
M. T. Morgan
A. S. Olson
W. W. Parkinson
O. Sisman

The design and the major part of the construction of a loop for the study of the stability and corrosion behavior of molten-salt fuels under irradiation were described earlier.[1] This loop was inserted in hole HB-2 of the LITR the last week in May and was filled with $NaF\text{-}ZrF_4\text{-}UF_4$ (62.5-12.5-25 mole %) on June 9 during a protracted reactor shutdown. Circulation was started as soon as sufficient fuel had been added to the pump but became erratic after 5 to 10 min and finally stopped completely. Fluoride fumes in the off-gas line from the jacket around the pump indicated a leak; so the loop was removed before the reactor was started.

The loop was carefully disassembled to avoid loss of uranium because over 5 kg of enriched fuel mixture had been used to charge the loop. Recovery of the fuel from the "nosepiece" at the in-pile end of the loop had to be carried out in a hot cell because of neutron activation acquired when the unfilled loop was exposed to reactor flux before the fuel was added. The leak was found in the weld joining the loop tubing to the discharge nipple at the bottom of the pump bowl. A view of the bottom of the pump bowl with the tubing broken away from the discharge nipple is shown in Fig. 14, with insets of the broken weld on the tube end and the nipple. Complete breaking of the weld probably occurred during disassembly of the loop or during cutting of the pump jacket rather than while the loop was in operation.

For clarity in depicting the details of the construction of the loop, the schematic drawing in an earlier report[1] is reprinted in Fig. 15. The bare loop, in its framework of support rods, is shown in a composite photograph, Fig. 16. Along with the air motor, the pump for the loop is shown mounted in the pump shield in Fig. 17.

Figure 18 (a composite photograph) shows the loop after tubular heaters had been attached to the loop tubing with stainless steel tape and after the thermocouples, thermal insulation, and a small part of the graphite and B_4C-Fe radiation shield blocks had been installed. The thermocouples were located at appropriate points, usually by welding directly to the loop tubing or to the bottom of a well. A composite of the completed loop, in the water jacket, ready for insertion in the reactor is shown in Fig. 19.

The jacket for enclosing the loop and pump in an inert atmosphere was tested for gas tightness, and the loop, with the pump superstructure replaced by a blank flange, was vacuum-tested at 800 to 1000°F with a helium leak detector before the assembly was inserted in the reactor.

After the loop was inserted in the reactor, it was pressure-tested at 1200 to 1500°F and 16 psig, and there was no perceptible loss in pressure over a 1-hr period even though the pump superstructure with its rotating shaft seal was in place. During installation of the loop in the reactor an unexpectedly long time was required to connect heater and thermocouple leads and air, water, and helium piping in the confined space available between the shielding and the instrument panel. Presented in Fig. 20 is a top view of the pump shield and supplementary shield, with the access plug removed, after the loop was installed in the reactor. After the insulated filling line and the air motor for the pump were connected, the shields were augmented with lead brick, and the photograph (Fig. 21) was made. Front and rear views of the instrument panel are shown in Figs. 22 and 23.

The piping at the reactor face is being revised to facilitate connection of the second loop when it is ready for insertion so that installation may be performed more rapidly. Modifications are also being made so that lag in the flow alarms for the jacket cooling water can be removed. The oil system for cooling the pumps is being rebuilt to incorporate more reliable pumps and improve flow and alarm instruments.

The connections of the loop tubing at the pump have been redesigned for the second loop to provide a fill and drain line. This will permit the loop to be charged with fluoride mixture containing no uranium, the mixture to be circulated at operating temperature, and the loop to be drained prior to insertion in the reactor. The danger of tube rupture caused by expansion of the fuel on melting

[1] W. E. Brundage *et al.*, *Solid State Semiann. Prog. Rep. Feb. 28, 1954*, ORNL-1677, p 17.

[redacted]
PHOTO 12997

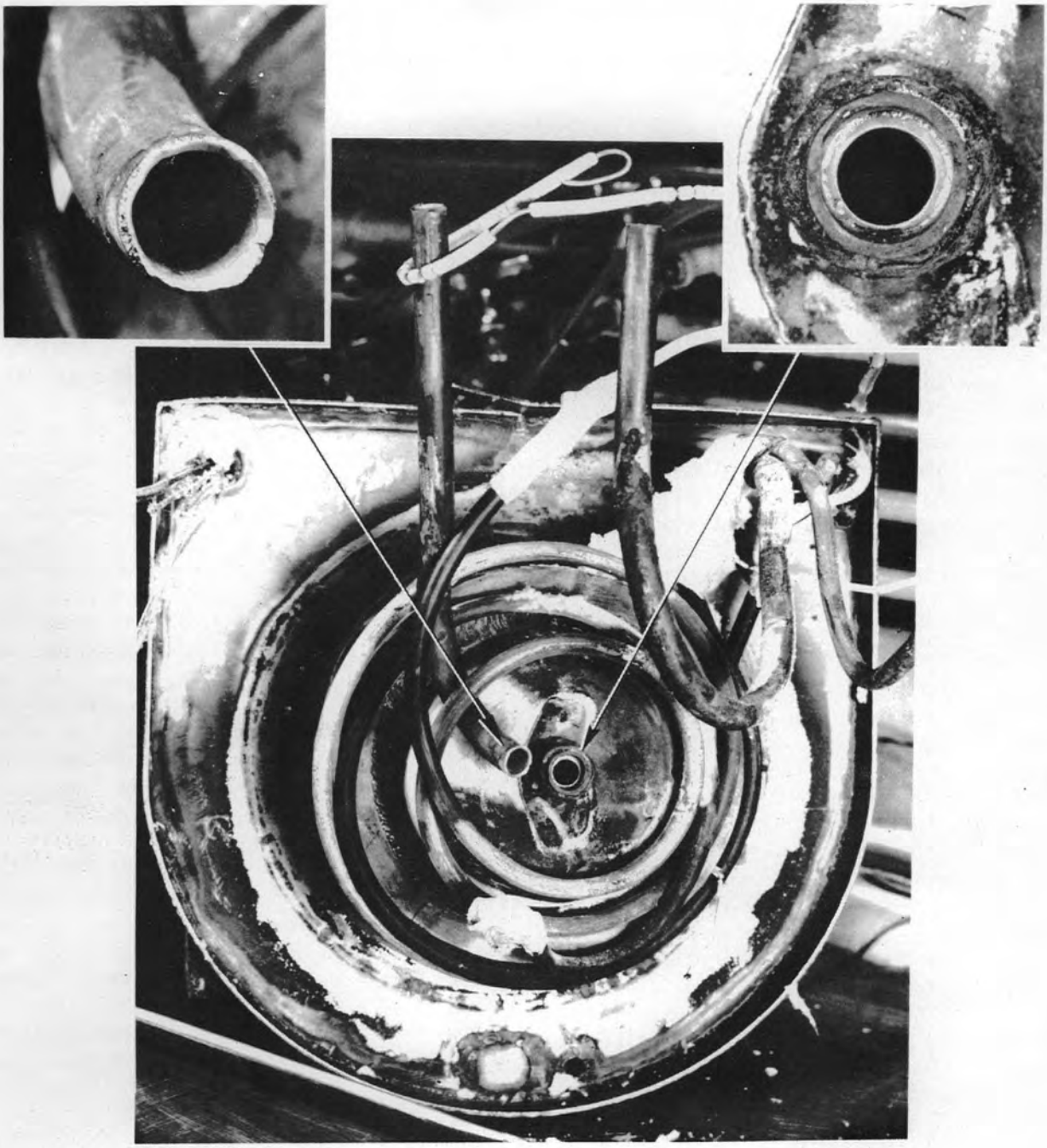

Fig. 14. Bottom of Fluoride Loop Pump Bowl Showing Defective Weld at Discharge Nipple.

[redacted] DWG. 23122

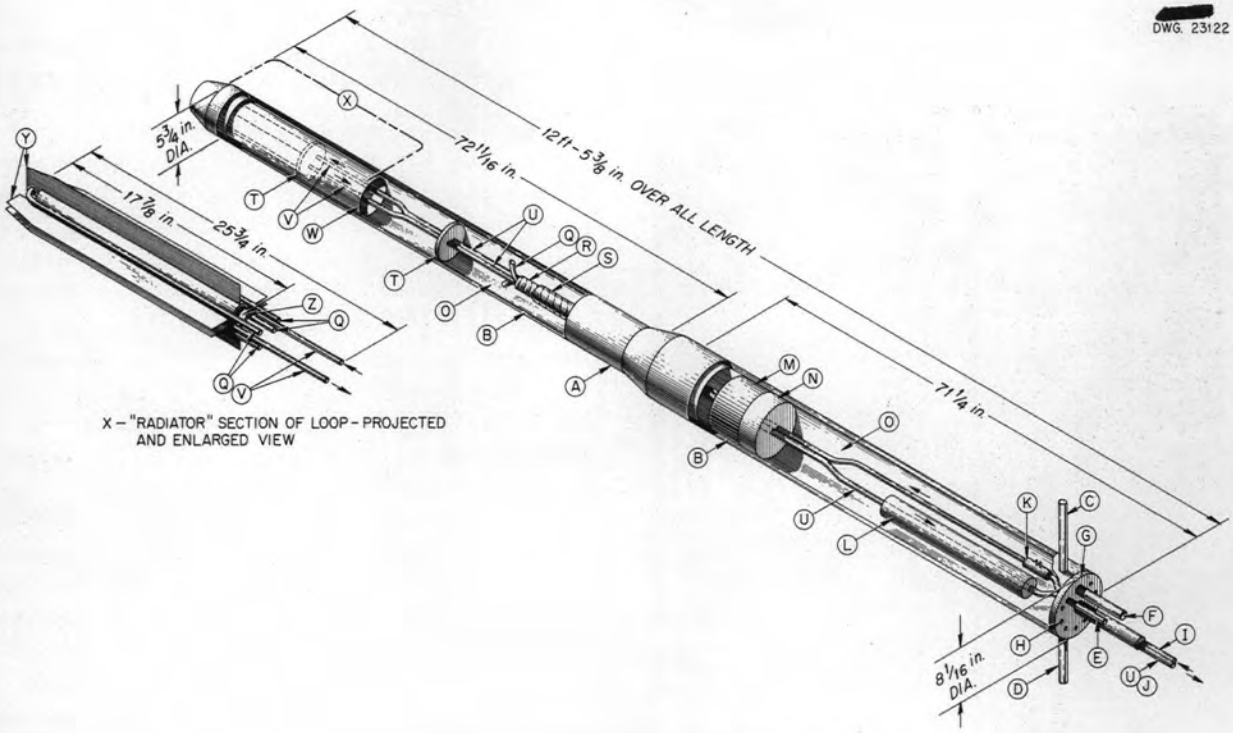

Fig. 15. LITR Fluoride-Fuel Loop Assembly.

[redacted] PHOTO 12998A

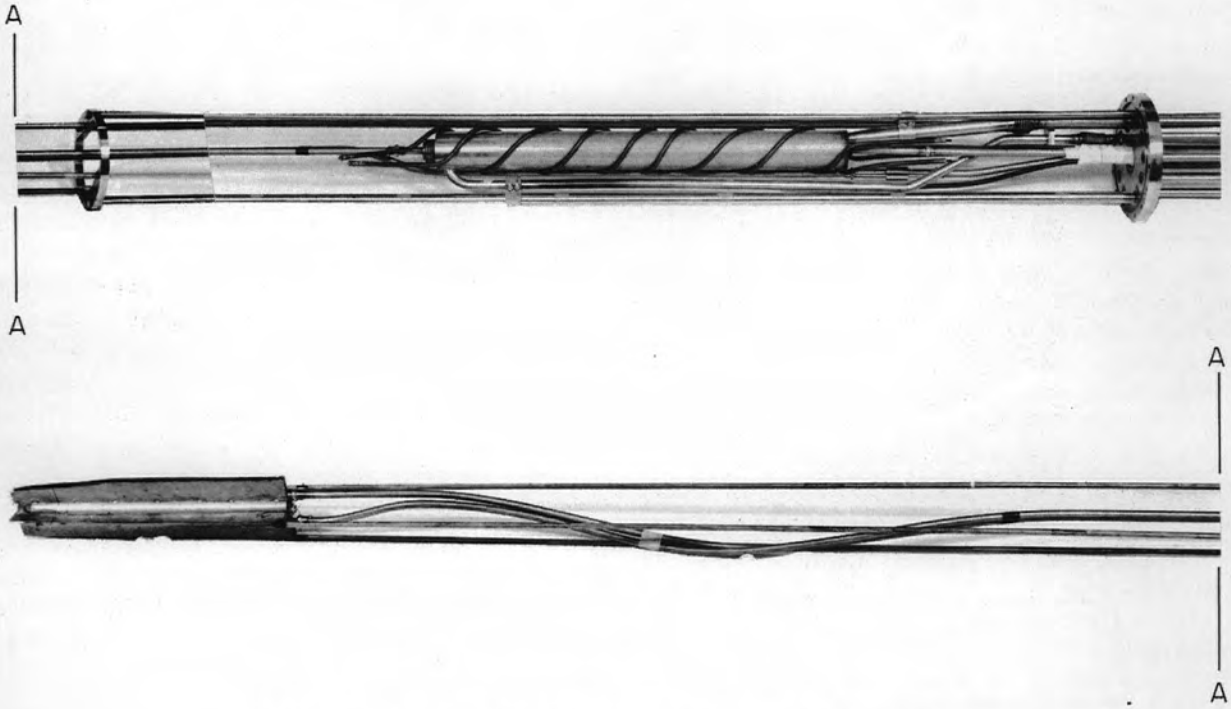

Fig. 16. Bare Fluoride-Fuel Loop with Support Framework.

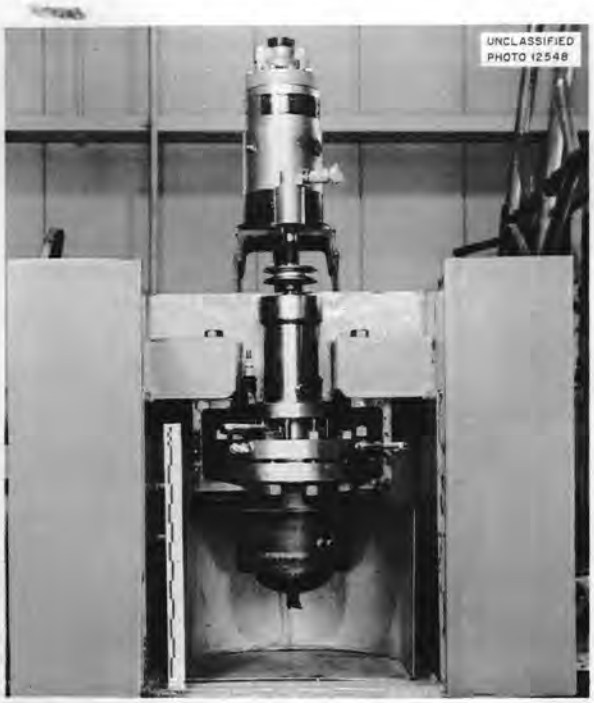

Fig. 17. Fluoride-Fuel Pump and Shield.

necessitates the draining and refilling feature, if operating tests are to be carried out. The necessary changes in the pump shield to accommodate the drain and fill line are being made.

The Metallurgy Division has agreed to perform all critical welding and has provided specifications for an improved weld joint developed for Inconel tubing. The components fabricated previously for the second loop are being changed to conform to the specifications for the new weld joints. A new flange for closing the rear of the jacket has been made in order to provide more space for making pipe connections to the large air lines required for the heat exchanger. The second loop is scheduled for insertion in the reactor in December.

A hydraulically operated door to match the withdrawal shield has been installed in a wall of a Solid State Division hot cell in preparation for handling of the loop after irradiation. A horizontal band saw has been modified for almost complete remote operation and is being installed in the hot cell. Other remotely operated handling tools for disassembling the loop have been made and are being tested.

ORNL GRAPHITE REACTOR SODIUM-INCONEL LOOP

W. E. Brundage W. W. Parkinson

The sodium-Inconel loop described previously[2,3] was removed from the ORNL Graphite Reactor after it had operated for 218 hr with the irradiated section at 1500°F. The temperature of the pump-cell section was held between 1025 and 1100°F, but that of the line entering the reactor ran somewhat higher; the temperature of the line emerging from the reactor was about 1500°F. Before insertion in the reactor, the loop had been operated at 800 to 1000°F for 80 hr while sodium was circulated through the loop and through a bypass filter circuit connected to the loop.

Two types of specimens were available from the loop: weighed plates of Inconel and of 300-series stainless steels and tube sections cut from the loop tubing. Specimens for metallographic examination were cut from the loop as shown in Fig. 24, from both the irradiated and unirradiated ends of the entering tube, from the same ends of the emerging tube, and from the U-section of tubing at the in-pile end of the loop where the leak occurred. In addition, control specimens had been retained of the as-received tubing used for each of the parts mentioned above. Photomicrographs of transverse sections of the tube wall after the conventional polishing and electrolytic etching in 10% oxalic acid are shown in Figs. 25 through 32. All metallographic examinations were done by R. J. Gray of the Metallurgy Division.

Figure 25 shows an as-received piece of the tube that was used as the control for the specimens shown in Fig. 26 (the unirradiated end) and in Fig. 27 (the irradiated end). Figure 28 shows an as-received portion of the tube used for the emerging tube, from which were taken the specimens shown in Fig. 29 (the unirradiated end) and in Fig. 30 (the irradiated end). The as-received control for the U-section at the irradiated end of the loop is shown in Fig. 31, while Fig. 32 shows a section from the U-bend.

The Inconel used for the U-bend was coarser grained than the metal for the entering and emerging tubes; it also lacked the intragranular carbide precipitate present in the other specimens. During operation of the loop, however, the precipitate

[2] W. E. Brundage and M. T. Morgan, *Solid State Semiann. Prog. Rep. Feb. 28, 1954*, ORNL-1677, p 19.

[3] C. D. Baumann *et al.*, *Solid-State Quar. Prog. Rep. Feb. 10, 1953*, ORNL-1506, p 13.

[redacted]

PHOTO 12998C

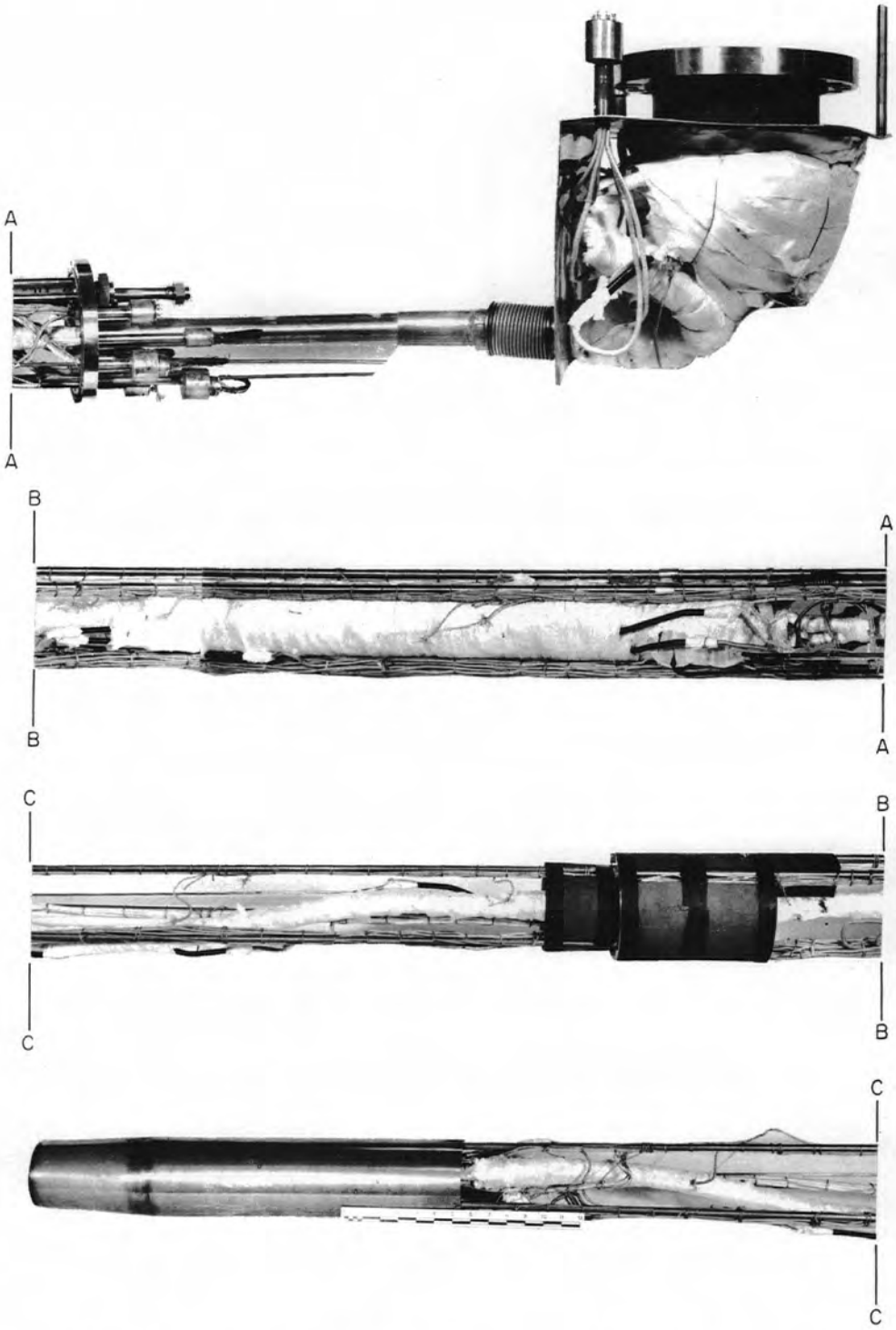

Fig. 18. Loop with Heaters, Thermocouples, Insulation, and Shielding.

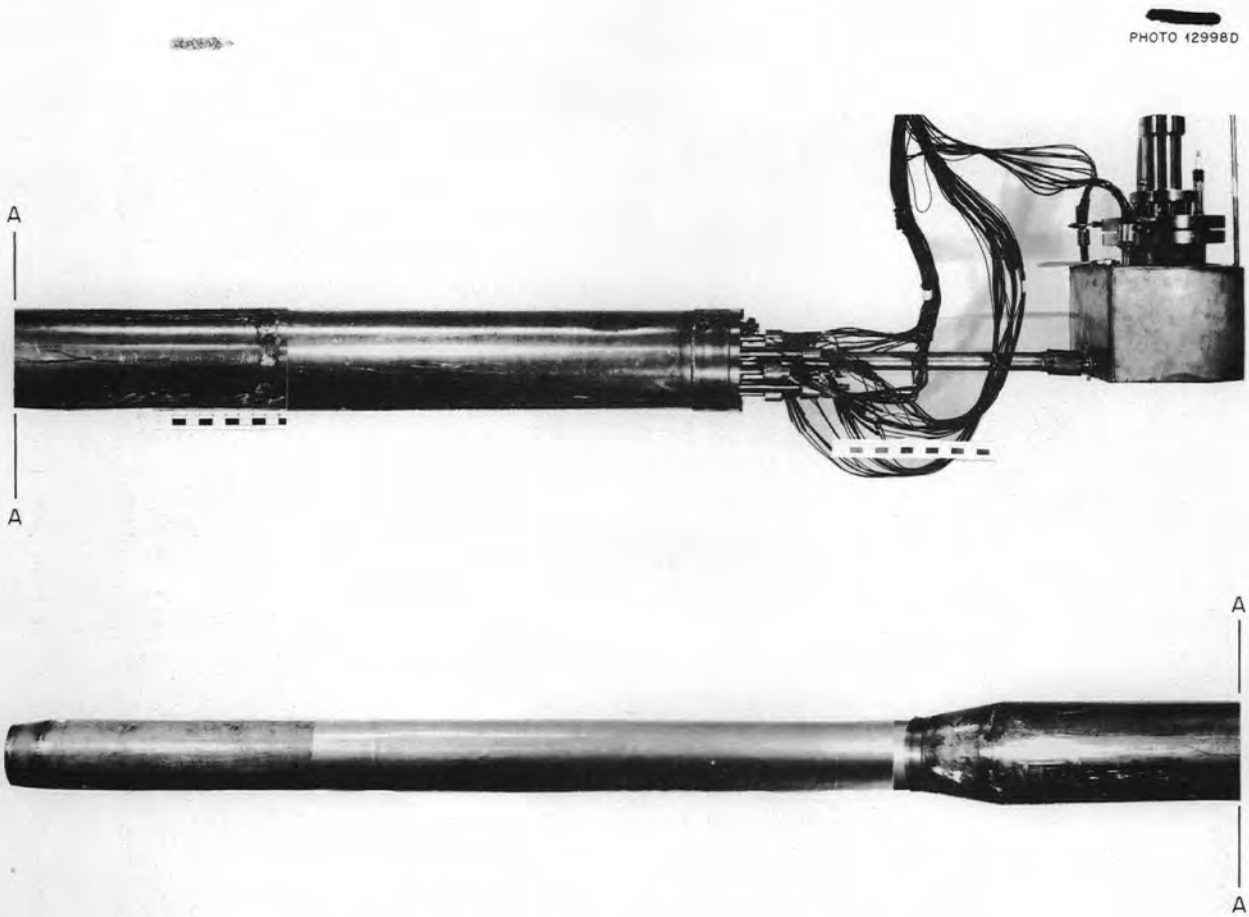

Fig. 19. Fluoride-Fuel Loop in Its Water Jacket.

appeared (Fig. 32) and outer-surface grain boundaries showed evidence of incipient fusion. This is significant, since the leak was found to be a ragged crack ¼ in. long across the peripheral surface of the U-bend. Electrical arcing that accompanied failure of the tubular heaters might have produced local overheating.

Three specimens from the entering and emerging tubing (Figs. 26, 27, and 30) show removal of the carbide precipitate near the surface exposed to sodium and also show grain growth in this region. The unirradiated end of the emerging tube (Fig. 29) did not undergo this loss of precipitate and showed no grain growth. The temperature at this point was not known precisely, and no explanation can be advanced at this time for the difference in this specimen.

The photomicrographs clearly show, except for the decarburization mentioned, that there is no perceptible corrosion effect on the Inconel by the sodium stream, either in the reactor radiation field or out of it. Examination of the specimen plates of Inconel and of various stainless steels will complete the work on sodium loops in the ORNL Graphite Reactor.

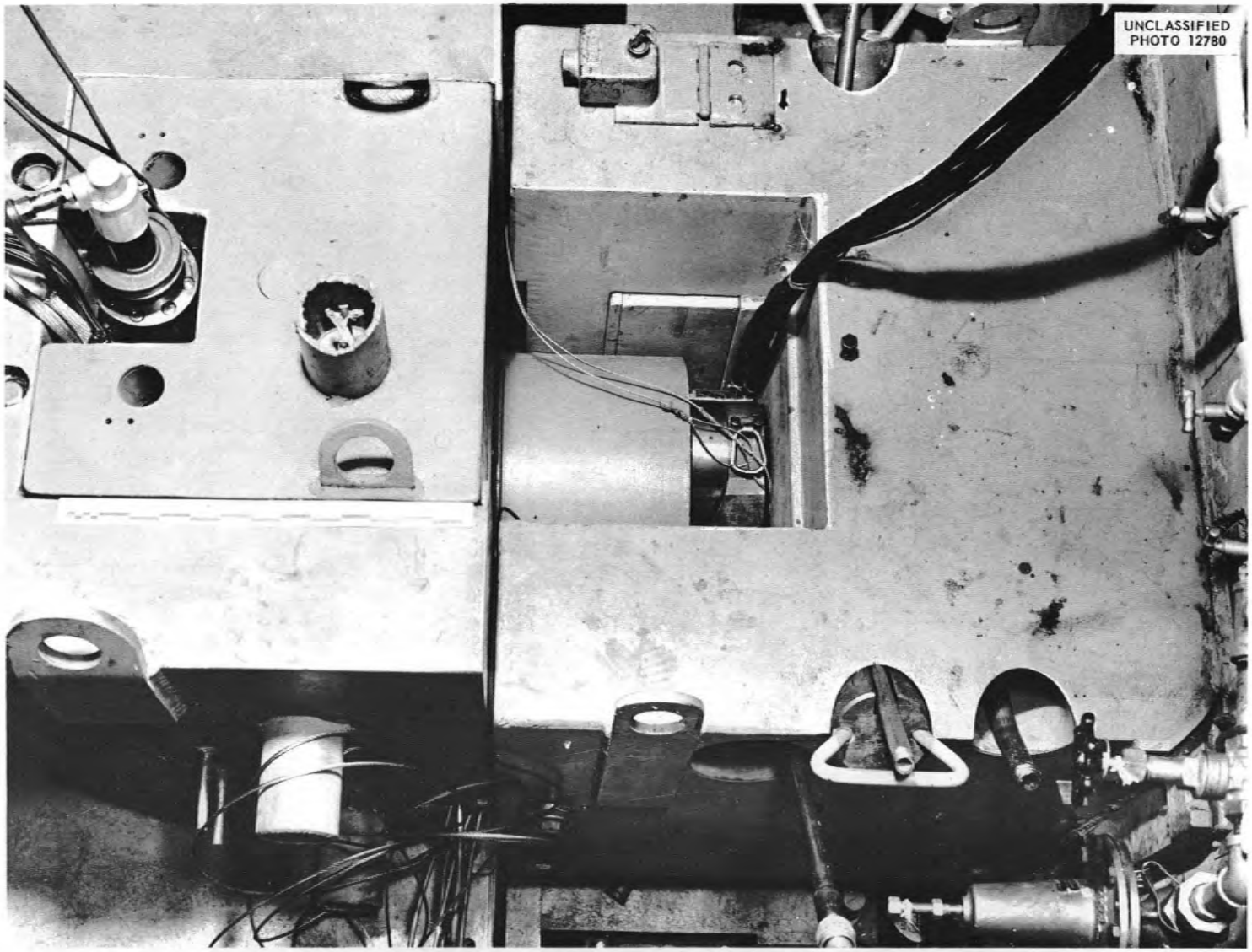

Fig. 20. Pump Shield and Supplementary Shield for Fluoride-Fuel Loop Installation.

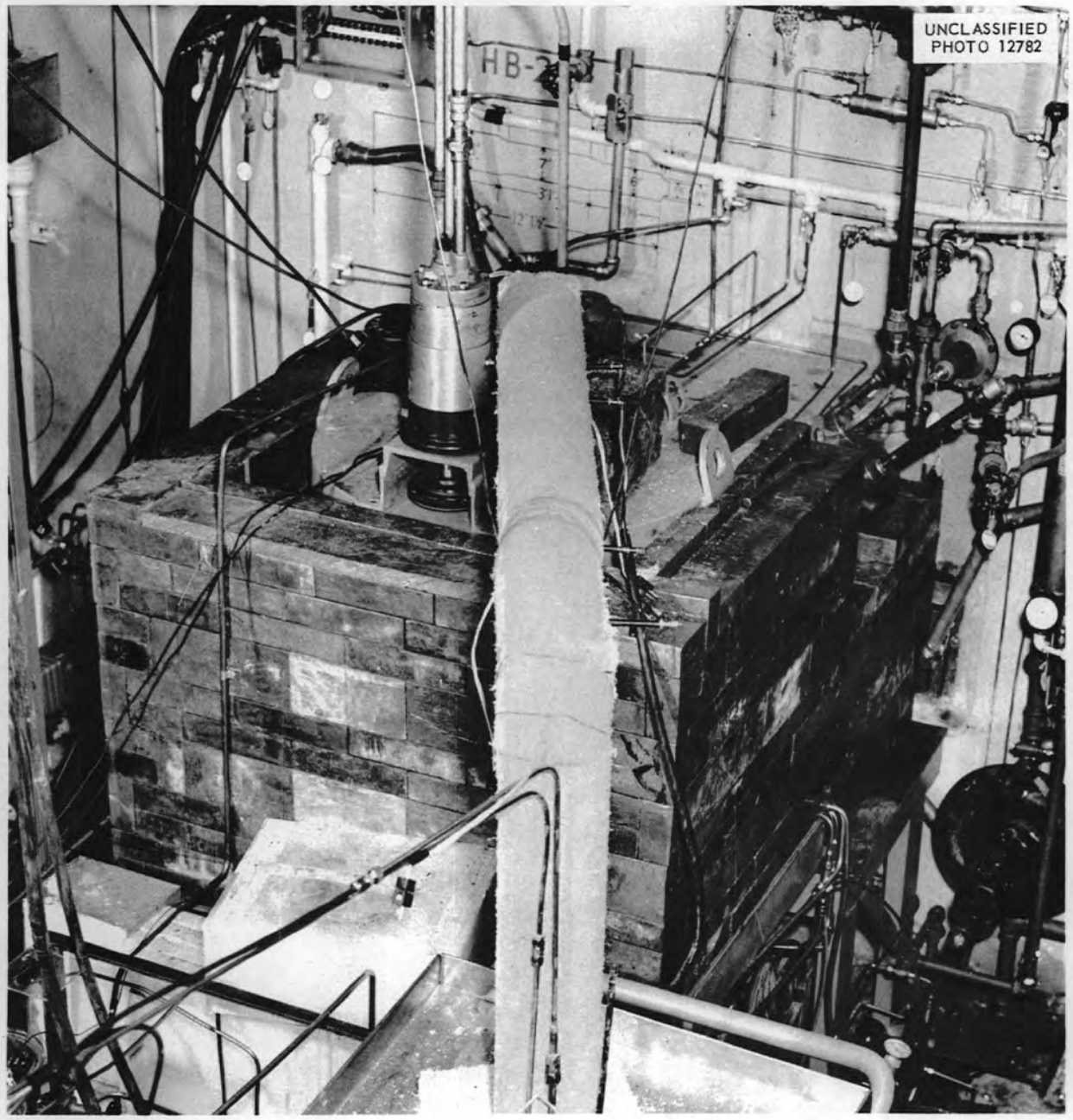

Fig. 21. Fluoride-Fuel Loop Shields with Lead Brick Added.

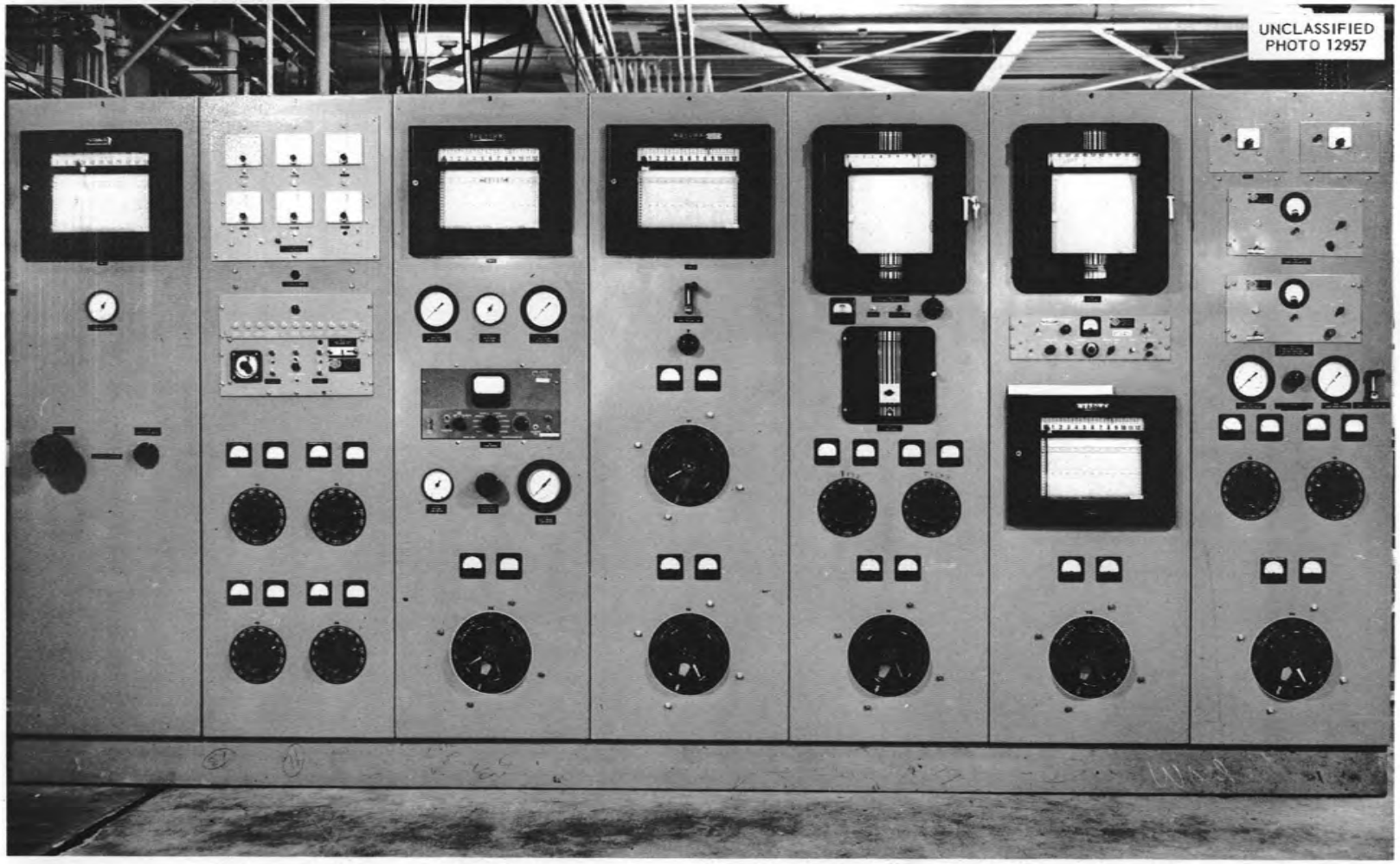

Fig. 22. Front View of Fluoride-Fuel Loop Control Panel.

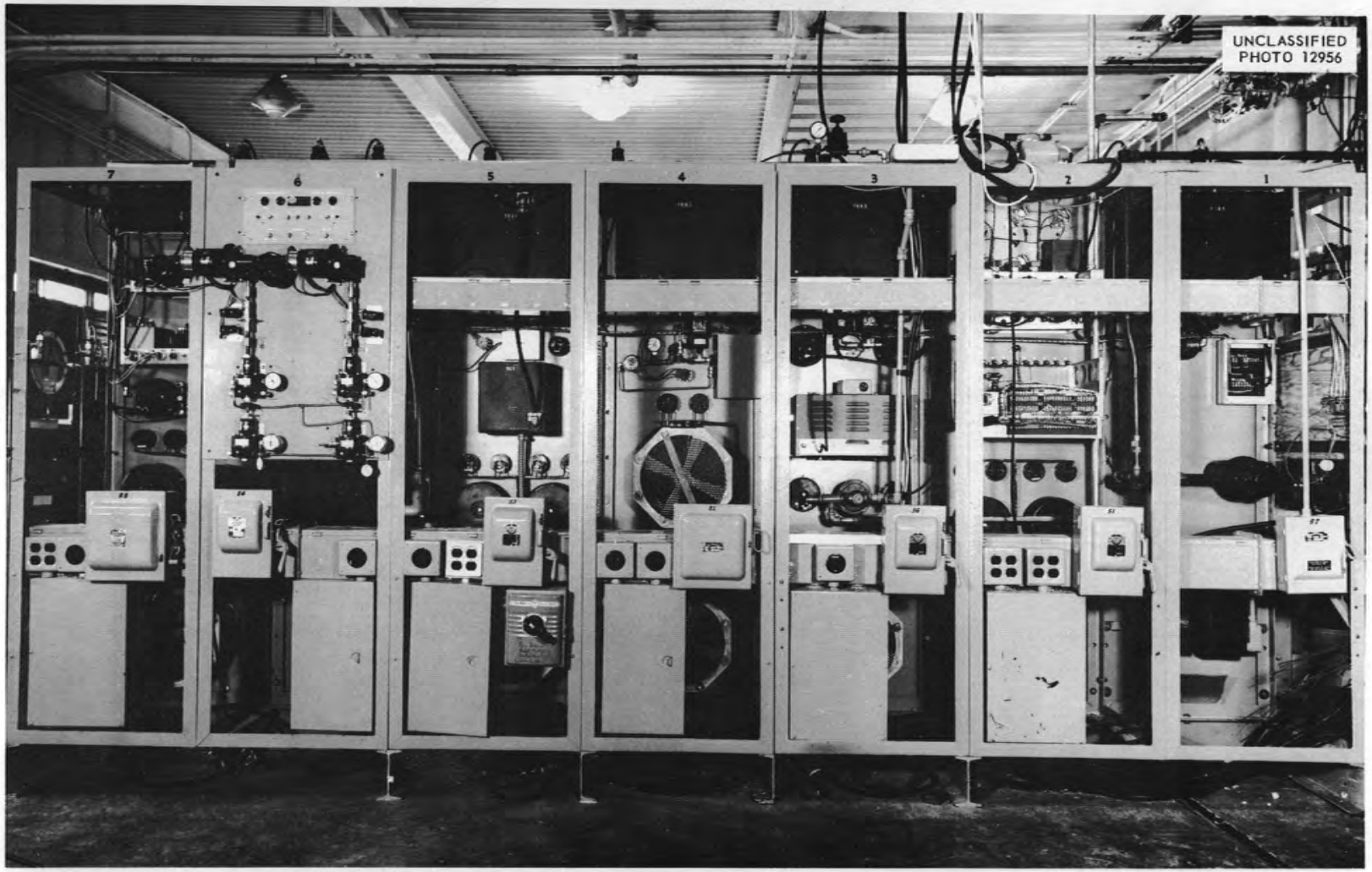

Fig. 23. Rear View of Fluoride-Fuel Loop Control Panel.

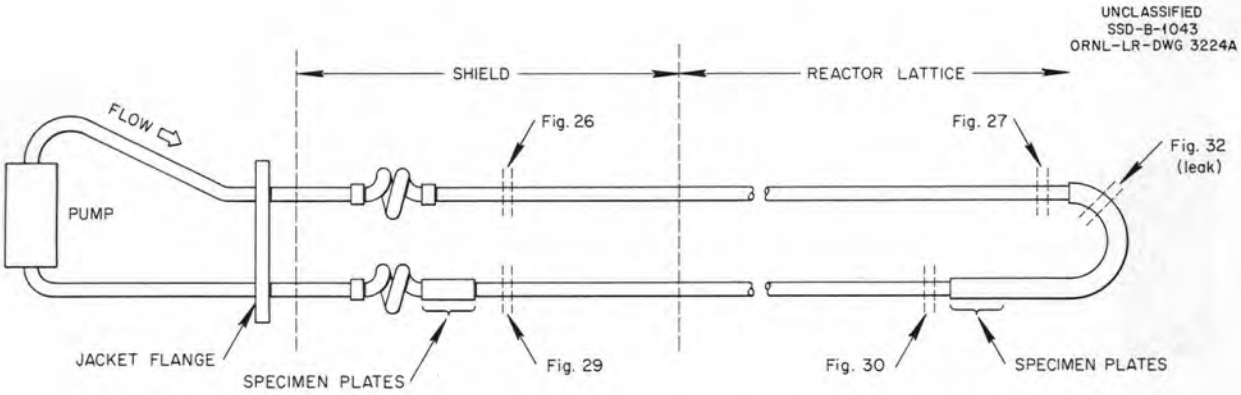

Fig. 24. Location of Specimens from Sodium-Inconel Loop.

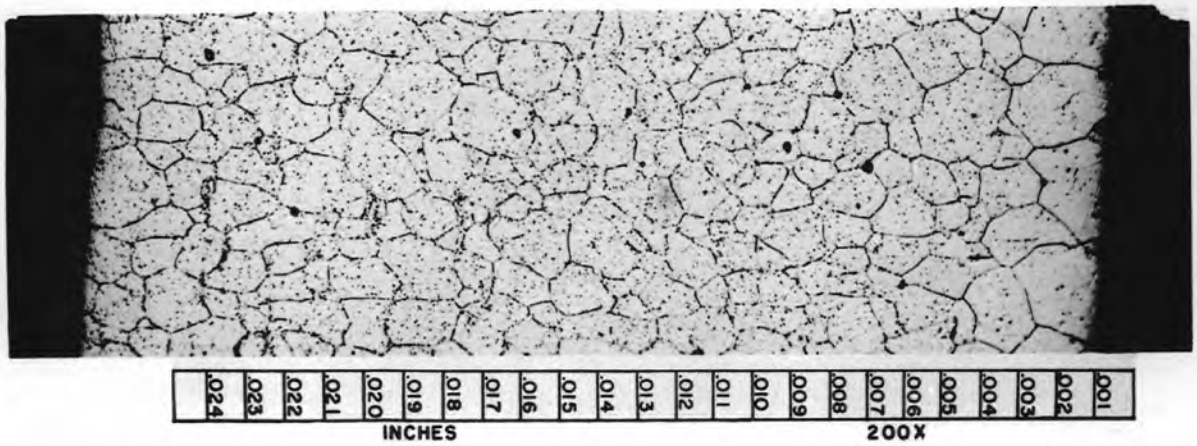

Fig. 25. As-Received Inconel Tube Used as Control for Specimens in Figs. 26 and 27.

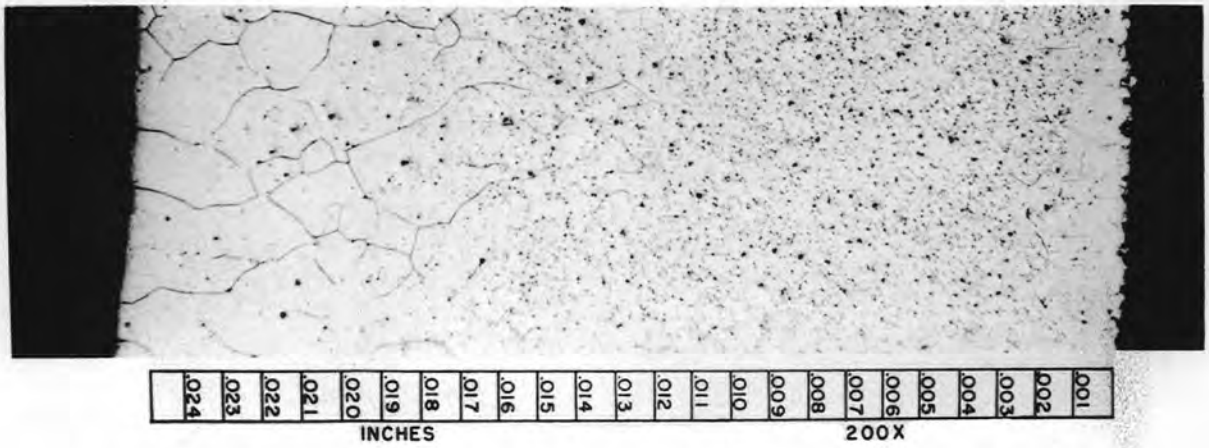

Fig. 26. Inconel Tube Exposed to Sodium at 1100 to 1300°F.

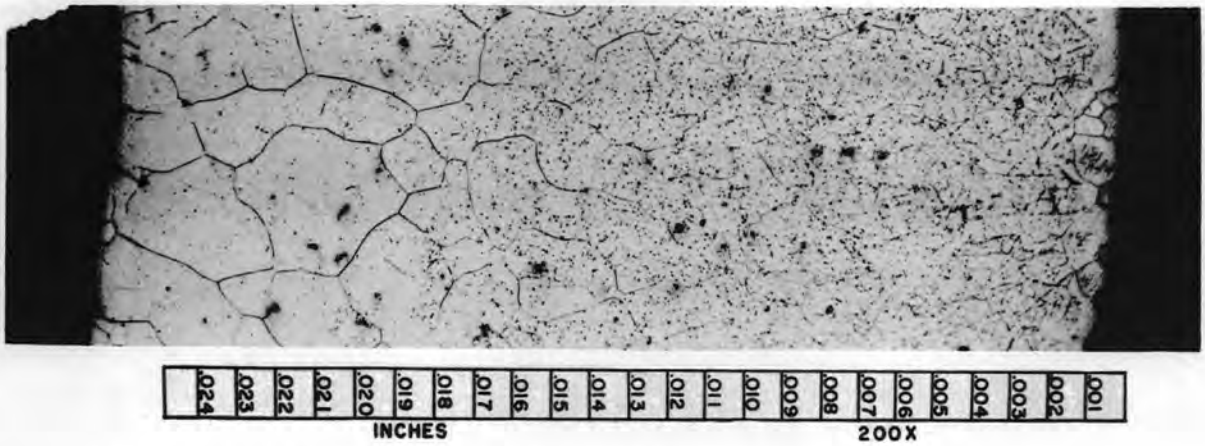

Fig. 27. Inlet Line of Inconel Tube Irradiated While Exposed to Sodium at 1500°F.

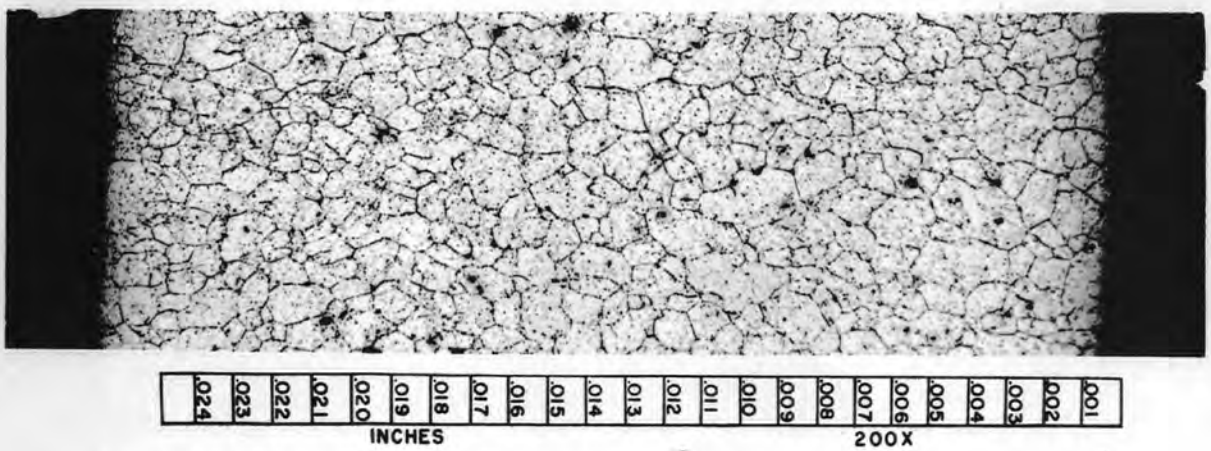

Fig. 28. As-Received Inconel Tube Used as Control for Specimens in Figs. 29 and 30.

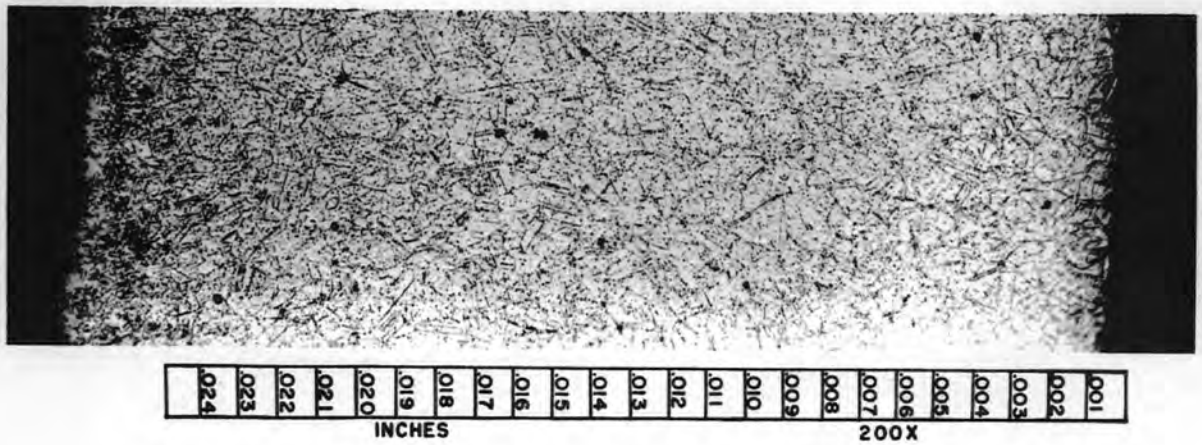

Fig. 29. Inconel Exposed to Sodium at 1500°F.

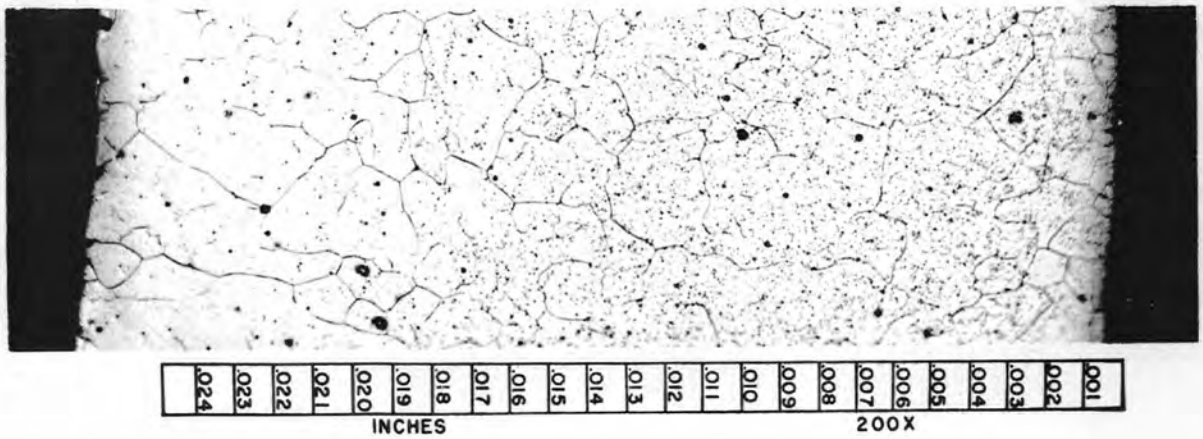

Fig. 30. Outlet Line of Inconel Tube Irradiated While Exposed to Sodium at 1500°F.

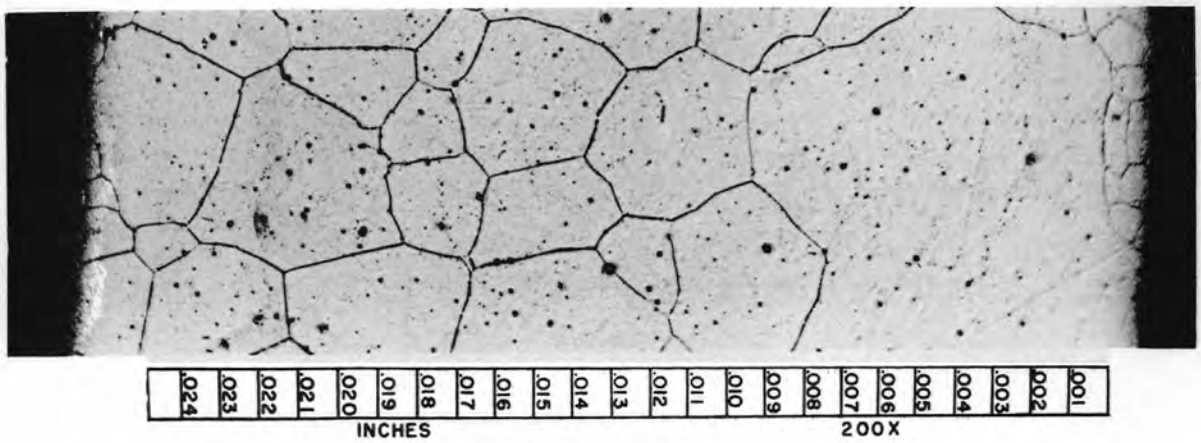

Fig. 31. As-Received Inconel Tube Used as Control for Specimen in Fig. 32.

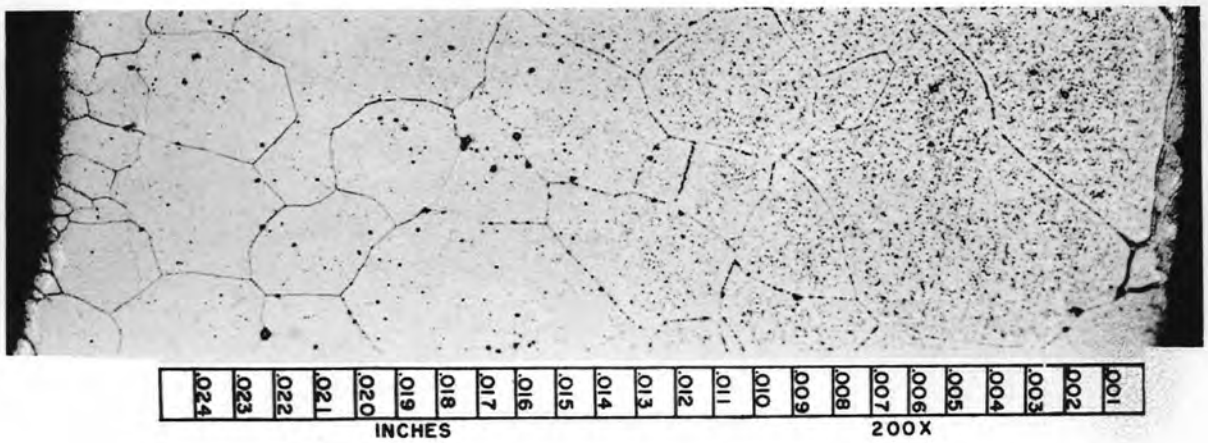

Fig. 32. U-Bend of Inconel Loop Irradiated While Exposed to Sodium at 1500°F.

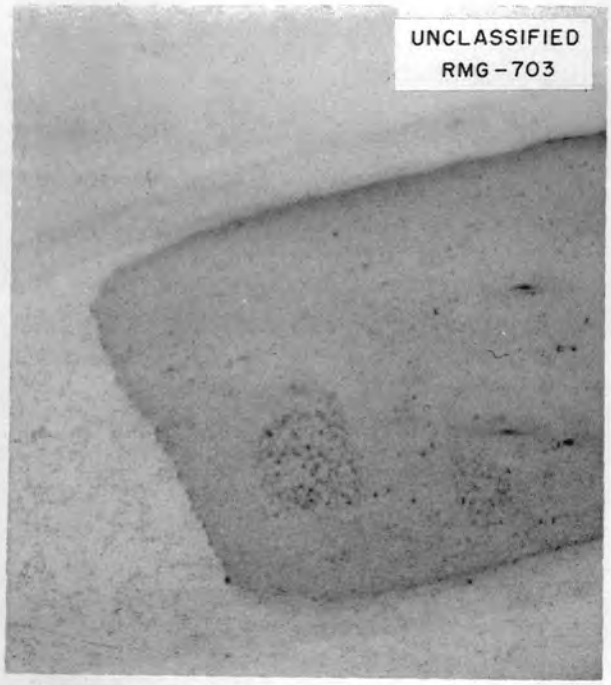

Fig. 33. Edge Seal of Transverse Section Showing Slight End Effect and Aluminum-Silicon Bond. 100X.

EFFECTS OF RADIATION ON THORIUM-URANIUM ALLOY FUEL PLATES

R. M. Carroll

The object of the experiment on the thorium-uranium alloy fuel plates was to determine the dimensional instability and change in the physical properties of the plate when approximately 1% of the total number of atoms in the alloy is fissioned. Thorium-uranium plates, clad with 52S aluminum, were rolled at 500°C; a 1.3% Si-Al barrier material was used to ensure a good mechanical bond (see Fig. 33). At this temperature and with this barrier material there was no intermetallic compound formation between the thorium and the aluminum.

Four 8 × 1 × 0.072 in. plates (Fig. 34) and one 28 × 1 × 0.072 in. plate of 98.9% Th–1.1% U^{235}, clad in aluminum, were fabricated by R. J. Beaver of the Metallurgy Division. The 28-in. plate and three of the 8-in. plates were irradiated in the MTR for nearly three months, at which time the plates were calculated to have undergone nearly 100% burnup of the U^{235}. The remaining 8-in. plate was retained as a control. The total irradiation of these plates was 4153 Mwd and an estimated

Fig. 34. Typical 8-in. Irradiated Specimen Showing Surface Defects.

integrated flux of 2.6×10^{21} neutrons/cm^2. The only apparent change in the specimens after irradiation was that the outline of the core was clearly visible for some reason, possibly because of selective corrosion; there was evidence of water erosion in the longitudinal surface defects, but there did not appear to be any blistering.

The dimensions of these specimens were determined with a remotely controlled measuring apparatus. This involved the comparison of the specimens with a standard by means of a dial gage, accurate to 0.0005 in. One of the basic limitations of the existing dimensional apparatus is that the length, width, and thickness have to be measured on the center line of the rectangular specimens. Width and thickness measurements were made at numerous positions along the length of the specimen; then the results were averaged, and the maximum deflection from the average was noted. These data are given in Table 1. The 28-in. specimen was too large for the equipment and so no dimensional measurements were made on it.

TABLE 1. DIMENSIONAL EFFECTS OF RADIATION ON THORIUM-URANIUM ALLOY FUEL PLATES

Specimen* Number	Preirradiation	Postirradiation	Maximum Deviation
	Width (in.)		
1	1.000	1.0015	0.0074
2**	1.000	1.0003	0.0019
3	1.000	1.0003	0.0025
4	1.000	1.0017	0.0081
	Thickness (in.)		
1	0.0725	0.0760	0.0072
2**	0.0725	0.0706	0.0011
3	0.0725	0.0759	0.0063
4	0.0725	0.0774	0.0022
	Length (in.)		
1	8.001	7.999	
2**	8.002	7.992	
3	8.002	8.003	
4	8.006	8.003	

*$8 \times 1 \times 0.072$ in.

**Not irradiated; used as a control.

The preirradiation data were furnished by R. J. Beaver. Dimensional measurements of the samples have indicated no significant change. The irradiated plates appear to be thicker than the control samples, although lack of accurate preirradiation measurements under the conditions of the remote measuring apparatus prevent any definite conclusion.

Radiographs had been made of the cores of the clad specimens before irradiation. After irradiation it was discovered that radiographs of the cores could be obtained by laying the samples on ordinary Lucite (Fig. 35) and leaving them overnight. The resolution of the resulting radiographs compared favorably with the resolution obtained in the preirradiation radiographs. No core dimensional changes could be detected.

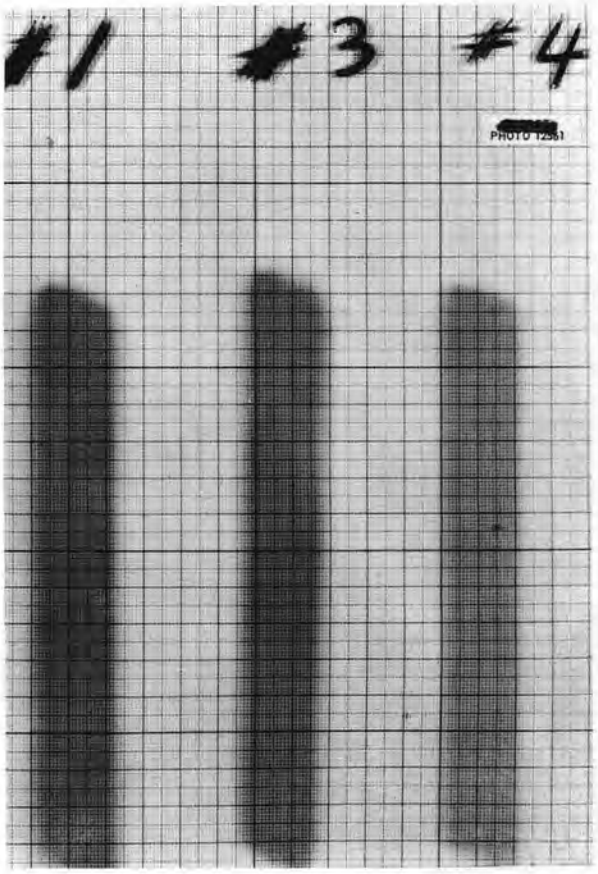

Fig. 35. Radiograph of the Irradiated Cores on Lucite.

A method of remotely measuring the thermal conductivity transversely through the samples was desired so that the bond between the clad and core could be nondestructively evaluated. Several methods were attempted, but all failed to produce the desired sensitivity; therefore the thermal conductivity tests were abandoned.

The densities of the samples were determined; then the clad was chemically stripped from the three 8-in. irradiated plates (Fig. 36), and the densities of the cores alone were measured. The data are given in Table 2. Also shown in Table 2 is a comparison of the core weight before rolling (furnished by R. J. Beaver) with that of the irradiated stripped core.

The heavier, postirradiated core weight may have been due to an incomplete stripping of the Si-Al barrier. The densities of the samples, both clad and unclad, indicated that the irradiated samples were approximately 1% less dense than the unirradiated control, but, since the irradiated cores themselves were also less dense, this does not indicate that voids had formed under the clad and had reduced the densities of the irradiated specimens.

The solution containing the dissolved clad was analyzed by G. R. Wilson, and it was determined that approximately 99.99% of the metal removed was aluminum containing 0.0011% uranium and less than 0.009% thorium. This suggests that very little diffusion occurred during rolling and irradiation.

In order to test the bond strength of the clad, a method of twisting samples sheared from the 28-in.

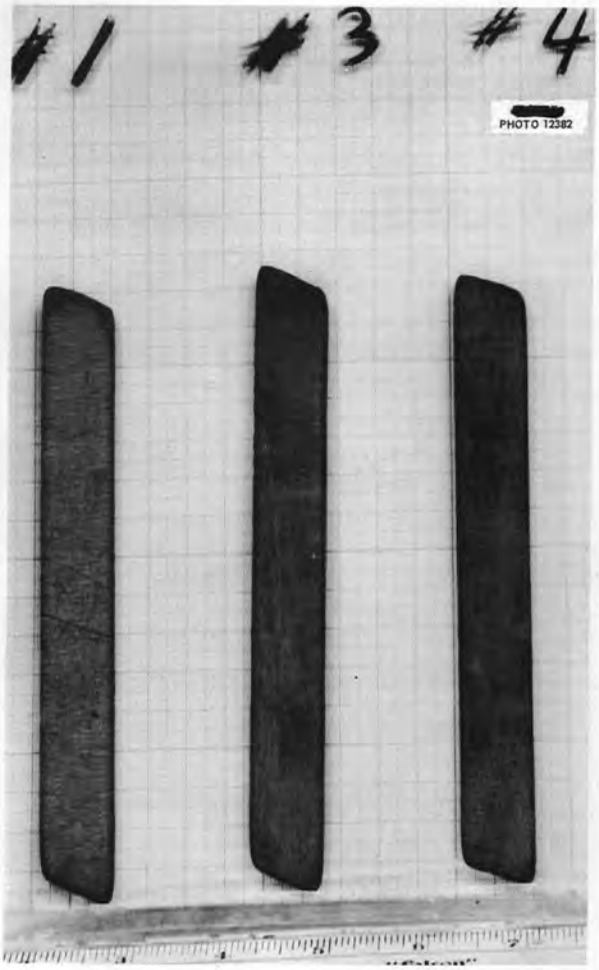

Fig. 36. Stripped Cores of the Three 8-in. Irradiated Specimens.

TABLE 2. EFFECT OF IRRADIATION ON DENSITY AND CORE WEIGHTS OF THORIUM-URANIUM FUEL PLATES

Specimen Number	Clad Specimen		Core			
	Density (g/cm^3)	Maximum Deviation	Density (g/cm^3)	Maximum Deviation	Preirradiation Weight (g)	Postirradiation Stripped Weight (g)
1	4.4231	0.0001	11.315	0.009	22.2229	22.2555
2*	4.5368	0.0005	11.538	0.007		
3	4.4330	0.0002	11.336	0.008	22.1020	22.1325
4	4.4233	0.0005	11.314	0.010	22.1578	22.2053

*Not irradiated.

plate was developed (see Fig. 37). This test consisted in holding one end of the sample in a fixed position and rotating the other end 45 deg in alternate directions. The length between the fixed end and the rotated end was 4 in.; so the rotation was the equivalent of a 90-deg twist for the standard 8-in. specimen. After several bends, the damage that occurred quickly reached a maximum, and further bends had no apparent effect. In no case did the clad break loose or fail in any gross manner. A second test of bond strength was a bend test in which a sample of the irradiated plate was bent 180 deg in a 0.1-in. radius one time only. The clad of the sample was fractured at the point of greatest stress, and the sample, along with

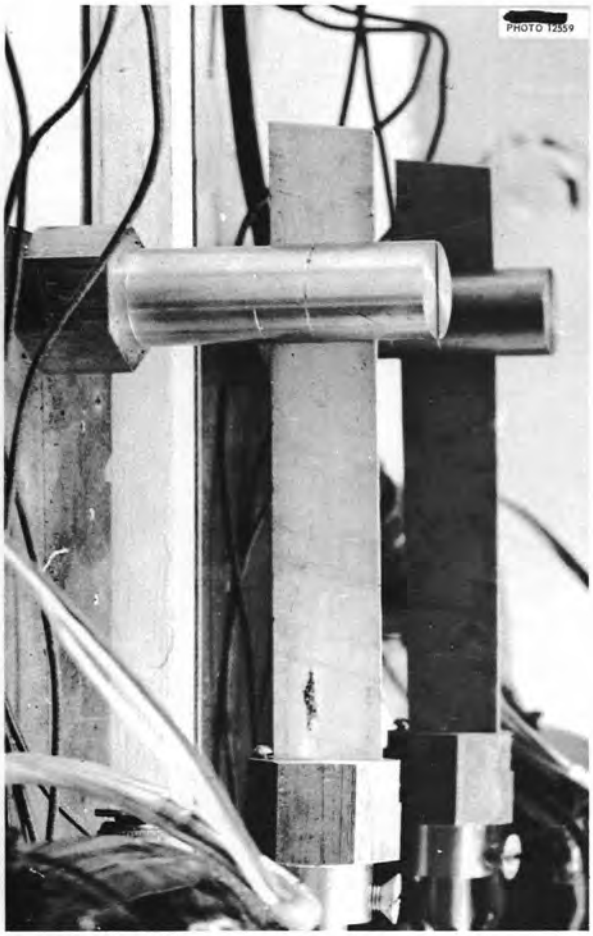

Fig. 37. Rotational Bond-Strength Apparatus with Specimen in Place and Mirror Located to Show Opposite Side. Note the dark, diagonal bands that appeared after several cycles.

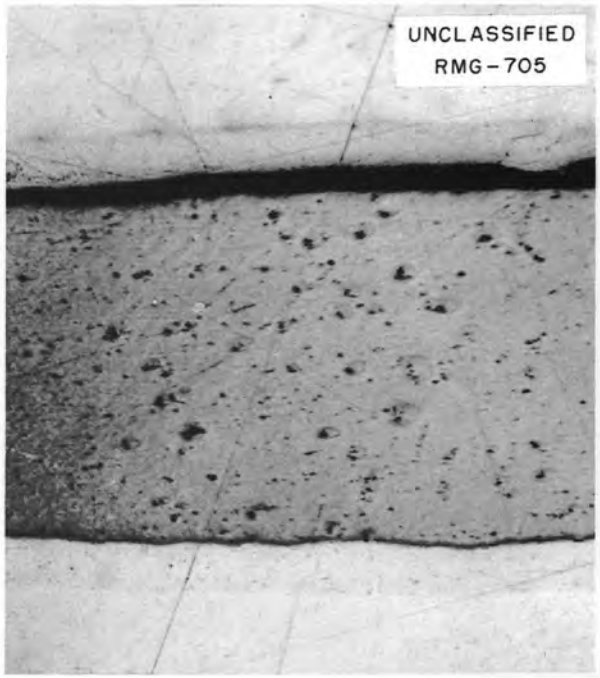

Fig. 38. Area Showing Separation of the Barrier and Clad from the Core Approximately ½ in. from Point of Fracture of 180-deg Bend Specimen. 100X.

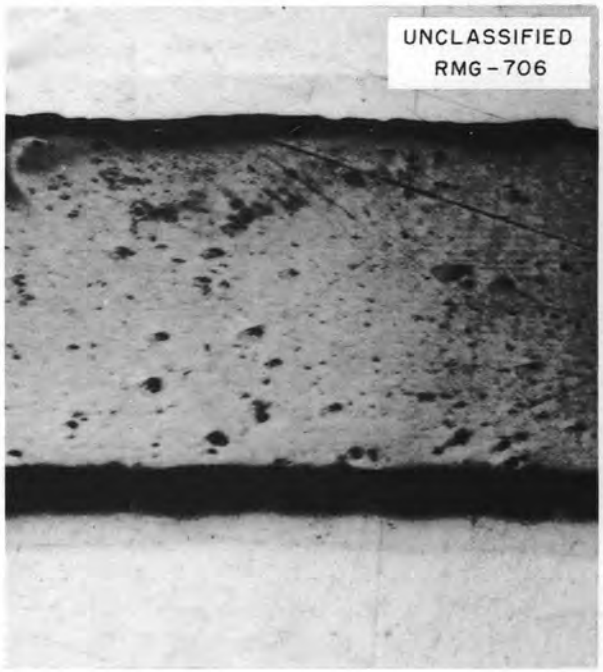

Fig. 39. Area Showing Separation of Core from Barrier on Both Sides Approximately ¼ in. from Point of Fracture of 180-deg Bend Specimen. 100X.

samples of unbent, irradiated plate and unirradiated plate, was delivered to M. J. Feldman for metallographic analysis (Figs. 38 and 39). His analysis indicated that there was no definite evidence of an intermetallic phase near the clad-core interface and that, in addition to fracture of the core and one side of the clad at the point of maximum bending, the bent sample showed separation of the core from the barrier layer for a distance of approximately ½ in. from the fracture. Comparison of the irradiated sample with a nonirradiated section showed a drastic increase in hardness of the core and a small increase in hardness of the clad after irradiation, as shown in Table 3.

Tests are now in progress to determine the chemical composition of the core and the amounts of U^{233} and U^{235} present. Although these fuel plates represent an early development in the bonding of aluminum to thorium, the bond appears to be quite strong and the entire element seems to be dimensionally stable with irradiation.

TABLE 3. HARDNESS MEASUREMENTS ON CORE AND CLADDING OF THORIUM-URANIUM FUEL PLATES

Material	DPH Hardness of Irradiated Samples	DPH Hardness of Nonirradiated Samples
Core – transverse	202/193*	120/113*
Core – longitudinal	198/180*	114/111*
Clad – transverse	88/81**	80/74**
Clad – longitudinal	90/85**	80/72**

*10.25-mm objective, 2-kg load.
**10.25-mm objective, 1-kg load.

FUSED SALTS

G. W. Keilholtz

TEMPERATURE AS A VARIABLE IN STATIC-CORROSION TESTS

W. R. Willis M. F. Osborne

The study of thermocouple errors in the static-corrosion tests reported previously[1] has been extended to include approximately 30 thermocouples. Figure 40 shows a plot of "true" surface temperature minus the indicated temperature vs air flow. This plot gives a band of corrections for a given air flow. All the thermocouples studied fall within this band. The results of these tests were used in an attempt to correlate the results of corrosion studies with the temperature history of static-corrosion tests. Of 13 capsules irradiated in the MTR, 4 showed corrosion to a depth greater than 10 mils; the other capsules were corroded to a depth of 3 ± 1 mils (see Table 4). There is no correlation between power generation, time in the reactor, or salt composition. In the four cases of deep penetration, grain growth did occur.

The temperature history was analyzed for temperature peaks of short durations, long-term high temperatures, and oscillatory behavior. In the four cases of deep penetration, the temperature histories show either that there was a high temperature for long duration or, as indicated by the very unusual temperature pattern along the capsule, that at least two of the three thermocouples were in error. In the nine cases showing 3 ± 1 mils of penetration, seven showed normal temperature histories. Two cases of high temperature, but of short duration, were observed; grain growth had occurred in one case but no obvious effects could be seen in the other.

[1] J. G. Morgan, W. R. Willis, and M. F. Osborne, *Solid State Semiann. Prog. Rep. Feb. 28, 1954*, ORNL-1677, p 22.

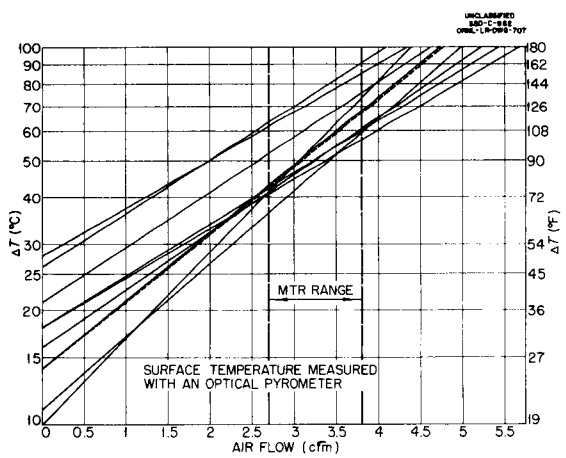

Fig. 40. Variation Between True Surface Temperature Measured with an Optical Pyrometer and Thermocouple Reading as a Function of Air Flow.

MTR STATIC-CORROSION TESTS

W. E. Browning

Investigation of the effect of radiation on static corrosion of Inconel by NaF-ZrF_4-UF_4 fused-salt fuel was continued. The last four of a series of capsules containing 4 mole % UF_4, 50 mole % ZrF_4, and 46 mole % NaF were irradiated in the MTR, three for 300 hr and one for 777 hr. Ordinarily, the capsules would have been irradiated with the metal-liquid interface temperatures nominally at 1500°F but, because of operational problems, they were actually in the range 1600 to 1700°F. Individual, 300-hr capsules may have experienced brief excursions as high as 1850, 2000, and 2200°F. The 777-hr capsule may have gone as high as 1900°F for approximately 1 min on two occasions during the six-week irradiation period. It was subjected to a thermal cycling with a 15-min period and an amplitude which diminished from 470°F to 0°F in 50 hr. The contents of the four capsules were removed; two samples were taken from each capsule by drilling with successively larger drills and were analyzed for U, Fe, Cr, and Ni. The uranium contents of the inner and outer samples were identical within experimental error. Iron, chromium, and nickel analyses showed a greater proportion of Cr and Fe and a greater ratio of Fe to Cr than are found in the original Inconel. Efforts are being made to reduce the possibility of contamination from steel tools used in sampling. Analytical results from earlier capsules in the same series have been obtained and are roughly consistent with these results, although the reproducibility is not adequate for a clear interpretation to be made. Metallographic examination showed an intergranular-void penetra-

TABLE 4. CORRELATION OF TEMPERATURE DATA AND CORROSION

Test No.	Power Density (w/cc)	Time (hr)	Grain Size	Depth of Penetration (mils)	Peak Temperature (°F)	Duration of Peak (hr)
201[a]	2500	116	Large	12	<2050	<116
209[a,b]	2500	406	Large	12	<2000	50
224[a]	2500	291	Large	14	<2000	100
501[a]	8000	140		12		
210	2500	10	Large	0		
213[a]	2500	575	Large	3	<2170	1
502	8000	350	Large	1		
204	2500	325		3	<2100	<<1
220[b]	2500	325		4		
409	3900	156		1		
410	3900	419		4		
411	3900	119		2		
503	8000	290		2		

[a]Temperature pattern unusual. [b]Temperature oscillations wild.

tion of from 2 to 5 mils in the 300-hr capsules and of 20 mils in the 777-hr capsule.[2]

A new series of capsules was irradiated in the MTR to compare NaF-ZrF_4 fused-salt fuels based on UF_3 with those based on UF_4. The property to be compared is the effect of fission on static corrosion of Inconel by the fuels at 1500°F. The series includes five capsules containing 1.79 mole % UF_3, 49.3 mole % ZrF_4, and 48.9 mole % NaF and five capsules containing 1.74 mole % UF_4, 48.2 mole % ZrF_4, and 50.1 mole % NaF. Each fuel generates 1100 w/cm^3 in the A-38 position in the MTR. Fuels with such low power density are used because of the limited solubility of UF_3 in NaF-ZrF_4 mixtures. Five of the six capsules that have been irradiated have been received at ORNL; three of them have been opened and two have been examined, one containing UF_3 and one containing UF_4. Both capsules were irradiated with the metal-liquid interface at 1500 ± 50°F. The UF_3 capsule experienced one temperature excursion to 1660 ± 50°F for less than 30 sec. The UF_4 capsule did not exceed 1550 ± 50°F. Each capsule was frozen two or three times during its history. Little evidence of corrosion could be seen in the UF_3 capsule. There was intergranular-void formation in the UF_4 capsule to a depth of about 1 to 2 mils.[2]

Analytical samples of the irradiated fuel were taken in the manner mentioned above. The uranium concentrations in the central and outer samples were identical within experimental error (±3%) and were of the value to be expected after burnup correction. Analyses for Fe, Cr, and Ni gave the following results: Fe, 0.03 to 0.14%; Ni, 0.01 to 0.05%; Cr, less than 10^{-4}%. There was no significant difference in Fe, Ni, and Cr compositions between the UF_3 and UF_4 capsules. Control capsules were run under the same conditions without radiation.

It would be unwise to draw conclusions on the basis of only one pair of samples; however, if these first results are confirmed by future capsule tests, UF_3 fuels may be considered to be quite desirable as far as radiation corrosion is concerned. Two UF_3 capsules and two UF_4 capsules in this series will be irradiated for six weeks each to amplify the apparent difference.

[2]M. J. Feldman *et al.*, *Metallographic Analysis of Capsules 239, 242, 243, 244, 256, and 257*, ORNL CF-54-8-128 (Sept. 9, 1954).

FACILITIES FOR HANDLING RADIOACTIVE MATERIALS

C. C. Webster

The stability of the fluoride fuel under irradiation and the extent of the corrosion of the container by the fuel are determined by making concentric corings of the salt and analyzing each for concentration of the original components and for the major constituents of the container material. These samples are put into solution within the hot cells and are then transferred to the Hot Analytical Chemistry Section for analysis. Work on the necessary transfer shields had been coordinated with the design and construction of the lead barrier in the Chemistry Section to improve transfer conditions and to reduce personnel exposure.

Two transfer carriers weighing 150 lb each and having 2 in. of lead shielding have been constructed and are now in use. Each carrier holds four 30-ml bottles, and each bottle is held in place by a spring clamp. A motor-driven decapper for removing the cap and a remotely controlled pipet that can be lowered into the bottle are provided. The bottles may be inserted into the carrier within the hot cells and can be left in the carrier during all sample-removal operations. The whole unit may then be returned to the hot cells for removal of bottles and the remaining fuel and may be reloaded with bottles filled with other samples.

Two lead storage units weighing 450 lb each and providing 3 in. of lead shielding were built for use when the transfer carriers are not available. The lead storage units have a capacity of four 50-ml volumetric flasks and can be loaded within the master-slave hot cells.

To facilitate the insertion into and removal from the hot cells of these lead transfer units and lead storage units, a metal table capable of holding 1 ton was constructed; this table can be rolled up to the back of the master-slave cells. The transfer or storage unit is placed on the little dolly and rolled down onto the cell table. The motor-driven pulley mounted on the back of the table is for easing the shield down the incline onto the cell table and for pulling the loaded dolly back onto the table.

REMOTELY OPERATED TUBE-SLITTING MACHINE

C. C. Webster

In the metallographic study of corrosion, when several transverse sections were taken from a single fluoride-fuel corrosion capsule, it was observed that corrosion was not consistent over the length of the capsule but appeared to be a function of the longitudinal temperature gradient. The method used for obtaining a longitudinal section is to pass the capsule longitudinally across a 10-mil-thick silicon carbide fine-grit wheel that slits the capsule down the center. The apparatus is so constructed that once the capsule is put into the gripping adapter the wheel cuts in such a way that one surface is in the plane of a diameter through the capsule. Various sizes of tube can be slit lengthwise by use of different gripping adapters. At present the apparatus has been used on only MTR-type fluoride-fuel capsules (0.100-in. ID and 0.200-in. OD) and has worked very satisfactorily. Figure 41 shows the area cut away by the abrasive wheel and the method of mounting the capsule for the cutting operation. Figure 42 is a diagram of the end plug and the body of a capsule after they were slit.

Figure 43 shows the entire apparatus prior to insertion in the hot cell. The capsule is clamped

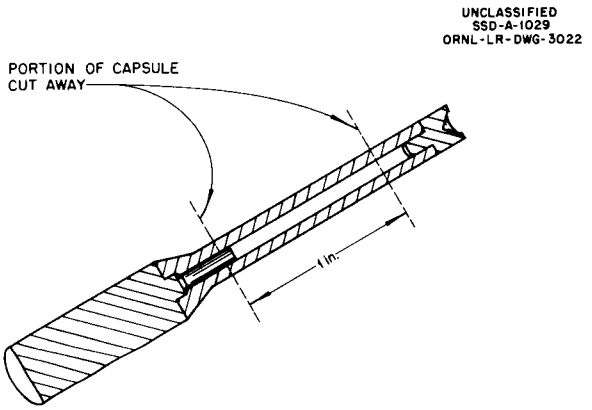

Fig. 41. MTR Fluoride-Fuel Corrosion Capsule.

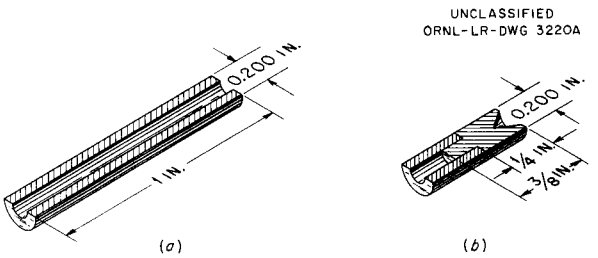

Fig. 42. End Plug, *b*, and Body, *a*, of the Capsule After Slitting.

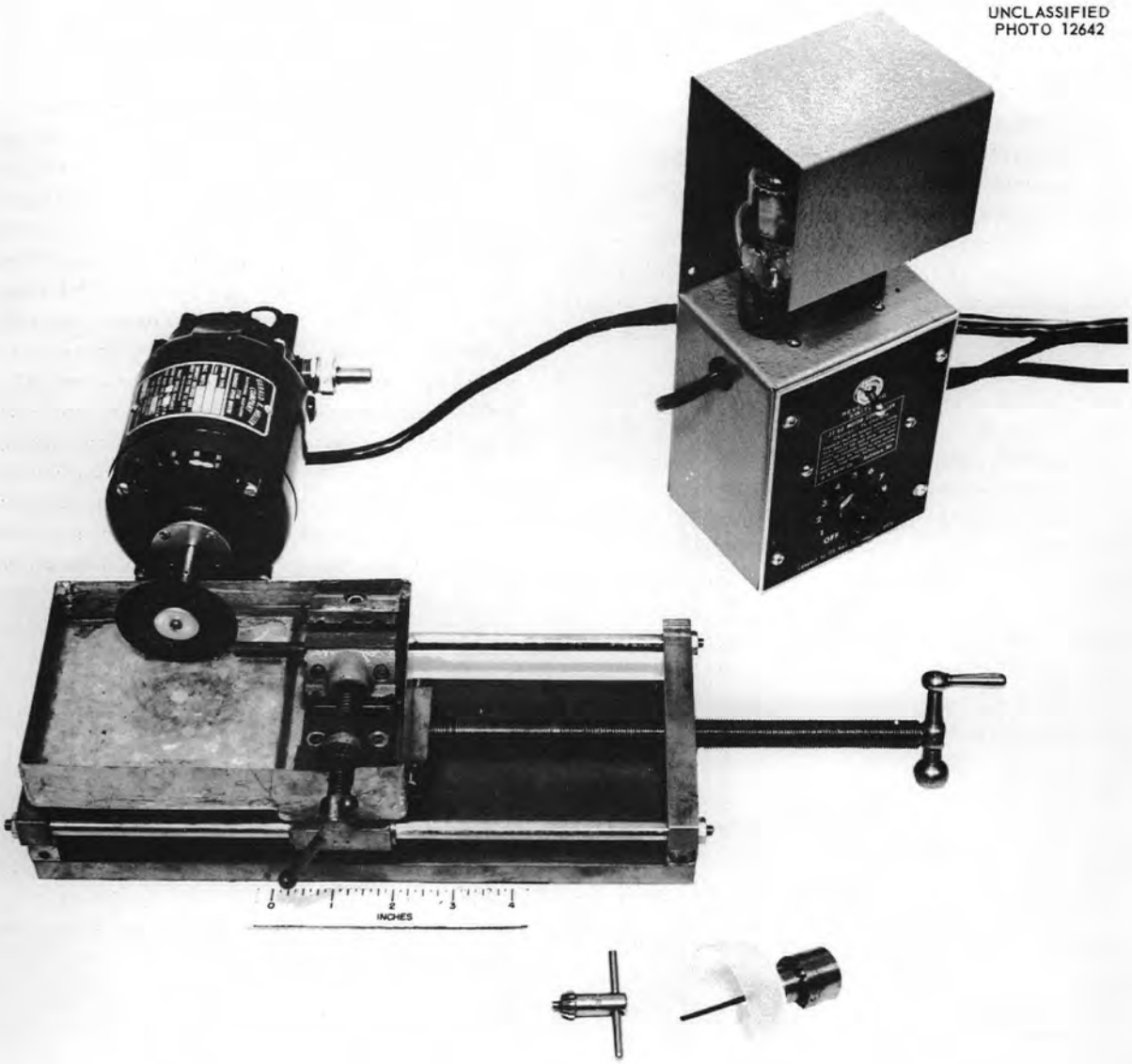

Fig. 43. Slitting Apparatus with Capsule in Position.

in the vise and is then fed into the wheel by means of a mechanical linkage that will later be replaced by a variable-speed motor and a contact cut-off switch. Since the abrasive wheel is rubber-based, it must be kept cool. As the area around the cut must also be kept cool to prevent any high thermal stresses from adding confusion to the corrosion studies, the wheel and specimen must be in a tray and must be covered with a splash shield so that a liquid coolant can be used. The coolant level is always kept above the bottom edge of the abrasive wheel, and, by cutting into the specimen from below, the coolant will be carried up into the cut so that the specimen need not necessarily be in the cooling medium. Because it does not react with the fluoride fuel at high temperatures to give off HF, carbon tetrachloride is used as a coolant and is forced into the tray from outside the cell by means of Tygon tubing and air pressure. The tray and the splash shield are attached to the mount for the vise and move with the specimen.

Once installed within the hot cell, such a remotely operated tube-slitting machine can be used for cutting longitudinal sections from various sizes

of tubing. For heavier-walled tubing, thicker abrasive wheels could be used. The following benefits are gained by this method of cutting:

1. The extent of the salt left on the tube walls may be observed.
2. Constrictions in tubes, loops, etc. may be observed without the material causing the trouble having to be removed or disturbed.
3. A well-exposed surface is provided so that the last traces of salt can be removed chemically.
4. A cut can be made through the bottom plug of a capsule so that crevice corrosion may be observed.
5. After the salt is removed chemically, by a method that does not attack the metal wall, the specimen can be electroplated so that the fuel-metal interface will not be rounded during the metallographic polishing operation.
6. Nearly half the capsule or tubing is left for further and more complete study if desired.

[3] J. G. Morgan *et al.*, *Solid State Semiann. Prog. Rep. Aug. 31, 1953*, ORNL-1606, p 40.

[4] C. C. Webster and J. G. Morgan, *Solid State Semiann. Prog. Rep. Feb. 28, 1954*, ORNL-1677, p 27.

ANALYSIS OF IRRADIATED FLUORIDE FUELS FOR URANIUM

M. T. Robinson

One of the regular steps in in-pile static-corrosion testing of fluoride fuels has been the analysis of the irradiated salt for uranium.[3] Any understanding of the results obtained must be based on a knowledge of the procedure necessary to prepare samples for analysis; the procedure is outlined in the flowsheet displayed in Fig. 44. The sampling operations have been previously described.[3,4] There are several major problems connected with sampling which are now being resolved. In the cutting and drilling operations it is possible for small chips of metal, either from the capsule or the drill, to get into the salt sample. To minimize this possibility, drills used recently have been carefully honed to remove burrs. A search is also being conducted for new drill materials. In the early use of the present sampling technique,[3] it was possible for dirt from the hot cells to inadvertently enter the salt samples during cutting and drilling. This

UNCLASSIFIED
SSD-C-1020
ORNL-LR-DWG-2686

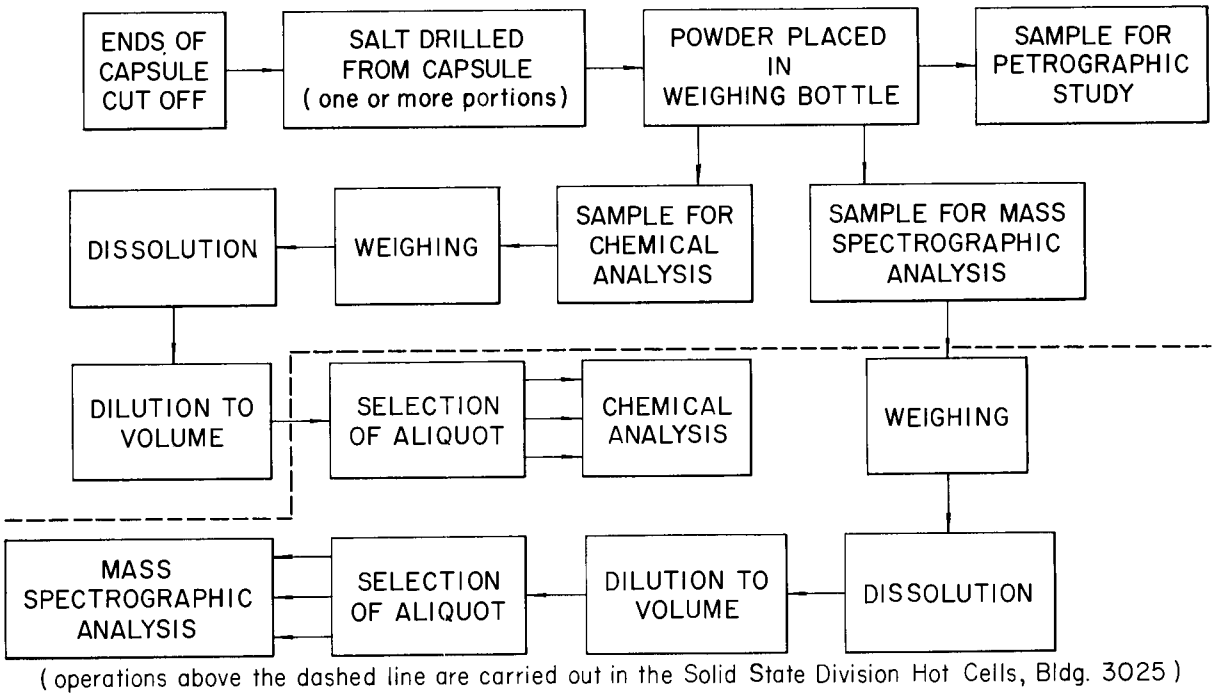

(operations above the dashed line are carried out in the Solid State Division Hot Cells, Bldg. 3025)

Fig. 44. Flowsheet of Operations in Analysis of Irradiated Fluorides.

has been minimized in the newer equipment.[4] The transfer operations are all possible sources of contamination; in several of them the salt is exposed to contamination from hot-cell dirt, from pieces of rubber from manipulator grips, etc. The observation of opaque material, sometimes in large amounts, during petrographic examination of irradiated fuel samples[5] indicates that, at one or another of the stages discussed above, foreign material may have been introduced into some of the samples. This will make the resulting uranium analysis low.

The samples obtained for chemical analysis were very small, often weighing no more than 10 mg. These samples are weighed in tared weighing bottles on a conventional chain-type analytical balance. The precision of weighing was about ±4%, instead of the usually negligible amount. This resulted in an abnormally high uncertainty in uranium analyses. After the samples are weighed, they are dissolved and the solutions are made up to volume in the hot cells. The resulting solutions formerly contained as little as 500 ppm of uranium. Such high dilution is undesirable because the titer may change appreciably on long standing. It seems reasonable to conclude that the uncertainty in uranium analyses may be as high as ± 5% or more, even for the usually precise (±2%) potentiometric titration. An increase of ten times in sample size (easily attainable) would restore this technique to its normal precision. Early this year the use of large samples was made a part of the procedure, and weighing errors were reduced to within the limits of analytical precision. Uranium concentrations are 20,000 ppm in aliquot solutions.

Similar remarks apply, in part, to the mass spectrographic analysis in which the samples taken are weighed by the analysts on a microbalance, which alleviates the effect of small sample size. However, the handling of the very small crucibles in the hot cells is not so delicate an operation as might be desired. The possibilities of adventitious matter entering the sample are high.

Because of the difficulties described above, the conclusions resulting from chemical analysis of the fuel have been of only limited value. Recently, however, a marked improvement has been seen as a result of continued efforts to improve sampling techniques and handling procedures. It now appears certain that uranium analyses can be carried out in a satisfactory manner. Since analytical results obtained recently make it appear that no appreciable segregation of uranium is taking place, the procedure of taking more than one sample from each capsule can be abandoned, if necessary. This will allow very much larger samples to be obtained, will make analyses more reliable, and will minimize the effects of foreign additions to the salt; or, if desired, the additional sample material can be used for other purposes.

[5] G. D. White and M. T. Robinson, *Solid State Semiann. Prog. Rep. Feb. 28, 1954*, ORNL-1677, p 28.

HIGH-TEMPERATURE CHECK-VALVE TESTS

W. R. Willis M. F. Osborne

As part of the developmental program for a miniature in-pile pump loop, an attempt was made to develop a high-temperature check-valve pump. Such a pump has the advantage of being a compact, completely sealed unit.

Figure 45 illustrates a test rig designed for the study of various types of check-valve designs and materials. The check valve allows flow in only one direction in each loop. Instruments were designed by J. De Lorenzo to control the salt flow by applying gas pressure to the tank as the salt made, and broke, contact with the two probes. The resistance to flow of the tubes was measured with water, and the rate of flow was calculated to be about 6 fps. The tubing used was 100-mil-ID Inconel. Flow of the salt was detected by the temperature distribution and by timing the flow cycle.

Four tests were run, by the use of this equipment, with Inconel, stainless steel, and Stellite 25 check balls. None of these materials produced successful results. The time of operation, before failure, varied from 30 min for the Inconel to 2 hr for the stainless steel. Except in the case of the stainless steel check balls, the valves could not be operated continuously because they would occasionally stick in both open and closed positions. When failure occurred it was abrupt, indicating sticking valves rather than a gradual stoppage of the system.

BENCH TEST OF MINIATURE IN-PILE LOOP

J. G. Morgan W. R. Willis
H. E. Robertson M. F. Osborne

Figure 46 shows an exploded view of the in-pile molten-salt pump described previously.[6] The rpm

[6] J. G. Morgan, *Solid State Semiann. Prog. Rep. Feb. 28, 1954*, ORNL-1677, p 30.

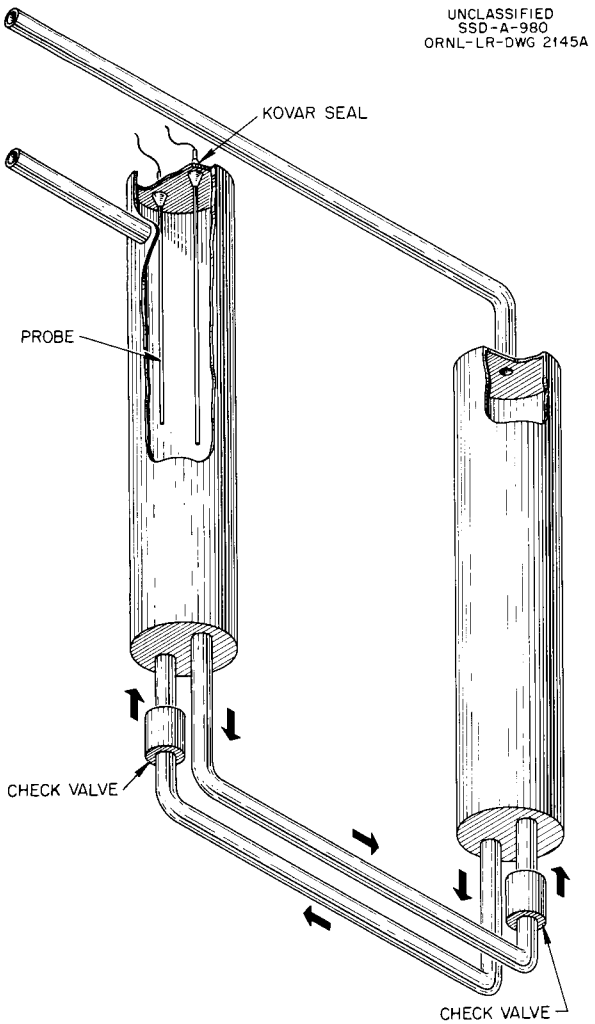

Fig. 45. Check-Valve Test Apparatus.

meter coil, *a*, measures the rotation of the shaft on which is mounted the motor armature, *b*. The Graphitar bearing is mounted in the bearing casing, *c*, above the impeller housing, *d*.

Figure 47 gives an assembled view of the pump loop with the surge tank, *a*. The pump contains an extra reservoir, *c*, to permit metered volumes of salt to be pumped into the surge tank and to calibrate the venturi, *d*; also shown is the furnace, *b*, for heating the pump and reservoir. From this performance test setup, pump speed vs head and pump speed vs flow can be determined.

The measurements in the bench test, run with molten salt at 1500°F, confirmed previous pump calibrations in which water was pumped. At 4500 rpm, a flow of 3.5 fps and a pressure drop of about 11 psi were obtained. These values show that the pump is easily capable of attaining the design value of flow for the in-pile model.

LIFE TESTS ON A REMOTE RPM METER, BEARINGS, AND SMALL ELECTRIC MOTOR UNDER IRRADIATION

J. G. Morgan H. E. Robertson

Components tests were conducted as a part of the LITR dynamic-loop development. In order to drive the molten-salt pump, it is desirable to use a variable-speed electric motor, record the shaft rotation, and align the shaft with lubricated bearings. The entire motor assembly will be just above the upper grid guide in the LITR and in an estimated thermal flux of 5×10^{11} neutrons·cm^{-2}·sec^{-1}. Hole 53 of the ORNL Graphite Reactor provided a comparable flux intensity and was therefore used for these tests.

A motor was mounted in a horizontal position with upper and lower armature-shaft bearings as shown in Fig. 48. In test No. 1, two lower bearings were used. The motor and rpm meter were canned and were inserted to the center line of the ORNL Graphite Reactor. Variables measured were resistance of motor winding, resistance of rpm coil, voltage applied to motor, current drawn by motor, temperature of lower Fafnir bearing, temperature of motor field, and rpm of motor shaft.

The Delco ac-dc motor is rated at 115 v, 0.9 amp, and $^1/_{15}$ hp and has Formvar-insulated wires. In test No. 1, mica, backed with a stainless steel plate, was substituted for the brush-holder plate. In test No. 2, fired Lavite was substituted for the brush-holder plate, asbestos-covered wire was used from the brush to the field coil, and glass tape was wrapped around the field coils. The rest of the construction features were unaltered; that is, fish-paper coil supports, plastic (paper-backed bakelite) commutator-segment spacers, and cardboard armature-shaft spacers were used.

The upper bearing (New Departure 77R6) and lower bearing (Fafnir DW-6) were packed with California Research Corporation grease No. RRG-3 (NLGI, Grade 2).

The remote rpm meter consists of a magnet fastened to the shaft which will rotate inside the gas-tight motor shell; on the outside is mounted a coil wound around a C-shaped iron core. As the shaft rotates, pulses are generated in the coil and

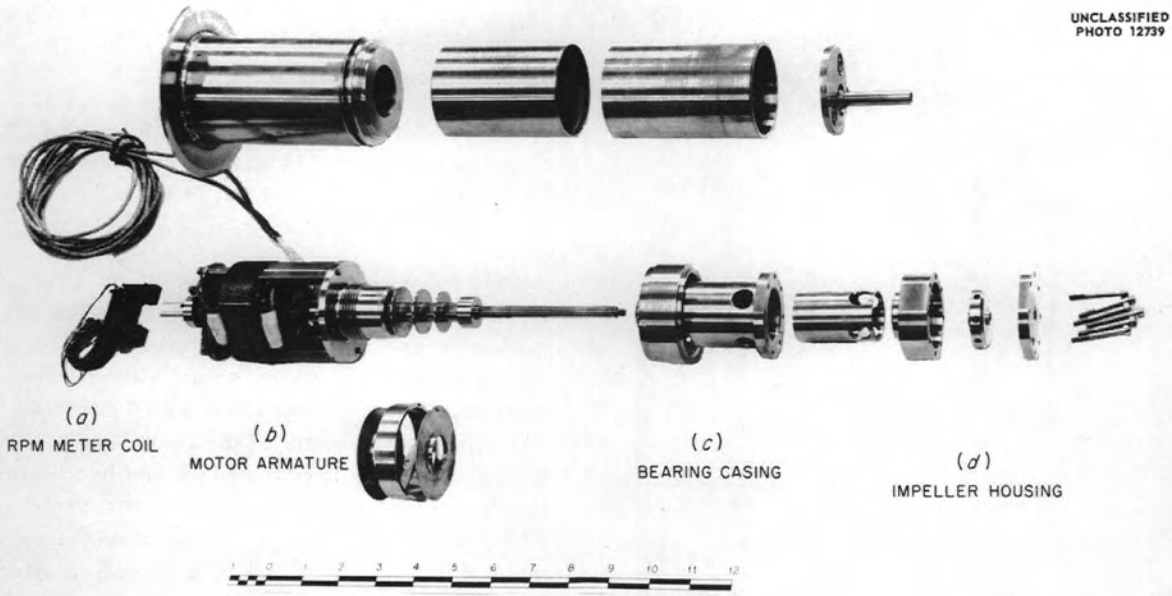

Fig. 46. In-Pile Molten-Salt Pump.

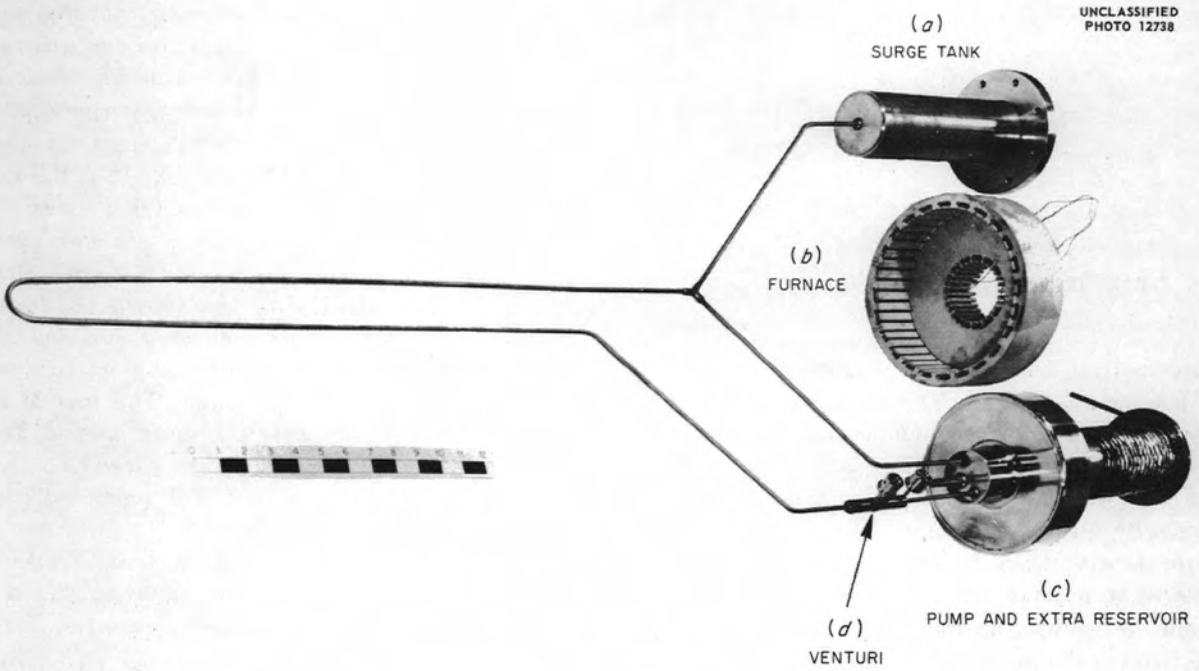

Fig. 47. Assembled Pump with Loop and Surge Tank.

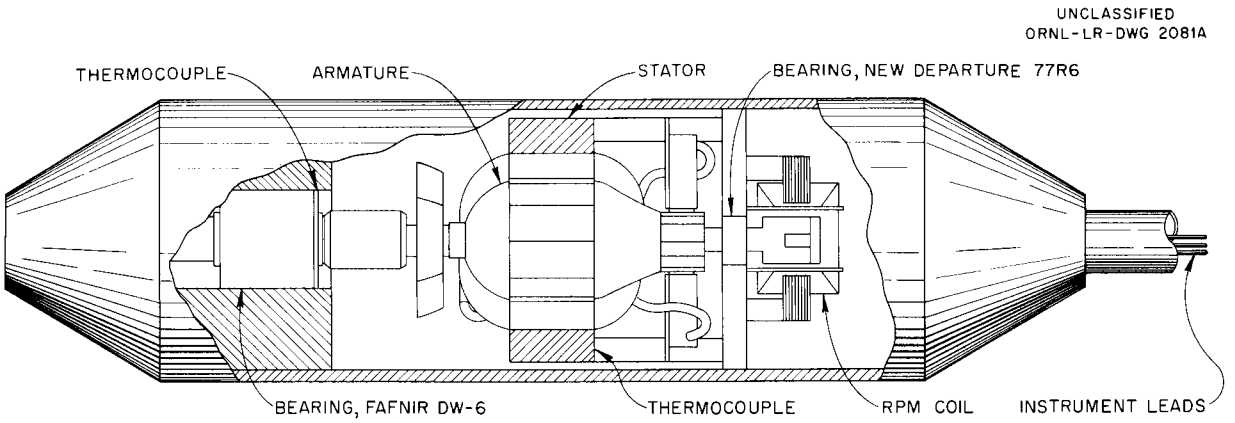

MOTOR: DELCO, AC-DC, 1/15 hp, SERVICE NO. 5047431
STATOR TAPE: GLASS
BRUSH HOLDER PLATE: MICA
RPM COIL: NO. 36 A.W.G. CEROC, 200-5500 TURNS
BEARING GREASE: RRG-2 (NLGI GRADE 2)

Fig. 48. Motor and RPM Meter Test Assembly.

are counted remotely by a frequency meter calibrated in rpm. The coil was wound with 36-gage Ceroc 200 magnet wire covered with glass tape impregnated with Glyptol. Summary data on the test conditions are given in Table 5.

The motors were examined, after irradiation, in the hot cell of Building 3025. Assistance was given in the hot-cell examination by J. Noaks and J. Crudele of Pratt & Whitney Aircraft Division.

The motor load in test No. 1 was abnormally great from the beginning, and the field-plate temperature was high. When the motor failed after 100 hr, the stator temperature rose to 182°C while the power was kept on. The suspicion that there was a cocked, upper bearing plate was confirmed upon postirradiation examination (Fig. 49). The sensing coil for the rpm meter functioned well; there was no resistance change or visual deterioration.

The motor used for test No. 2 operated for as long as it would be expected to under normal conditions. However, postirradiation inspection showed that the commutator segments had loosened because of deterioration of the plastic commutator-segment spacer (Fig. 50). The bearing grease proved to be adequate and was essentially unaffected as evidenced by the constant-power demand by the motor at constant rpm. The rpm coil also showed no resistance change nor visible breakdown (Fig. 51). The brush wear appeared to be normal.

A high-temperature motor is being constructed with glass-insulated wire, mica, and high-altitude brushes.

TABLE 5. CONDITIONS OF TEST MOTOR AND RPM METER ASSEMBLY

	Test No. 1	Test No. 2
Motor load		
d-c voltage	60	33
Current, amp	0.45	0.20
Shaft speed, rpm	4500	4500
Fafnir bearing temperature, °C	45	45
Motor field-plate temperature, °C	65	40
Time of operation, hr		
At 4500 rpm	100	648
In flux*	84	613

*Thermal flux, 5×10^{11} neutrons·cm^{-2}·sec^{-1}; ratio of fast to thermal, 1; gamma field, 4.4×10^5 r/hr.

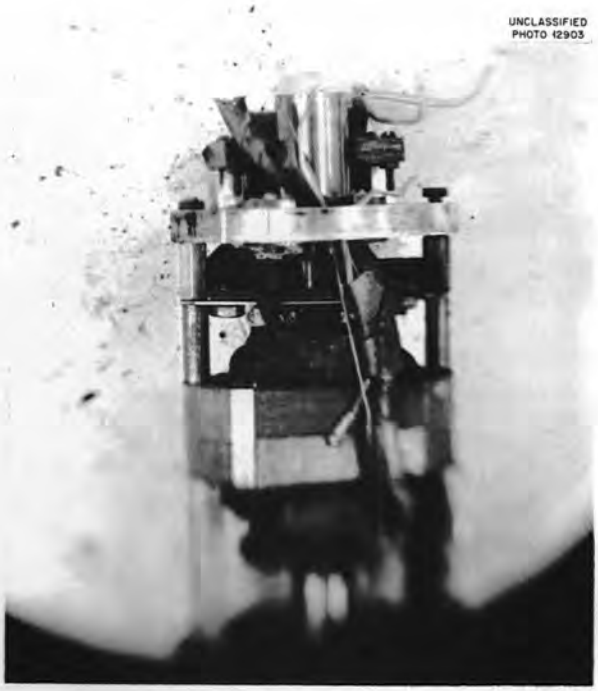

Fig. 49. Irradiated Motor After Failure Caused by Cocked Upper Bearing Plate.

Fig. 50. Armature of Irradiated Motor with Commutator Segments Loosened Because of Deterioration of Plastic Spacers.

DESIGN CALCULATIONS FOR MINIATURE CIRCULATING LOOP

M. T. Robinson D. F. Weekes

The series of calculations reported previously[7] for the miniature circulating loop has been extended to include some new configurations of the loop. The model finally selected is shown in Fig. 52. Fuel, flowing at a velocity characterized by its Reynolds number, *Ref*, enters the loop at the point $s = 0$, at a temperature T_f°, where s is the distance measured along the center line of the fuel column from the fuel entrance to any given point along the exchanger. Heat produced in the fuel by the fission process is removed by cooling air flowing in the annulus surrounding the fuel loop. Air, flowing at a velocity characterized by its Reynolds number, *Rea*, enters the annulus at the two planes $s = 0$ and $s = S$, at a temperature T_a°, and leaves the system at $s = S/2$, where S is the total length of the exchanger. In passing around the loop, the fuel is first cooled slightly, then heated strongly as it passes through the high-flux region, and finally cooled to its original temperature as it leaves the loop at $s = S$.

The loop is supposed to be mounted in position C-48 of the LITR in such a manner that the tip is in the region of maximum thermal-neutron flux.[8] The fuel assumed is composition 44 (NaF-ZrF_4-UF_4, 53.5-40-6.5 mole %), which generates a fission power of 510 w/cc in this situation.[9] No external heating is provided. The fuel tube is 0.200 in. ID, 0.300 in. OD, and the inside diameter of the cooling-annulus outer tube is 0.600 in. The value of S is 205 cm (80.71 in.).

The principal part of the calculation is the evaluation of the mixed-mean temperature of the fuel, T_f, as a function of s. The computation scheme used previously has been adapted for use on the electronic analog computer ("pile simulator") of the

[7] M. T. Robinson, *Solid State Semiann. Prog. Rep. Feb. 28, 1954*, ORNL-1677, p 29.

[8] M. T. Robinson, *Solid State Semiann. Prog. Rep. Feb. 28, 1954*, ORNL-1677, p 27.

[9] G. W. Keilholtz *et al.*, *Solid State Semiann. Prog. Rep. Feb. 28, 1954*, ORNL-1677, p 20.

Fig. 51. Irradiated RPM Coil.

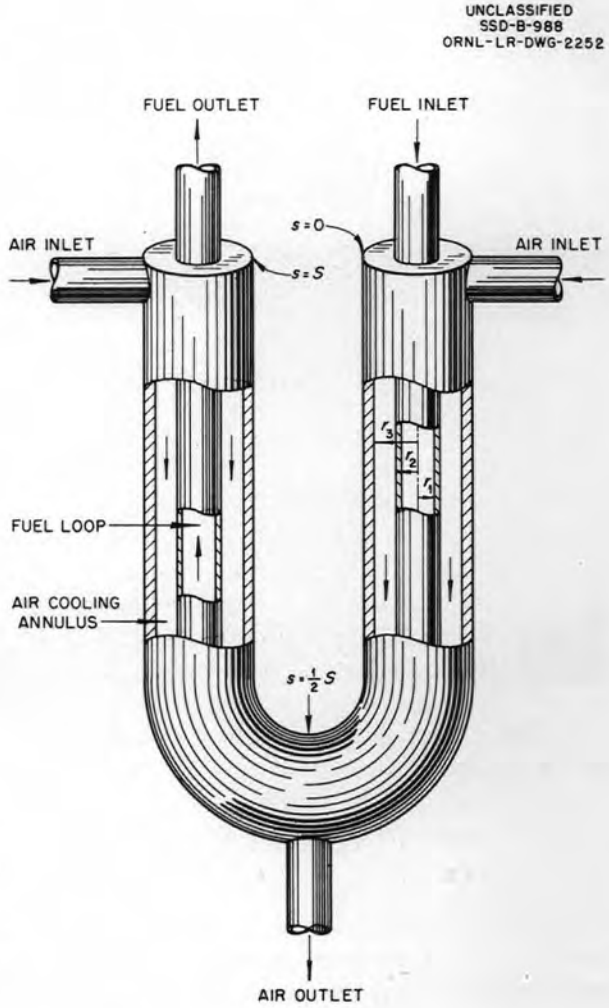

Fig. 52. Miniature Circulating Loop Model Used for Design Calculations.

Reactor Controls Department of the ORNL Instrumentation and Controls Division.[10] Calculations are being made subject to the condition that T_f be the same at both $s = 0$ and $s = S$. The procedure is to evaluate by approximation a quantity y_0 from which the temperatures T_f° and T_a° can be calculated. Some typical results are given in Figs. 53 and 54.

FUSED-SALT FILLING APPARATUS

W. E. Browning C. C. Webster

An apparatus has been assembled for filling experimental equipment with measured quantities of fluoride fuels in the molten condition at high levels of purity. Full use was made of experience of the groups at Y-12 in handling the liquid fuel. The filling apparatus is equipped with a vacuum system for leak-testing and purging gases from the system, a liquid-nitrogen-cooled charcoal trap for purifying helium used in applying pressure to move the liquid fuel, furnaces and electrical resistance

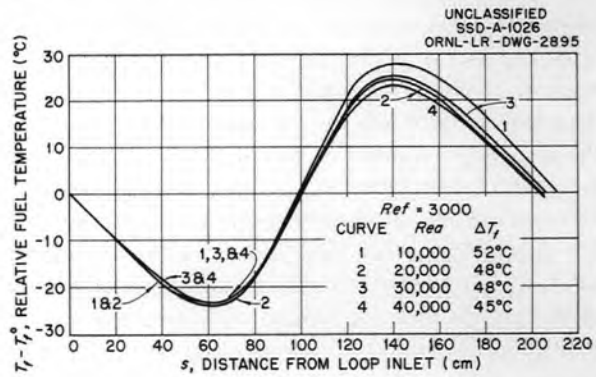

Fig. 53. Effect of Air Velocity on Fuel Temperature Profile.

[10] J. J. Stone and E. R. Mann, *Oak Ridge National Laboratory Reactor Controls Computer*, ORNL-1632 (March 30, 1954).

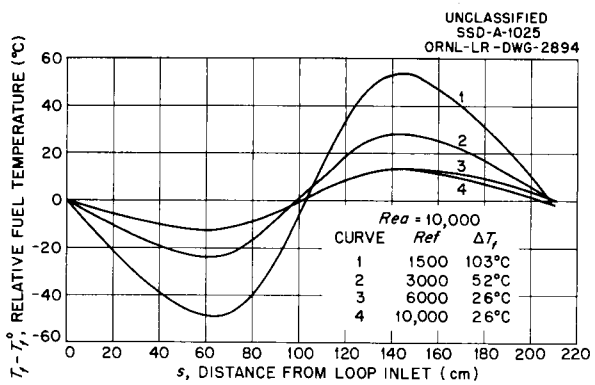

Fig. 54. Effect of Fuel Velocity on Fuel Temperature Profile.

heaters for all parts of the fluid-fuel system, electrical-probe level detectors, and a network of thermocouples spotted at typical points throughout the system. Transfer lines of Inconel are joined with Swagelok connectors. Ambient helium seals are used during assembly to exclude the atmosphere. Liquid-volume measurement is done in a metering tank equipped with a number of probes of measured lengths. Fluid flow is regulated by manipulating helium pressures and is finally halted by freezing a transfer line with the use of a wet asbestos sponge.

When the transfer from the metering tank to the experimental equipment is completed, the transfer line is heated locally and pinched shut, with the fuel molten inside. A pinch clamp is used to hold the tube closed vacuum-tight while it is severed at a different point, cleaned out, evacuated, pinched closed again, and welded shut by heating the outside of the pinched evacuated tube. The excess tubing is cut off near the weld, and a second precautionary weld is made. The experimental apparatus is thus filled, and the fill tube is welded shut without the fuel being exposed to the atmosphere. The apparatus has been operated four times, and each time there was an improvement. The equipment for transferring molten fuel to the experimental apparatus is shown in Fig. 55. The furnace for heating a 10-in.-dia pot containing 50 lb of fuel has nine sides, each side consisting of a 110-v element. The furnace, variac, and all the accessory equipment are mounted on a metal table built on casters.

The technique used for closing the filling tube to the apparatus is to crimp the tube in a hydraulic C-clamp equipped with $\frac{1}{16}$-in. flat jaws while the fuel is still molten; then the fuel is frozen and the fill tube is cut off 2 in. below the crimp, the salt is drilled out completely with a drill a few thousandths larger than the inside diameter of the tube to give a clean surface for welding, and the tube is attached to a vacuum system and evacuated, purged with helium, and re-evacuated. The tube is next crimped off less than 1 in. below the first crimp by the same hydraulic C-clamp employing $\frac{1}{2}$-in. flat jaws this time. After the upper end of the $\frac{1}{2}$-in. flat portion is spot-welded, the tubing is cut off below the spot weld with bolt cutters and then butt-welded.

REMOVAL OF Xe^{135} FROM FLUORIDE FUELS

M. T. Robinson
W. A. Brooksbank[12]
D. E. Guss[11]
T. L. Trent[13]

Brief experimental work reported two years ago[14] indicated that, although Xe^{135} could be easily purged from fluoride fuels by means of helium, its natural rate of escape was very low. A program has been initiated to repeat the previous work and to extend it to systems more nearly representative of actual reactor conditions. The importance of such a program has been pointed out by Meem;[15] a detailed proposal for the program has been presented elsewhere.[16] A four-channel gamma-radiation spectrometer has been constructed by the Instrumentation and Controls Division for use in monitoring the Xe^{135} concentration in a flowing stream of helium. A capsule has been designed on the basis of the one used previously[14] but has been substantially improved. Position HB-3 of the LITR will be used for the capsule experiments.

CALCULATION OF CONCENTRATIONS OF FISSION PRODUCTS IN FLUORIDE FUELS

M. T. Robinson
L. H. Lund

The fission process has numerous chemical consequences in systems in which it takes place. In

[11] USAF.

[12] Analytical Chemistry Division.

[13] Engineering and Mechanical Division.

[14] M. T. Robinson and D. D. Davies, *Solid State Quar. Prog. Rep. Aug. 10, 1952*, ORNL-1359, p 19.

[15] J. L. Meem, *The Xenon Problem in the ART*, ORNL CF-54-5-1 (May 3, 1954).

[16] M. T. Robinson, *Release on Xenon from Fluoride Fuels: Proposal for an Experimental Program*, ORNL CF-54-6-4 (June 2, 1954).

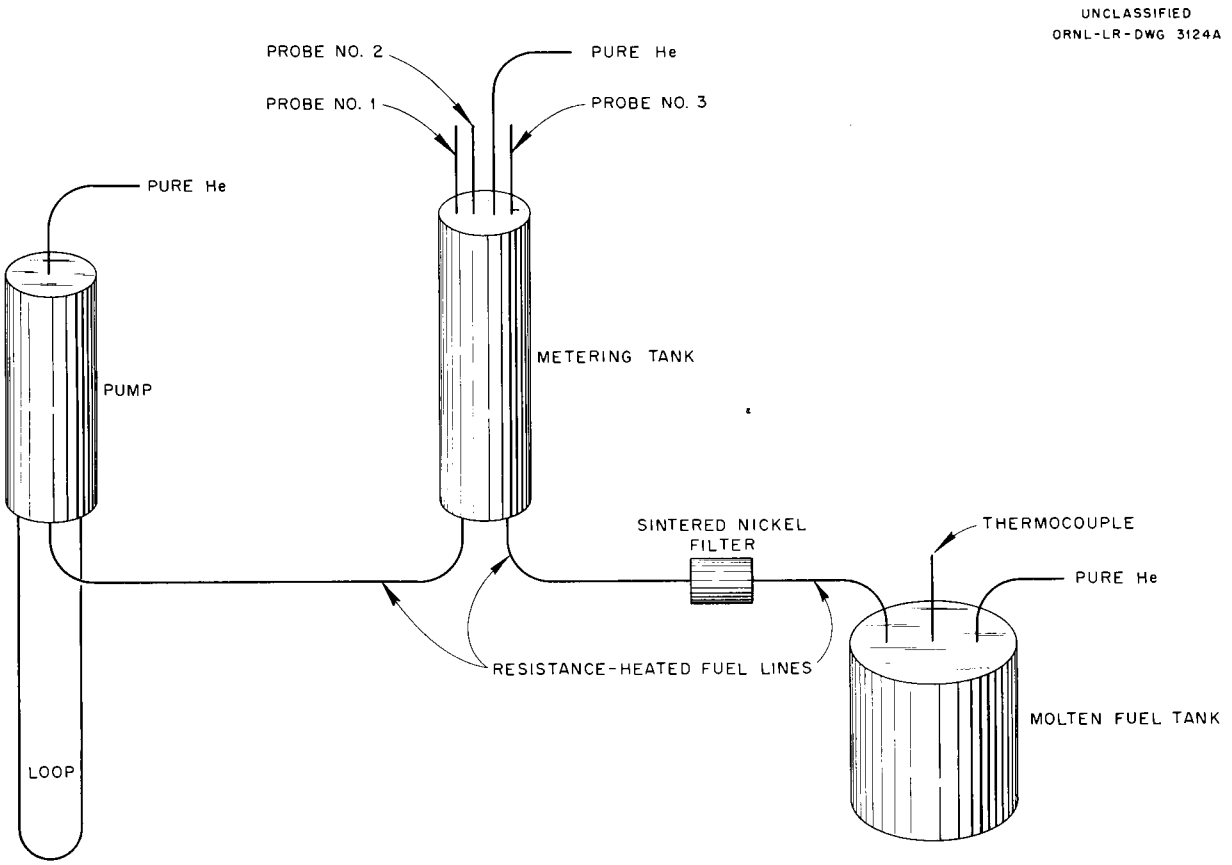

Fig. 55. Molten Fuel Filling Apparatus.

fluid systems, certain of the fission-product elements may either accelerate or inhibit corrosive attack on the container. In addition, there are possible chemical reactions resulting from differences of oxidation state between the fission products and the original uranium. In ANP fluoride fuels, this latter situation may be illustrated by the processes

$$UF_4 \xrightarrow{\text{fission}} RbF + CsF + F_2$$

$$UF_4 \xrightarrow{\text{fission}} 2PdF_2$$

$$3UF_4 \xrightarrow{\text{fission}} GaF_3 + PmF_3 + 2UF_3$$

which demonstrate the formation of strong oxidizing agents, "conservation" of oxidation state, and formation of strong reducing agents, respectively.

The concentration of various fission-product elements have been calculated previously for only the asymptotic case of long, reactor operating time where a stationary state can be assumed.[17,18] However, for proper analysis of in-pile tests and for study of aircraft reactors, it is necessary also to study the time dependence of the various element concentrations in the early part of a reactor fuel cycle. A very rough calculation indicates that at the beginning of a cycle there will be an over-all tendency toward an excess of oxidizing agent which will decrease with time and ultimately tend toward reducing conditions.

A detailed calculation of the concentration of any fission-product nuclide as a function of irradiation time is simple in principle. It is necessary to solve only a system of first-order differential equa-

[17] G. Scatchard *et al.*, *Chemical Problems of Non-Aqueous Fluid-Fuel Reactors*, MIT-5001, p 22–30 (Oct. 15, 1952).

[18] R. F. Newton, *Effects of Fission Products on Performance of a Reactor Using Fluoride as Solvent for Fuel*, ORNL CF-54-5-40 (May 7, 1954).

tions in which

$$\dot{x}_i = y_i + \lambda_{i-1}x_{i-1} - \lambda_i x_i \ , \tag{1}$$

where y_i is the direct fission yield of the ith nuclear species, λ_i is its decay constant, λ_{i-1} is the decay constant of its parent, and the quantity x_i is a sort of concentration defined by

$$x_i = \frac{n_i}{n_u \sigma_f \phi} \ , \tag{2}$$

where n_i and n_u are the numbers of nuclei per unit volume of the ith fission-product species and of U^{235}, respectively, σ_f is the fission cross section of U^{235}, and ϕ is the thermal flux. The terms on the right side of Eq. 1 represent the creation of the ith species from fission and from decay of its parent and its own decay to its daughter.

The fission yields, y_i, are not deducible directly from the familiar plot of fission yield vs mass number. Actually, theoretical understanding of the distribution of nuclear charge in fission leaves much to be desired. In only a very few cases are relevant experimental data available. For engineering calculations it seems sufficient to use the empirical approach of Glendenin *et al.*,[19] who employ the hypothesis of equal charge displacement, based on the liquid-drop-model discussion of the fission process of Bohr and Wheeler.[20] This theory has been used to calculate the fission yields of each nucleus that occurs in fission which has a half life greater than 1 min and which occurs in a mass chain having a yield greater than 0.01%.

Calculation of the concentrations x_i as functions of time will be made on the electronic analog computer ("pile simulator") in the Reactor Controls Department of the Instrumentation and Controls Division.[21]

FISSION-PRODUCT CORROSION STUDY

C. C. Webster

One of the environmental factors which could affect the corrosion of the fluoride fuel systems is the fission-product concentration. A preliminary survey made by Kertesz and co-workers of the Materials Chemistry Division suggests that this may be the case. To carry out such a study it is necessary for fission products to be present in a molten fuel in the absence of neutrons.

To give the high concentration of fission products per unit volume of fuel it was necessary to irradiate a fuel of high uranium concentration in the solid form to trap the fission products. A water-cooled facility was constructed and was installed in position C-46 of the LITR (Fig. 56). The fluoride fuel of composition 41 (12 mole % UF_4, 25 mole % ZrF_4, 63 mole % NaF) was made into solid bars 1 in. long by 0.1 in. in diameter in a nickel mold under a helium atmosphere. An Inconel capsule (Fig. 57) was constructed so that it could be welded shut without the bar being melted and so that it can be reopened in the hot cell after irradiation. The solid bar must then be removed quickly as a single piece and transferred to an unirradiated Inconel container; this container is then evacuated, purged with helium, and welded closed in the hot cell. The capsule is then put into a shielded furnace and heated to 1500°F for two weeks.

Upon completion of the heating cycle, the capsule will be opened in the hot cell, and the fuel will be drilled out and divided into three samples; a portion will be used for petrographic study to detect any oxidation or reduction, a portion will be used for mass spectrographic study to determine burnup, and a third portion will be chemically analyzed. The capsule will be slit on the remotely controlled slitting machine for a metallographic study (cf. "Remotely Operated Tube-Slitting Machine," this report). At least two concentric samples can be taken from a capsule of this size by remote means.

In addition to the above test of irradiated fuel in unirradiated capsules, there will be tests involving unirradiated fuel in irradiated capsules, irradiated fuel in irradiated capsules, unirradiated fuel in unirradiated capsules, and control tests of unirradiated fuel put into unirradiated capsules in the absence of oxygen and water vapor.

The irradiation of both the solid fuel bars and the Inconel capsules will be for a four-week period. If it is found that the reactor water will keep the temperature of the samples down to a sufficiently low value, consideration will be given to a new

[19] L. E. Glendenin, C. D. Coryell, and R. R. Edwards, Paper 52 in *Radiochemical Studies: The Fission Products*, NNES, Vol. IV-9, Book 1, p 489–516, McGraw-Hill, New York, 1951.

[20] N. Bohr and J. A. Wheeler, *Phys. Rev.* 56, 426 (1939).

[21] J. J. Stone and E. R. Mann, *Oak Ridge National Laboratory Reactor Controls Computer*, ORNL-1632 (March 30, 1954).

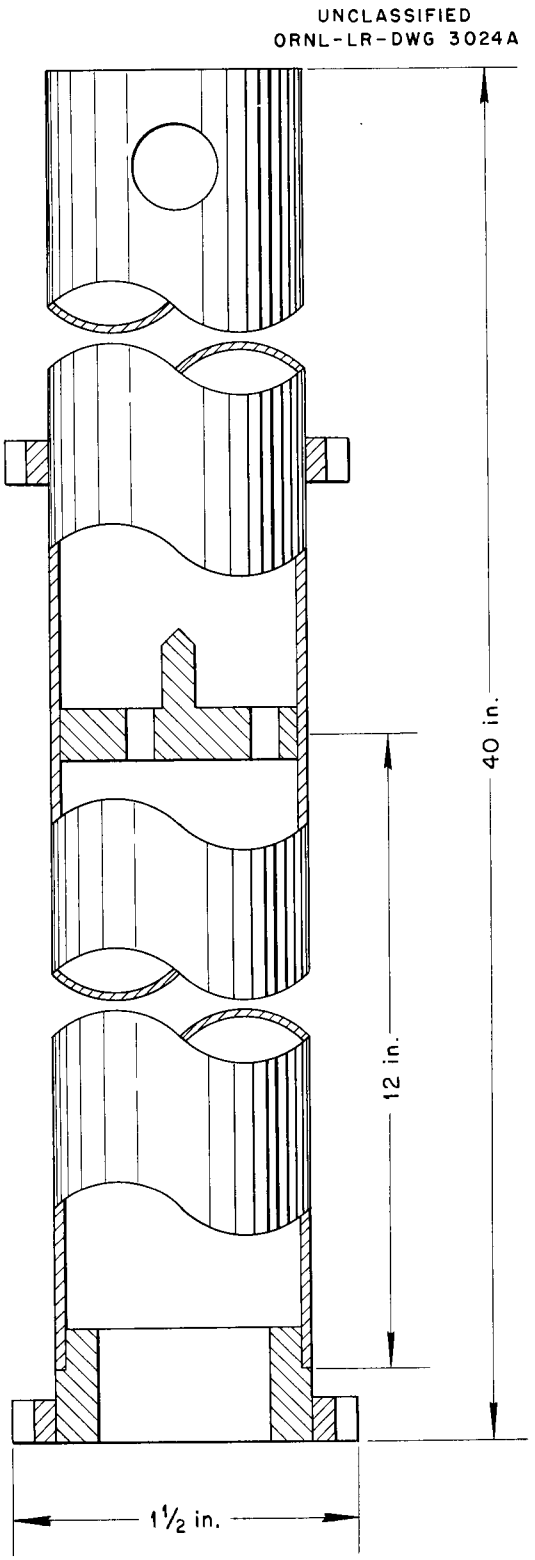

Fig. 56. Water-Cooled Facility for LITR Hole C-46.

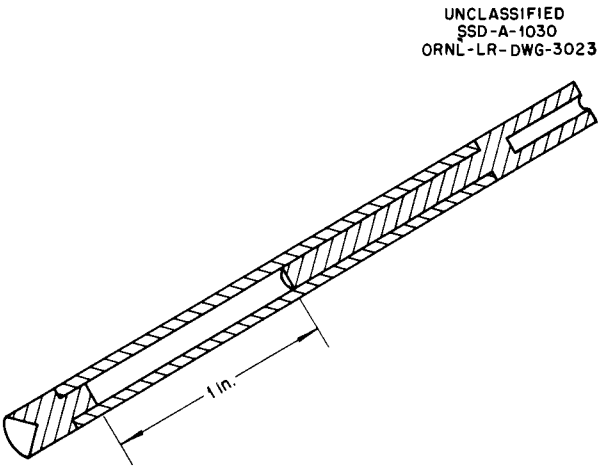

Fig. 57. Fission-Product Corrosion Capsule.

series in which a fuel with high uranium concentration will be used to give a higher concentration of fission products during the high-temperature portion of the test.

ASSAY OF U(III)-U(IV) SYSTEMS BY MAGNETIC MEANS

M. T. Robinson

It has frequently been suggested that mixtures of U(III) and U(IV) compounds might be assayed by making use of the paramagnetic properties of the two ions. A brief theoretical investigation of the magnetic moments of these ions was made by conventional methods, with crystalline field effects neglected. The various possible configurations of the valence electrons and the resulting magnetic moments for the two extreme cases of *LS* and *jj* coupling are given for each ion in Table 6. The two values given in certain cases result from ambiguities in the coupling scheme. Table 7 lists some of the experimental data for the magnetic moments and Weiss constants of several uranium compounds taken from papers by other investigators.[22,23,24] Comparison of these tables suggests that the U(III) and U(IV) ions have the configurations $5f^3$ (or $5f6d^2$) and $5f^2$ (or $5f6d$),

[22] J. K. Dawson, *J. Chem. Soc.* **1951**, 429; *ibid.*, p 2889; J. K. Dawson, *J. Chem. Soc.* **1952**, 1185.

[23] N. Elliott, *Phys. Rev.* **74**, 498 (1948); N. Elliott, *Phys. Rev.* **76**, 431 (1949).

[24] W. V. Goddell, *Cyclotron Irradiation of Fused Fluorides in Inconel at Elevated Temperatures*, NAA-SR-208, pp 24, 31 (Jan. 26, 1953).

TABLE 6. CALCULATED MAGNETIC MOMENTS OF URANIUM IONS

Ion	Electronic Configuration	Magnetic Moment (Bohr magnetons)	
		LS Coupling	*jj* Coupling
U(III)	$5f^3$	3.618	4.066
	$5f^2 6d$	4.663	5.032 5.041
	$5f6d^2$	3.618	3.946 3.935
	$6d^3$	0.775	1.549
U(IV)	$5f^2$	3.578	3.833
	$5f6d$	3.578	3.737
	$6d^2$	1.633	1.960

TABLE 7. EXPERIMENTAL MAGNETIC MOMENTS OF URANIUM IONS

Compound	Magnetic Moment (Bohr magnetons)	Weiss Constant (°K)	Reference
UF_3	3.0		*a*
UCl_3	3.03	−29	*b*
UBr_3	3.29	+25	*b*
UI_3	3.31	+5	*b*
UF_4	3.30	102, 147	*b, c*
KUF_5	3.30	122	*c*
K_2UF_6	3.45	108	*c*
Na_3UF_7	3.40	290	*c*

[a]W. V. Goddell, *Cyclotron Irradiation of Fused Fluorides in Inconel at Elevated Temperatures*, NAA-SR-208, pp 24, 31 (Jan. 26, 1953). The value of 13.1×10^{-6} emu/g for the magnetic susceptibility of UF_3 at room temperature was used to estimate the magnetic moment, on the assumption that Curie's law is obeyed.

[b]J. K. Dawson, *J. Chem. Soc.* **1951**, 429; *ibid.*, p 2889; J. K. Dawson, *J. Chem. Soc.* **1952**, 1185.

[c]N. Elliott, *Phys. Rev.* **74**, 498 (1948); N. Elliott, *Phys. Rev.* **76**, 431 (1949).

respectively, with some quenching by the crystalline field being evident in each case. The magnetic moments of the two species are so closely similar as to be indistinguishable, at least for analytical purposes.

A further complication in magnetically assaying the fluoride fuels is that they consist of quite dilute solid solutions of UF_4 and/or UF_3 in diamagnetic salts. Table 8 gives some data from the work of Dawson[22] on solid solutions of UF_4 in ThF_4 and shows the importance of solid-solution formation on the magnetic moment of U(IV).

TABLE 8. MAGNETIC MOMENT OF U(IV) IN UF_4-ThF_4 SOLID SOLUTIONS*

UF_4 Concentration (mole %)	Magnetic Moment (Bohr magnetons)	Weiss Constant (°K)
100	3.30	102
94.9	3.30	102
86.2	3.20	78
67.6	3.17	68
39.7	3.11	56
20.6	2.82	22
10.4	2.92	25

*J. K. Dawson, *J. Chem. Soc.* **1951**, 429; *ibid.*, p 2889; J. K. Dawson, *J. Chem. Soc.* **1952**, 1185.

It is concluded that the magnetic properties of the two ions cannot be used in any practical method of assaying U(III) and U(IV) in the presence of each other.

C_7F_{16}-UF_6 IRRADIATION

W. E. Browning

An experiment is being conducted to determine, in a very rough fashion, the effect of reactor irradiation on a 20% solution of UF_6 in C_7F_{16}. This material is of interest to the Shielding Section of the Physics Division for simulating liquid fuels in dynamic-shielding experiments, and the experiment is being conducted with the aid of personnel from that division. Three nickel capsules were charged with the two components to make a 7-g solution in each. Normal uranium was used. Two capsules

were irradiated in appropriate secondary containers in a water-cooled hole in the ORNL Graphite Reactor for 63 hr at a thermal flux of 6×10^{11} neutrons·cm^{-2}·sec^{-1}. This exposure corresponds to 25 times the fission density expected in the shielding experiment with enriched uranium. The capsules were opened in a special gas manifold, and gas pressures were determined. The pressure inside the irradiated capsules was shown to have been greater than 50 but less than 100 psia. The pressure in the unirradiated capsule was not perceptibly different from the vapor pressures of the two components (about 4 psia). The gas in the capsules was analyzed by infrared absorption spectrometry at K-25 and contained CF_4, C_2F_6, C_7F_{16}, and other fluorocarbon compounds not identified. No UF_6 could be detected in the gas sample. Pressure measurements at −80 and −190°C were consistent with these analyses. The irradiated capsules were full of a nonvolatile (at 25°C) greenish powder that was insoluble in C_7F_{16}. The powder will be analyzed for uranium. The unirradiated capsule contained no residue except a faint chalkiness on its inner wall. Additional capsules are being irradiated for $\frac{1}{100}$ of the accumulated exposure. It is interesting to compare the power density of 5×10^{-2} w/cc in this experiment with the 1000 to 5000 w/cc in capsules containing fluid fluoride fuel.

Part II

UNCLASSIFIED PROJECTS

CONTENTS

PART II

SUMMARY 61

SOLID STATE REACTIONS 65
Neutron Irradiation of Indium Antimonide 65
Energy Levels in n-Type Germanium Irradiated at Room Temperature 71
Mobility in Bombarded n-Type Germanium 75
Radiation Effects on Lead-Wire Insulation 76
Bombardment of Rectifiers 78
Radiation Effects in Ionic Crystals 79
Magnetic Susceptibility Studies 81
Degeneracy and Effective Mass in Germanium 85
Irradiation Effects in Zircon Single Crystals 85
Unirradiated and Irradiated Piezo Quartz 86

ENGINEERING PROPERTIES 90
Properties of Reactor-Irradiated Ceramics 90
X-Ray Diffraction Patterns of Irradiated Elastomers 91
Radiation Effects on Plasticized Polyvinyl Chloride 91
Calculation of the Dynamic Young's Modulus and the Viscous Modulus from the Resonance Curves 93

CRYSTAL PHYSICS 97
Work-Hardening in Copper Crystals 97

SPECIAL PROJECTS 111
Neutron Irradiation of LiF 111
Paramagnetic Resonance in Irradiated Materials 112
Dielectric Constant and Loss Tangent of Irradiated Plastics at Microwave Frequencies 113
Thermal Conductivity of Dielectrics at Low Temperatures 115
Thermal- and Electrical-Conductivity Studies 115
A Rocking-Curve Adapter for the Norelco Wide-Range Diffractometer 117
Shielding for an X-Ray Diffractometer 120

SUMMARY

SOLID STATE REACTIONS

Neutron Irradiation of Indium Antimonide. Hall coefficient and resistivity measurements as a function of temperature have been made on both n- and p-type single-crystalline samples of InSb after successive periods of exposure in the ORNL Graphite Reactor. Effects caused by the introduction of tin, a donor impurity, were minimized by shielding the specimens with cadmium and indium foil from those neutrons leading to indium transmutation. The results of these measurements indicate conclusively that lattice defects produced by fast-neutron bombardment convert p-type InSb to n-type. In addition, they appear to act as shallow electron traps in n-type material. The mobility of carriers is markedly decreased by the bombardment-produced defects, but the mobility, as well as the carrier concentration that results from bombardment-produced energy states, can be almost completely restored to their original values by the appropriate heat treatment. An attempt has been made to correlate the various, possible, simple defects expected in the InSb structure with the nature of energy levels introduced by fast-neutron bombardment.

Energy Levels in n-Type Germanium Irradiated at Room Temperature. James and Lark-Horovitz have theorized that in germanium each Frenkel defect introduces four localized states into the forbidden energy band: a shallow vacant site which lies about 0.05 ev below the bottom of the conduction band, a deep-lying vacant state, and two occupied states which lie near the top of the filled band.

Measurements were made of conductivity and Hall coefficient vs temperature of irradiated n-type germanium. Analysis of the results indicates that the two-vacant-state model suggested by James and Lark-Horovitz is justified experimentally, even though ϵ_s, the depth of the shallow trap, is greater by about a factor of 4 than the predicted value of 0.05 ev; this value of 0.20 ev agrees with the experimental results obtained by the Purdue group who worked with deuteron-bombarded n-type germanium.

No explanation has been found for the apparent increase of the shallow-trap depth by the low-temperature annealing of irradiated germanium.

Mobility in Bombarded n-Type Germanium. The Hall mobility μ_H is decreased by bombardment over the range 77°K to room temperature. An exposure of 7.9×10^{15} fast neutrons/cm^2 decreases the mobility by about 50% at room temperature and by more than an order of magnitude at 77°K.

Low-temperature annealing (152°C) after bombardment produces more extensive healing of lattice damage than was previously suspected. The amount of irradiation required to remove lattice-scattering behavior from germanium appears to be directly dependent on the original charge-carrier concentration.

Radiation Effects on Lead-Wire Insulation. Insulated wires were run into the ORNL Graphite Reactor as if they were leads to a sample, and the effect of radiation on the insulation resistance was studied. Insulating materials studied were undoped glass, doped glass, rubber and Nylon, polyvinyl, polyethylene, rubber, and Teflon. The resistance change produced by reactor radiation was several orders of magnitude larger than that produced by gamma and beta radiation. In addition to the resistance change, a voltage developed between the two conductors (shield and conductor) after an exposure of a day or so.

Bombardment of Rectifiers. The conductivity of both p- and n-type silicon point-contact rectifiers under irradiation was determined several years ago. Since that time techniques have been improved; therefore check measurements were made. The present measurements agree with the earlier one in that the conductivity decreases monotonically during the initial stage of bombardment and also disclose that the rectifier becomes ohmic after sufficient irradiation, a fact not found in the past because of lead-wire effects. Radiation had caused the insulation of the lead wire used at that time to decrease in resistance until its resistance was comparable to that of the sample. Radiation also produced some rectification in the lead wires, as well as voltages of the order of 0.5 v in lead-wire insulation. These effects were minimized in the present measurements.

Radiation Effects in Ionic Crystals. Unirradiated, synthetic potassium chloride crystals annealed at elevated temperatures were found to undergo resistivity changes similar (but less drastic) to those observed for irradiated crystals.

The ionic-conductivity apparatus has been improved so that accurate measurements from 10^{16} to 10^{6} ohms over the range 21 to 720°C were possible. Further improvements will be made.

Magnetic Susceptibility Studies. The magnetic susceptibility of an InSb, *p*-type, single-crystal cube containing 1.1×10^{16} carriers/cm^3 at 77°K has been measured as a function of temperature. At about 210°K the Hall coefficient temperature measurements show that the properties of this specimen change from extrinsic to intrinsic. A large diamagnetic component to the magnetic susceptibility is generated as the temperature is increased into the intrinsic range; this is as predicted on the assumption that the electrons in InSb have a low effective mass.

The susceptibility of five samples of unirradiated germanium has been measured as a function of temperature. Because one of the samples was purer than any other germanium sample yet obtained it will be used to represent the contribution of the germanium lattice in future analyses of germanium data. Two *n*-type samples were found to have unusually high carrier concentrations and to be degenerate throughout the temperature range measured. The ratios of rest mass to effective mass of the electron were 4.2 and 4.6, probably because the carrier concentrations were high. Two *p*-type samples were also found to be degenerate throughout the temperature range measured. The mass ratio for sample BTP-5 has been tentatively established as 5.8, and the ratio of the rest mass of the electron to the effective mass of the carrier is lower than previously reported values.

A study was made of the dependence of diamagnetic susceptibility on temperature for *n*-type germanium converted to *p*-type by irradiation. Although there is a difference between the curve of a pure specimen and that of a specimen bombarded into the intrinsic range, this difference does not appear to be the theoretically expected spin contribution of 7×10^{17} cm^{-3} electrons. Rather, the difference is attributed to both a decrease in the negative coefficient of the susceptibility of the lattice and an increase in the temperature dependence of the number of free current carriers as a result of bombardment. The study indicates that the interstitial atom does not possess a residual-spin magnetic moment at the conductivity minimum as implied by the James–Lark-Horovitz model of bombardment-produced energy levels. It may be that the resultant spin is absent because the energy levels produced by the defects form a narrow degenerate band of states; the lower bands would then be completely filled at the conductivity minimum and there would be no spin unbalance.

Degeneracy and Effective Mass in Germanium. Cyclotron resonance measurements have indicated that there is an eightfold special degeneracy in *n*-type germanium. Use of the degeneracy factor of 8, rather than the factor of 6 that was previously assumed in the Fermi-Dirac distribution function, gave a much better fit to data. The use of eightfold degeneracy, however, assumes that the energy surfaces are spheres in *k* space, whereas experimental results indicate that the energy surfaces are quite eccentric ellipsoids of revolution. It also appears that the energy minima in *k* space correspond to the Brillouin zone boundary for which only a fourfold degeneracy is expected. Calculations are now in progress to include these additional features in the treatment of *n*-type susceptibility data.

Irradiated Effects in Zircon Single Crystals. Many natural zircon crystals are disordered as a result of alpha radiation emitted by impurity atoms of the uranium-actino series and of the thorium series which occupy normal zirconium sites in the space lattice. The crystals which are disordered by internal alpha emissions are estimated to have an age of 10^{9} years; the alpha particles have energies of approximately 6 Mev.

An attempt has been made to compare the disorder produced by the internal alpha radiation with that produced by bombardment of zircon single crystals with fast neutrons. Irradiations up to 2.8×10^{20} fast neutrons/cm^2 have produced a highly distorted lattice, but long-range order was maintained.

Although fast neutrons should be more effective than energetic alpha particles in producing displacements, it is reported that the zircon lattice may be disordered by 10^{17} α/mg. If this is true, processes other than the alpha-displacement process must contribute to the disorder.

Unirradiated and Irradiated Piezo Quartz. Specific diamagnetic susceptibility vs temperature curves were determined for three specimens of crystalline quartz cut from a pair of matched piezoelectric crystals. One specimen was subjected to no irradiation, while the other two were subjected

to irradiations at 100°C of 5×10^{19} and 3.3×10^{20} fast neutrons/cm^2. The number of paramagnetic centers per cubic centimeter produced in the crystals by bombardment was calculated for an assumed spin of ½. Fast-neutron bombardment apparently produces a maximum number of paramagnetic centers at about 2×10^{19} neutrons/cm^2; appreciable density changes also begin to occur at this value.

Two absorption bands in the visible spectrum and one in the ultraviolet spectrum are produced. The paramagnetic centers probably are associated with the ultraviolet band, since the two bands in the visible spectrum reached a peak and then began to decrease with further irradiation; the ultraviolet band continued to increase up to the maximum irradiation (10^{18} neutrons/cm^2) that was optically studied.

ENGINEERING PROPERTIES

Properties of Reactor-irradiated Ceramics. Two sets of ceramic specimens have been exposed to integrated epithermal fluxes of about 1×10^{20} and 2×10^{20} neutrons/cm^2. A third set is being irradiated in the MTR at an exposure of about 10^{21} neutrons/cm^2.

The specimens of shorter exposure have been visually inspected only. The aluminum foil in which the specimens were wrapped and many of the specimens were thinly coated with a white solid. Pyrex glass developed surface cracks visible at 10X magnification, $BaO{\cdot}TiO_2$ crumbled under irradiation, and the MgO specimens stuck together and broke when attempts were made to pry them apart. Most of the ceramics darkened in color. A thorough investigation has begun of the effect of irradiation on other properties of the ceramics, and annealing studies will be made of some of the properties.

X-Ray Diffraction Patterns of Irradiated Elastomers. To obtain crystalline x-ray patterns of elastomers it is necessary to irradiate the elastomers in a stretched condition. It was found that Co^{60} irradiation of a natural-rubber formulation 32A43 destroyed the crystalline peaks at 21 and 24 deg and that the elastomer retained a large permanent set. An unstretched specimen showed no crystalline peaks on the x-ray diffraction curve, and no changes were produced by irradiation. The x-ray changes occurred long before any change was detected in the Young's modulus of unstretched specimens.

Radiation Effects on Plasticized Polyvinyl Chloride. The dynamic Young's modulus and the viscous modulus of polyvinyl chloride with various proportions of plasticizer were measured for various degrees of irradiation in the ORNL Graphite Reactor. It was found that although unplasticized polyvinyl chloride softens with irradiation, heavily plasticized formulations harden with irradiation.

Calculation of the Dynamic Young's Modulus and the Viscous Modulus from the Resonance Curves. An exact expression has been derived for obtaining the dynamic Young's modulus and the corresponding viscous modulus from the resonance curves. The band width is used at 0.9 maximum amplitude rather than at the 0.7 used in the previous equation. For materials having very high internal friction, such as polyvinyl chloride, the resonance curve is too broad to have a band width at 0.7 maximum amplitude. Either band width may be used below a viscous-to-Young's modulus ratio of about 0.3.

CRYSTAL PHYSICS

Work-Hardening in Copper Crystals. The stress-strain relationship in copper single crystals at low temperatures has been found to be linear rather than parabolic, as had been assumed from high-temperature data on face-centered-cubic metals. Deformation of copper crystals by slip results in both a mobile defect (vacancy) and an immobile defect (dislocation). The vacancies can be removed by an anneal of 300°K or less, but removal of the dislocations requires an anneal at higher than 500°K. Dislocations seem to be primarily responsible for work-hardening. The change in residual resistivity (measured at 4.2°K) attributed to dislocation scattering has a parabolic relationship to stress. From the data collected on the relationship between the stress and strain, the resistivity and flow stress, and the slip-line length and flow stress, the resistivity of a unit length of dislocation has been determined.

SPECIAL PROJECTS

Neutron Irradiation of LiF. The accuracy in the study of equivalence of x-ray lattice parameter and of the density changes in neutron-irradiated LiF crystals has been improved in two ways: the use of crystals of about one-third the thickness of the thinnest crystal previously studied has reduced the possibility of error in the attenuation calculation, and the shielding of crystals with cadmium has further reduced the attenuation. The epicad-

mium neutrons were shown to produce no detectable attenuation in the crystals. The x-ray and the density changes in neutron-irradiated LiF were found to be equivalent within 5%, and the radiation-induced defect is consequently of the Frenkel type.

Paramagnetic Resonance in Irradiated Materials. A rectangular-transmission resonant cavity has been built to operate in the TE_{101} mode at 9.150 kmc. It was found that frequency stabilization of the klystron was necessary to permit observation of the weak resonances induced by radiation.

A proton-resonance gauss meter has been constructed for measuring the magnetic field. The apparatus is being calibrated with alpha-alpha-diphenyl-beta picryl hydrazyl, which has a resonance g factor of 2.0038 and a half-width of about 3.7 gauss.

Dielectric Constant and Loss Tangent of Irradiated Plastics at Microwave Frequencies. The loss tangents and dielectric constants of polyethylene, polystyrene, and Teflon were measured at 1, 3, and 8.6 kmc after irradiations up to 8×10^{18} thermal neutrons/cm^2. The change in loss tangent was greatest for Teflon, with an increase by a factor of 7.3 at 1 and 3 kmc and 2.1 at 8.6 kmc after an exposure of 2×10^{18} neutrons/cm^2. The loss tangent of polyethylene increased by a factor of 2.5 at 1 and 3 kmc and showed no measurable change after an exposure of 8×10^{18} neutrons/cm^2 at 8.6 kmc. Any changes in the loss tangent of polystyrene at the three frequencies remained within the range of error for irradiations of 2×10^{18} neutrons/cm^2.

The dielectric constant of Teflon increased by 2.3% at 1 and 3 kmc and by 1.5% at 8.6 kmc for exposures of 10^{18} and 2×10^{18} neutrons/cm^2. Dielectric constants of polyethylene and polystyrene showed no change for exposures of 8×10^{18} neutrons/cm^2.

Thermal Conductivity of Dielectrics at Low Temperatures. Thermal-conductivity measurements have been conducted on a single quartz crystal in the liquid-helium, liquid-nitrogen, and liquid-hydrogen ranges. A maximum in the thermal conductivity of quartz was found at about 11°K. Measurements are now being made on single crystals of KCl, Al_2O_3, and very-high-purity germanium.

Thermal- and Electrical-Conductivity Studies. Thermal- and electrical-conductivity measurements on cast ductile iron were extended to the range 100 to 700°C in which both decreased by about a factor of 2. Rockwell hardness at room temperature decreased from 94B before the sample was heated to high temperature to 69B after being heated, but thermal- and electrical-conductivity values had not changed when the sample was returned to the lower temperatures.

Thermal-conductivity and electrical-resistivity measurements of 94% Cu–6% Al and 92% Cu–8% Al were made at temperatures up to 850°C. The thermal conductivity of both alloys increases with increasing temperatures.

A Rocking-Curve Adapter for the Norelco Wide-Range Diffractometer. An adapter has been designed for the Norelco wide-range diffractometer to extend its use to the study of large single crystals. Crystals up to 1 in. in diameter and $\frac{3}{8}$ in. thick can be rotated by an induction motor and at the same time may be rocked slowly about the conventional axis of the diffractometer by a synchronous clock drive. The adapter permits rapid orientation determinations and rocking-curve studies of cubic single crystals.

Distortion and disorder induced in single crystals by plastic deformation or nucleon bombardment make normal x-ray measurements very difficult. With the adapter and a very narrow x-ray collimating slit many large Bragg-angle reflections may be determined, and lattice parameter measurements can be made with an accuracy of ±0.005% in large, randomly oriented crystals.

Qualitative rocking curves are obtained by locating the desired reflections and then using the diffractometer in the normal manner. Quantitative analyses may be obtained by taking fixed-time counts at Geiger-tube intervals of 0.025 deg.

Shielding for an X-Ray Diffractometer. A G-E diffractometer has been modified to permit examination of irradiated specimens that measure up to 5 r on contact. Lead shielding has been provided with ports and doors so that specimens may be inserted in the holder and the instrument may be operated without overexposure of personnel.

SOLID STATE REACTIONS

NEUTRON IRRADIATION OF INDIUM ANTIMONIDE

J. W. Cleland J. H. Crawford, Jr.

The electrical properties of certain semiconductors are markedly altered by nucleon bombardment at or near room temperature. Studies of germanium[1-5] and silicon[1] reveal that lattice defects resulting from collisions of nucleons with lattice atoms introduce localized energy states in the forbidden energy band which may act as electron traps or hole traps. In silicon these two types of traps appear to be equally effective in removing charge carriers, and essentially intrinsic behavior is produced after prolonged bombardment.[6] In germanium, however, the hole traps appear to be quite shallow,[3] and some of the electron traps lie sufficiently deep in the forbidden energy band to act as acceptors in p-type material, causing conversion from n- to p-type material after adequate irradiation. Investigations of radiation effects have been extended to include the intermetallic compound InSb. (The high-purity single crystals used in these experiments were furnished by M. Tannenbaum of the Bell Telephone Laboratories.) Both poly- and single-crystalline specimens have been irradiated in the ORNL Graphite Reactor, and changes in both carrier concentration and mobility have been determined.

The electrical properties of InSb have been extensively studied[7-9] and in many respects are quite similar to those of silicon and germanium. The compound is distinguished, however, by a narrow forbidden energy gap E_g and an extremely large electron mobility. Recent studies by Tannenbaum and Maita[9] on single-crystalline, high-purity InSb indicate that E_g is temperature dependent and is approximately 0.18 ev at 300°K and that the room-temperature electron mobility is as large as 4×10^4 $cm^2 \cdot v^{-1} \cdot sec^{-1}$. Because of the large electron-to-hole mobility ratio (approximately 85 at 300°K), p-type material for even moderate carrier concentration ($\sim 10^{16}$) is in the intrinsic range well below room temperature.

Indium antimonide is one of a series of semiconducting intermetallic compounds formed between elements of the third and fifth groups of the periodic system. It crystallizes in the zinc-blende lattice which would reduce to the diamond lattice if only one type of atom were involved. Because of its binary nature, this compound offers the possibility of a greater variety of simple defects than do the elemental semiconductors. There may be a vacancy either in an indium or an antimony vacant lattice site, and an interstitial atom may possess either three or five outer electrons. In addition, the ordered arrangement of indium and antimony atoms in the lattice admits the possibility of an additional type of lattice damage not present in elemental structures. As a high-energy recoil from the collision of a neutron nears the end of its range, the rate of energy loss to the lattice becomes so large that a region variously estimated to contain between 1,000 and 10,000 atoms is heated to very high temperatures ($\sim 10^4$ °K) and is rapidly quenched ($\sim 10^{-11}$ sec). This so-called "thermal spike"[10] permits the rearrangement or interchange of atoms which may then be quenched into their new positions. Disordering of an ordered Cu_3Au alloy has been explained by this mechanism.[11] Similar effects are a distinct possibility in InSb but their observability would depend on a number of factors, including the extent of their influence on measurable properties, the mobility of the constituent atoms at the temperature of irradiation, and the magnitude of

[1] For a review of early work, see K. Lark-Horovitz, "Nucleon-bombarded Semi-conductors," p 47–69 in *Conference on Semi-conducting Materials*, ed. by H. K. Henisch, Academic Press, New York, 1951.

[2] J. W. Cleland *et al.*, *Phys. Rev.* **83**, 312 (1951).

[3] J. W. Cleland *et al.*, *Phys. Rev.* **84**, 861 (1951).

[4] E. E. Klontz and K. Lark-Horovitz, *Phys. Rev.* **86**, 643 (1952); see also, E. E. Klontz, unpublished thesis, Purdue University.

[5] W. L. Brown, R. C. Fletcher, and K. A. Wright, *Phys. Rev.* **92**, 591 (1953).

[6] J. W. Cleland, J. H. Crawford, Jr., and J. C. Pigg, unpublished work.

[7] H. Welker, Z. Naturforsch, 7a, 744 (1952); *ibid.*, 8a, 248 (1953).

[8] R. G. Breckenridge, W. R. Hosler, and W. Oshinsky, *Phys. Rev.* **91**, 243 (1953).

[9] M. Tannenbaum and J. P. Maita, *Phys. Rev.* **91**, 1009 (1953).

[10] F. Seitz, *Discussions Faraday Soc.* **No. 5**, 271 (1949); see also, J. C. Slater, *J. Appl. Phys.* **22**, 237 (1951). Recent studies [J. A. Brinkman, *On the Nature of Radiation Damage in Metals*, NAA-SR-198 (Dec. 22, 1952)] indicate that the atomistic (displaced atom) approach and the thermodynamic (thermal spike) approach are not necessarily mutually exclusive but should be applied to the initial and final portions of the range of the high energy ion, respectively.

[11] S. Siegel, *Phys. Rev.* **75**, 1823 (1949).

the excess free energy of the disordered region. In view of these considerations, radiation effects in this material might be expected to be more complex than in germanium or silicon.

A preliminary report of this work,[12] based on results obtained on polycrystalline InSb, indicates that the influence of impurities introduced by transmutations on carrier concentration is comparable to, if not greater than, that caused by lattice defects produced by fast neutrons. This behavior results from the extremely large capture cross section of indium for the neutron spectrum encountered in the reactor and from the decay product tin being a donor impurity when substituted for an indium atom in the InSb lattice. Although its cross section is considerably smaller, antimony also transmutes to the donor impurity tellurium. Therefore, in order to study separately the effects resulting from fast-neutron-induced lattice defects, it is necessary to minimize the introduction of chemical donors by shielding the specimen from those neutrons for which the indium cross section is large. After the effects produced by transmutations were accounted for, these early results indicated conclusively that certain of the bombardment-produced lattice defects act as electron traps in low-resistivity n-type InSb.

High-purity single-crystal specimens of both p- and n-type InSb were given successive exposures in the ORNL Graphite Reactor at a temperature of about 25°C. The samples were wrapped with cadmium and indium foil of sufficient thickness to greatly reduce the incident flux of thermal and resonance neutrons responsible for transmutations. Conductivity measurements during irradiation at the temperature of bombardment are of little value in following the progress of the irradiation, since the samples employed are already in the intrinsic range at 25°C. Consequently, Hall coefficient and resistivity measurements were made as a function of temperature in the range from 77 to 300°K after each exposure.

In order to investigate the effect of short exposures on p-type InSb and to examine the shielding efficiency of the cadmium and indium foil, a p-type sample with an initial hole concentration of $n_h^0 = 1.1 \times 10^{16}$ cm^{-3} at 77°K was given a relatively short exposure ($nvt_f \cong 2 \times 10^{16}$), followed by a vacuum anneal at 350°C for 40 hr. The fast flux as employed here is that flux of neutrons whose energy is greater than 0.1 Mev. The absolute value of this flux may be in error by as much as a factor of 2. Relatively, however, this scale of integrated flux is consistent with that used in refs. 1, 2, 3, and 12. Semilog plots of the Hall coefficient R and of the resistivity ρ vs reciprocal temperature of the specimen for each condition are shown in Figs. 58 and 59, respectively. The large decrease in hole concentration in the extrinsic range, which is almost removed by the heat treatment, indicates that fast-neutron-produced lattice defects serve as hole traps in p-type InSb. The slope and the curvature of the R and ρ curves after the exposure (curves II) seem to indicate the existence of one group of relatively shallow hole traps which are distributed in energy. The slope of the log ρ vs $1/T$ curve in

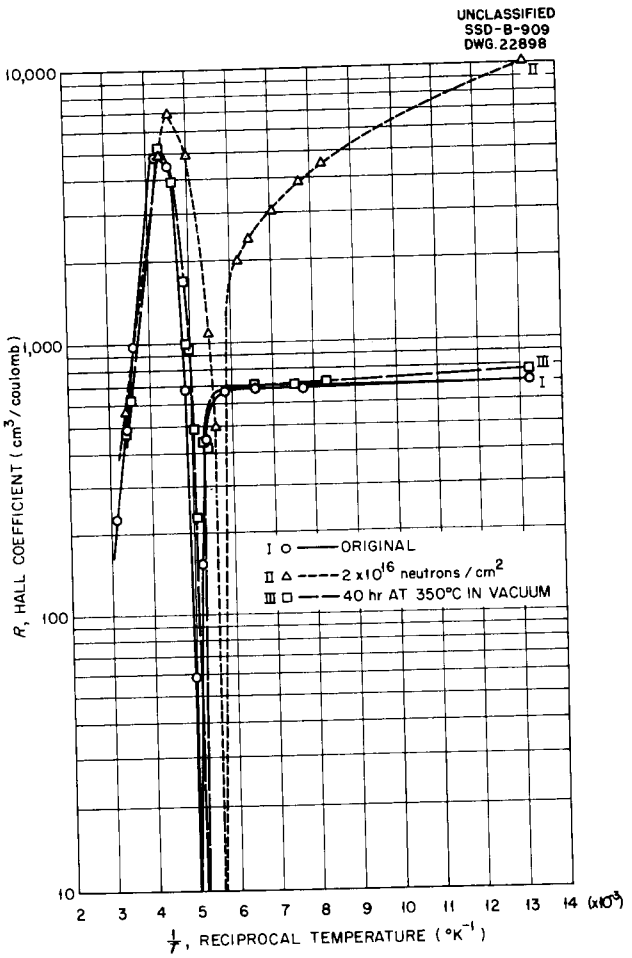

Fig. 58. Hall Coefficient vs Temperature of Irradiated p-Type InSb.

[12] J. W. Cleland and J. H. Crawford, Jr., *Phys. Rev.* 93, 894 (1954).

the initial portion of the extrinsic range, where the slope is relatively constant, corresponds to an energy of approximately 0.02 ev. If this value, or twice this value,[13] is a representative depth of the more numerous traps in this group, the bending down of the curve toward lower temperature indicates an appreciable concentration of more shallow hole traps.

Comparison of the value of R at 77°K before irradiation and after heat treatment subsequent to irradiation indicates that the final hole concentration was decreased by approximately 1×10^{15} cm^{-3}, presumably through the introduction of an equivalent number of donor impurities by transmutations. Actually, because of the shielding geometry of the sample holder employed, the shielding was not completely effective. Consequently, a leakage of thermal and resonance neutrons amounting to about 6% of the integrated fast flux, an amount which would account for the observed decrease of n_h, is not unreasonable.

The conductivity of both n- and p-type samples measured at 77°K after successive irradiations is plotted as a function of nvt_f in Fig. 60. The n-type sample decreases in conductivity monotonically toward a saturation value, whereas the conductivity of the p-type sample first decreases rapidly, passes through a minimum value, and then increases toward the same saturation value approached by the n-type sample. This behavior suggests that p-type InSb is converted to n-type by the action of bombardment-produced defects alone. Hall coefficient measurements taken concurrently with the above conductivity data confirm this view and further indicate that both the sample that was originally p-type and the n-type sample tend to approach the same saturation value of electron concentration n_e^*, which is about

[13] Whether the value yielded by the slope, or twice that value, corresponds to the ionization energy of a discrete level depends on the statistical situation; see N. F. Mott and R. W. Gurney, *Electronic Processes in Ionic Crystals*, p 157–160, Oxford University Press, London, 1948.

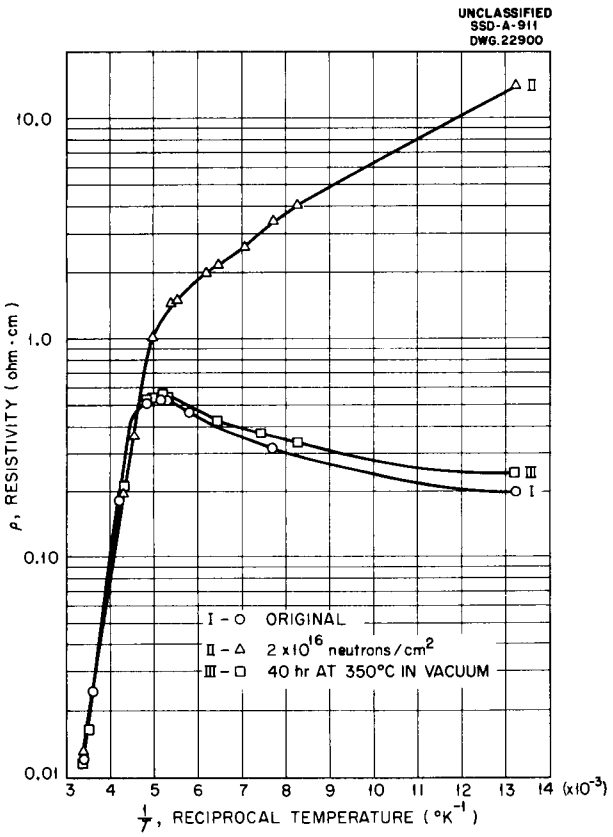

Fig. 59. Resistivity vs Temperature of Irradiated p-Type InSb.

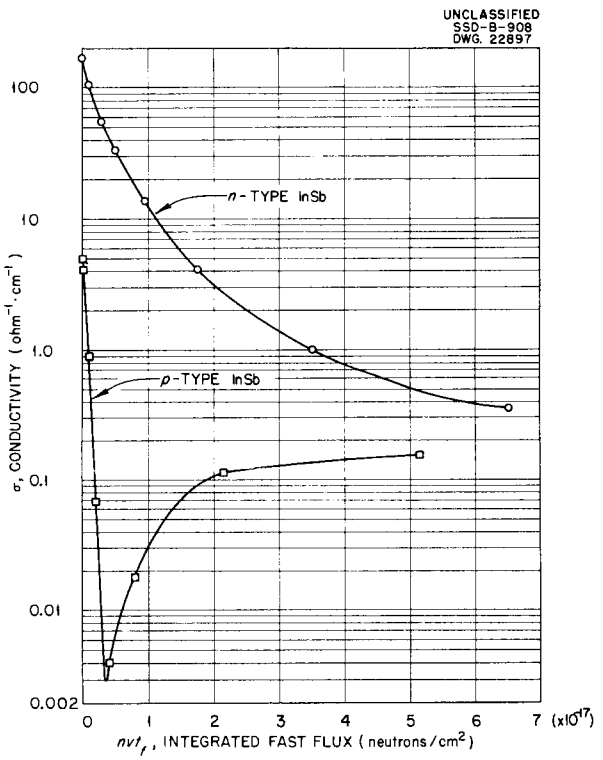

Fig. 60. Conductivity at −196°C vs Integrated Fast Flux for InSb.

7×10^{14} cm^{-3} at 77°K. Representative log R vs $1/T$ curves for these two specimens are shown in Fig. 61. The curves of the sample that was originally p-type are labeled P and those of the n-type sample are labeled N. The original values are represented by P_0 and N_0. Curve P_1, taken after a moderate exposure, is for the p-type sample shortly after its conversion to n-type; P_2 and N_2 indicate the approach to a common saturation after a relatively long exposure, and P_3 and N_3 were obtained after a vacuum anneal at 350°C for 40 hr.

The log R vs $1/T$ curve for a sample in the condition of complete saturation would presumably lie somewhere between P_2 and N_2 of Fig. 61. If this saturation condition is due only to defects and is unaffected by the introduction of donors by transmutations and room-temperature annealing of defects (see below), an n-type sample with $n_e^0 < n_e^*$ at a given temperature would be expected to show an increase in n_e on bombardment. Therefore, should the Hall coefficient curve of such a specimen intersect that representing the saturation condition in the extrinsic range, it would be expected to rotate around the point of intersection toward a coincidence with the saturation curve as a result of irradiation. These considerations would then indicate that the rate of decrease or the rate of increase of n_e in n-type material would depend strongly on n_e^0 and the particular temperature employed for measurement. In p-type InSb, however, the rate of removal of holes is not expected to be as markedly dependent on n_h^0, although it might be somewhat temperature sensitive. For the specimens considered above ($n_h^0 = 1.1 \times 10^{16}$ cm^{-3} and $n_e^0 = 1.6 \times 10^{16}$ cm^{-3}), the initial rate of hole removal is about four times as great as that for electrons at 77°K.

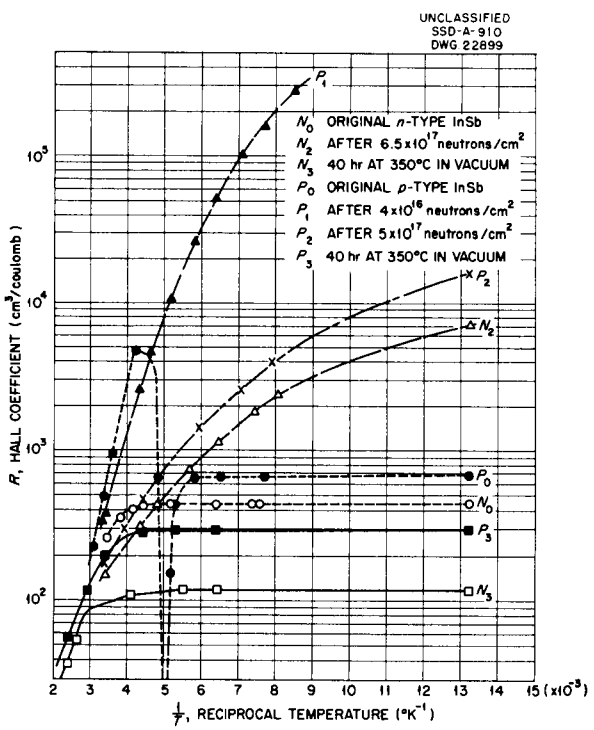

Fig. 61. Hall Coefficient vs Temperature of Irradiated InSb.

It is evident from curves P_3 and N_3 of Fig. 61 that an appreciable increase in donor concentration remains in both samples after the defects have been annealed. For the p-type sample, this increase is sufficiently great to produce as an end result an n-type sample with $n_e = 2.4 \times 10^{16}$ cm^{-3}. This corresponds to a total increase in donor concentration of 3.5×10^{16} cm^{-3}, which amounts to approximately 7% of the total integrated fast flux, $nvt_f = 5 \times 10^{17}$ neutrons/cm^2, and is in reasonable agreement with the magnitude of shield leakage estimated above. Similar considerations for the n-type sample indicate that the donor concentration increase of 4.5×10^{16} cm^{-3} is again about 7% of the 6.5×10^{17} nvt_f received.

The introduction of donors by transmutations in no way invalidates the statement that p-type InSb is converted to n-type by the action of fast-neutron-produced lattice defects alone. Since the half lives of the more important activities of indium are short compared with the time interval between irradiation and subsequent measurement, the donor concentration caused by leakage would be a linear function of the integrated flux. Examination of Fig. 60 reveals that conversion is indicated at an nvt_f less than 4×10^{16} neutrons/cm^2, a fact also borne out by curve P_1 of Fig. 61. Since this exposure corresponds to the introduction of only about 2.8×10^{15} chemical donors (less than one-third of the original acceptor concentration), conversion must result from defect hole traps which lie above the middle of the forbidden band and consequently may act as donors in n-type InSb. It is possible, however, that the introduction of chemical donors may affect to some extent the actual position of the saturation condition mentioned above. This point will be considered in more detail.

Both electron and hole mobilities in single crystals are decreased as a result of irradiation. This is in

agreement with previous observations on polycrystalline material.[14] The electron mobility at 77°K for the n-type sample of Fig. 61 before irradiation is 6.6×10^4 $cm^2 \cdot v^{-1} \cdot sec^{-1}$. It is decreased to 2.2×10^3 $cm^2 \cdot v^{-1} \cdot sec^{-1}$ after an exposure of $nvt_f = 6.5 \times 10^{17}$ neutrons/cm^2. That the major portion of this decrease is produced by additional scattering from bombardment-induced lattice defects is indicated by the effect of vacuum-annealing, which restores the mobility to 1.5×10^4 $cm^2 \cdot v^{-1} \cdot sec^{-1}$. The residual additional scattering after the anneal may be due to both an increase in impurity scattering associated with the additional chemical donors and to scattering from any defects not removed by heat treatment. Since the mobility that would result from lattice scattering alone at 77°K, which can be estimated by extrapolating the results of Tannenbaum and Maita,[15] appears to be approximately 10^6 $cm^2 \cdot v^{-1} \cdot sec^{-1}$, the observed mobilities quoted above are due almost entirely to impurity scattering. According to the Conwell-Weisskopf theory of impurity scattering,[16] the mobility, when limited by impurity scattering alone, is approximately inversely proportional to the concentration of ionized impurities. For the sample in question, the chemical-donor concentration after irradiation is 3.8 times the original value, whereas the mobility has been decreased by a factor of 4.4. It may therefore be concluded that the increase in scattering that remains after vacuum anneal is due principally to the increase in donor concentration as a result of transmutations.

Before considering the nature of the defects which are the principal cause of the behavior described, it is desirable to examine the saturation condition approached by both types of specimens. If the defect levels alone were responsible for this saturation, the limiting value would be of aid in determining the positions of such levels. Since chemical donors are introduced simultaneously with defects, each measurement after a certain period of irradiation denotes the consequences that result from defect introduction into a material whose chemical impurity concentration is no longer the original one. Therefore, if the transmutations are completely effective as donors before heat treatment, curve P_2 of Fig. 61 should be referred to P_3 rather than to P_0 and N_2 to N_3 instead of to N_0. If the decay product is displaced from its position to an interstitial position by some agency, its action will be essentially the same as that of a displaced atom. This point was mentioned in ref. 1, where the possibility of displacement as a result of recoil from the radiation emitted during decay was considered. It has been pointed out to the authors by H. P. Yockey that recoil from the gamma ray emitted on neutron capture is great enough to displace the activated atom before decay, a process quite similar to the Szilard-Chalmers reaction. If the rate of chemical-donor introduction ever attained predominance, n_e of the n-type sample would show an increase and, in the initially p-type sample, would exceed n_e^* after prolonged exposure. Examination of Fig. 60 shows that this is not the case, since the conductivity of the n-type sample decreases monotonically with exposure. However, the rate of approach to saturation might be expected to be increased for the p-type sample and to be decreased for the n-type sample, with the result that the data would indicate a higher value of the limiting conductivity and final carrier concentration than that caused by the defect concentration alone. Consequently, the saturation condition produced by defects is expected to lie nearer P_2 than to N_2. This expectation is supported by the conductivity curve of the p-type sample in Fig. 60, which shows little change after an exposure of $nvt_f = 2 \times 10^{17}$ neutrons/cm^2. Thus it is expected that 4.5×10^{14} $cm^{-3} < n_e^* < 7 \times 10^{14}$ cm^{-3} at 77°K.

In any attempt to explain the observed electrical behavior in terms of specific properties of various defects, the following groups of localized states, whose existence is inferred from experiment, must be accounted for: (1) a shallow group of electron traps below the conduction band which cause a decrease in n_e in n-type material with $n_e^0 > n_e^*$, (2) a wide distribution above the valence band of shallow hole traps whose presence is indicated in Fig. 58, and (3) a second group of hole traps which, in order for conversion to be explained, must lie above the middle of the forbidden band and which may therefore act as donors in n-type material. The last group of states may be a continuation of the distribution mentioned in (2). It will be assumed that the major result of fast-neutron collisions with lattice atoms is the generation of Frenkel defects

[14] J. W. Cleland and J. H. Crawford, Jr., *Phys. Rev.* 93, 894 (1954).

[15] M. Tannenbaum and J. P. Maita, *Phys. Rev.* 91, 1009 (1953).

[16] E. Conwell and V. F. Weisskopf, *Phys. Rev.* 77, 388 (1950).

and that as many indium atoms as antimony atoms are displaced.

Four possible single defects can be expected for a binary compound, since there are two possible interstitial atoms and two possible vacant lattice sites. Since either one of the two types of interstitials, indium and antimony, may release electrons on ionization, they are expected to give rise to donor levels or hole traps. James and Lark-Horovitz[17] have considered in detail the ionization of interstitial atoms in diamond-lattice semiconductors, and they find that, if the dielectric constant is large, the first ionization potential may be calculated to a good approximation from a hydrogenic model. To this approximation, the first ionization potentials of both interstitial indium and antimony atoms are expected to be identical. The dielectric constant of InSb is unknown, but if it is of the same magnitude as that of germanium, the primary ionization energy is expected to be about 0.05 ev. In this treatment the ionization energy is inversely proportional to the effective mass and the square of the dielectric constant. From indications given in ref. 10, it appears that m_e^*/m is considerably less than unity. Hence, for a dielectric constant the same as that for germanium, the ionization energy is decreased below this value. Since the remaining electrons on a singly ionized interstitial atom are more strongly bound, with the result that the dielectric constant of the lattice is not expected to have so large a shielding effect as in the case of a neutral atom, the second ionization energy for both indium and antimony might be expected to be greater than the small forbidden energy gap[15] in InSb. It therefore appears likely that only one donor level or hole trap is introduced for each interstitial atom.

The situation is not so clear in the case of the two types of vacant lattice sites. James and Lark-Horovitz[17] have also examined the localized states associated with vacancies in germanium and silicon, but complications arising from the complex nature of the wave functions in the diamond lattice and from the large perturbations introduced by vacant lattice sites prevent a quantitative estimation of the positions of these energy levels. Consequently, they found it necessary to use experimental indications in order to place these levels in their model of the band scheme. Therefore, only differences that might be expected in InSb between vacant indium and antimony sites are indicated. An indium vacancy has associated with it five extra electrons from the neighboring antimony atoms. From an atomistic point of view, if the perturbation is not so great as to destroy the tendency for covalent bond formation, there exist three half-filled orbitals and one complete orbital in the region of the vacancy. An antimony vacancy, on the other hand, contains three extra electrons from the neighboring indium atoms. Hence, there exist three half-filled orbitals and one that is completely empty. It therefore seems reasonable to assume that the energy required to place an additional electron into a vacancy (to ionize a vacancy) might be quite different in the two cases. Use of the band theoretical approach of ref. 17 also indicates marked differences, since the perturbing effect of the missing ion core, which causes localized states to split out of the valence band, is due to an absence of three charges in the case of indium and an absence of five in the case of antimony. Because of the complexity of the electronic structure and the large perturbations mentioned above, it is difficult to estimate with any certainty how the differences between these vacancies affect their energies of ionization.

For want of a better approach, a vacancy will be considered as being analogous to a free atom with the same numbers of valence electrons as there are extra electrons in the region of the vacancy. The addition of an electron to an antimony vacancy would, therefore, result in four half-filled orbitals, in contrast to two half-filled and two completely filled orbitals for an indium vacancy plus an electron. Since half-filled subshells in atoms or ions are known to be more stable than other partially filled subshells, this analogy suggests that the stabilization of the antimony vacancy that results from the addition of an electron would tend to reduce the energy required to introduce the excess electron below that required for the indium vacancy, for which a stabilization is not expected. In this view, therefore, an antimony vacancy would correspond to an acceptor with a smaller ionization energy than that of the acceptor created by the indium vacancy. Since the energy required to introduce a second electron would be expected, because of coulombic repulsion, to be considerably greater in either case, it might reasonably be expected to correspond to an acceptor state in the conduction band for the small value of E_g in InSb. Hence, higher levels will not be considered.

[17] H. M. James and K. Lark-Horovitz, *Z. physik. Chem.* 198, 107 (1951).

The above remarks are concerned only with the localized states arising from separate defects. Since equal quantities of each type of defect are expected to be produced by irradiation, the resultant nature of each defect state is determined by the redistribution of the electrons arising from the interstitial atoms to positions of lowest energy. The situation resulting from the tentative model postulated above is shown schematically in Fig. 62. It is expected that the shallow donors associated with the interstitial atoms will lose their electrons to the lower-lying acceptors created by lattice vacancies and may therefore behave as electron traps. The states corresponding to the vacancies have been labeled according to the atomistic picture described, and those states corresponding to the indium vacancies have been arbitrarily placed above the center of the forbidden band in order to account for the experimental observation that donors are introduced. Since these states are now occupied, the antimony vacancy acts as a hole trap, whereas the indium vacancy plays the dual role of being a hole trap in *p*-type material and a donor in *n*-type material. It should be noted that there are twice as many electron traps as there are states in the two lower levels. Because of the inhomogeneous distribution of defects resulting from bombardment and because of perturbations arising from interactions between defects, the associated energy levels are expected to be broadened. This broadening is indicated roughly in Fig. 62 by the width of the levels.

It should be emphasized that a number of assumptions are involved in this model; the principal ones are as follows: (1) the hydrogenic model is applicable to interstitial atoms, and the atomistic analogy accounts for differences in ionization energy of the states created by lattice vacancies; (2) there is no difference in annealing rate at room temperature for the various defects under consideration; (3) essentially all the bombardment-produced defects can be treated in terms of Frenkel defects. The implications of the first assumption have been indicated. As to the second assumption, it is impossible, because of the method of measurement, to estimate at this time either the extent of annealing or the amount of differential annealing that takes place during irradiation and prior to the time of measurement; further experimental studies would have to be made before such an estimate could be given. It is known in the case of germanium that an extensive rearrangement of disorder of some sort occurs at as low as 110°K but that such activity is essentially complete at 220°K, with little further rearrangement taking place in the room-temperature range.[18,19] If appreciable differential annealing does take place in InSb at room temperature, extensive modification of the proposed model would be required. The third assumption does not include effects associated with the formation of defect clusters and thermal spikes. In this connection, it should be pointed out that, although the ordered arrangement of indium and antimony atoms may be disordered as a result of thermal spikes, there are no experimental observations which, according to past experience with germanium and silicon, explicitly require the postulation of effects associated with thermal spikes for their explanation. It appears that more extensive studies of electrical properties and studies of structure, as well, are necessary to determine whether such disordered regions are actually introduced into this material by fast-neutron bombardment.

There is little doubt but that alternative models of defect energy levels might be constructed which would also account satisfactorily for the experimental observations considered here.

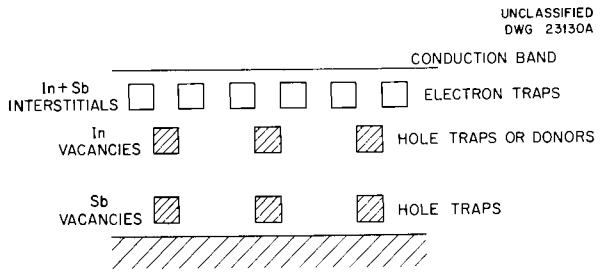

Fig. 62. Band Scheme of Irradiated InSb.

ENERGY LEVELS IN *n*-TYPE GERMANIUM IRRADIATED AT ROOM TEMPERATURE

J. W. Cleland J. H. Crawford, Jr.

A theoretical examination of the electronic nature of interstitial atoms and lattice vacancies by James and Lark-Horovitz[20] indicates that in germanium

[18] J. H. Crawford, Jr., J. W. Cleland, D. K. Holmes, and J. C. Pigg, *Phys. Rev.* **91**, 243 (1953).

[19] J. H. Forster, H. Y. Fan, and K. Lark-Horovitz, *Phys. Rev.* **91**, 229 (1953).

[20] H. M. James and K. Lark-Horovitz, *Z. physik. Chem.* **198**, 107 (1951).

these defects may be multiply ionized. The results of their analysis suggest that each Frenkel defect introduces four localized states into the forbidden energy band: a shallow vacant state which lies approximately 0.05 ev below the bottom of the conduction band and is capable of trapping electrons, a deep-lying vacant state which is located near the top of the filled band and which may behave as an acceptor, and two occupied states which act as shallow hole traps near the top of the filled band. It is possible to gain considerable information about the shallow electron trap from an examination of the curvature of the σ vs nvt_f curves. In addition, recent measurements of the Hall coefficient as a function of temperature on bombarded n-type germanium permit a more detailed analysis of the energy-level structure associated with bombardment-produced lattice defects.

According to the model of James and Lark-Horovitz, it is possible to describe the electron concentration in n-type germanium in terms of a simple two-level scheme. The deep trap or acceptor is completely effective in trapping electrons, while the trapping efficiency of the shallow vacant state is dependent on both the temperature and the free-electron concentration. If it is assumed that the hole concentration arising from the intrinsic process is negligible and that all chemical impurities are completely ionized, the electron concentration n_e is given by

$$n_e = n_e^0 - N_s^- - N \ , \tag{1}$$

where n_e^0 is the initial electron concentration produced from ionized chemical impurities, N_s^- is the concentration of occupied shallow traps, and N is the concentration of both deep and shallow traps. By use of the law of mass action it can be shown that

$$N_s^- = \frac{n_e N K_s}{1 - n_e K_s} \ , \tag{2}$$

where K_s is the equilibrium constant for the trapping process and is given by

$$K_s = \frac{h^3 e^{\epsilon_s/kT}}{\gamma(2\pi m_e kT)^{3/2}} \ , \tag{3}$$

where γ is the ratio of statistical weights caused by spin for the final and initial states of the level,[21] m_e is the electron effective mass, and ϵ_s is the depth of the shallow trap. Substitution of Eq. 2 in Eq. 1 yields

$$n_e = \frac{(n_e^0 - 2N)K_s - 1 + \sqrt{[(n_e^0 - 2N)K_s - 1]^2 + 4K_s(n_e^0 - N)}}{2K_s} \ . \tag{4}$$

The initial rate of change of n_e with defect introduction is then

$$\left(\frac{dn_e}{dN}\right)_{N=0} = -\left(\frac{1 + 2K_s n_e^0}{1 + K_s n_e^0}\right) \tag{5}$$

and is a function of K_s and n_e^0 only. This rate is directly proportional to the initial change of electron concentration for each incident fast neutron. If it is assumed that the defect concentration at the minimum of the σ vs nvt_f curve is equal to the initial electron concentration, $(dn_e/dN)_{N=0}$ is directly available from experiment and K_s may be determined from Eq. 5; ϵ_s is then directly obtainable if γ and m_e are known. According to the theory,[20] the shallow trap can be identified with a singly ionized interstitial atom; hence $\gamma = 1$. For m_e the values of cyclotron resonance measurements made by Lax and co-workers[22] have been used; these values include the effect of spatial degeneracy of energy surfaces in k space[23] $[m_e = (\omega_s^2 m_x m_y m_z)^{1/3} = 0.51\ m_0$, where $\omega_s = 4]$. Hence

$$\epsilon_s = 8.63 \times 10^{-5} T(34.42 + \ln K_s T^{3/2}) \ . \tag{6}$$

The results of the analysis of initial slopes of σ vs nvt_f curves for a number of n-type samples exposed under a variety of conditions are listed in Table 9. It is evident from the values of ϵ_s that reasonably consistent results are obtained by use of this model. Samples 9 and 10, which do not yield data in agreement, exhibit a very broad minimum in the σ vs nvt_f curve and apparently have an inhomogeneous impurity distribution. The data for sample 11 were obtained at −78°C, and reasonable agreement is indicated even at this temperature.

Equation 4 has also been used to calculate a bombardment curve. The calculated points are

[21] J. H. Crawford, Jr. and D. K. Holmes, *Proc. Phys. Soc. (London)* **67**, 294 (1953).

[22] B. Lax *et al.*, *Phys. Rev.* **93**, 1418 (1954).

[23] This relationship was pointed out by H. Schweinler.

TABLE 9. VALUES OF K_s AND ϵ_s OBTAINED FROM INITIAL RATES OF CHANGE OF n_e DURING BOMBARDMENT, CALCULATED FROM THE SIMPLE TWO-ACCEPTOR-LEVEL MODEL

Sample	$\left(\frac{dn_e}{dN}\right)_{N=0}$	n_e^0 (cm^{-3})	Temperature (°K)	K_s ($cm^3 \times 10^{-16}$)	ϵ_s (ev)
1	1.42	8.9×10^{14}	304	6.95	0.213
2	1.63	2.03×10^{15}	300	8.40	0.205
3	1.67	7.4×10^{15}	313	2.74	0.194
4	1.85	1.12×10^{16}	313	5.05	0.211
5	1.74	1.18×10^{16}	309	2.41	0.187
6	1.76	1.21×10^{16}	313	2.54	0.193
7	1.75	1.24×10^{16}	313	2.42	0.191
8	1.86	2.02×10^{16}	309	3.04	0.194
9	2.07	1.58×10^{16}	313		
10	2.50	2.43×10^{17}	300		
11	1.87	2.92×10^{14}	195	229.0	0.184
					Av 0.197

compared with the experimental curve in Fig. 63. For purposes of analysis the concentration of electrons during the bombardment is expressed relative to the initial concentration (n_e/n_e^0), and the exposure is given in terms of N/n_e^0 on the assumption that $N = n_e^0$ at the point of conversion to p-type (the conductivity minimum). Since the electron concentration was inferred from the conductivity measured during irradiation and from the initial value of mobility, it was inherently assumed that the mobility is unaffected by bombardment. As will be shown later, this is not necessarily a good assumption because, even at room temperature, a considerable decrease in mobility may be expected for an exposure of this magnitude ($nvt_f = 5 \times 10^{16}$). However, for the initial half of the curve and the end, this assumption is expected to yield reasonably good values for n_e. A rather good fit to the curve was obtained by letting $K_s = 3.6 \times 10^{-16}$ cm^3, which corresponds to $\epsilon_s = 0.199$ ev. This value is in good agreement with the values listed in Table 9.

It is possible to test the model more stringently by using Eq. 4 to calculate the temperature dependence of electron concentration in a bombarded n-type sample. For $n_e > 2N$, Eq. 4 predicts a transition with increasing temperature from a condition in which all the shallow traps are occupied to a condition in which they are completely empty. Since in the derivation of Eq. 4 the intrinsic process is neglected and it is assumed that all chemical donors are completely ionized, the electron concentration is temperature independent both above and below this transition region. When all shallow traps are filled, $n_e = n_e^0 - 2N$, a condition which readily permits fixing the value of N from experimental data.

Curves of log n_e vs $1/T$ for an n-type sample after various periods of irradiation and treatment are shown in Fig. 64. The values of n_e were obtained from Hall coefficient measurements and corrected for impurity scattering by the method of Johnson and Lark-Horovitz[24] as modified by Fan.[25] Curve I is that of the sample before bombardment, curves II, III, and IV were taken after exposures of 2.9×10^{15}, 5.8×10^{15}, and 7.8×10^{15} fast neutrons/cm^2, respectively. Curve V was taken while the specimen was cooling from the short-time (~10 min) heat of

[24] V. A. Johnson and K. Lark-Horovitz, *Phys. Rev.* 82, 977 (1951).

[25] Discussed in a thesis by J. H. Forster, Purdue University, 1953 (unpublished).

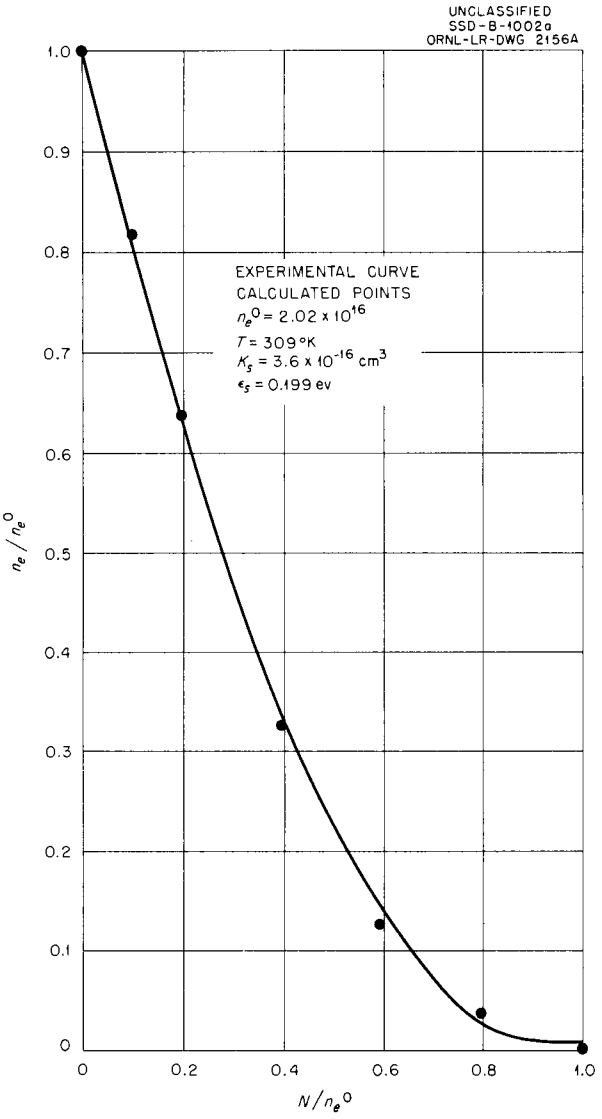

Fig. 63. n-Type Germanium n_e/n_e^0 vs N/n_e^0.

152°C it had been given subsequent to the final exposure. In Fig. 65 the curves calculated from Eq. 4 with $\epsilon_s = 0.20$ ev are compared with the experimental points of curves IV and V of Fig. 64. Curve IV yields excellent agreement with the model when $n_e^0 = 2.80 \times 10^{16}$ cm^{-3} and $N = 1.27 \times 10^{16}$ cm^{-3} are used. In the case of curve V, however, with $N = 1.23 \times 10^{16}$ cm^{-3}, agreement is not good because the model predicts a much more rapid initial rise of n_e with temperature in the transition range. It appears that the heating has not only

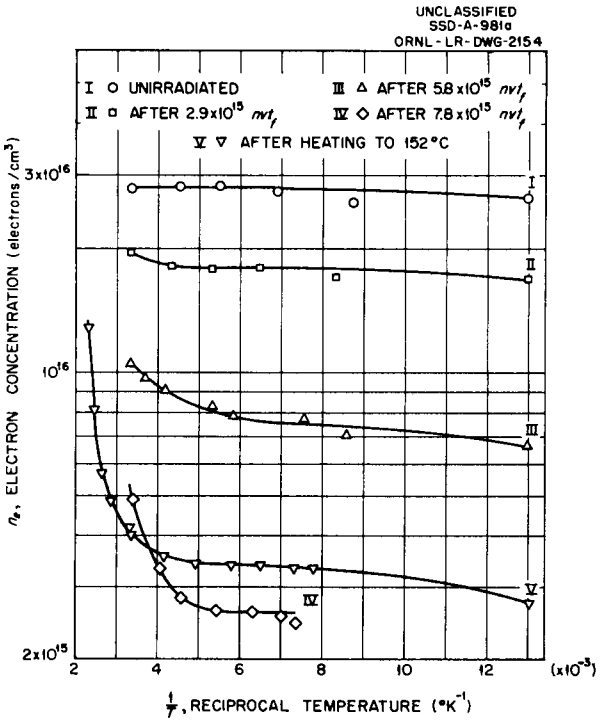

Fig. 64. Temperature Dependence of Electron Concentration in Bombarded Germanium.

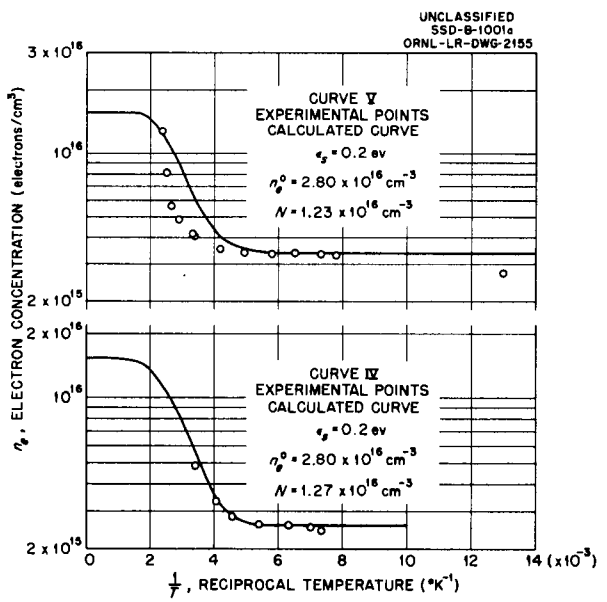

Fig. 65. Comparison of Experiment with the Two-Level Model.

caused some annealing, which increased the low-temperature value of n_e from 2.6×10^{15} to 3.4×10^{15} cm^{-3}, but has also increased the shallow-trap depth. A value of ϵ_s of about 0.3 ev is necessary to fit the data of curve V.

In summary, it appears that the two-vacant-state model suggested by James and Lark-Horovitz[26] is justified experimentally, even though ϵ_s is greater by about a factor of 4 than the theoretically predicted value (~0.05 ev). Tests of the model by three different approaches all gave consistent results, and the shallow state appears to lie approximately 0.2 ev below the bottom of the conduction band. The Purdue group found similar indications when they used deuteron-bombarded n-type germanium.[27] Low-temperature annealing of irradiated germanium appears to increase the shallow-trap depth; the reason for this behavior is not known at the present time.

MOBILITY IN BOMBARDED n-TYPE GERMANIUM

J. W. Cleland J. H. Crawford, Jr.

Studies of the effect on mobility by fast-neutron bombardment near room temperature have been made on several n-type germanium specimens. The Hall mobility μ_H has been obtained from the Hall constant R and measurements of the resistivity ρ as a function of temperature; $\mu_H \equiv R/\rho$ and is related to the true drift mobility μ by $\mu_H/\mu = r$, where r is the Hall parameter ($r = n_e eR$). In Fig. 66 μ_H is plotted as a function of temperature after each exposure for one specimen which received a moderate total exposure ($nvt_f = 7.9 \times 10^{15}$ neutrons/cm^2). Curve I was obtained before bombardment; curves II, III, IV, and V were taken after cumulative exposures of 2.9×10^{15}, 5.8×10^{15}, 7.2×10^{15}, and 7.9×10^{15} fast neutrons/cm^2, respectively; curve VI was obtained after the specimen was heated to 152°C for about 10 min subsequent to the total exposure. It is evident that the mobility is decreased by bombardment over the entire temperature range. After a total exposure of 7.9×10^{15} fast neutrons/cm^2, a decrease in μ_H by a factor of 2 occurs at room temperature, and, at 77°K, μ_H is decreased by more than an order of magnitude.

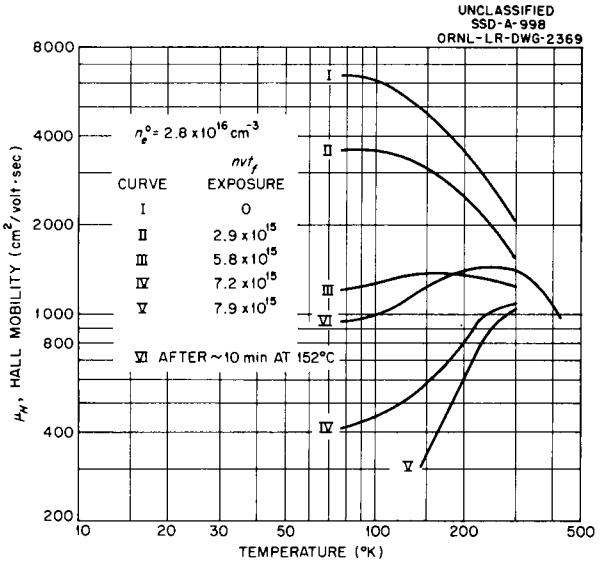

Fig. 66. Hall Mobility vs Temperature for Bombarded n-Type Germanium.

The negative temperature coefficient, evident in curve I, which is characteristic of charge-carrier scattering by thermal vibrations of the lattice ($\mu_L \alpha T^{-3/2}$), is rapidly removed by exposure; curve V possesses an approximately T^2 dependence. This behavior indicates that irradiation introduces additional scattering centers which scatter carriers more effectively at low temperature. It is interesting to note that the short anneal subsequent to exposure markedly improved the mobility over the entire range and restored to an appreciable extent the lattice-scattering temperature dependence. This behavior, coupled with indications in the preceding section that the same heat treatment increased the depth of the shallow electron traps, seems to indicate that low-temperature annealing produces more extensive healing of lattice damage than was previously suspected.

Figure 67 is a plot of μ_H vs T for a specimen that was given much heavier exposure (up to 2×10^{17} fast neutrons/cm^2) and that had a large, initial carrier concentration ($n_e \sim 7 \times 10^{17}$ cm^{-3}). Curve I refers to the original specimen, and curves II, III, IV, V, and VI were obtained after exposures of 7.2×10^{16}, 1.27×10^{17}, 1.61×10^{17}, 1.84×10^{17}, and 2.01×10^{17} fast neutrons/cm^2. In many respects these curves exhibit the same qualitative behavior as those of Fig. 66. It should be pointed out, however, that for this specimen a considerably greater

[26] H. M. James and K. Lark-Horovitz, *Z. physik. Chem.* **198**, 107 (1951).

[27] K. Lark-Horovitz, "Nucleon Bombardment of Semiconductors," paper presented at the Michigan meeting of the American Physical Society, 1954.

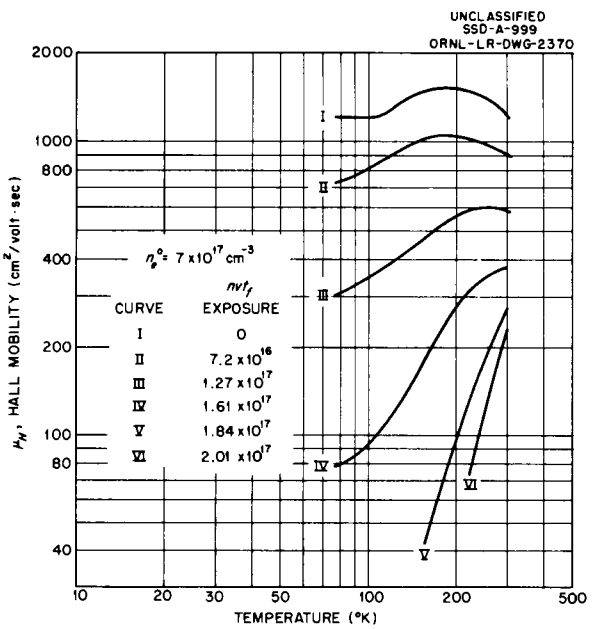

Fig. 67. Hall Mobility vs Temperature for n-Type Germanium Irradiated up to 2.01×10^{17} nvt.

exposure is necessary to remove lattice-scattering behavior in the high-temperature range. In fact, the specimen represented by curve II (which still shows a definite maximum) has received an exposure about ten times as long as that given to the specimen represented by curve V of Fig. 66; the latter shows almost no trace of the lattice-scattering process. This behavior seems to indicate that the charge-carrier concentration is an important variable in the scattering process introduced by irradiation. Another important feature not apparent from Fig. 66 is that the temperature dependence of μ_H is enhanced by exposure. Whereas in curve V of Fig. 66 μ_H is apparently dependent on T^2 in the low-temperature region, curves V and VI of Fig. 67 yield approximate $T^{3.2}$ and $T^{6.3}$ dependences, respectively. Hence, a much more complex functional dependence of μ_H on T, rather than a simple power-law dependence, is indicated.

The mobility data on bombarded germanium are not sufficiently extensive at the present time to warrant a detailed analysis in order to determine the nature of the scattering mechanisms associated with lattice damage. On the basis of the temperature dependence of the mobility of heavily irradiated material, however, it appears reasonable to assume that the increased scattering cannot be due solely to charged center scattering, a process which, according to the Brooks-Herring theory,[28] yields a mobility approximately proportional to $T^{3/2}$.

RADIATION EFFECTS ON LEAD-WIRE INSULATION

J. C. Pigg C. C. Robinson[29]

The investigation of the effect of reactor irradiation on wire insulation has been resumed. Previous data[30] have shown that the effect of such irradiation is to decrease the insulation resistance by several orders of magnitude. Some insulations fail entirely under prolonged exposure. The technique used in the previous experiments has been improved, and several types of insulation have been studied.

The insulation resistance was measured between the conducting wire and a braid shield, both made of the same material. Measurements were made with a General Radio Company, type 729-A megohmmeter, which has a usable range from 10^3 to 5×10^{10} ohms.

The wires were run into the ORNL Graphite Reactor as if they were leads to a sample. Each wire terminates inside the reactor on a bakelite board and is tied by means of a glass tape. The bakelite board is mounted inside an aluminum torpedo. Each shield terminates outside the torpedo and is mechanically and electrically connected to the torpedo. Outside the reactor, the wire is terminated inside a Plexiglas box to protect the terminals from contamination by dust. The conductor and shield are connected to female Burnbach plugs which are also mounted inside the Plexiglas box.

The behavior of the insulations tested so far can be seen in Figs. 68 through 74.

Readings taken with the wire biased positive are designated "forward," and those taken with the shield biased positive are designated "reverse."

The changes in the insulation resistance produced by reactor radiation are several orders of magnitude larger than those reported to be pro-

[28] H. Brooks, *Phys. Rev.* **83**, 879 (1951); discussed in detail by P. P. Debye and E. M. Conwell, *Phys. Rev.* **93**, 693 (1954).

[29] On loan from USAF.

[30] J. C. Pigg, *Phys. Quar. Prog. Rep. Sept. 20, 1950*, ORNL-865, p 106.

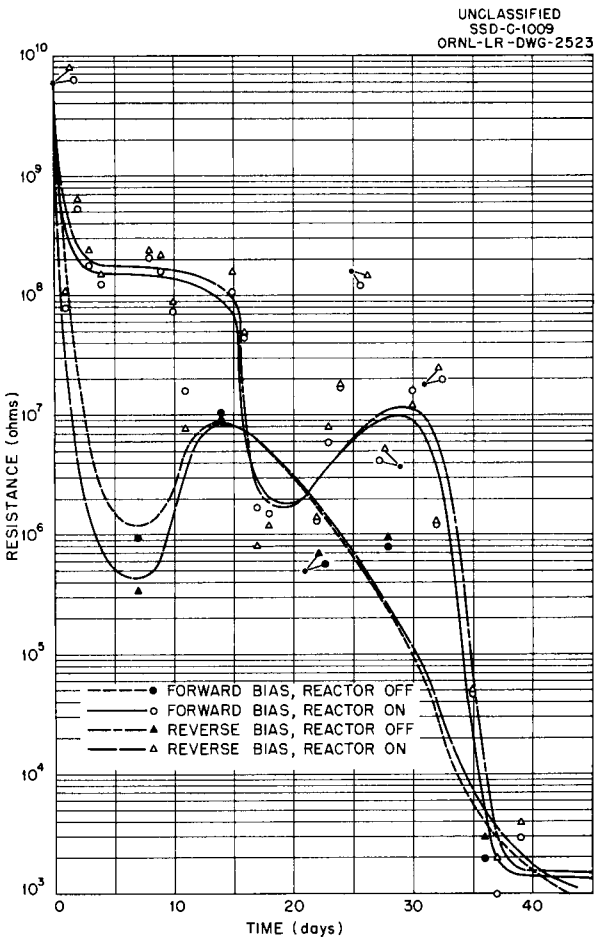

Fig. 68. Resistance vs Irradiation Time in Hole C for Copper-Shielded Copper Wire with Undoped Glass Insulation.

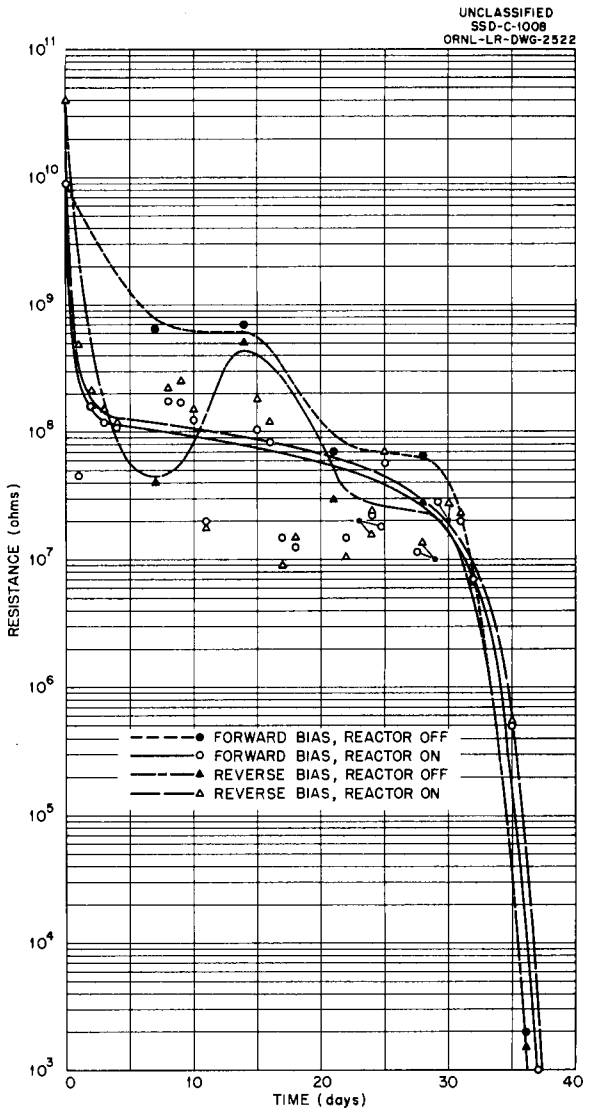

Fig. 69. Resistance vs Irradiation Time in Hole C for Copper-Shielded Copper Wire with Double Glass Insulation.

duced by gamma and beta radiation.[31,32] The actual change is greater than the measured value because only about half the wire is in the radiation field. The observed points show considerable scatter. This scatter is believed to be caused by leakage at the terminal which changes with the relative humidity.

The wires shown in Figs. 73 and 74 were exposed in hole 50-N. The flux level in hole 50-N is about a factor of 100 lower than that in hole C.

In addition to the change in resistance, voltages are developed between the conductor and the shield. The voltage is not apparent when the wire is first placed in the reactor, although a strong gamma field is present. After an initial exposure of a day or more, the voltages may be observed. When a 10^8-ohm resistor is connected between the shield and the conductor, the equilibrium voltage measured across the resistor varies from about 0.01 v when the reactor is off to as much as 0.5 v when the reactor is operating at full power.

[31] A. J. Warner, F. A. Muller, and H. G. Nordlin, *J. Appl. Phys.* **25**, 131 (1954).

[32] C. Mannal, *Nucleonics* **12**, No. 6, 49 (1954).

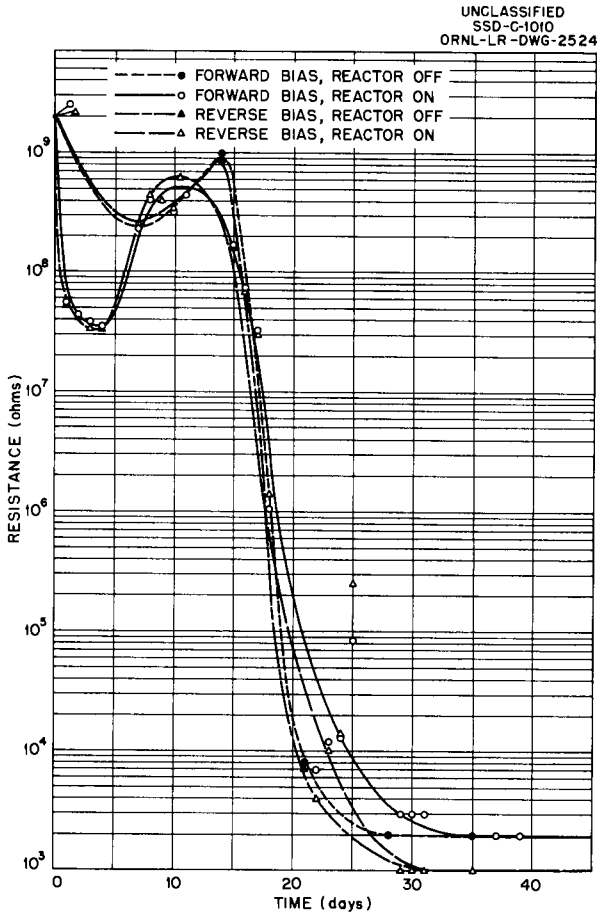

Fig. 70. Resistance vs Irradiation Time in Hole C for Copper-Shielded Wire with Rubber and Nylon Insulation.

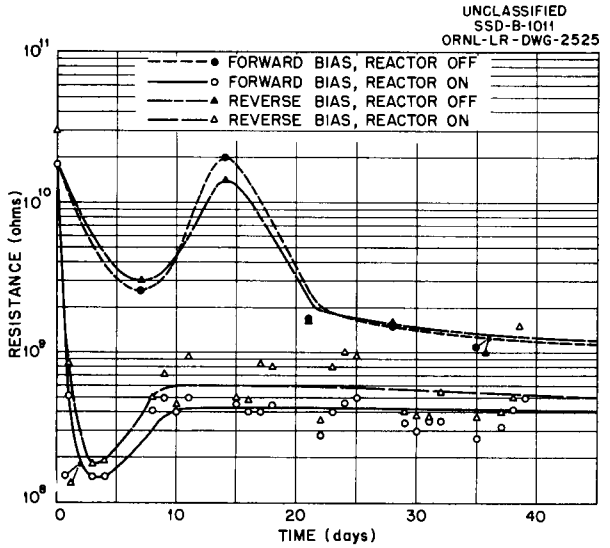

Fig. 71. Resistance vs Irradiation Time in Hole C for Copper-Shielded Copper Wire with Surprenant Polyvinyl Insulation.

BOMBARDMENT OF RECTIFIERS

J. C. Pigg C. C. Robinson

Silicon point-contact rectifiers were bombarded several years ago during a survey of reactor radiation effects on semiconductors and semiconductor devices.[33–35] The behavior of all the different point-contact silicon rectifiers was similar. The conductivity decreased monotonically in both the forward and the reverse direction. Both *n*- and *p*-type silicon crystals[36–38] decrease in conductivity under irradiation. Thus the behavior of the silicon point-contact diode is in agreement with the behavior that would be expected of the bulk material.

Because of subsequent development in the technique of making electrical measurements on high-resistance samples while under reactor irradiation, it seemed desirable to repeat the point-contact experiment and to study the behavior of silicon junction diodes which had recently become available.

Figure 75 shows the behavior of a Sylvania 1N21 silicon point-contact diode. The behavior of the initial portion is in essential agreement with the earlier experiments. However, after the reactor shutdown, the behavior is different. In the previous work the rectifying efficiency decreased but the sample never became ohmic. In Fig. 75, sample Si-P-1 is ohmic after 9.5×10^3 min in hole 51-N of the ORNL Graphite Reactor.

The error in the previous experiments was probably caused by failure of the lead insulation. The

[33] W. E. Johnson and K. Lark-Horovitz, *Phys. Quar. Prog. Rep. March, April, May 1948*, ORNL-51, p 131.

[34] W. E. Johnson, *Phys. Quar. Prog. Rep. June, July, Aug. 1948*, ORNL-159, p 88.

[35] K. Lark-Horovitz and J. C. Pigg, *Phys. Quar. Prog. Rep. June 15, 1949*, ORNL-366, p 36.

[36] W. E. Johnson, K. Lark-Horovitz, and J. C. Pigg, *Phys. Quar. Prog. Rep. Sept., Oct., Nov. 1948*, ORNL-228, p 53.

[37] J. W. Cleland, J. H. Crawford, Jr., J. C. Pigg, and K. Lark-Horovitz, *Physics of Solids Institute Quar. Prog. Rep. April 30, 1951*, ORNL-1095, p 35.

[38] J. W. Cleland *et al.*, *Physics of Solids Institute Quar. Prog. Rep. July 31, 1951*, ORNL-1128, p 12.

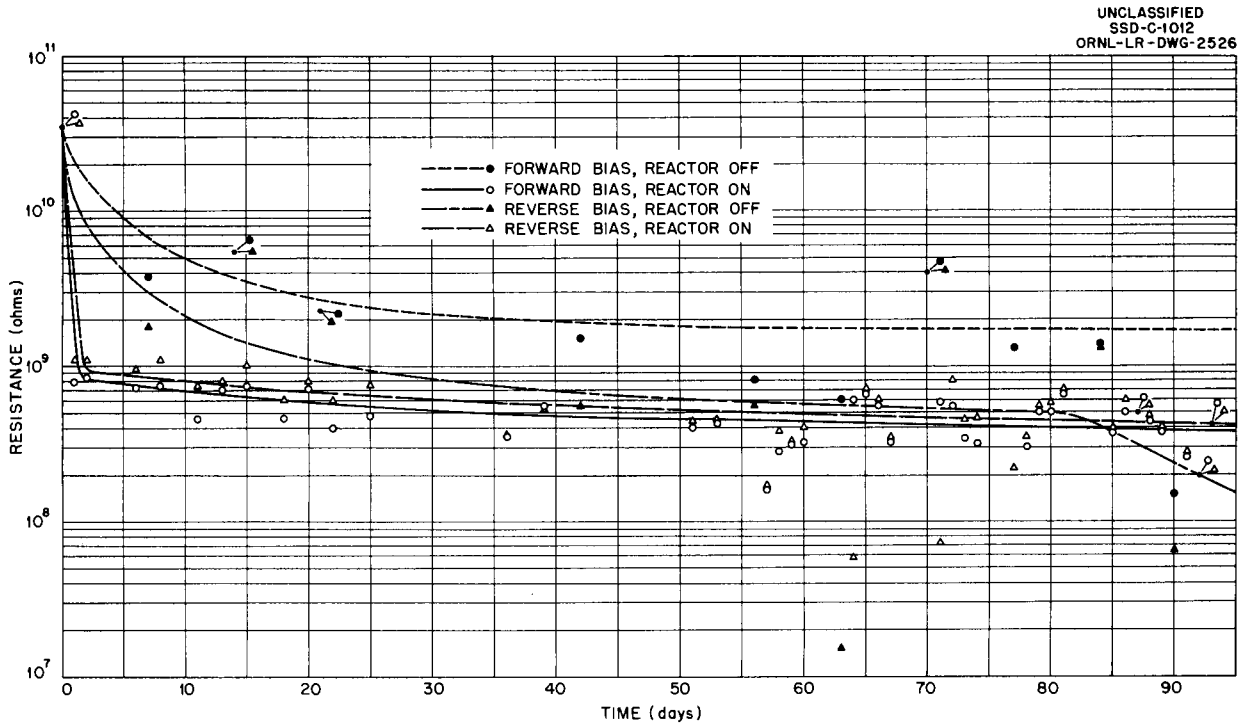

Fig. 72. Resistance vs Irradiation Time in Hole C for Aluminum-Shielded Aluminum Wire with Polyethylene Insulation.

lead insulation in use at that time decreased in resistance until its resistance was comparable to that of the sample. In addition, rectification has been observed in lead-wire insulation while it was being irradiated. Another possible source of error is in the voltages produced in lead wires during irradiation. The samples were measured at a 1.0-v bias. Voltages of the order of 0.5 v have been produced in insulation by irradiation. By maintaining circuit symmetry with respect to ground and by using insulation which has been found to maintain a large resistance compared with that of the sample, these effects have been minimized.

Figure 76 shows the behavior of a Texas Instruments, Inc. PN junction silicon diode type 600. The forward current changes in the same manner as that seen in the point-contact diode. The reverse current, however, increases until the sample is almost ohmic, then decreases at a somewhat lower rate than the forward current until ohmic behavior is reached.

Sample Si 600-2 in Fig. 76 reaches ohmic behavior after about 1.4×10^3 min. Sample Si-P-1 reaches ohmic behavior after 9.5×10^3 min. In neither case, however, is the original resistivity of the bulk material known. The crossover of the characteristics in Fig. 76 seems to be real. The cause of this crossover is not yet understood.

RADIATION EFFECTS IN IONIC CRYSTALS

C. M. Nelson

The research during this period was directed to a study of the ionic conductivity of potassium chloride crystals that had not been irradiated. Although the synthetic crystals from The Harshaw Chemical Co. had been formed in a melt in which they were very slowly cooled, they underwent changes similar to those that are observed[39] when irradiated crystals are annealed at elevated temperatures. Apparently, however, irradiation greatly enhances these changes; therefore it was decided that a study should be made on unirradiated crystals so that the effect of irradiation could be determined

[39] C. M. Nelson, *Solid State Semiann. Prog. Rep. Aug. 31, 1953*, ORNL-1606, p 80; *Solid State Semiann. Prog. Rep. Feb. 28, 1954*, ORNL-1677, p 44.

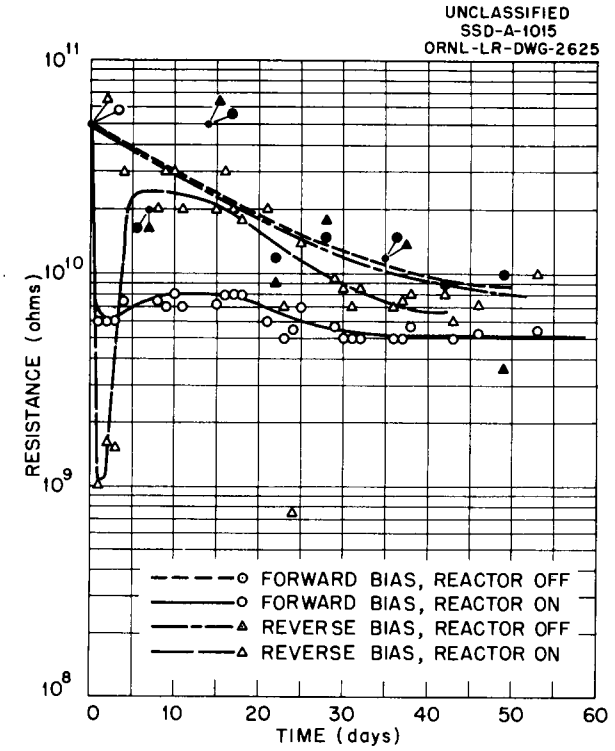

Fig. 73. Resistance vs Irradiation Time in Hole 50-N for Copper-Shielded Copper Wire with Rubber Insulation.

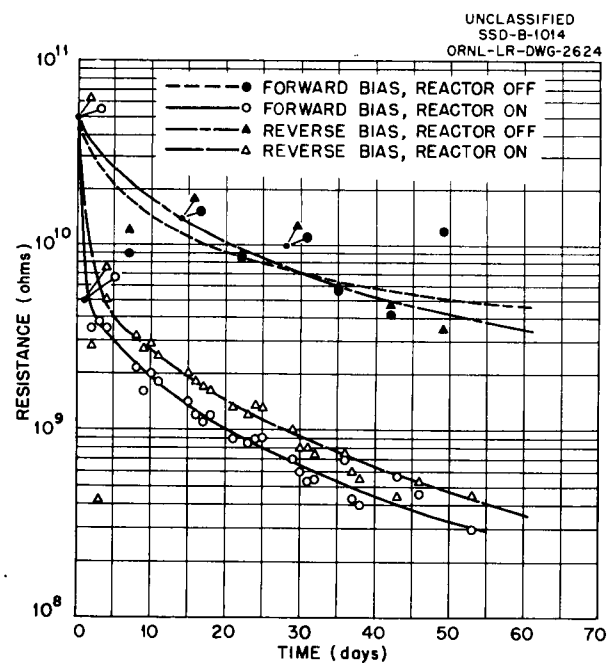

Fig. 74. Resistance vs Irradiation Time in Hole 50-N for Copper-Shielded Copper Wire with Teflon Insulation.

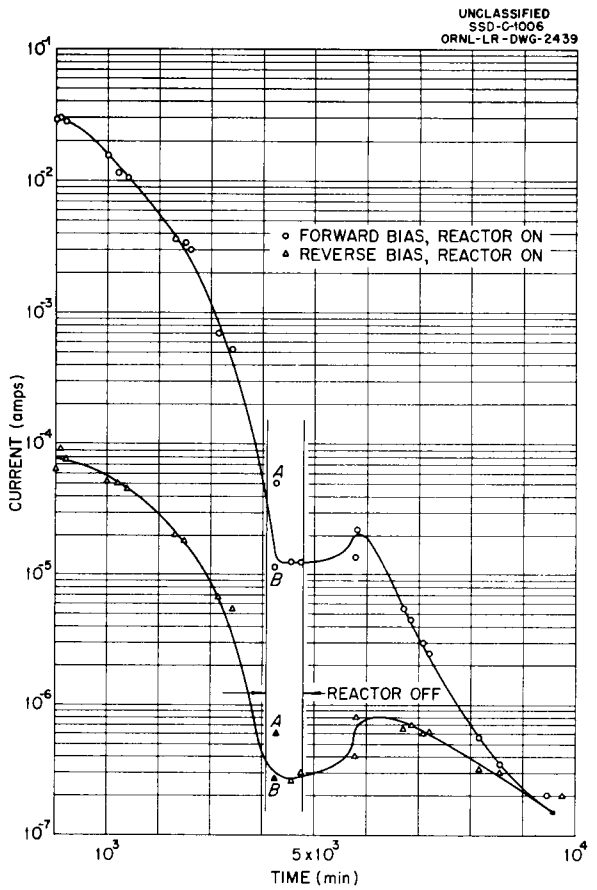

Fig. 75. Forward and Reverse Currents at 1.0 v vs Irradiation Time for Sample Si-P-1.

and so that the results would have a quantitative basis.

The ionic-conductivity apparatus has been improved, and measurements have been made from 21 to 720°C with confidence. This involves a range in resistance of 10^{16} to 10^{6} ohms. Difficulty in securing good electrode contacts is experienced above 600°C. Conductivity paints appear to fail in this region. Du Pont silver, Rubalt graphite, and Hanovia platinum bright paints have been used. Instead of a constant applied d-c voltage, a pulse technique will be used to check the previous results.

A considerable amount of effort has been expended on the development of the conductivity apparatus and the associated measuring circuit. It was found necessary to improve the performance of the vibrating-reed electrometer in order to obtain dependable data. As a result of this development, confidence can be placed in measurements indi-

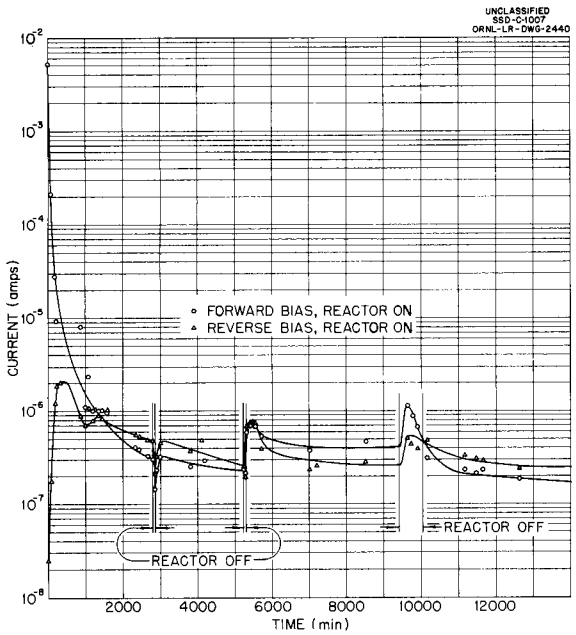

Fig. 76. Forward and Reverse Currents at 1.0 v vs Irradiation Time for Sample Si-600-20.

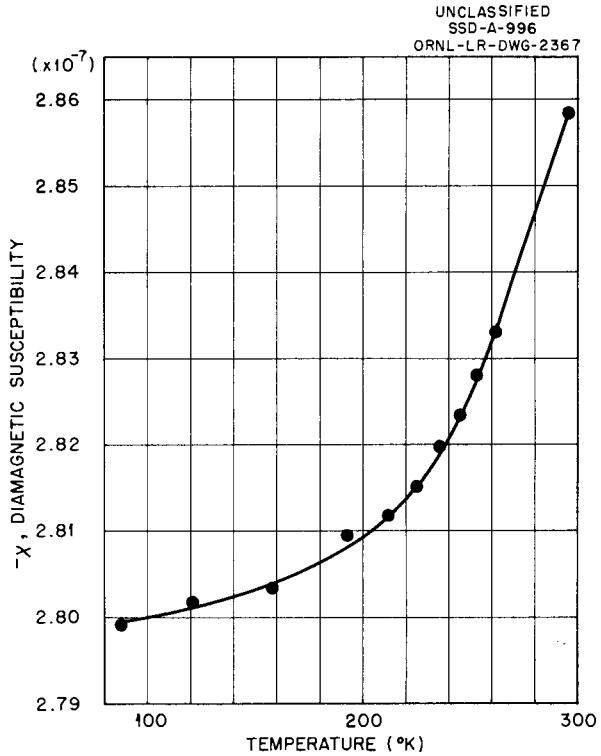

Fig. 77. Magnetic Susceptibility of *p*-Type InSb.

cating a resistance of 10^{16} ohms. The electrometer head and the complete circuit are inside an aluminum box, with individual shielding on the leads. Operations are performed externally. Further improvements are in progress. Within the next few weeks another switch for reversing the battery leads to the circuit will be installed. The new switch will have a Bodine motor to reverse polarity automatically and also to give the crystal a pulsed voltage.

MAGNETIC SUSCEPTIBILITY STUDIES

Indium Antimonide (D. K. Stevens). The temperature dependence of the magnetic susceptibility of one specimen[40] of InSb, a *p*-type single-crystal cube containing approximately 1.1×10^{16} carriers cm^{-3} at 77°K, has been measured. The results of these measurements are shown in Fig. 77.

The Hall coefficient temperature characteristics of this specimen, curve I of Fig. 58, indicate that there is a change from extrinsic to intrinsic properties with increasing temperature in the neighborhood of 210°K. Because of the complexity of the processes involved, it is not possible to carry out a quantitative analysis of the magnetic data in this temperature range. However, from the knowledge of the ratio of mobility of the electrons to holes[41] in InSb, $\mu_n/\mu_p \cong 85$, conduction electrons would be expected to be approximately 36 times as effective magnetically as holes.[42,43] This, in combination with the probable low effective mass of electrons[41] in InSb, would indicate that a large diamagnetic component to the magnetic susceptibility should be generated as the temperature is increased into the intrinsic range. Qualitatively, this behavior is apparent in Fig. 77, in which the concentration of intrinsic electrons is still increasing at 300°K.

Unirradiated Germanium (D. K. Stevens). In addition to those previously reported,[44] the sus-

[40] Sample supplied by M. Tannenbaum, Bell Telephone Laboratories, Summit, N. J.

[41] M. Tannenbaum and J. P. Maita, *Phys. Rev.* **91**, 1009 (1953).

[42] W. Shockley, *Electrons and Holes in Semiconductors*, Chap. 11, Van Nostrand, New York, 1950.

[43] G. Busch and E. Mooser, *Z. physik. Chem.* **198**, 23 (1951).

[44] D. K. Stevens, J. H. Crawford, Jr., and J. W. Cleland, *Solid State Semiann. Prog. Rep. Aug. 31, 1953*, ORNL-1606, p 71.

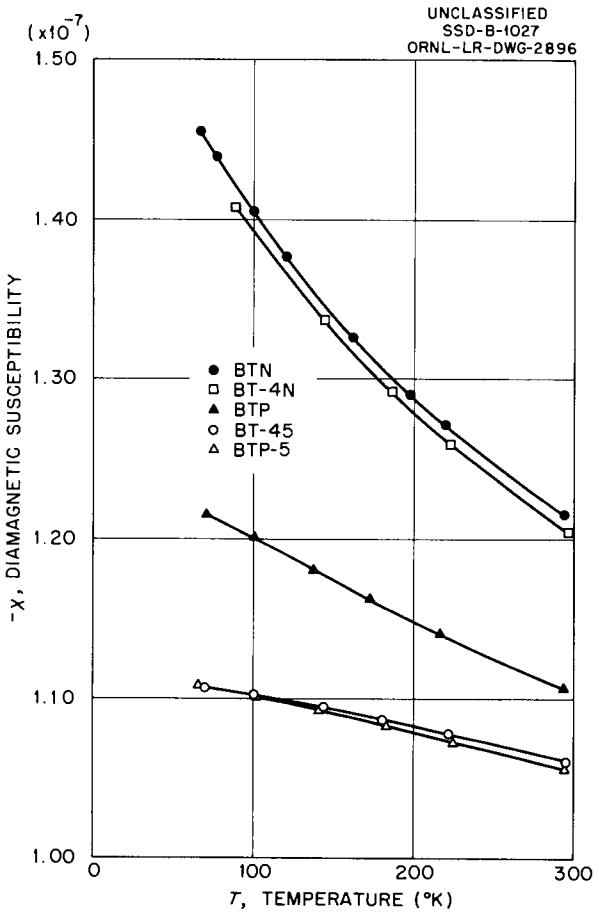

Fig. 78. Diamagnetic Susceptibility of Germanium.

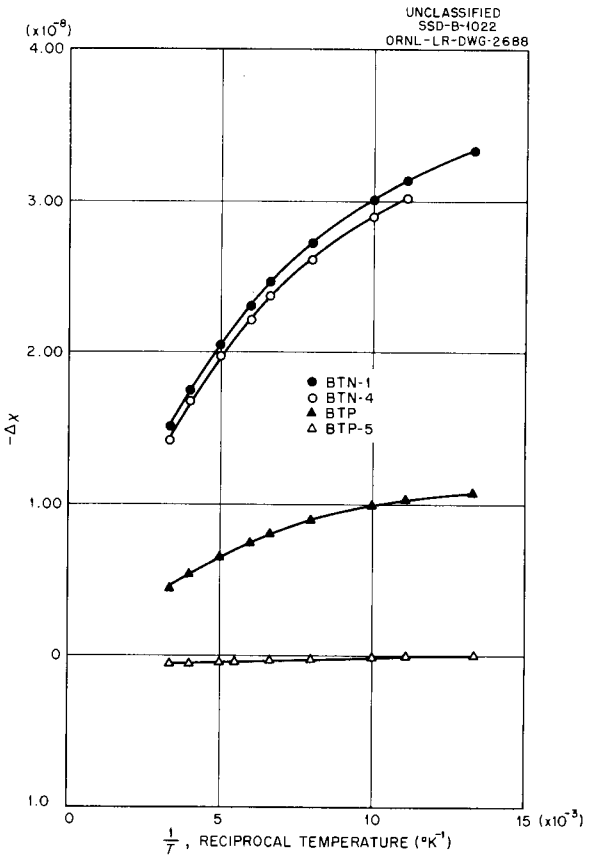

Fig. 79. Carrier Contribution to Susceptibility of Germanium.

ceptibility of five samples[45] of germanium has been measured as a function of temperature; the curves for these measurements are shown in Fig. 78. One sample (BT-45) was higher in purity than any other sample yet measured and will therefore replace that of ORD-7D as being representative of the contribution of the germanium lattice in the analysis of the data from other germanium samples.

When plotted vs $1/T$, the carrier contribution is expected to yield a straight line until degeneracy sets in, whereupon a concave, downward curvature is imparted. It is evident from Fig. 79 that the two n-type samples, BTN-1 and BTN-4, are degenerate throughout the temperature range measured. The carrier concentration in each of these samples was 9×10^{18} cm^{-3}. The ratio of the rest mass to the effective mass of the electron, calculated from the maximum slope of the difference curve extrapolated to zero, was 4.2 for BTN-1 and 4.6 for BTN-4. The smallness of these values compared with previously obtained values is undoubtedly due, in part, to the high concentration, and thus degenerate nature, of the carriers in these cases.[44,46]

Samples BTP and BTP-5 are p-type germanium containing 3.9×10^{18} and 6.7×10^{16} carriers cm^{-3}, respectively. The difference curves for BTP also appear to be degenerate throughout the range of measurement, and the calculated ratio of the rest mass of the electron to the effective mass of the carrier (~3.5) is lower than previously reported values. The mass ratio calculated from the data on BTP-5 is 5.8. This value, however, is only

[45] Samples supplied by C. S. Fuller, Bell Telephone Laboratories, Murray Hill, N. J.

[46] J. H. Crawford, Jr. and D. K. Stevens, *Solid State Semiann. Prog. Rep. Feb. 28, 1954*, ORNL-1677, p 43.

tentative and is subject to correction at a later date.

The susceptibility vs temperature curve for one sample of p-type gold-doped germanium[47] has been obtained. The data are being analyzed at the present time.

Bombarded Germanium (J. H. Crawford, Jr. and D. K. Stevens). In the last semiannual report[48] the effect of fast-neutron bombardment on the magnetic susceptibility χ of germanium was reported. This study has been continued, and the specimen, originally n-type, has been converted to p-type by additional bombardment. Since, for charge-carrier concentrations of less than about 5×10^{15}, the carrier contribution to the susceptibility is below detection with the present equipment at room temperature, examination of curves in this concentration range should reveal the contribution of trapped carriers and also the effect of lattice disordering on the susceptibility of the lattice.

In Fig. 80 the diamagnetic susceptibility vs temperature curves are compared with a high-purity, n-type specimen. Curve 0 was obtained on a hyperpure, zone-leveled, n-type specimen[49] which is intrinsic at room temperature ($n_e = 1 \times 10^{13}$ cm^{-3} in the extrinsic range). Curves I and II were obtained on sample Sb-11 before conversion, while curves III and IV were taken after the specimen had been converted to p-type. Bombardment and carrier-concentration data which correspond to each curve are summarized in Table 10; also listed are the values of the slopes of the respective curves. It

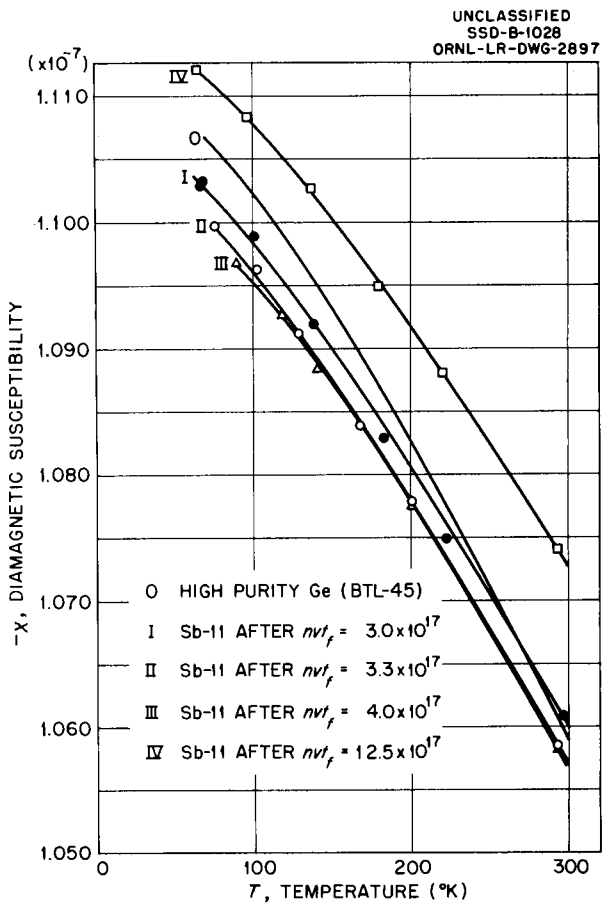

Fig. 80. Diamagnetic Susceptibility vs Temperature of Germanium After Irradiation.

TABLE 10. BOMBARDMENT AND CARRIER-CONCENTRATION DATA ON GERMANIUM

Curve	Specimen	Exposure (hr)	Type of Germanium	Carrier Concentration at $T = 300°K$ (cm^{-3})	$\left(\frac{d\chi}{dT}\right)_{T=300°K}$ (10^{-11} cgs units)
0	BTL-45	0	n	1×10^{13}	2.44
I	Sb-11	103	n	8×10^{15}	2.16
II	Sb-11	114	n	5×10^{15}	2.16
III	Sb-11	140	p	$<1 \times 10^{15}$	2.17
IV	Sb-11	463	p	3×10^{16}	1.89

[47] Sample supplied by W. C. Dunlap, Knolls Laboratory, General Electric Company, Schenectady, N. Y.

[48] D. K. Stevens, J. W. Cleland, and J. H. Crawford, Jr., *Solid State Semiann. Prog. Rep. Feb. 28, 1954*, ORNL-1677, p 45–46.

[49] Supplied by C. S. Fuller of the Bell Telephone Laboratories.

is evident from both Fig. 80 and Table 10 that the irradiation has lowered the rate of increase of diamagnetism with decreasing temperature by a small factor. The slope at room temperature before irradiation is -2.44×10^{-11} cgs units as compared with -2.16×10^{-11} after exposure.

The $\Delta\chi$ vs $1/T$ curves for the various irradiations with reference to the hyperpure specimen are plotted in Fig. 81. The curves are numbered in the same manner as in Fig. 80. Also shown (curve 0′) is the expected paramagnetic contribution of 7×10^{17} cm^{-3} trapped electrons (the initial conduction electron concentration of Sb-11), if each electron exerts its spin paramagnetism and if a zero Weiss constant is assumed. In the comparison of these curves, only the temperature dependence should be considered. This follows from the fact that the relative precision for the experimental points on a $-\chi$ vs T curve is better than ±0.1%, whereas, because of the calibration technique, the absolute precision of any point relative to the susceptibility of O_2 at NTP is no better than ±0.3%. Hence it is only the shape of the $-\chi$ vs T curve that is important.

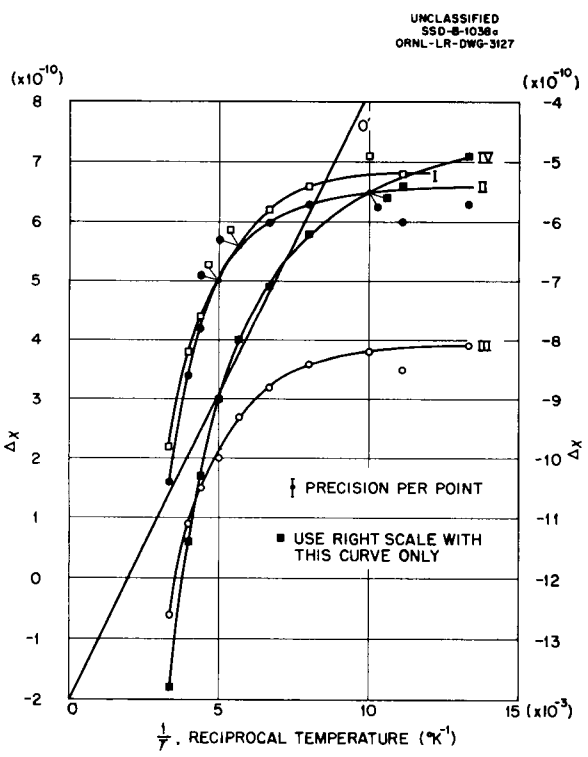

Fig. 81. Change in Diamagnetic Susceptibility with Irradiation.

It is evident from curves I, II, and III of Fig. 81, whose temperature dependences are virtually identical, that although there is a decrease in diamagnetism it is not due to 7×10^{17} free spins. It may be that some of the change is caused by the introduction of paramagnetic centers. However, if such is the case, their concentration is markedly temperature dependent, a condition which does not correspond with the present ideas about the nature of energy levels that are associated with defects. It appears more reasonable to attribute the change to a decrease in the negative temperature coefficient of the susceptibility of the lattice resulting from lattice disorder.

As can be seen from Table 10, curve IV was obtained after an irradiation of about four times that of curves I, II, and III. In this case $n_h = 3 \times 10^{16}$ at 300°K, a contribution which should produce a measurable carrier contribution. However, Hall coefficient measurements indicate that the ionization energy for hole production is so large that n_h decreases to about 1×10^{14} at dry-ice temperature. The carrier contribution would be evident at only the high end of the temperature range. The result would then be that the negative temperature coefficient of the $-\chi$ vs T curve would be further decreased at high temperature. The data in Table 10 confirm this expected behavior. The $-\chi$ vs T curve for this exposure (curve IV in Fig. 81) has a form similar to the ones for the shorter irradiations, except for the effect of the decreased temperature dependence at high temperature.

According to the James–Lark-Horovitz model of bombardment-produced energy levels,[50] in originally n-type material at the conductivity minimum, the following situation obtains: each interstitial atom is singly ionized, while each vacancy has two extra electrons (one comes from the conduction band). Hence, the interstitial atom would be expected to possess a residual-spin magnetic moment. The concentration of such interstitial atoms would be equal to the original electron or donor concentration. The work done here indicates that such is not the case. One reason, not previously considered for the absence of resultant spin, is the possibility that the energy levels produced by the defects form a narrow degenerate band of states.

[50] H. M. James and K. Lark-Horovitz, *Z. physik. Chem.* 198, 107 (1951).

The situation at the conductivity minimum would then correspond to completely filled lower bands, and no spin unbalance would result. This view received support from recent paramagnetic resonance measurements on silicon containing occupied donors[51] (T = 4.2°K). No resonance absorption was observed until the donors were partly emptied by either deforming the crystal or by compensation doping with acceptors. If this explanation is correct, some paramagnetism should be noted at low temperature in heavily irradiated converted germanium, since in this case the defect levels will only be partly filled. This point will be tested in future experiments.

DEGENERACY AND EFFECTIVE MASS IN GERMANIUM

D. K. Stevens J. H. Crawford, Jr.

In the previous report[52] the $-\chi_c$ vs $1/T$ curves for both n- and p-type carriers in germanium were calculated from the Fermi-Dirac distribution function, and a degeneracy factor of 6, exclusive of spin degeneracy, was used. Since that time cyclotron resonance measurements[53] have indicated that there is an eightfold spatial degeneracy in n-type germanium, because energy surfaces at the bottom of the conduction band have minima in the eight [111] directions in k space. Hence, eightfold degeneracy was used in the density-of-states term and a much better fit to the data was obtained (see Fig. 82). In this treatment of the data, however, it was assumed that this family of energy surfaces are spheres in k space, since the effective mass used in the expression for the density of states is identical with that for orbital motion of electrons in the magnetic field. Experiment[53] suggests that this is not the case at all, since the data are best fitted by energy surfaces which are quite eccentric ellipsoids of revolution. In addition, since it appears that the energy minima in k space correspond to the Brillouin zone boundary,[54] only fourfold spatial degeneracy of states is expected. Calculations which include these additional features in the treatment of n-type susceptibility data are now in progress.

[51] R. C. Fletcher *et al.*, *Phys. Rev.* 94, 1392 (1954).

[52] J. H. Crawford, Jr. and D. K. Stevens, *Solid State Semiann. Prog. Rep. Feb. 28, 1954*, ORNL-1677, p 43.

[53] B. Lax, H. J. Zeiger, R. N. Dexter, and E. S. Rosenblum, *Phys. Rev.* 93, 1418 (1954).

[54] C. Herring, private communication.

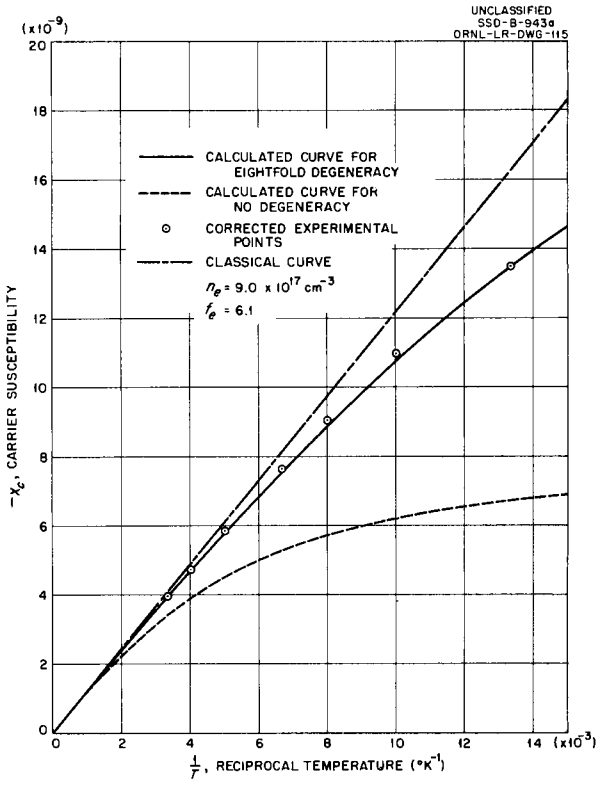

Fig. 82. $-\chi_c$ vs $1/T$ for n-Type Germanium.

Analysis of p-type magnetic susceptibility data is also being made on the basis of recent information from cyclotron resonance experiments.[55]

IRRADIATION EFFECTS IN ZIRCON SINGLE CRYSTALS

M. C. Wittels F. A. Sherrill

The effect of fast-neutron bombardment on zircon ($ZrSiO_4$) is of particular interest because many natural zircon crystals are partially or completely disordered as a result of "internal" alpha irradiation. This internal alpha irradiation is due to alpha emission from impurity atoms of the uranium-actino series and thorium series which occupy normal zirconium sites in the space lattice. A more or less homogeneous internal alpha irradiation occurs when these impurities are randomly distributed and when they are of sufficient concentration so that localized disordering will not result. Since these alpha particles have energies of approximately 6

[55] R. N. Dexter, H. J. Zeiger, and B. Lax, *Phys. Rev.* 95, 557 (1954).

Mev, an attempt could be made to compare the effects of fast charged particles and the effects of fast neutrons in producing displacements in the zircon lattice. Unfortunately, those crystals which are disordered by natural alpha emissions are estimated[56] to have an age of 10^9 years; obviously, the physical history of the crystals during this long period cannot be known, and therefore a quantitative analysis is impossible. Nevertheless, some qualitative observations can be made.

The fast-neutron bombardment of ordered single crystals with fluxes ranging up to 2.8×10^{20} neutrons/cm^2 produces a highly distorted lattice that maintains considerable long-range order. The distortion that results from frozen-in displacements expands the lattice anisotropically (Fig. 83) and causes a density reduction of approximately 4%. Rotation, Weissenberg, and precession x-ray diffraction patterns show that the single-crystal zircon lattice is retained throughout the bombardment. Laue transmission photographs (Fig. 84) reveal the distortion and mosaic structure induced in the lattice as a result of the irradiation. The diffuse streaks in the central zone of the Laue pattern probably indicate a type of short-range ordering process that occurs during the bombardment. These diffuse reflections were observed when monochromatic radiation was employed, and it is anticipated that they can be analyzed by means of bent-crystal techniques.

[56] P. M. Hurley and H. W. Fairbairn, *Bull. Geol. Soc. Amer.* **64**, 659 (1953).

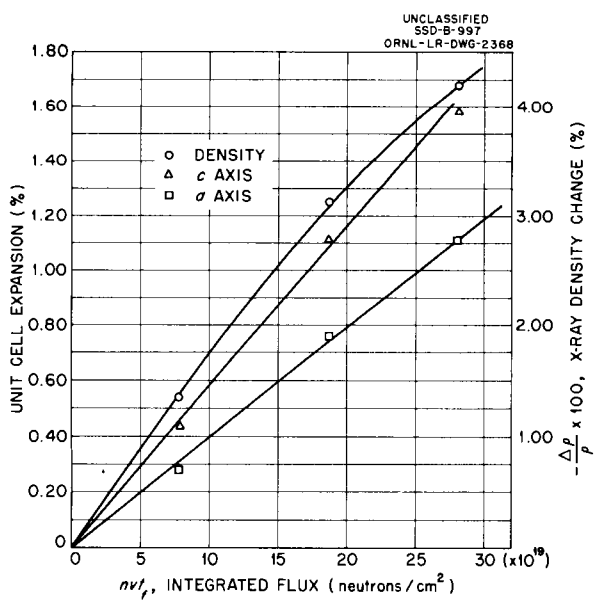

Fig. 83. Effect of Radiation on Density and Unit-Cell Expansion for a Zircon Single Crystal.

Preliminary annealing studies of these neutron-irradiated crystals show that the thermal stability of defects is extremely high. The distention and distortion of heavily bombarded crystals is only slightly annealed at 1100°C. At approximately 1600°C most of the damage was annealed; single-crystal x-ray diffraction patterns revealed the return to a more perfect lattice. These annealing studies are being continued.

Since the effectiveness in producing displacements in solids is greater for fast neutrons than for energetic alphas by one or two orders of magnitude, a more efficient disordering process would be expected to occur from neutron bombardment. Observers[56] of alpha-irradiated crystals indicate that the lattice is disordered by a total alpha bombardment of approximately 10^{17} α/mg. If this analysis is correct, then processes other than the alpha-displacement process apparently contributed to the disorder, since considerable order is retained in crystals bombarded by 2.8×10^{20} neutrons/cm^2.

UNIRRADIATED AND IRRADIATED PIEZO QUARTZ

D. K. Stevens H. C. Schweinler
M. C. Wittels

The specific diamagnetic susceptibility vs temperature curves for three specimens of crystalline quartz cut from a pair of matched piezo-electric natural crystals are shown in Fig. 85, where curve I is of an unirradiated cube and curves II and III are of cubes subjected to fast-neutron bombardments at 100°C of 5×10^{19} and 3.3×10^{20} neutrons/cm^2, respectively. Density reductions of 2% and 14.6% also resulted from these bombardments. After irradiation the specimens were faintly colored magenta and were transparent.

From the slopes of Curie plots of data obtained by subtracting curve I from each of the other two curves (see Fig. 86), values for the number of paramagnetic centers per cubic centimeter introduced into the crystals by bombardment have been calculated for an assumed spin of $\frac{1}{2}$ and are listed in the last column of Table 11. The values ob-

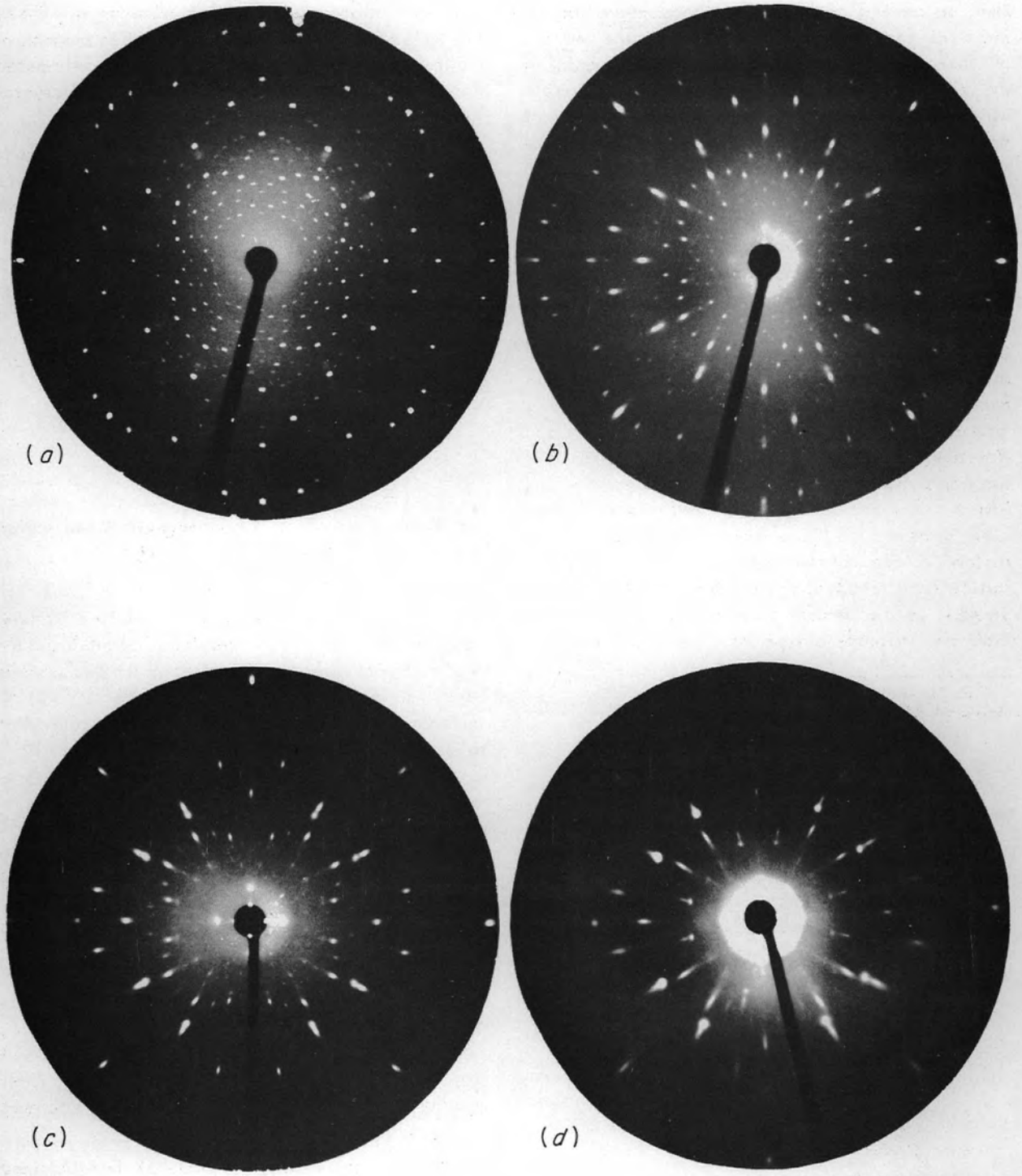

Fig. 84. Laue Transmission Photographs of a Zircon Single Crystal After Various Bombardments. (*a*) Unirradiated; (*b*) $nvt_f = 7.8 \times 10^{19}$; (*c*) $nvt_f = 1.72 \times 10^{20}$; (*d*) $nvt_f = 2.8 \times 10^{20}$.

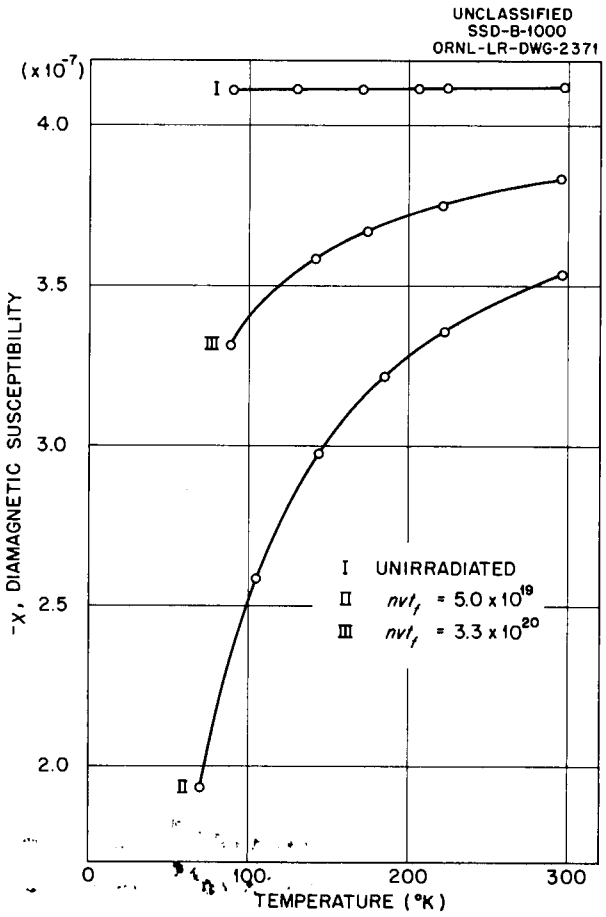

Fig. 85. Diamagnetic Susceptibility of Piezo Quartz.

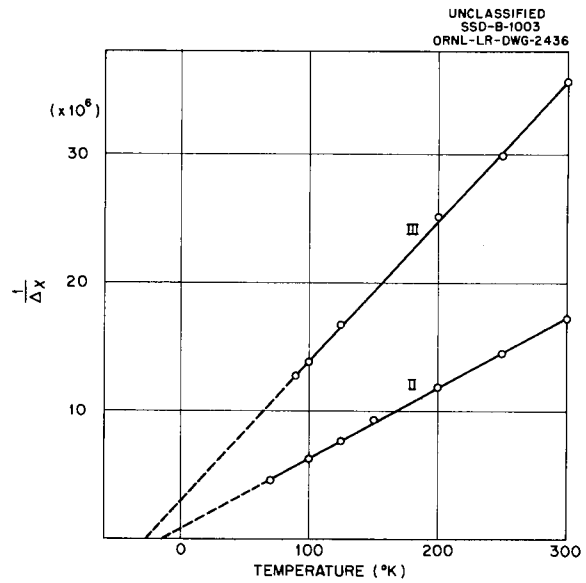

Fig. 86. Curie Plot of Paramagnetic Contribution of Irradiated Quartz.

tained by McClelland[57] from changes of the room-temperature susceptibility for shorter irradiations at 30°C are also listed. It would appear that the maximum number of paramagnetic centers produced by fast-neutron bombardment is obtained by irradiations of approximately 2×10^{19} neutrons/cm^2. It is to be noted that at this level of irradiation appreciable density changes begin to occur.[58]

Optical studies[59] down to 2000 Å for irradiations up to 10^{18} neutrons/cm^2 have shown that in crystalline quartz two absorption bands in the visible spectrum and one in the ultraviolet are produced by neutron bombardment. Absorption in the two visible bands decreased with irradiation after an initial increase, whereas the ultraviolet band continued to increase at the longest irradiation studied ($\sim 10^{18}$ neutrons/cm^2). It would appear that the paramagnetic centers produced by bombardment are associated with the ultraviolet band, since specimens II and III were transparent and were faintly colored magenta. More extensive optical and magnetic studies are planned.

The results of a least-squares analysis of the experimental data are also listed in Table 11. The form of the equation chosen,

$$-\chi \times 10^7 = \frac{A}{T + \Delta} + B + CT \ ,$$

was suggested by the $-\chi$ vs T plot of the unirradiated specimen and the Curie plot of the differential data. For a given set of measured data (χ, T), the values of A, B, and C are found to vary linearly with Δ, the Weiss constant. In the case of the short irradiation, the sum of the squares of the residuals appears to minimize near a value of Δ predicted by the Curie plot, but this was not true for the long irradiation. If the predicted Δ values are to be used as the criteria in the choice of the

[57] J. D. McClelland, *Effect of Neutron Bombardment Upon the Magnetic Susceptibility of Various Oxides*, NAA-SR-263 (Nov. 15, 1953).

[58] M. C. Wittels and F. A. Sherrill, *Solid State Semiann. Prog. Rep. Aug. 31, 1953*, ORNL-1606, p 98.

[59] E. W. J. Mitchell and E. G. S. Paige, *Proc. Phys. Soc. (London)* B67, 262 (1954).

constants for the equation, then B, which presumably is the quartz-lattice contribution to the total susceptibility at absolute zero, will apparently increase with irradiation. At first thought an increase in diamagnetic susceptibility might be expected as the density uniformly decreases. When the minima of the sum of the squares of the residuals are used as the criteria, this trend in B with irradiation is not found. A trend in the value of C with irradiation also is apparent when Δ is used as the basis for choice.

Work on irradiated quartz is to be extended.

TABLE 11. EFFECTS OF BOMBARDMENT ON THE NUMBER OF PARAMAGNETIC CENTERS IN PIEZO QUARTZ CRYSTALS

Curve	Density (g/cm^3)	Fast-Neutron Irradiation (neutrons/cm^2)	Δ (°K)	A	B	C	$r^2 \times 10^6$ [a]	Paramagnetic Centers of ~~½ spin~~ Spin ½ (number/cm^3)[b]	(number/cm^3)[c]
I	2.650	0	0	−0.4931	4.4982	6.94×10^{-5}	2.23	2.1×10^{17}	
II	2.598	5.0×10^{19}	0	−136.9	3.8503	5.31×10^{-4}	1951.0	5.71×10^{19}	7.6×10^{19}
			6	−157.8	3.9896	2.43×10^{-4}	117.0	6.58×10^{19}	
			15	−192.05	4.2087	-1.78×10^{-4}	14.31	8.01×10^{19}	
III	2.263	3.3×10^{20}	0	−61.91	3.997	$+1.59 \times 10^{-4}$	6.78	2.25×10^{19}	3.3×10^{19}
			10	−75.45	4.077	$+1.4 \times 10^{-5}$	14.47	2.74×10^{19}	
			20	−90.59	4.159	-1.30×10^{-4}	28.0	3.29×10^{19}	
			27	−102.2	4.218	-2.30×10^{-4}	38.0	3.72×10^{19}	
d		0.52×10^{19}						6.1×10^{19}	~~6.1×10^{19}~~
d		3.76×10^{19}						8.5×10^{19}	~~8.5×10^{19}~~

[a] The residual between the measured value of χ and that computed by using the proposed equation and the calculated constants.

[b] Calculated from the value of A $(= n\beta^2/\rho k)$.

[c] Calculated from slope of Curie plot.

[d] J. D. McClelland, *Effect of Neutron Bombardment upon the Magnetic Susceptibility of Various Oxides*, NAA-SR-263 (Nov. 15, 1953).

ENGINEERING PROPERTIES

PROPERTIES OF REACTOR-IRRADIATED CERAMICS

C. D. Bopp O. Sisman
R. L. Towns

The study of the radiation-induced changes that occur in ceramic materials is making progress. This work has been undertaken in cooperation with J. R. Johnson and other members of the Ceramics Laboratory of the Metallurgy Division. A list of the materials that are being studied is given in Table 12. Two sets of specimens have been irradiated for integrated epithermal neutron fluxes of about 1×10^{20} and 2×10^{20} neutrons/cm^2. A third set

TABLE 12. DENSITY AND COMPOSITION OF CERAMICS

Material	Density (g/cm^3)	Composition
BeO	3.0	98% BeO, minor impurities
Cermet	6.0	30% Al_2O_3, 70% Cr, minor impurities
Glass (silica)	2.2	99.8% SiO_2
Glass (pyrex)	2.23	80% SiO_2, 4% Na_2O, 14% B_2O_3, 2% Al_2O_3, minor impurities
Glass (lead)	5	80% PbO, 20% SiO_2
Glass (plate)		
Glass (window)	2.4	72% SiO_2, 15% Na_2O, 12% CaO, 1% Al_2O_3
ZrO_2	5.6	99% ZrO_2, minor impurities
HfO_2	8.0	95% HfO_2, 5% ZrO_2
Zircon	4.5	99% $ZrO_2 \cdot SiO_2$
Al_2O_3 (single crystal)	4.0	99.5+% Al_2O_3
MgO (hot-pressed)	3.3	98% MgO, minor impurities
MgO (single crystal)	3.58	99.5+% MgO, minor impurities
SiC	3.2	99% SiC, minor impurities
Quartz (single crystal)	~~3.58~~ 2.66	99.9% SiO_2, minor impurities
Thoria	9.7	98% ThO_2, minor impurities
Steatite 228	2.6	98% $MgO \cdot SiO_2$, minor impurities
Forsterite 243	2.7	98% $2MgO \cdot SiO_2$, minor impurities
Cordierite 202	2.0	98% $2MgO \cdot 2Al_2O_3 \cdot 5SiO_2$, minor impurities
Zircon 475	3.6	95% $ZrO_2 \cdot SiO_2$
Spinel (single crystal)	3.6	99% $2Al_2O_3 \cdot 7MgO$
Lava A	2.3	A natural aluminum silicate of indefinite composition
ZrO_2 550	3.5	95% ZrO_2, minor impurities
Muscovite mica	2.8	99% $H_2KAl_3 \cdot (SiO_4)_3$, minor impurities
Al_2O_3 582	3.5	90% Al_2O_3, 10% ($CaO \cdot SiO_2$ and/or $MgO \cdot SiO_2$)
$BaO \cdot TiO_2$	5.6	88% $BaO \cdot TiO_2$, 8% $MgO \cdot ZrO_2$, 4% $CaO \cdot ZrO_2 \cdot SiO_2$
TiO_2 192	4.0	95% TiO_2, 5% (clay + ZrO_2)
Kennametal 151-a		70% TiC, 10% (Cb and/or Ta), 20% Ni

of specimens will be irradiated in the MTR for about 10^{21} neutrons/cm^2.

The specimens are disks about ¾ in. in diameter and 20 to 40 mils thick. For the Hanford irradiations a stack of about eight specimens of each material was wrapped in aluminum foil. Several packets were placed in an aluminum can; the can was then evacuated and filled with helium. Irradiation was made in a water-cooled channel.

Visual inspection of the specimens that were irradiated for the shorter time showed that the aluminum foil wrapping and the outer portion of many of the specimens were thinly coated with a white solid. The MgO (hot-pressed) specimens had stuck together, and they broke when an attempt was made to pry them apart; none of the other specimens were stuck. A white coating which contains a large amount of magnesium was thickly caked about the MgO specimens. All the ceramics were darkened except for $BaO{\cdot}TiO_2$ and silica glass, which changed little in color. Spinel developed a yellow color and MgO a blue color; the color of the other ceramics was either brown or gray. The only ceramics that showed visible radiation-produced defects were $BaO{\cdot}TiO_2$, which was crumbled, and pyrex glass, which had surface cracks visible at 10X magnification.

The following measurements are now in progress: change in weight and thickness, density, x-ray diffraction, electrical resistivity, thermal conductivity, dielectric strength, flexural strength, dynamic modulus, Tukon hardness, arc resistance, crystallography, stored energy, and differential thermal analysis. The last three tests will be made by the Ceramics Laboratory. It is planned to study the effect of annealing for some of the nondestructive tests.

X-RAY DIFFRACTION PATTERNS OF IRRADIATED ELASTOMERS

C. D. Bopp G. E. Klein
R. L. Towns

In order to obtain crystalline x-ray diffraction patterns for elastomers, it is necessary to stretch them. Since elastomers, after irradiation, stretch very little without breaking, it was necessary to irradiate the elastomer in the stretched condition. The specimen was protected from ozone attack during irradiation by enclosing it in a helium-filled vessel. A Co^{60} source was employed for the irradiation.

Figure 87 shows the x-ray diffraction patterns for stretched, irradiated, natural-rubber formulation 32A43.[1] The effect of irradiation is to destroy the crystalline peaks at 21 and 24 deg (2θ). The effect of radiation on the pattern of an unstretched specimen which does not show the crystalline peaks is given in Fig. 88; the amorphous halo is changed little by radiation. The patterns were taken by a method already described.[2]

In addition to the change in x-ray pattern, the stretched specimen showed large permanent set. The exposure was insufficient to affect the mechanical properties of unstretched specimens.[3]

RADIATION EFFECTS ON PLASTICIZED POLYVINYL CHLORIDE

C. D. Bopp R. L. Towns

The radiation-induced change in polyvinyl chloride which contained various proportions of plasticizer was studied by measuring the dynamic Young's modulus and viscous modulus.[4] The results are shown in Table 13. Plasticized formulations contained 52 and 25 parts of dioctyl phthalate per 100 parts of polymer (Table 14). Irradiation of the material was conducted in water-cooled hole 19 of the ORNL Graphite Reactor.

It appears that two of the unplasticized formulations are slightly softened, although the softening is barely within the sensitivity of measurement, which is limited for these materials because thickness is not uniform. Softening has been found previously[5] for unplasticized polyvinyl chloride. Of the plasticized formulations, the one with the smallest proportion of plasticizer shows small change at low exposure, but later becomes hard; the one with the greatest amount of plasticizer is hardened even for the low exposure. This behavior suggests opposite radiation effects for polymer and plasticizer. The predominant radiation-induced

[1] O. Sisman, R. L. Towns, C. D. Bopp, and W. K. Kirkland, *Physics of Solids Institute Quar. Prog. Rep. April 30, 1951*, ORNL-1095, Table 5.1, p 76.

[2] C. D. Bopp and G. E. Klein, *Solid State Semiann. Prog. Rep. Aug. 31, 1953*, ORNL-1606, p 96.

[3] C. D. Bopp, O. Sisman, W. K. Kirkland, and R. L. Towns, *Solid State Semiann. Prog. Rep. Aug. 31, 1953*, ORNL-1606, p 88.

[4] C. D. Bopp, R. L. Towns, O. Sisman, and W. K. Kirkland, *Solid State Semiann. Prog. Rep. Feb. 28, 1954*, ORNL-1677, Table 5, p 59, units of exposure should have been expressed as 10^9 rep.

[5] J. Byrne *et al.*, *Ind. Eng. Chem.* 45, 2551 (1953).

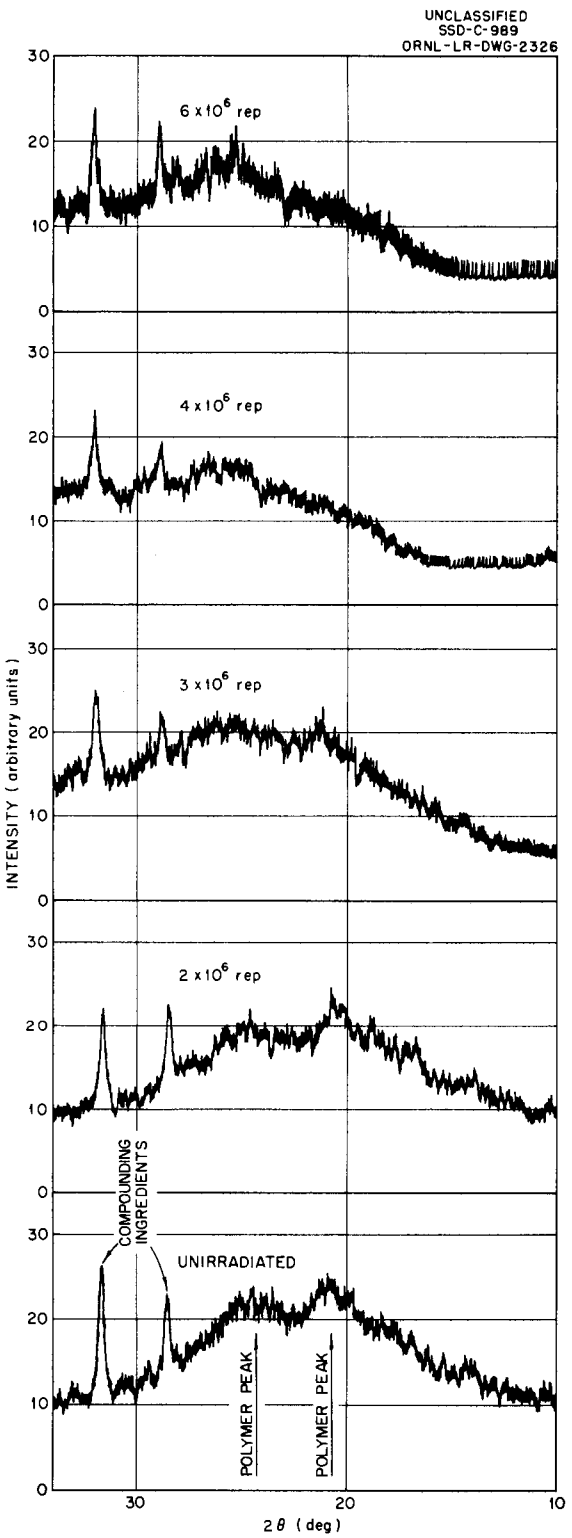

Fig. 87. X-Ray Diffraction Patterns of Rubber Stretched 315%.

changes are chain cleavage for the polymer and cross-linking for the plasticizer. This explanation fits the behavior of a previously tested polyvinyl chloride formulation that contains less plasticizer and that was observed to soften for short irradiation periods but to harden for long irradiation periods.[6]

[6] C. D. Bopp and O. Sisman, *Radiation Stability of Plastics and Elastomers*, ORNL-1373, p 45 (July 23, 1953).

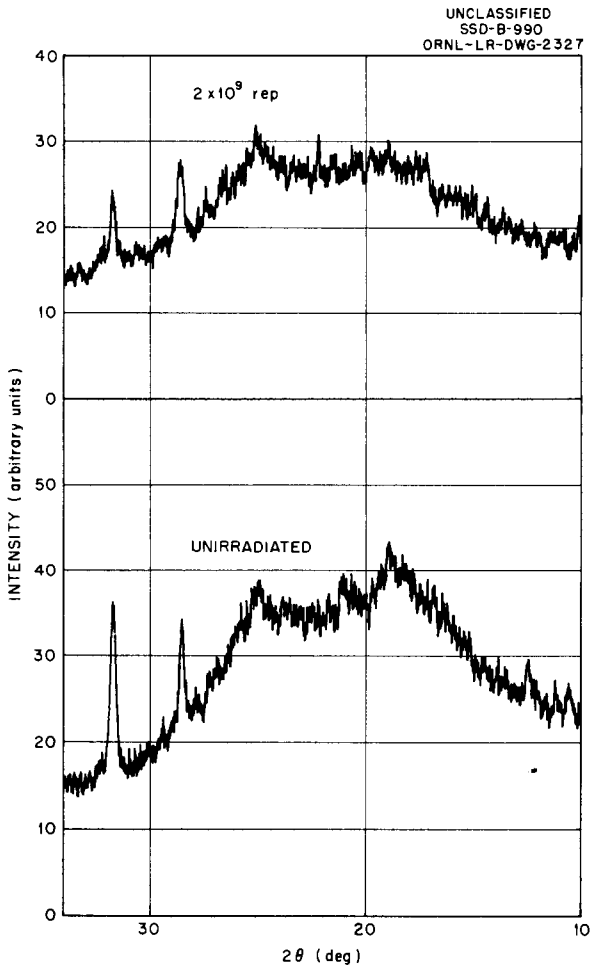

Fig. 88. X-Ray Diffraction Patterns of Unstretched Rubber.

TABLE 13. DYNAMIC PROPERTIES OF IRRADIATED POLYVINYL CHLORIDE*

Formulation (See Table 14)	Irradiation Exposure (10^{18} neutrons/cm^2)**	Dynamic Young's Modulus (10^9 dynes/cm^2)	E_2/E_1, Ratio of Viscous Modulus to Yaung's Modulus
8700 (rigid)	0	30	0.025
	0.6	30	0.025
8750 (rigid)	0	42	0.025
	0.6	40	0.025
400 × 75 (rigid)	0	38	0.025
	0.6	36	0.025
80770 (25 parts dioctyl phthalate)	0	6	0.30
	0.6	5	
	3.6	15	0.07
2042 (52 parts dioctyl phthalate)	0	1.3	0.7
	0.6	4	0.6
	3.6	14	0.09

*Measured at 25°C in the frequency range 10^2 to 10^3 cps.

**An integrated flux of 10^{18} neutrons/cm^2 is, for polyvinyl chloride, approximately equivalent to from 2×10^9 to 5×10^9 rep.

CALCULATION OF THE DYNAMIC YOUNG'S MODULUS AND THE VISCOUS MODULUS FROM THE RESONANCE CURVES

C. D. Bopp

Determination of the dynamic Young's modulus and the viscous modulus from resonance curves has already been discussed;[3,7] however, in determining the moduli for polyvinyl chloride a new complication was encountered. The Young's modulus and the viscous modulus depend upon the frequency which gives maximum amplitude of vibration and on the band width of the resonance curve. For most materials previously studied, the resonance curves are sufficiently sharp that the equations[7] previously used are good approximations; however, they are not applicable for plasticized polyvinyl chloride, which gives very flat resonance curves.

Figures 89 and 90 show that the present method, developed below, agrees well with the previous method until the modulus ratio (E_2/E_1) approaches about 0.3. The dotted lines were calculated from the previous method; the points for the solid lines were calculated by the present method.

[7]C. D. Bopp, R. L. Towns, O. Sisman, and W. K. Kirkland, *Solid State Semiann. Prog. Rep. Feb. 28, 1954*, ORNL-1677, p 55.

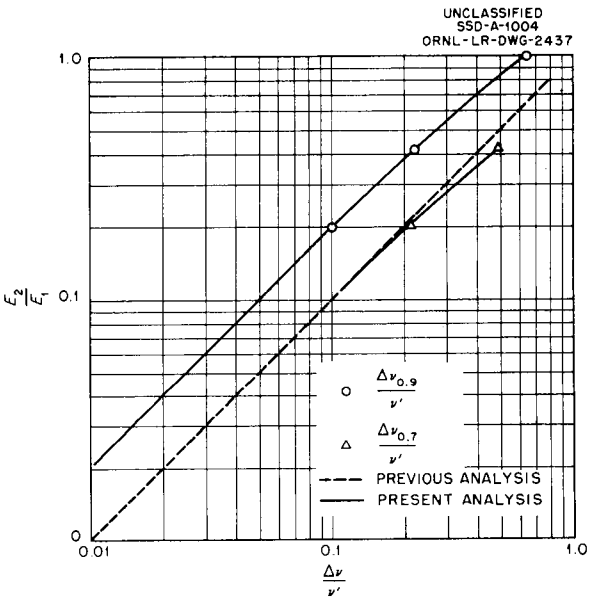

Fig. 89. Relation of Modulus Ratio to Band Width.

Figures 89 and 90 relate the dynamic Young's modulus E_1 and the viscous modulus E_2 to two parameters of the frequency-amplitude curve (Fig. 91): the frequency which gives maximum amplitude,

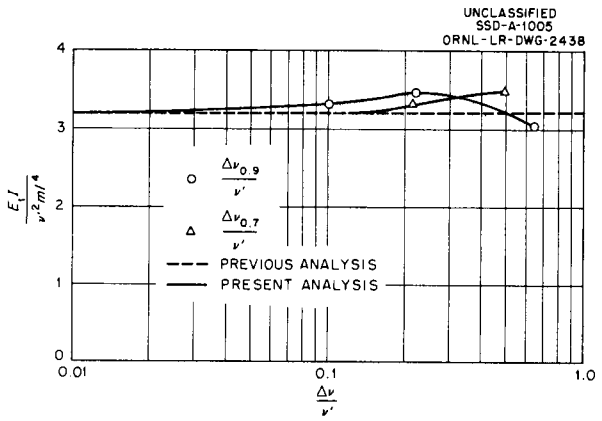

Fig. 90. Relation of Dynamic Young's Modulus to Band Width.

TABLE 14. GEON (POLYVINYL CHLORIDE) FORMULATIONS*

Components	Parts by Weight
Rigid Geon Compounds	
8700 Gray	
Geon 404HI**	100
Stabilizer RS 31 (tin)	2
TiO_2	3
Atomite ($CaCO_3$)	17
Calcium stearate	2
Malacco black chip	1
	125
8750 White	
Geon 103EP**	100
Stabilizer RS 31 (tin)	2
TiO_2	10
Calcium stearate	2
Carlisle wax	2
Violet master batch	0.4
	116.4
Geon 400 × 75 Rigid (516-7-50-3)	
Geon 400 × 75 (A 562)	100.0
Ferro 120 (barium ricinoleate)	1.5
DS 207 (dibasic lead stearate)	0.5
Carnauba wax	0.5
	102.5

TABLE 14 (continued)

Components	Parts by Weight
Flexible (Plasticized) Geon Compounds	
Geon 2042 (516-7-50-1)	
Geon 101	100
Dioctyl phthalate	52
BLC	10
Clay	7
Litene wax	0.5
	169.5
Geon 80770 (516-7-50-2)	
Geon 103EP**	100
Dioctyl phthalate	25
Paraplex G-60	6
1-V-4 (barium organic stabilizer)	2
2-V-4 (cadmium organic stabilizer)	4
Ferro 900 (epoxy stabilizer)	2
Barium stearate	1
8440 violet master batch	0.4
	140.4

*Plastics furnished by the B. F. Goodrich Research Center.

**Geon 404HI, Geon 103EP, etc. indicate different commercial polymers, some of which may be copolymers.

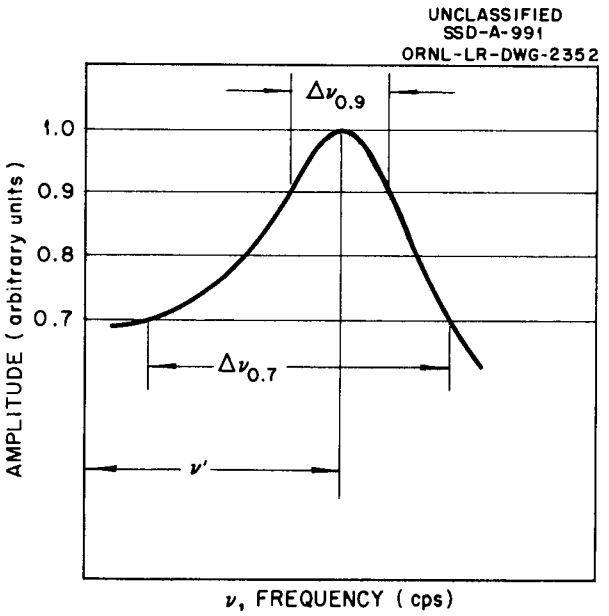

Fig. 91. Broad Resonance Curve.

ν' in cycles per second, and the band width or breadth of the resonance curve, $\Delta\nu$ in cycles per second. The band width determines both the ratio E_2/E_1 (Fig. 89) and a dimensionless group (Fig. 90) which includes ν', E_1, the moment of inertia I, and the weight per unit length m. Band width is usually taken at 0.7 of maximum amplitude $\Delta\nu_{0.7}$, but for very broad curves it is advantageous to use the band width at 0.9 of maximum amplitude $\Delta\nu_{0.9}$.

The test specimen is a clamped-free bar (Fig. 92, method A) which is vibrated transversely by shaking the clamped end with a driver; the same frequency-amplitude relation as for method A is measured if the bar is shaken, as in method B, by a driver near the clamped end, although the clamped end itself is stationary. With the latter method, less interference is found from the resonant frequencies of the driver.

The equation for free vibration with internal friction neglected, is

$$E_1 I \frac{\partial^4 y}{\partial x^4} + m \frac{\partial^2 y}{\partial t^2} = 0 \quad , \tag{1}$$

where

x = the axis taken coincident with the longitudinal axis of the bar,

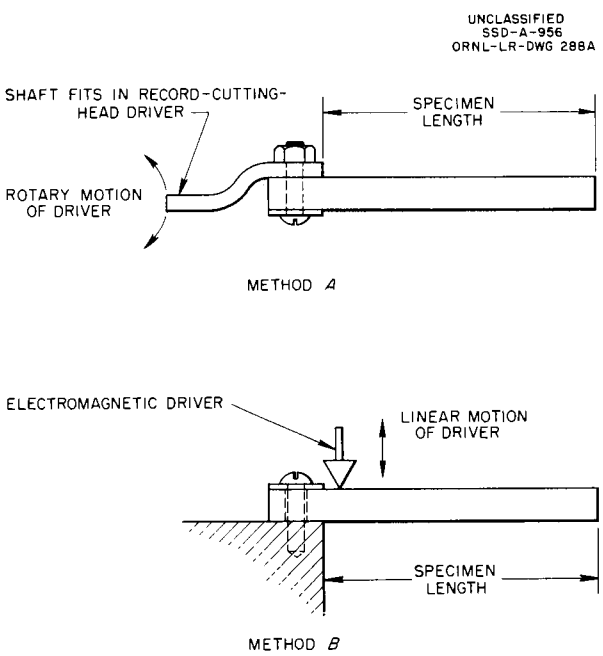

Fig. 92. Vibrating Apparatus.

y = the value of the displacement at a distance x from the clamped end,

E_1 = the dynamic Young's modulus,

I = the moment of inertia of the cross-sectional area ($I = ba^3/\sqrt{12}$ for width b and thickness a),

t = the time,

m = the mass per unit length.

The equation for forced vibration is obtained by use of the transformation

$$y = Re(Y_0 + Y)\, e^{i\omega t} \quad , \tag{2}$$

where

Y_0 = the maximum value of the sinusoidal displacement at the point of attachment of the driver,

Y = the parameter defined by Eq. 2,

ω = the frequency in radians/sec,

and Re signifies that only the real part is retained. Substituting Eq. 2 into Eq. 1 gives

$$\frac{\partial^4 Y}{\partial x^4} - a^4 Y = a^4 Y_0 \quad , \tag{3}$$

where $a^4 = m\omega^2/(E_1 I)$.

The solution of Eq. 3 for the boundary conditions of method A, Fig. 92, gives for the free end of the bar

$$\frac{y}{Y_0} = Re[1 + f(al)]\, e^{i\omega t} \quad , \tag{4}$$

where

$f(al)$ = $(\cos al + \cosh al)/(1 + \cos al \cosh al)$,

l = the specimen length.

Equation 4 is suitable for the case of a constant-driving displacement which is independent of frequency. For constant-force driving in which the driver has large mass and small stiffness,

$$Y_0 = \frac{F_0}{\omega^2} \quad , \tag{5}$$

where F_0 is a constant which is independent of frequency.

Substituting Eq. 5 into Eq. 4 gives for "constant-force driving"

$$\frac{y}{F_0} = Re\, \frac{1}{\omega^2} [1 + f(al)]\, e^{i\omega t} \quad . \tag{6}$$

From the theory of thermal currents[8] the equation of free vibration, including the effect of internal friction, is

$$E_1 I \frac{\partial^4 y}{\partial x^4} + C \frac{\partial^5 y}{\partial x^4 \partial t} + m \frac{\partial^2 y}{\partial t^2} = 0 \quad , \tag{7}$$

where C is a complex number. Since it is inversely proportional to frequency for thermal insulators,[9] C may be written as

$$C = -\frac{E_2 I}{\omega} \quad . \tag{8}$$

Combining Eqs. 7 and 8 and introducing the abbreviation

$$E^* = E_1 - iE_2 \tag{9}$$

yield an equation identical with Eq. 1 except for E_1 being replaced by E^*. Again the solution is given by Eq. 6 except that a is now a complex number which is defined in terms of E_2 and E_1 by

$$a = \frac{m\omega^2}{E^* I} \quad , \tag{10}$$

where E^* is defined by Eq. 9.

It is believed that Eq. 4, in which a is complex, is an adequate approximation for the experimental conditions described.[10] Resonance curves were prepared by plotting the modulus of $1 + f(al)$ (which, by Eq. 4, is approximately proportional to amplitude) vs the square of the real part of al (which is proportional to frequency). The band width and frequency parameters, ν' and $\Delta\nu$, were measured for these curves and are plotted in Figs. 89 and 90.

[8] M. Pasler, *Z. Physik* 122, 357 (1944).

[9] C. Zener, *Proc. Phys. Soc. (London)* 52, 152 (1940).

[10] C. D. Bopp, O. Sisman, W. K. Kirkland, and R. L. Towns, *Solid State Semiann. Prog. Rep. Aug. 31, 1953*, ORNL-1606, p 88.

CRYSTAL PHYSICS

WORK-HARDENING IN COPPER CRYSTALS

T. H. Blewitt R. R. Coltman
J. K. Redman

The mechanism by which metals harden during plastic deformation has been of interest to the solid-state physicist for many years. Taylor[1] introduced the concept of the dislocation and developed a detailed theory of work-hardening based on the interaction of these imperfections. While it has been clear for some time that many of the details of Taylor's theory required modification, many scientists continued to accept the general concept that work-hardening arises from the interaction of dislocations.

The advent of the Frank-Read[2] mechanism for the generation of dislocations removed one of the troublesome details of the Taylor theory and stimulated considerable theoretical research pertaining to plastic deformation. At present the best theoretical approach to the theory of work-hardening seems to be the Frank-Read source. Several new ideas concerning work-hardening have developed from this approach. Mott[3] has developed a detailed theory of work-hardening very similar to that of the original Taylor theory. In place of individual dislocations, however, Mott has postulated a lattice of super dislocations consisting of individual dislocations generated by a Frank-Read source. According to this scheme a sessile dislocation acts as a barrier to the motion of dislocations, and a back stress set up by dislocations piled up at the barrier would stop generation by the Frank-Read source. Van Bueren[4] has postulated another scheme by which the dislocation becomes blocked: the energy dissipated by the creation of vacant lattice sites locks the dislocation loop.

Koehler,[5] on the other hand, has suggested that hardening, at least in the initial stages of plastic deformation, results from an exhaustion of Frank-Read sources. Since the stress to operate a source varies inversely with its length, this scheme assumes that the longest sources become expended as a result of vacancy-locking and that the hardening occurs as the shorter sources become operative.

The success of these theoretical treatments, which have ignored the effects of thermal energy, has been judged primarily by their ability to fit experimental stress-strain curves. Unfortunately, experimental data at low temperatures, particularly in the case of face-centered-cubic (fcc) metals, were not available, and it was necessary to compare the theoretical treatments with data obtained at relatively high temperatures. It has thus been assumed that the parabolic stress-strain relationship obtained at high temperatures was fundamental for fcc metals. Recent experiments[6] have indicated, however, that at low temperatures the stress-strain relationship in copper single crystals is a linear one. It is clear from this work that the effect of temperature on the work-hardening of fcc metals is much different from that customarily assumed. It was the aim, then, of this experimental work to remedy, as much as possible, the deficiency of experimental data on the low-temperature deformation of single crystals.

The investigation can be divided into three categories: (1) the study of the effect of the temperature of deformation on the residual resistivity in the hope that information on the hardening process could be obtained; (2) the investigation of the effect of temperature on the appearance of slip lines, which was motivated by a suggestion from Mott[3] that a linear stress-strain curve should result when macroscopic slip lines are absent; (3) the desire to obtain further information on low-temperature deformation by an apparent, mechanical twinning mechanism.

The general experimental methods relating to the sample preparation, the tensile elongation, the measurement and computation of the stress-strain curves, and the measurement of the electrical resistivity have been previously described.[6] It may be pertinent, however, to note that the residual electrical resistivity of all samples, regardless of the temperature of deformation, was determined by the measurement of the resistance at 4.2°K. Consideration of the magnitude of the change in resistivity resulting from plastic deformation re-

[1] G. I. Taylor, *Proc. Roy. Soc. (London)* A145, 362 (1934).

[2] F. C. Frank and T. Read, Pittsburgh Symposium on Plastic Deformation of Crystalline Solids, May 1950, U.S. Office of Naval Research Report NAVEXOS-P-834, p 44 (unpublished).

[3] N. F. Mott, *Phil. Mag.* 43, 1151 (1952).

[4] H. G. van Bueren, *Acta Metallurgica* 1, 464 (1953).

[5] J. S. Koehler, *Phys. Rev.* 86, 52 (1952).

[6] T. H. Blewitt, *Phys. Rev.* 91, 1115 (1953).

quires the determination of this property at a low temperature.

The change in electrical properties produced by plastic deformation is characterized by a change in the residual resistivity, with virtually no change in the phonon scattering. Normally, the residual-resistivity change arising from defects introduced as a result of severe tensile deformation does not exceed 5×10^{-8} ohm-cm. The thermal scattering is of the order of 2×10^{-6} ohm-cm at 300°K, 2×10^{-7} ohm-cm at 78°K, and less than 1×10^{-10} ohm-cm at 4.2°K. Measurements of the resistivity at temperatures above 20°K thus require an accurate determination of the geometrical factors changed by the deformation, as well as an accurate determination of the temperature if the change in residual resistivity is not to be obscured by the thermal scattering. Considerable advantage thus arises in measuring the resistivity at 4.2°K.

The primary purpose in studying the appearance of slip lines was to determine whether these markings could be detected when a linear stress-strain curve resulted. The appearance of strain markings as a function of deformation at both room temperature and at liquid-helium temperature was measured. The following technique was used.

The samples were prepared in the manner previously indicated,[6] with, however, a square rather than a circular cross section. The samples were polished electrolytically at −50°C with an electrolyte made from 1 part methyl alcohol and 3 parts concentrated HNO_3. They were then deformed to a shear strain of about 0.05, and the surface was examined. After the examination of the slip lines, the samples were deformed to an additional shear strain of 0.20 and were then electrolytically polished. Following an examination of the surface to ensure that all false markings had been eliminated, the samples were again elongated by a shear strain of 0.05 and the markings examined. This procedure, which was repeated until fracture occurred, enabled the study of slip lines as they were introduced by the deformation.

It was discovered that no lines could be observed by the above technique when the usual bright-field illumination was used in the microscopy. Slip lines did become immediately visible when the technique of dark-field illumination was used. This technique consists in introducing the illuminating beam parallel to the surface to be examined. Projections from a flat surface then reflect the illumination into the microscope. When this technique is used, slip lines should appear as light lines in a dark field.

Earlier results[6] show that plastic deformation of single crystals produces a defect which is highly mobile at 300°K. It was found that these mobile defects, presumably vacant lattice sites, play only a secondary role in the mechanism of work-hardening. The hardening is apparently the result of another defect, probably the dislocation. It would be expected, upon consideration of the temperature at which recovery occurs, that the defects responsible for the hardening of copper would have negligible mobility at temperatures below 500°K. It is assumed that the change in resistivity associated with the deformation of samples at a low temperature (less than 78°K) is the result of both the mobile defects, which will be arbitrarily denoted as vacancies, and the immobile defects, which will be arbitrarily denoted as dislocations. It is also assumed that after an anneal at 300°K the vacancies will not contribute to the resistivity and that the change in resistivity will depend only on the dislocations created during the deformation.

Experiments were first made on specimens deformed at 4.2°K. The measurement of the resistance was made without the crystal being removed from the liquid-helium bath. The geometrical factor, area/length, was computed from the elongation of the specimen on the assumption that the density did not change. It was previously found that the rate of work-hardening was dependent on the crystal orientation; consequently, crystals of widely variant orientations were chosen as specimens. The orientations of the samples are shown by the sterographic net of Fig. 93, and the stress-strain curves are shown in Fig. 94. It is interesting to note that the data from these two figures verify the observation[6] that a linear stress-strain relationship exists at 4.2°K except near the origin. Further, the slope of the line is dependent on the initial crystal orientation; the rate of work-hardening was found to increase as the specimen axis approached the dodecahedral plane. In Fig. 95 the change in electrical resistivity is plotted as a function of the shear strain. The resistivity-strain relationship reflects the orientation dependence. In Fig. 96 a certain amount of dispersion between samples is observed, but it appears that the change in resistivity is fundamentally associated with the shear stress. There appears to be a parabolic

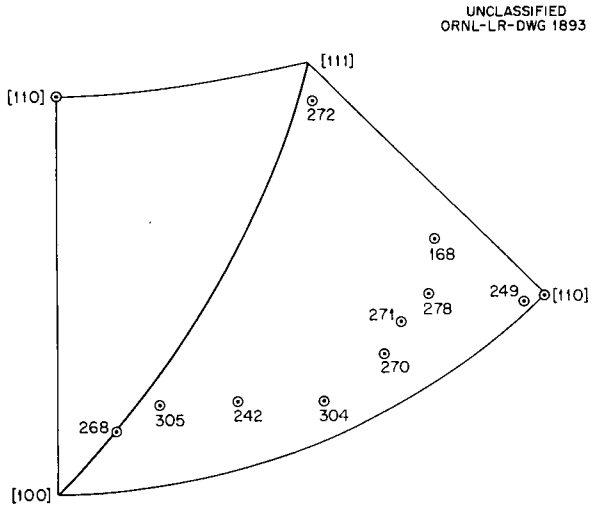

Fig. 93. Stereographic Net Showing the Orientations of the Copper Crystals.

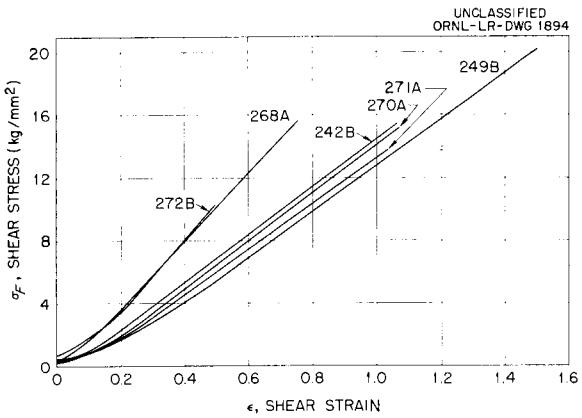

Fig. 94. Stress-Strain Curves of Copper Crystals Deformed at 4.2°K.

relationship between the resistivity change and the shear stress. For comparison purposes the parabola $\rho_{(D+V)} = 1.3 \times 10^{-10}\,\sigma_F^2$ is plotted in Fig. 96.

In order to establish the temperature at which the vacancies move, sample 270A was annealed at 78°K and then at 300°K. Only a very small fraction of the resistance, which probably does not lie outside experimental error, was recoverable after 16 hr at 78°K. On the other hand, it appears that a 16-hr anneal at 300°K is sufficient for recovery of the majority of the resistance associated with

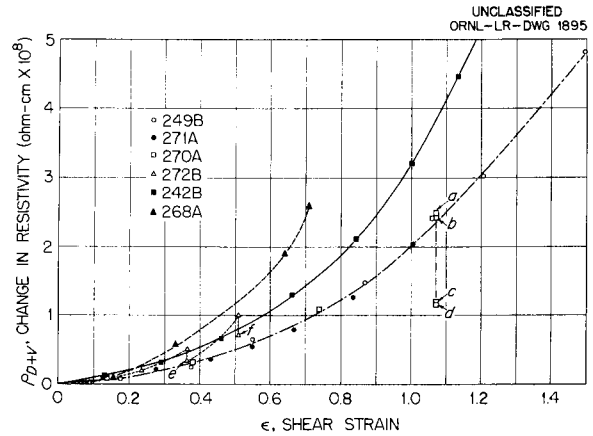

Fig. 95. Change in Residual Resistivity $\rho_{(D+V)}$ of Crystals Deformed at 4.2°K as a Function of Shear Strain. The initial residual resistivity ranges from 1.1×10^{-9} ohm-cm (272B) to 2.6×10^{-9} ohm-cm (249B). The letters denote the resistivity after annealing: (*a*) 270A, unannealed; (*b*) 270A, 16 hr at 78°K; (*c*) 270A, 16 hr at 300°K; (*d*) 270A, 40 hr at 300°K; (*e*) 272B, 1 hr at 300°K; (*f*) 272B, 1 hr at 300°K. Samples 268A and 272B were slipping by duplex slip throughout the stress-strain curve, whereas sample 249B was slipping by single slip.

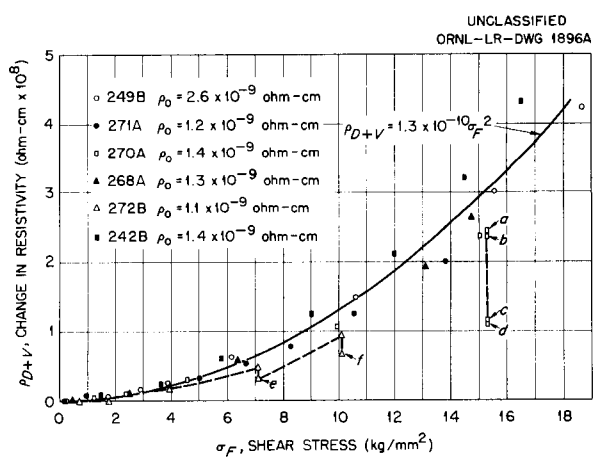

Fig. 96. Change in Residual Resistivity of Crystals Deformed at 4.2°K as a Function of the Shear Stress. The letters have the same meaning as in Fig. 95.

the vacancies. It was later established that essentially no further resistance change could be observed at 300°K after the first hour. It is interesting to note from the data in Fig. 96 that the change in resistance is about equally divided between scattering caused by vacancies and that caused by dislocations.

It is clear that the resistivity change associated with dislocations is of fundamental interest to the theory of work-hardening. Measurements of resistance at 4.2°K were therefore made on crystals of the same orientation which had been deformed at 78, 200, and 300°K and annealed to remove the scattering from vacancies. The results of this investigation are shown in Fig. 97, where the change in resistivity is plotted as a function of the shear stress. Groups of crystals of two different orientations were used. With the exception of samples 304E and 305C, which were deformed at 4.2°K and measured before the sample was allowed to warm up, each point was determined by measuring the resistance after the sample had received a 1-hr anneal at 300°K. The changes in resistance, then, of crystals 304A, B, C, D and crystals 305A, D, E result from the scattering of immobile defects or, for the purpose of this discussion, from the dislocations introduced during the deformation.

Consider the implication of these data along with the stress-strain curves of Figs. 98 and 99. It should be noted that the relationship between the shear stress and the change in resistivity attributed to dislocation scattering seems to be independent of the temperature of deformation. This relationship is given by

$$\rho_D = 9 \times 10^{-11} \sigma_F^2 \text{ ohm-cm} ,$$

where

ρ_D = change in resistivity attributed to dislocations,

σ_F = shear stress in kg/mm^2.

From the fact that the stress-strain curve is temperature dependent, it is clear that the deduction previously made (that the resistivity arising from the cold-work-induced defects is fundamental to the shear stress) is verified by the data of Figs. 97, 98, and 99.

The value of the initial residual resistivity (ρ_0) was measured in a large number of crystals; a wide

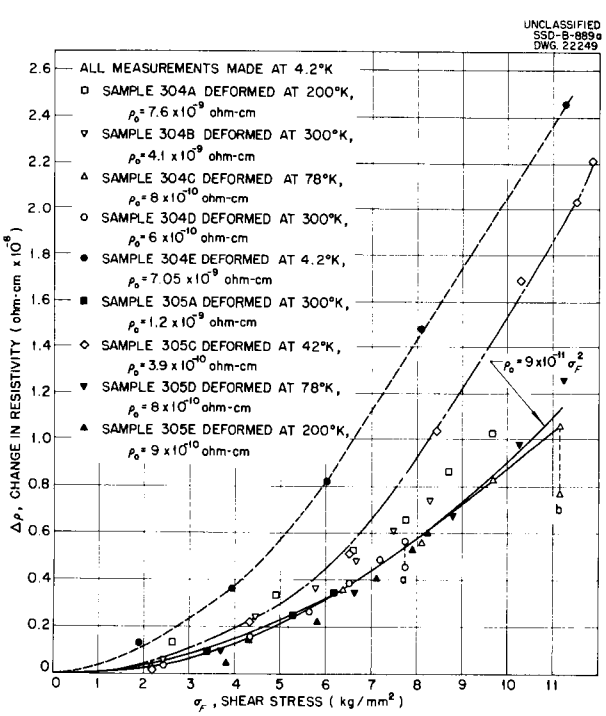

Fig. 97. Change in Residual Resistivity in Samples Deformed at Various Temperatures.

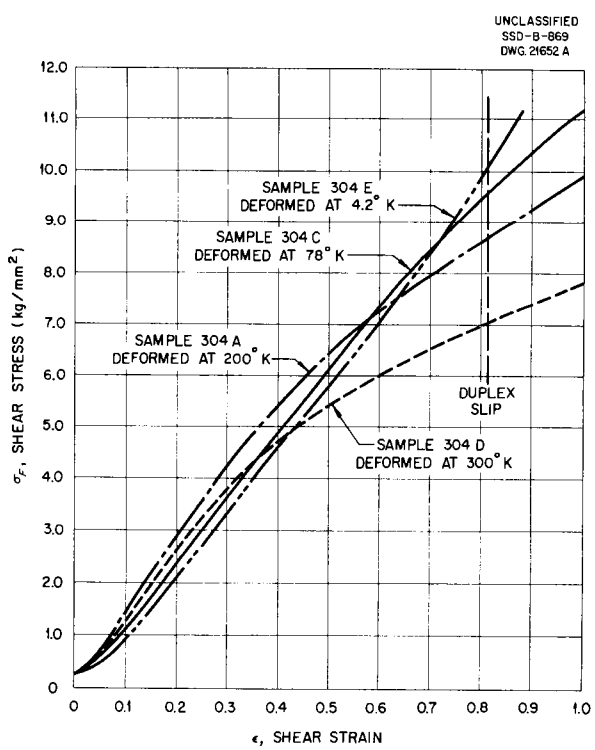

Fig. 98. Stress-Strain Curves of the 304 Samples.

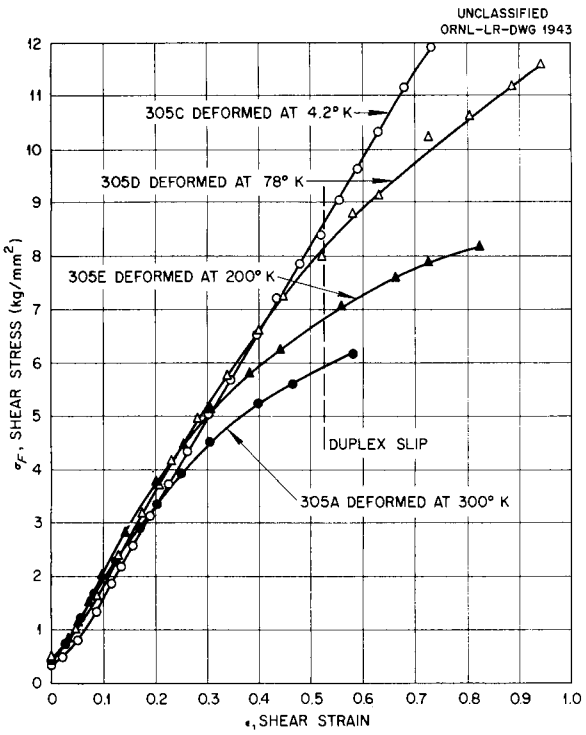

Fig. 99. Stress-Strain Curves of the 305 Samples.

variation in ρ_0 was observed. The value of ρ_0 in annealed single crystals was found to vary from 3×10^{-10} to 2×10^{-8} ohm-cm. The crystals of the 305 series are indicative of this variation. It is not clear whether the defects responsible for this variation are chemical or structural defects, although there are some indications that they may be of the latter type. From a consideration of the data of Figs. 98 and 99 it would appear that these defects only slightly affect the mechanical properties. More defects, however, seem to result from the deformation of the samples with high initial residual resistivity than from the deformation of samples with low initial residual resistivity.

The annealing kinetics of plastically deformed samples appear to depend on the initial residual resistivity. Those samples which have a high initial resistance recover their conductivity, whereas samples with low initial resistivity show only slight recovery after anneal. The results obtained when samples of different initial resistivity are annealed following plastic deformation are given in Table 15.

The crystal growth rate was varied to determine the role of mosaic boundaries on the initial residual resistivity. Crystals grown at a lowering rate of

TABLE 15. EFFECT OF ANNEALING ON THE RESIDUAL RESISTIVITY OF WORKED COPPER CRYSTALS

Sample No.	Resistivity			Amount of Deformation Shear Stress (kg/mm^2)
	Initial (ohm-cm $\times 10^8$)	After Deformation (ohm-cm $\times 10^8$)	After Anneal at 1000°C for 3 hr (ohm-cm $\times 10^8$)	
304A	0.76	1.79	0.95	9.6
304B	0.41	1.147		8.3
304C	0.080	1.14	0.830	11.2
304D	0.06	0.63	0.52	7.7
304E	0.705	3.166		11.2
305A	0.12	0.472		6.2
305C	0.039	2.291		11.9
305D	0.080	1.308	0.908	11.2
305E	0.090	0.720	0.636	7.9
326A	0.501	0.729	0.517	5.3
326C	0.393	0.660	0.331	5.3
326F	0.323	0.593	0.280	5.3

9 in./hr were found to have a highly developed substructure in comparison with samples grown at a lowering rate of $1\frac{1}{2}$ in./hr. The Laue back-reflection photograph of sample 342A which was grown at the more rapid rate is shown in Fig. 100 for comparison with a photograph of sample 343A which was grown at the slower rate. These boundaries contribute a resistivity of less than 2×10^{-9} ohm-cm, since there is no apparent difference in the resistivity of the two samples. The results of the resistance measurements are shown in Table 16. There is a correlation between the initial residual resistivity and the temperature of the molten copper prior to the crystal growth. The resistivity of specimens grown from a melt which reached 1500°C is consistently lower than that of samples grown from a melt whose temperature did not exceed 1200°C.

TABLE 16. INITIAL RESIDUAL RESISTIVITY OF COPPER CRYSTALS 342 AND 343

Sample No.	Resistivity (ohm-cm $\times 10^8$)
342A	0.514
342B	0.492
342C	0.389
342D	0.396
342E	0.351
343A	0.588
343B	0.594
343C	0.575
343D	0.528

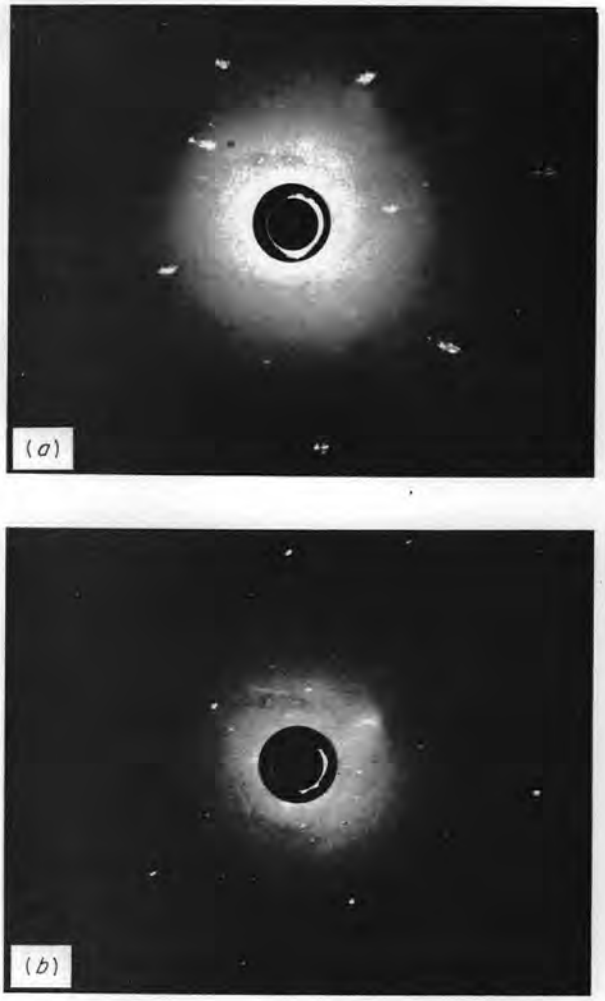

Fig. 100. Laue Back-Reflection Photograms. (*a*) Sample 342A grown at 9 in./hr; (*b*) sample 343A grown at $1\frac{1}{2}$ in./hr.

In the present investigation the slip lines on four copper crystals were studied. Three of them were deformed at 300°K and the fourth at 4.2°K. All showed consistently that the length of the slip lines (the direction perpendicular to the slip direction and lying in the slip plane) decreases as a function of the shear strain. The appearance of the slip lines as a function of the shear strain is shown in Figs. 101 through 104. The accompanying stress-strain curve is shown in Fig. 105. It was discovered that for large strains at room temperature the lines decreased in length as a result of fragmentation. On the other hand, the lines observed in sample 278A, which was deformed at 4.2°K, did not show this apparent fragmentation. The fragments formed at 300°K appeared to be as long as the individual lines formed at 4.2°K. Figure 106 shows the typical fragmentation observed for high strains at 300°K in sample 278B, while Fig. 107 shows the absence of such fragmentation in sample 278A. The dependence on the length of the slip lines (at high strains each fragment is considered to be an individual line) as a function of the strain is shown in Fig. 108. It should be noted that there is considerable variation in the observed length of the slip lines. The lengths should be considered as an average value, with the longest line being about twice the length

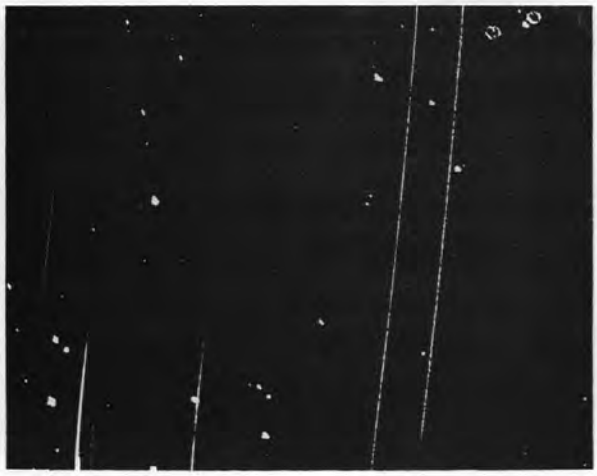

Fig. 101. Slip Lines in Copper Crystal 168B. Total shear strain, 0.046; strain increment visible, 0.046. 1000X. Reduced 38%.

Fig. 102. Slip Lines in Copper Crystal 168B. Total shear strain, 0.388; strain increment visible, 0.049. 1000X. Reduced 38%.

Fig. 103. Slip Lines in Copper Crystal 168B. Total shear strain, 0.884; increment of strain visible, 0.065. 1000X. Reduced 38%.

Fig. 104. Slip Lines in Copper Crystal 168B. Total shear strain, 1.14; increment of strain visible, 0.060. 500X. Reduced 36%.

of the shortest line. It should be noted that no evidence for cross slip was observed in any of the four samples considered. Furthermore, there was no evidence for fine slip in the linear stress-strain regions.

It has previously been reported[7] in the case of high-purity copper single crystals that the mode of deformation changes after large strains at 4.2°K. It has been suggested that this new mechanism may be deformation by a twinning process. Direct evidence for the formation of twins as given by diffraction experiments is quite difficult to obtain, since the previous deformation by slipping has distorted the lattice to such an extent that Laue photographs cannot be utilized. Direct evidence has been obtained by M. C. Wittels and F. A. Sherrill that two orientations were present in a crystal deformed to brittle fracture at 4.2°K. The two orientations were detected by a rocking-curve

[7] T. H. Blewitt, *Phys. Rev.* 91, 1115 (1953).

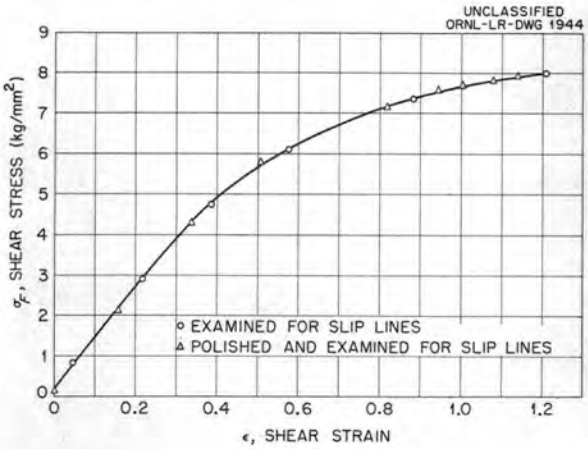

Fig. 105. Stress-Strain Curve of Crystal 168B. Temperature of deformation, 300°K.

Fig. 106. Slip Lines in Copper Crystal 278B Deformed at 300°K. Total shear strain, 0.709; increment of strain visible, 0.026. 1000X. Reduced 36%.

Fig. 107. Slip Lines in Copper Crystal 278A Deformed at 4.2°K. Total shear strain, 0.604; increment of strain visible, 0.010. 1000X. Reduced 38%.

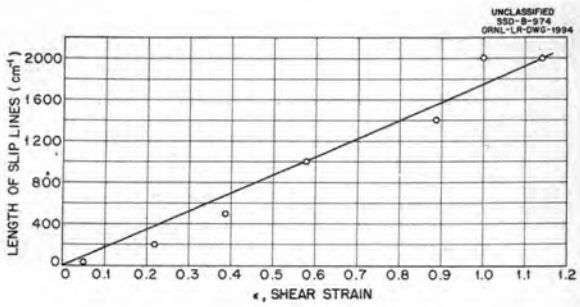

Fig. 108. Change in Length of Slip Lines as a Function of the Shear Strain.

technique which permits the observation and measurement of very weak reflections. A description of this rocking-curve apparatus will be published in the near future.

The deformation of copper crystals at 4.2°K proceeds by the normal slip process until the flow stress exceeds a value of 12 kg/mm^2. The load-elongation curve is relatively smooth; there were no discontinuities even when an expanded scale was used on the tensile machine. At a flow stress ranging from 12 to 16 kg/mm^2, depending on the orientation, the load-elongation curve begins to show pronounced discontinuities. A typical curve illustrating the onset of these discontinuities is given in Fig. 109. Associated with each discontinuity is an audible click; the intensity of the noise is proportional to the magnitude of the discontinuity. As the deformation continues, it becomes apparent that both the slip process and the additional mechanism responsible for the discontinuities are occurring simultaneously. This latter process of deformation will be termed "apparent twinning." As the process continues, the apparent twinning becomes more predominant and finally is the principal mechanism of deformation. The load-elongation curve for the region where deformation proceeds principally by twinning is illustrated in Fig. 110. It should be noted that there is no appreciable work-hardening as the load

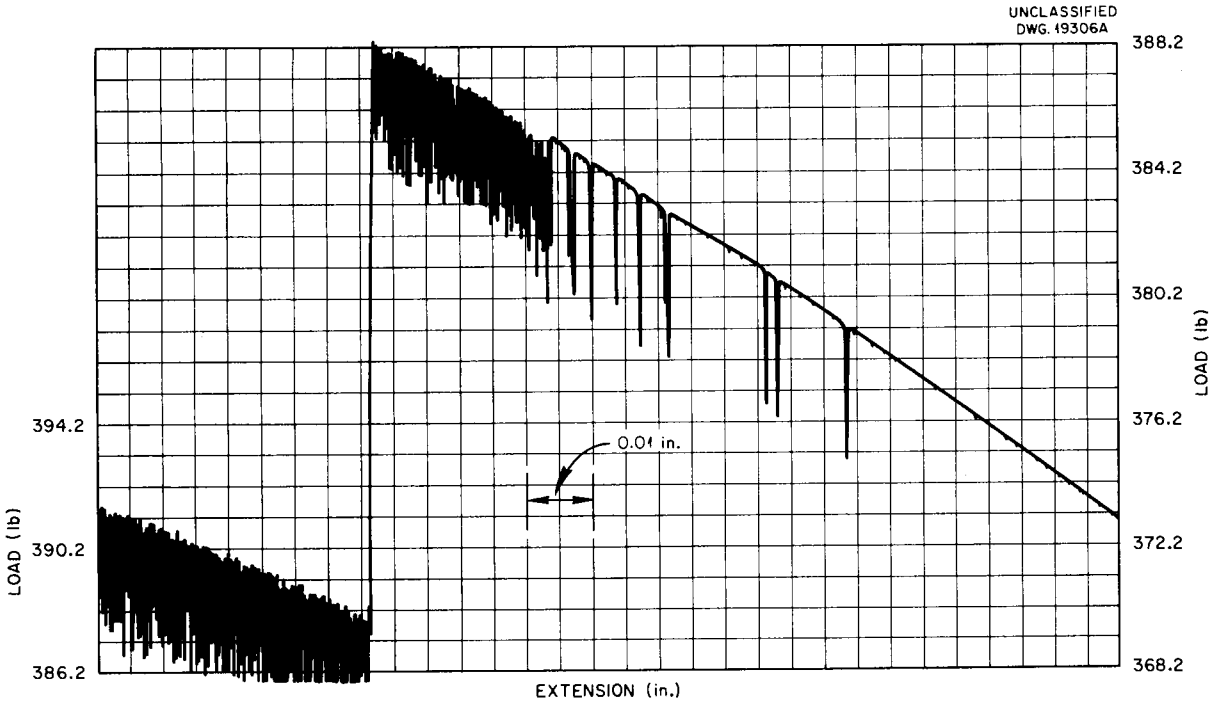

Fig. 109. Onset of "Apparent Twinning" in Copper Crystal 263B. Deformation temperature, 4.2°K; since the sample is still work-hardening, slip continues in addition to the twinning.

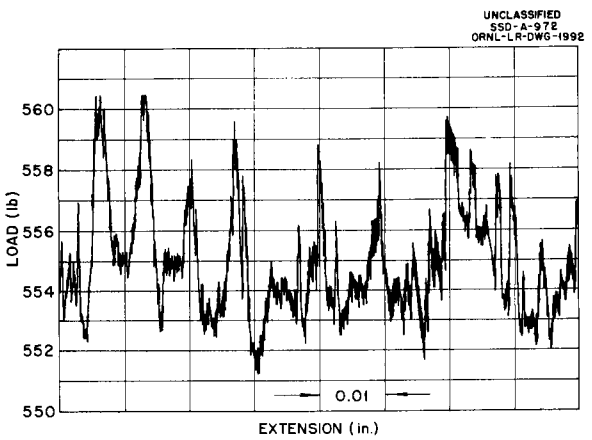

Fig. 110. Deformation by "Apparent Twinning" in Copper Crystal 240A. Deformation temperature, 4.2°K.

rises and falls with elongation. The sample finally fractures with an abrupt release of the load in a manner which is characteristic of brittle failure. Figure 111 shows the load-elongation curve at the fracture point. This behavior has been consistently observed in many samples.

The strain markings associated with the phenomenon of apparent twinning are shown in Fig. 112. This photomicrograph was made from sample 278A, which had a square cross section. It is apparent that the markings shown are of a very different nature from the slip lines. These strain markings seem to persist well into the interior of the crystals; they cannot be obliterated by removal of a surface layer. This is in sharp contrast to slip lines, which may be removed by a brief electropolish. The photomicrograph of Fig. 112 was made after an extensive electropolish of the surface. The angles between the edges of the crystal and the apparent twins, as well as the angle between the surfaces, were measured. From these data and the orientation of the crystals it was determined that, within experimental error, the markings from the apparent twins coincided with [111] planes. The measurements were difficult to make, and the error in the angle between the twin plane and the specimen axis may be as high as 5 deg. The onset of the apparent twinning appears to be dependent on the loading rate. When the cross-head speed is decreased, the deformation proceeds with a higher percentage of slip.

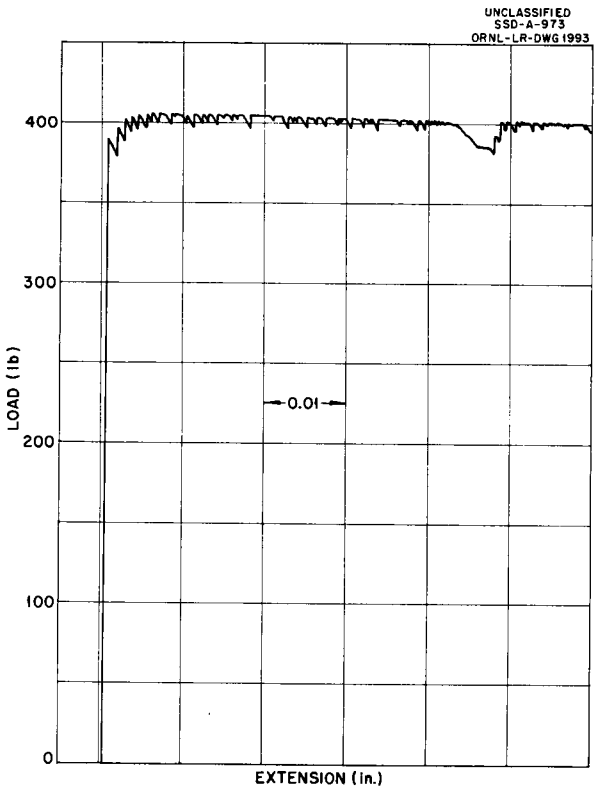

Fig. 111. Brittle Fracture in Copper Crystal 240A. Deformation temperature, 4.2°K.

Apparent twinning is also observed at 78°K in a sample whose orientation is such that it work-hardens very rapidly. This phenomenon has also been observed by Jamison and Blewitt[8] on neutron-irradiated copper crystals deformed at 78°K. The mechanical behavior of the irradiated copper is similar to that of α-brass.

It is well known that the residual resistivity results from scattering by either structural or chemical defects. It is, of course, impossible to show unequivocally that the residual resistivity results from the presence of one particular defect. The data obtained in the study of the changes in residual resistivity seem to indicate that the deformation of single crystals by slip results in the formation of at least two types of defects. One type is highly mobile at temperatures below 300°K, and these defects are termed "vacancies," more from the standpoint of convenience than from experimental evidence. Of course, from theoretical considerations[9] vacancies would be expected to form during plastic deformation, but the experimental evidence that the change in resistivity results from vacancies is very meager at this time. It is assumed that the more immobile defects (the other type) that result in the resistivity which is not recoverable at 300°K are dislocations. It is further assumed that these defects are primarily responsible for the work-hardening. This assumption is based on the observation that the mobile defects[7] have little influence on the work-hardening. Although it would appear that a portion of these immobile defects are certainly dislocations, there is no direct evidence that only those defects which contribute to the work-hardening are measured. Despite this objection it appears at the present time that these assumptions are reasonable.

For an interpretation of the data, a model of plastic flow similar to that suggested by Mott[10] but in slightly modified form will be assumed. At 0°K it can be considered that there are N_0 Frank-Read generators per cubic centimeter present in the annealed single crystal. Under the action of an applied shear stress σ_F, a number $N(\sigma_F)$ of these generators will become active and generate dislocation loops. It can be assumed that these loops will move a distance $R(\sigma_F)$ and become blocked by a barrier of some sort. The blocking will result in a pileup of $n(\sigma_F)$ dislocation loops which will set up a stress field locking the Frank-Read generator. The modification of Mott's theory introduced here is that the distance of movement, $R(\sigma_F)$, of the dislocation and the number of loops generated before locking, $n(\sigma_F)$, are, in general, allowed to be dependent on the internal state of the crystal at the particular stage of the deformation process. A simplifying assumption that the loops are circular will be made. This latter assumption may introduce some error, since the type of barrier will influence to some extent the geometry of the loops. In accordance with this model for plastic deformation it is necessary to determine experimentally the number and distribution of active generators, $N(\sigma_F)$, the number of loops each source generates prior to becoming locked, $n(\sigma_F)$, and the distance $R(\sigma_F)$ between the source and the barrier. Knowledge of these quantities will then furnish a

[8] R. E. Jamison and T. H. Blewitt, *Phys. Rev.* 91, 237 (1953).

[9] F. Seitz, *Advances in Physics* 1, 43 (1952).

[10] N. F. Mott, *Phil. Mag.* 43, 1151 (1952).

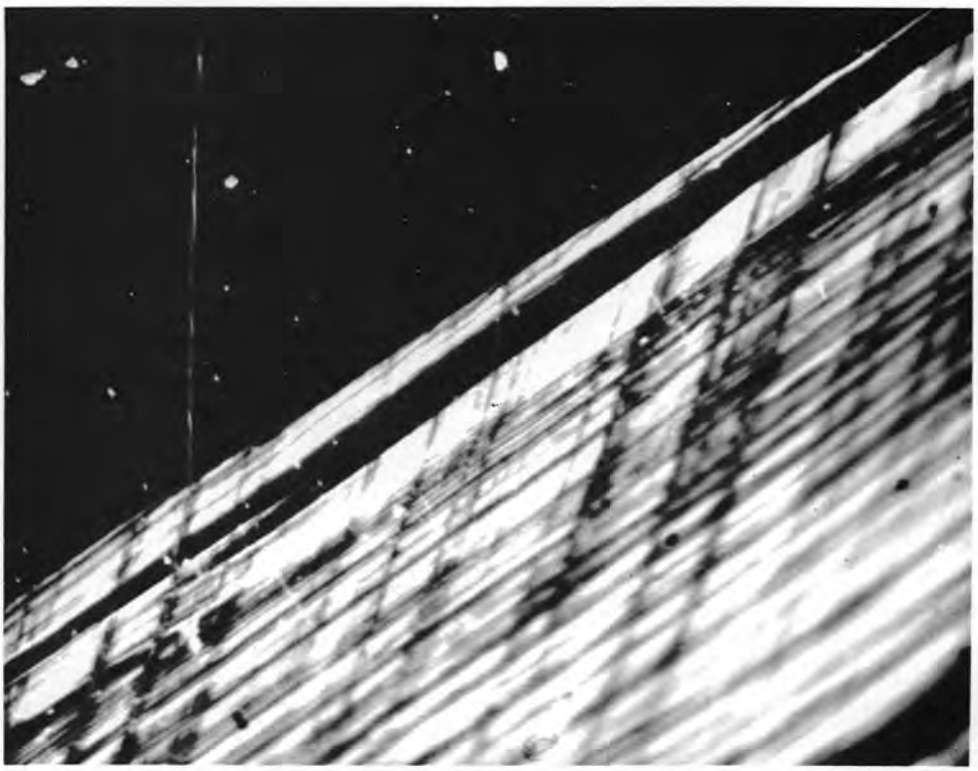

Fig. 112. Photomicrograph of "Deformation Twins" in Copper Crystal 278A. Dark field illumination. 500X.

test for the validity of the dislocation model suggested above. Some progress in this direction may be made by considering the resistivity and slip-line data in conjunction with the stress-strain relationship.

With the use of Koehler's suggestion[11] of the exhaustion of Frank-Read sources and the assumption that, at a given stress σ_F, a number, $dN(\sigma_F)$, of new generators will become active, it can be assumed that each of these new generators spins out $n(\sigma_F)$ dislocation loops before becoming locked; thus, a total of $n(\sigma_F)\, dN(\sigma_F)$ dislocation loops are formed as a result of the additional stress $d\sigma_F$ and are assumed to be circular and of radius $R(\sigma_F)$. These additional dislocation loops would, then, give an additional resistivity of

$$\frac{d\rho_D}{d\sigma_F} = 2\pi R(\sigma_F)\, n(\sigma_F)\beta \frac{dN(\sigma_F)}{d\sigma_F} , \tag{1}$$

where β is the resistivity per centimeter of dislocation loop (it will be assumed that the ratio of length of screw to line dislocation will remain constant throughout the deformation). Further, the additional strain is

$$\frac{d\epsilon}{d\sigma_F} = \pi R^2(\sigma_F)\, n(\sigma_F) b \frac{dN(\sigma_F)}{d\sigma_F} , \tag{2}$$

where b is the Burgers vector and ϵ is the shear strain. By dividing Eq. 2 by Eq. 1,

$$\frac{d\epsilon}{d\rho_D} = \frac{R(\sigma_F) b}{2\beta} . \tag{3}$$

If the linearity of the experimental stress-strain curve at 4.2°K and the data in Fig. 97, which show a parabolic relationship between ρ_D and σ_F, are considered, the following equation can be written:

$$\frac{d\rho_D}{d\epsilon} = 1.8 \times 10^{-10} \left(\frac{d\sigma_F}{d\epsilon}\right)^2 . \tag{4}$$

[11] J. S. Koehler, *Phys. Rev.* 86, 52 (1952).

By taking $d\sigma_F/d\epsilon$ at 14 kg/mm^2/unit strain, which is applicable for a crystal of the orientation of sample 168B,

$$\frac{d\rho_D}{d\epsilon} \approx 2.6 \times 10^{-8}\,\epsilon\,. \tag{5}$$

Slip lines can be interpreted as resulting from the intersection of the dislocation loop with the surface of the crystal. In accordance with the assumption that the loops are circular, the average length of slip line, L, will then be in the neighborhood of R. From Fig. 108 it can be seen that

$$\frac{1}{L} = 1.8 \times 10^3\,\epsilon\,, \tag{6}$$

or

$$R \approx \frac{5 \times 10^{-4}}{\epsilon}\,. \tag{7}$$

The data from sample 168B, which was deformed at 300°K, is applicable at 4.2°K in view of the fact that the length was found to be independent of the temperature in sample 278B. The latter data, although yielding the same result as 168B was not nearly as complete.

By solving the theoretical relation, Eq. 3, for β, the resistivity per centimeter of dislocation line, and using the experimental results for R and $d\rho_D/d\epsilon$ in Eqs. 5 and 7,

$$\beta = \frac{R(\sigma_F)b}{2} \cdot \frac{d\rho_D}{d\epsilon} \tag{8}$$

$$\approx 2.3 \times 10^{-19} \text{ ohm-cm per cm of dislocation line.}$$

The value in Eq. 8 should be compared with the value of 4×10^{-21} computed by Hunter and Nabarro.[12] The discrepancy between the two values may arise, in part, from the stacking faults. Herdenreich and Shockley[13] point out that dislocations will split into two components and that a stacking will result from the separation. The computation of Hunter and Nabarro does not consider the scattering caused by stacking faults. Koehler[14] indicates that stacking faults will result in an extended dislocation having a scattering cross section of the same order as that determined in the above computation.

It is pertinent to note that the resistivity data, along with the theoretical result (Eq. 3), predict that $R(\sigma_F)$ must vary as $1/\epsilon$ if the constancy of β is to be accepted. The fact that the length of the slip line varies as $1/\epsilon$ offers some evidence for a correlation of the length of the slip line to the distance the dislocation loop has moved.

The length of dislocation line formed as a result of the deformation may be computed from the magnitude of ρ_D in conjunction with the value of β. If β is taken as 2×10^{-19} ohm-cm per centimeter of dislocation line, a crystal severely deformed at 300°K will have 3×10^{10} cm of dislocation lines per cubic centimeter. Crystals severely deformed at 4.2°K, on the other hand, will approach a value of 10^{11} cm of dislocation lines per cubic centimeter.

The data of Figs. 95, 96, and 97 show that $\rho_{(D+V)}$, the sum of residual resistivities arising from vacancies and dislocations generated during deformation, is given by an equation of the type

$$\rho_{(D+V)} = k\sigma_F^2\,. \tag{9}$$

Since it is observed that ρ_D, the resistivity arising from the generated dislocations, is given by a similar equation

$$\rho_D = k'\sigma_F^2\,, \tag{10}$$

it follows that the scattering from generated vacancies will be given by the equation

$$\rho_V = k''\sigma_F^2\,. \tag{11}$$

Since ρ_V and ρ_D have the same dependence on σ_F^2, it would appear that they are generated by a similar process. It would seem reasonable to suppose that both defects are generated by the interaction of dislocation loops with other imperfections. Since the variables $N(\sigma_F)$ and $n(\sigma_F)$ in the adopted model are unknown, any attempt at describing the type of barrier interacting with the loops to form vacancies would probably be dangerous. However, k'' shows a greater dependence on the initial residual resistivity ρ_0 than does k'. It would seem, then, that the defects originally present play some role in the formation of vacancies. In order of magnitude, the value of k' is equal to k''. According to Jongenburger's compu-

[12] S. C. Hunter and F. R. N. Nabarro, *Proc. Roy. Soc. (London)* **A220**, 542 (1953).

[13] R. D. Herdenreich and W. Shockley, *Report on Strength of Solids*, P 57, London Physical Society, 1948.

[14] J. S. Koehler, private communication.

tation,[15] one vacancy will contribute a resistivity of 1.9×10^{-28} ohm-cm. Since 1 cm of dislocation line will contribute 2×10^{-19} ohm-cm, it can be deduced that about 10^9 vacancies are created per centimeter of dislocation line at any point in the deformation process. For single crystals severely deformed at room temperature, about 3×10^{19} vacancies are created. For samples severely worked at liquid-helium temperature, the density of vacancies will approach 10^{20}.

It is not clear whether the variation in the initial residual resistivity ρ_0 results from chemical or structural defects. The defects would appear, however, to be structural, since raising the temperature of the melt consistently reduced the value of ρ_0. It may be that there is sufficient short-range order in the melt so that something similar to a dislocation structure is still present. Raising the temperature would remove some of these defects and change the growth pattern in the crystal so that fewer structural defects would be grown into the crystal. On the other hand, an equally valid argument can be made that by raising the temperature gaseous impurities are being drawn off or that fractional distillation of the impurities is resulting. There is some difficulty in understanding the role of trace impurities in the pronounced difference in the annealing of cold-worked single crystals of different initial residual resistivity. Regardless of the cause, it is quite important to note this disparity when annealing studies are being made. Results of annealing studies of polycrystalline samples would be especially suspect.

It has been suggested that thermal energy reduces the rate of work-hardening in high-purity copper crystals at high strains by aiding in the release of trapped dislocations; thus, the back stress caused by the pileup of dislocations is reduced sufficiently to enable new Frank-Read generators to become activated. Frank had previously demonstrated[16] that such a process could enable slip lines to cross a grain boundary. The data presented here support this scheme. On the basis that ρ_D, the resistivity set up by dislocations, is independent of the temperature of deformation for any given flow stress, thermal energy would, in accordance with the model previously presented, reduce the effectiveness of the barriers and thus reduce the internal stress field. It can be considered, then, that deformation occurs at a temperature $T > 0$. For small strains T will have negligible influence on the work-hardening, since the internal stress field coupled with the thermal energy will not be sufficient to enable the dislocation loops either to climb over the barrier or to set new Frank-Read generators into action. As the strain increases, however, the internal stress will increase in magnitude; coupled with the thermal energy, this will enable the dislocation loops to circumvent the barriers. This process may explain the relatively early deviation of the high-temperature stress-strain curves from linearity. Physically, the number of barriers will continue to increase; however, the number of effective barriers will remain constant.

Thus R, the distance between the source and the barrier, will be a constant for the region where the thermal energy is sufficient to allow the loop to get over the barriers. Consequently, at strains exceeding the one where the curve is no longer linear, the term $d\rho_D/d\epsilon$ must be a constant in accordance with Eq. 8. Thus ρ_D should vary as

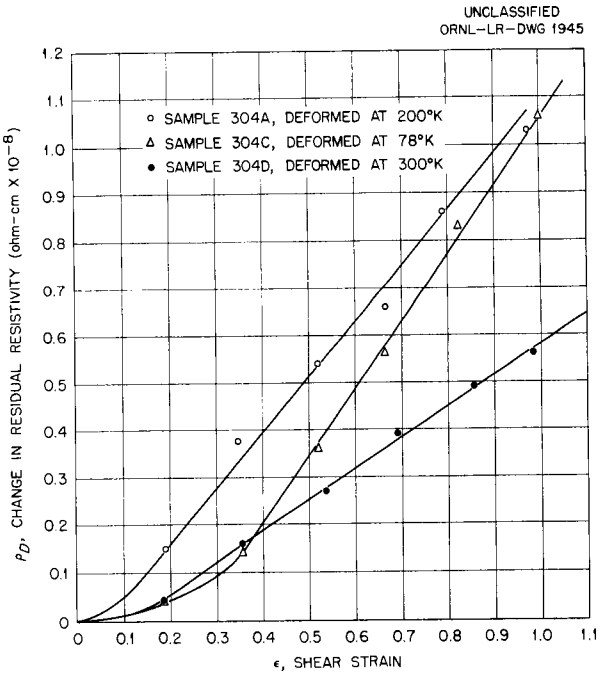

Fig. 113. Change in Residual Resistivity ρ_D as a Function of Strain for the 304 Samples.

[15] P. Jongenburger, *Phys. Rev.* 90, 710 (1953).

[16] F. C. Frank and T. Read, Pittsburgh Symposium on Plastic Deformation of Crystalline Solids, May 1950, U.S. Office of Naval Research Report NAVEXOS-P-834, p 89 (unpublished).

ϵ^2 when the stress-strain curve is linear but as ϵ when the stress-strain curve becomes parabolic. Furthermore, since $d\rho_D/d\sigma_F$ is independent of the stress-strain relationship, it is required that the strain vary as the square of the flow stress in accordance with the equation below when the thermal energy is sufficient to reduce the effectiveness of the barriers.

$$\frac{d\rho_D}{d\epsilon} = \frac{d\rho_D}{d\sigma_F}\frac{d\sigma_F}{d\epsilon} \quad . \tag{12}$$

It is observed in Figs. 98 and 113 that these two considerations are not in conflict with observed data.

It should be further noted that the slip lines in Figs. 103 and 104 (which represent high strains) are fragmented, thus offering visible evidence that the dislocation loops get over the barriers. Such fragmentation is not visible in Figs. 101 and 102, where a linear stress-strain curve results. It should also be noted that fragmentation is not found at high strains in Fig. 107, which depicts a specimen highly deformed at a low temperature.

SPECIAL PROJECTS

NEUTRON IRRADIATION OF LiF

D. Binder W. J. Sturm

The previous work[1,2] on the equivalence of x-ray lattice parameter and density changes in neutron-irradiated LiF crystals depended on the analysis of nonuniform irradiations. The lattice expansion in LiF is caused by alphas and tritons from the $Li^6(n,\alpha)H^3$ reaction. For exposures in the ORNL Graphite Reactor most of the displacements are initiated by thermal neutrons, and the large cross section at these low energies causes an attenuation in the neutron flux on passing through the crystal. This attenuation was calculated in order to determine a yield for the reaction at the surface (proportional to the x-ray change) and an average volume yield (proportional to the density change).

Two methods used in the present work have reduced the dependence on calculation. The first involves the use of a crystal approximately one-third as thin as the thinnest crystal previously used. The second involves the use of cadmium-shielded crystals, utilizing the smaller epicadmium reaction cross section to reduce the attenuation.

The very thin crystal was 2.6 cm square by 0.075 cm thick and was exposed to a thermal flux of 6×10^{16} neutrons/cm^2. In Fig. 114 is plotted the change in x-ray lattice parameter, $(\Delta a/a)_x$, vs the change in density lattice parameter, $(\Delta a/a)_\rho$, after irradiation (the uppermost point) and after thermal anneals at successively higher temperatures from 315 to 550°C. The slope of the line for the case of exact equivalence of $(\Delta a/a)_x$ and $(\Delta a/a)_\rho$ is not unity because of a small neutron attenuation still present. The slope is sufficiently near unity, however, to substantiate the conclusion of the previous report[2] that $(\Delta a/a)_x$ and $(\Delta a/a)_\rho$ are equivalent within 10%. Calculations of this slope, based on an isotropic distribution of neutrons incident upon an infinite slab, yield a value of 1.06, which is in very good agreement with the experimental value of 1.05.

The smaller reaction cross section for epicadmium neutrons reduces neutron attenuation in the LiF crystals but lengthens the time for irradiation. The cadmium ratio for a "$1/v$" detector, or the ratio of the reaction yield for the total flux to the yield for the epicadmium flux, is about 20. The irradiation time for cadmium-shielded crystals is then at least 20 times longer, multiplied by an additional factor for flux depression in the neighborhood of a cadmium shield. In Fig. 115 the uppermost points represent the results of an irradiation of 500 hr of two crystals surrounded by 0.030-in. cadmium shields. This is to be compared with the result of a nonshielded 30-hr irradiation in Fig. 114.

Two crystals, one twice as thick as the other, were chosen for this experiment to check the efficiency of the shield. For a cadmium ratio of 20, there need be only a 5% leak to make the thermal neutrons as effective as the epicadmium neutrons. In Fig. 115 are shown the results of the irradiation and successive anneals of the two crystals. If there had been a leak, the thicker crystal would have displayed a large slope. Since

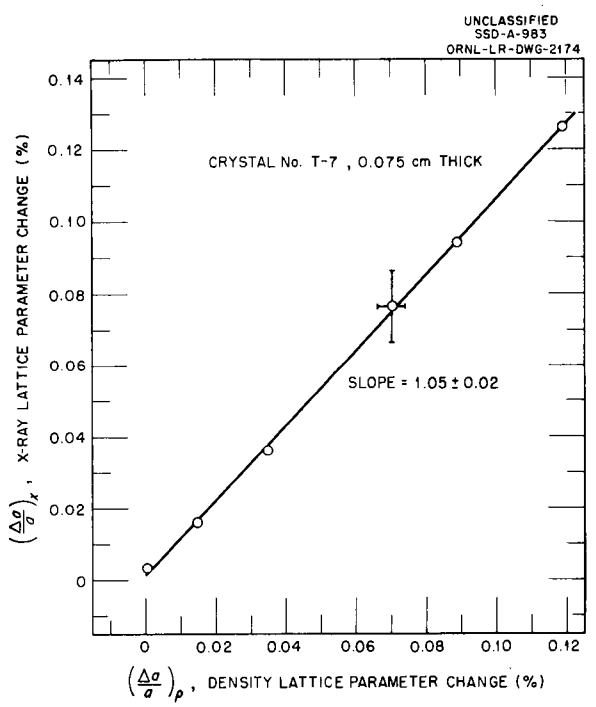

Fig. 114. X-Ray Lattice Parameter Change vs Density Lattice Parameter Change for a 0.075-cm-thick Crystal.

[1] D. Binder and W. J. Sturm, *Solid State Semiann. Prog. Rep. Aug. 31, 1953*, ORNL-1606, p 101.

[2] D. Binder and W. J. Sturm, *Solid State Semiann. Prog. Rep. Feb. 28, 1954*, ORNL-1677, p 66.

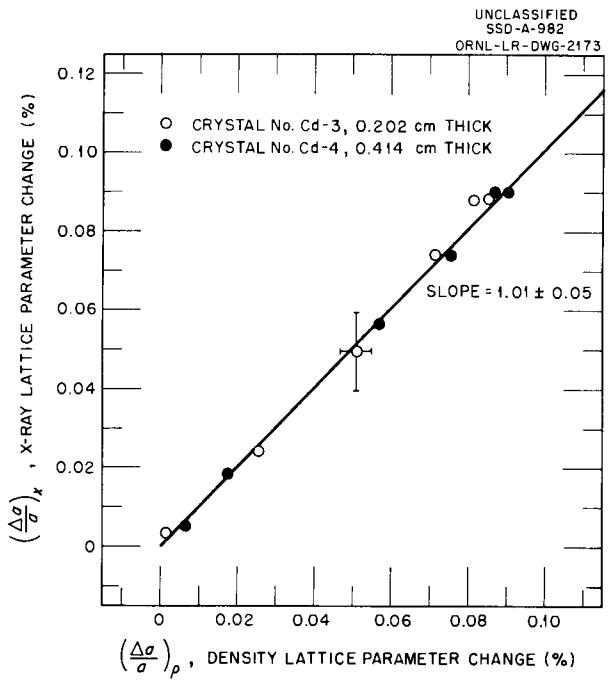

Fig. 115. X-Ray Lattice Parameter Change vs Density Lattice Parameter Change for Cadmium-Shielded Crystals.

the points lie along the same line, within error, there are no detectable effects caused by thermal neutrons.

The epicadmium neutrons can be shown to produce no detectable attenuation in these crystals. It is adequate to follow the path of an average neutron in an isotropic flux which travels a distance χ, twice the perpendicular distance from the surface of the crystal. The yield for the reaction is

$$Y(\chi) = \int_{E_1}^{\infty} n(E)\,\sigma(E)\,dE \quad ,$$

where $n(E)$ is the number of neutrons at energy E, $\sigma(E)$ is the cross section at E, and E_1 is the cadmium cutoff. The cross section $\sigma(E)$ varies as $E^{-1/2}$, and $n(E)$ initially varies as $1/E$ (resonance flux) and varies as $1/Ee^{-N\sigma(E)x}$ (for a path length χ), where N is the number of atoms per cubic centimeter.

By setting E_1 = 0.4 ev and integrating,

$$Y(x) = \frac{A}{x}\left(1 - e^{-N\sigma_0 x/4}\right) \quad ,$$

where A is a constant and σ_0 is the cross section for thermal neutrons. The neutrons enter from both sides, and if x_0 is the thickness of the crystal, the ratio of the yield at the surface to the yield throughout the volume is the slope S of the curve, or

$$S = \frac{1 - Y(2x_0)}{2\overline{Y(x)}} \quad .$$

The calculated value of S for the thick crystal is 1.02, and for the thin crystal it is 1.00. The average of the two values is in agreement with the experimental slope of 1.01 ± 0.05.

The thin-crystal run produced an x-ray lattice parameter change 5% ± 2% higher than the density lattice parameter change, with an attenuation calculation predicting 6% in the case of exact equivalence. In the cadmium runs, $(\Delta a/a)_x$ was 1% ± 5% higher than $(\Delta a/a)_\rho$, with a similar calculation predicting 1%. It is concluded that x-ray and density changes in neutron-irradiated LiF are equivalent within 5%.

If, as has been discussed in earlier reports, the displacements produced in LiF under neutron irradiation lead to Frenkel defects, the x-ray and density changes would be equivalent. If, however, these displacements result in Schottky defects, the density change would be larger. Thus, as a consequence of the measurements discussed above, it is concluded that the lattice expansion in neutron-irradiated LiF is predominantly due to Frenkel defects.

PARAMAGNETIC RESONANCE IN IRRADIATED MATERIALS

R. A. Weeks

A rectangular-transmission resonant cavity has been built to operate in the TE_{101} mode at a resonant frequency of 9.150 kmc. The Q_l (loaded Q) of the cavity has been measured in the neighborhood of the resonant frequency by use of the standing-wave technique;[3] the Q_l is approximately 1300. This value of Q_l has been used to calculate the detector power variation that arises from frequency deviations caused by ripple on the reflector voltage and the filtering effect of the resonant cavity.[4] The calculated power variation is in approximate agreement with the observed

[3] C. G. Montgomery, *Technique of Microwave Measurements*, p 333, McGraw-Hill, New York, 1947.

[4] *Ibid.*, p 332.

variation. These results indicated that frequency stabilization of the klystron was necessary if the weak resonances induced by radiation were to be observed. To meet the need of constant frequency, a Pound i-f stabilization system[5,6] is being constructed.

A proton-resonance gauss meter[7] has been constructed to measure the magnetic field. A preliminary investigation of the magnet field indicated a stability of better than 1 part in 20,000 and a homogeneity of better than 1 part in 10,000 over a circle of approximately a 1-in. radius parallel to the pole caps.

Calibration of the apparatus is being made by using known weights of a free radical, alpha-alpha-diphenyl-beta picryl hydrazyl; the powder has a resonance with a g factor of 2.0038 and a half-width of 3.7 gauss.[8]

DIELECTRIC CONSTANT AND LOSS TANGENT OF IRRADIATED PLASTICS AT MICROWAVE FREQUENCIES

R. A. Weeks

The loss tangent, tan δ, and the dielectric constant, e' of polyethylene, polystyrene, and Teflon[9] have been measured at 1, 3, and 8.6 kmc after exposure to integrated thermal fluxes up to 8×10^{18} neutrons/cm^2. Figures 116, 117, 118, and 119 are plots of loss tangent vs integrated flux for these materials at these frequencies. It is apparent from these data that Teflon shows the greatest changes for the least exposure of the three materials; tan δ increases by a factor of 7.3 ± 0.5 at 1 and 3 kmc and 2.1 ± 0.5 at 8.6 kmc for 2×10^{18} neutrons/cm^2. In polyethylene tan δ increases by a factor of 2.5 ± 0.5 at 1 and 3 kmc for 8×10^{18} neutrons/cm^2; any change in tan δ at 8.6 kmc is within the range of error of the measurement. In polystyrene any changes were less than the range of error at the three frequencies for 2×10^{18} neutrons/cm^2. In Fig. 118 the curve indicates a slight increase at 10^{18} neutrons/cm^2 over the preirradiation value and then a decrease at 2×10^{18}

[5] *Ibid.*, p 70.

[6] R. V. Pound, *Proc. I.R.E.* 35, 1405 (1947).

[7] N. J. Hopkins, *Rev. Sci. Instr.* 20, 401 (1949).

[8] C. A. Hutchison and R. C. Pastor, *Phys. Rev.* 81, 282 (1951).

[9] R. A. Weeks, *Solid State Semiann. Prog. Rep. Feb. 28, 1954*, ORNL-1677, Table 7, p 78.

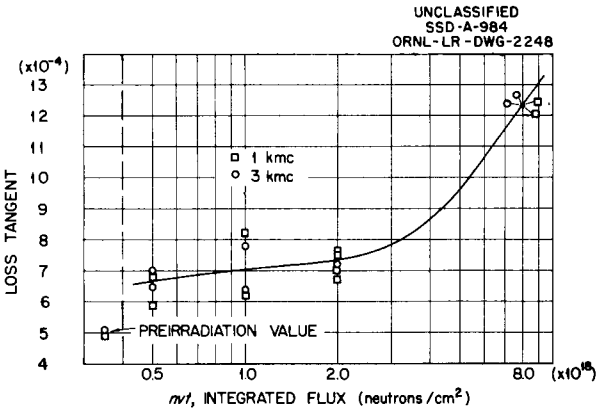

Fig. 116. Loss Tangent of Irradiated Polyethylene at 1 and 3 kmc.

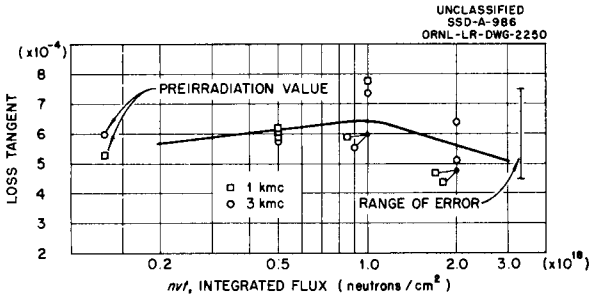

Fig. 117. Loss Tangent of Irradiated Polystyrene at 1 and 3 kmc.

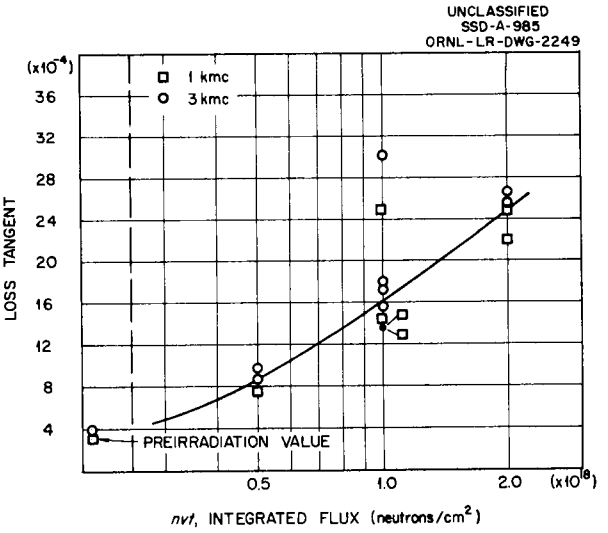

Fig. 118. Loss Tangent of Irradiated Teflon at 1 and 3 kmc.

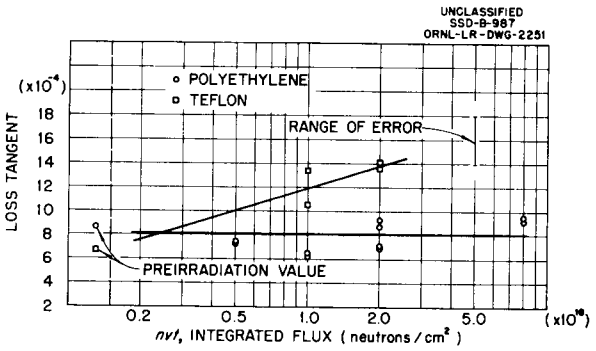

Fig. 119. Loss Tangent of Irradiated Polyethylene and Teflon at 8.6 kmc.

neutrons/cm^2. Although the indicated change is within the range of error, the observed points are consistent at the three values of irradiation. Until further refinements are made in the measurement technique and the range of error is reduced, the curve in Fig. 118 should be regarded as very tentative.

Only in Teflon were changes in e' observed. For 10^{18} and 2×10^{18} neutrons/cm^2 and at 1 and 3 kmc, e' was observed to increase by 2.3% ± 1.0% and at 8.6 kmc by 1.5% ± 1%. In polystyrene any changes in e' were well within the range of error of ±1% at all frequencies and up to 2×10^{18} neutrons/cm^2. The same was true of polyethylene up to 8×10^{18} neutrons/cm^2.

Three Teflon samples, one for the 1- and 3-kmc frequencies and two for the 8.6-kmc frequency, of 14 samples had anomalous values. These values are given in Table 17 and are plotted in Figs. 117 and 119. The anomalous values are approximately twice those found in the other samples with the same exposure and at the same frequencies. It has been observed that the samples with anomalous values of tan δ were irradiated in containers in which there were no other Teflon samples. The samples have all been irradiated in hole 19 of the ORNL Graphite Reactor. In this facility the aluminum containers are surrounded by the water coolant, and occasionally they leak slightly. If the Teflon samples with anomalously high values were in such containers, then absorption of water by the samples, with the loss characteristics of water in the microwave region, would explain the anomaly. In an effort to test this idea, eight samples were sealed in polyethylene bags before they were placed in the containers for irradiation.

TABLE 17. LOSS TANGENT OF IRRADIATED TEFLON AT VARIOUS FREQUENCIES

Sample No.	Tan $\delta \times 10^4$ [a] for Exposures (thermal neutrons/cm^2)			
	0	0.5×10^{18}	1×10^{18}	2×10^{18}
		1 kmc[b]		
7	4.5	7.5		
8	4.3		25.0[c]	
10	3.4		13.8	
13[d]	2.4		14.3	
14[d]	2.7		13.6	
15[d]	2.5			25.3
16	2.4			22.6
	Av 3.2			
		3 kmc[b]		
6	3.4	9.8		
7	5.9	8.9		
8	6.3		30.2[c]	
10	6.0		15.7	
13	2.5		18.1	
14	2.5		17.2	
15	2.5			27.2
16	2.6			26.8
	Av 4.0			
		8.6 kmc[b]		
7	7.6		23.6[c]	
8	8.6		13.4	
13[d]	4.7		10.9	
14[d]	5.0		25.1[c]	
15[d]	5.0			14.1
16[d]	5.5			13.6
	Av 6.1			

[a] Each value of tan δ is the average of two measurements on each sample.

[b] Same sample for 1 and 3 kmc, different sample for 8.6 kmc.

[c] Anomalous values.

[d] Sealed in polyethylene bags; sample 14 (8.6-kmc sample) bag was open when removed from container.

When the containers were opened after irradiation, the condition of the bags was noted. Only the bag containing a sample for the 8.6-kmc frequency had opened between the time that the container was sealed and then opened after irradiation. This

one sample had an anomalous value of tan δ. It should be noted that the water absorptivity of Teflon does not change appreciably for irradiations[10] in the same facility up to approximately 10^{18} neutrons/cm^2. The exposure for some of the anomalous values was 10^{18} neutrons/cm^2 and longer. The results of the above experiment are inconclusive.

Neither the polyethylene nor the polystyrene samples had unusually large values for tan δ in 27 samples and irradiations ranging from 0.5×10^{18} to 8×10^{18} neutrons/cm^2. Polyethylene and polystyrene show a slight increase in water absorptivity for an integrated flux[11] of 10×10^{18} neutrons/cm^2. The water absorptivity of the three materials is approximately the same.

In view of the approximately equal water absorptivities of the three materials, it would be expected that a few of the 27 polyethylene and polystyrene samples would have anomalous values. Since this did not occur, the water-absorption hypothesis does not seem adequate to explain the Teflon anomaly.

The change in tan δ in the irradiated samples of Teflon and polyethylene is apparently frequency sensitive. For Teflon the greatest increase is at 1 and 3 kmc, a factor of 7.3 ± 0.5 for 2×10^{18} neutrons/cm^2. The increase at 8.6 kmc is a factor of 2.1 ± 0.5 for 2×10^{18} neutrons/cm^2. In polyethylene the increase at 1 and 3 kmc is a factor of 2.5 ± 0.2 for 8×10^{18} neutrons/cm^2, and at 8.6 kmc the change, if any, is within the range of error.

In a previous measurement[12] of the attenuation of a polyethylene-insulated coaxial cable irradiated in hole B of the ORNL Graphite Reactor, an increase of approximately 15% in attenuation was observed for 2.6×10^{18} neutrons/cm^2 at a frequency of 4.06 Mc. If the decrease in tan δ between 1 and 8.6 kmc of the irradiated samples and the 15% increase in attenuation observed at 4 Mc are considered, it is probable that the increase in tan δ as a function of irradiation will be greatest in the frequency range 4 Mc to 1 kmc.

[10] O. Sisman and C. D. Bopp, *Physical Properties of Irradiated Plastics*, ORNL-928, p 91 (June 29, 1951).

[11] *Ibid.*, p 81.

[12] R. A. Weeks and D. Binder, *Effect of Radiation on the Dielectric Constant and Attenuation of Two Coaxial Cables*, ORNL-1700, p 11 (March 19, 1954).

THERMAL CONDUCTIVITY OF DIELECTRICS AT LOW TEMPERATURES

A. Foner Cohen

The cryostat described in an earlier report[13] has been tested at liquid- and solid-hydrogen temperaatures. It is possible, therefore, by use of liquefied helium, liquid and solid hydrogen, and liquid and solid nitrogen, to carry out thermal-conductivity measurements over an almost continuous temperature range from approximately 1.7 to 80°K. Under some circumstances, measurements can be extended to approximctely 300°K.

Thermal-conductivity measurements on a single quartz crystal described in an earlier report[13] included the liquid-helium and liquid-nitrogen temperature ranges. Additional measurements in the hydrogen range have been carried out, and a maximum in thermal conductivity was found at about 11°K, in qualitative agreement with the observations of Berman.[14] Measurements are currently being carried out with single crystals of KCl, Al_2O_3, and very-high-purity germanium.

THERMAL- AND ELECTRICAL-CONDUCTIVITY STUDIES

A. Foner Cohen L. C. Templeton

Ductile Iron. Thermal-conductivity and electrical-resistivity measurements on cast ductile iron have been extended to higher temperatures.[15] The results are shown in Figs. 120 and 121. In the temperature range from 100 to 700°C, the electrical conductivity decreases by a factor of 2. Approximately the same behavior is evidenced in the thermal-conductivity decrease. Hardness measurements on the sample, before and after the thermal and electrical measurements, were carried out; Rockwell hardness, scale B, before heating to high temperature was 94 and afterward was 69. The softening of the material, when it was subjected to elevated temperatures, did not affect the thermal- or electrical-conductivity values, as determined by making measurements at the lower temperatures after the high-temperature tests.

[13] A. Foner Cohen, W. J. Sturm, and L. C. Templeton, *Solid State Semiann. Prog. Rep. Feb. 28, 1954*, ORNL-1677, p 68.

[14] R. Berman, *Proc. Roy. Soc. (London)* **A208**, 90 (1951).

[15] A. Foner Cohen and L. C. Templeton, *Solid State Semiann. Prog. Rep. Feb. 28, 1954*, ORNL-1677, p 67.

Aluminum Bronzes. Measurements of the thermal conductivity and the electrical resistivity of the alloys 94% Cu–6% Al and 92% Cu–8% Al have been extended to higher temperatures than those reported earlier.[16] The experimental method was somewhat different from the one used in the earlier lower-temperature experiments and will be reported at some other time. As was anticipated, the thermal conductivity of both alloys continues to increase with increasing temperature. Figures 122 and 123 show results of thermal-conductivity and electrical-resistivity measurements. The highest temperature at which data were obtained

[16] A. Foner Cohen and L. C. Templeton, *Solid State Semiann. Prog. Rep. Feb. 28, 1954*, ORNL-1677, p 70.

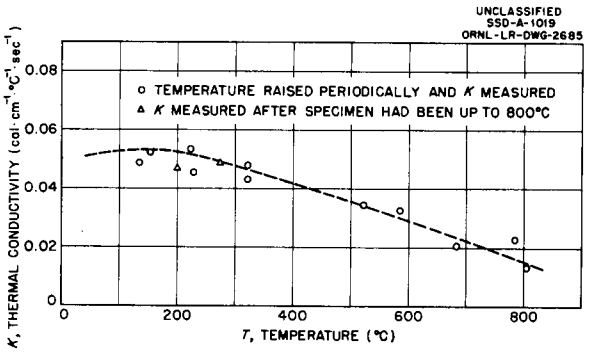

Fig. 120. Thermal Conductivity vs Temperature of Ductile Cast Iron.

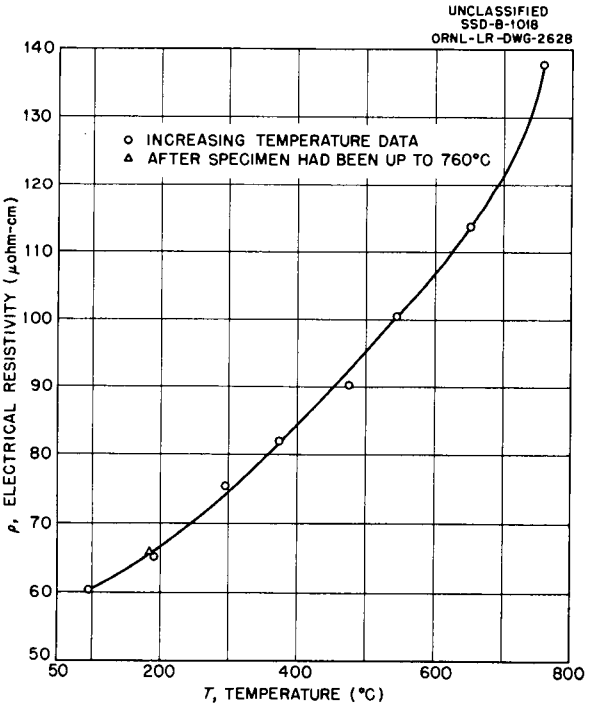

Fig. 121. Electrical Resistivity vs Temperature of Ductile Cast Iron.

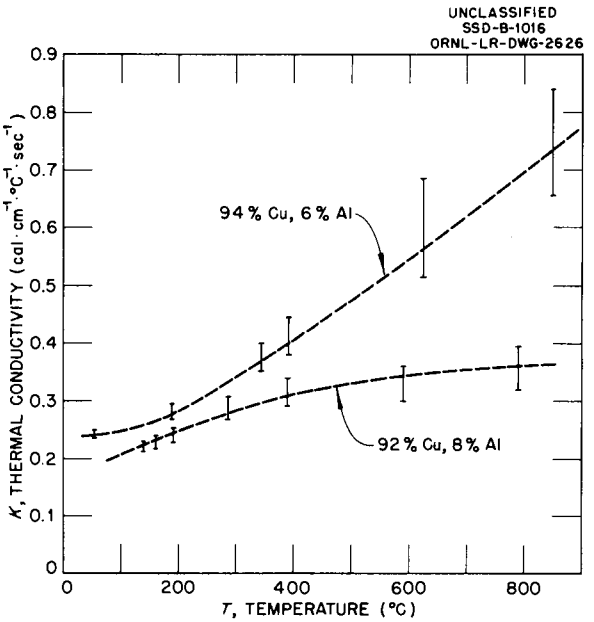

Fig. 122. Thermal Conductivity of Aluminum Bronze.

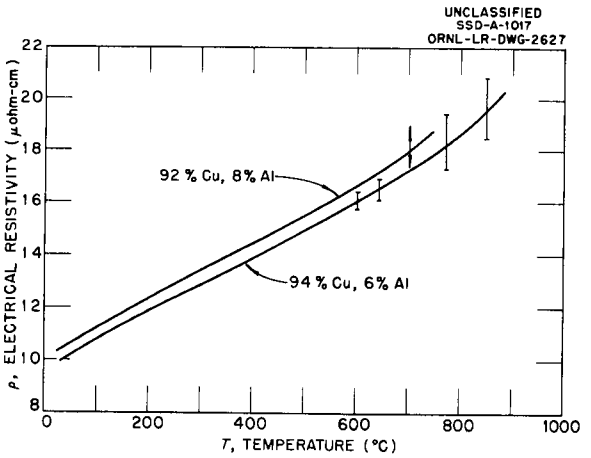

Fig. 123. Electrical Resistivity of Aluminum Bronze.

was about 850°C. Assignment of absolute thermal-conductivity values in these experiments was uncertain by the amount indicated in Fig. 122. In the case of 94% Cu–6% Al, which was almost as good a conductor as aluminum, it was decided to check the qualitative dependence of the heat conductivity of the alloy by using aluminum as a standard. These experiments were carried out to about 540°C, and they confirm the temperature dependence of the heat conductivity shown.

A ROCKING-CURVE ADAPTER FOR THE NORELCO WIDE-RANGE DIFFRACTOMETER

F. A. Sherrill M. C. Wittels

The Norelco wide-range diffractometer was designed primarily for the study of polycrystalline materials with random orientation, but it has become desirable to extend its use to the study of large single crystals. An adapter was designed by R. J. Fox and fabricated by N. E. Wilkins of the Central Machine Shop and is called the "Fox Spinner." The application of this instrument in rapid orientation determinations of cubic single crystals and in rocking-curve studies is presented in the following discussion.

Crystals up to 1 in. in diameter and $\frac{3}{8}$ in. in thickness are mounted with Cenco Universal red wax so that a flat face is coplanar with the top surface of the ring. This ring (Fig. 124) is then placed with its outer edge in contact with three V-grooved steel rollers equally spaced around the ring and coplanar with it. One of the rollers is the driver for ring rotation, and the other two are spring-loaded idlers. This six-contact-point suspension (two contact points per roller) positions the top face of the steel ring and the specimen face so that the surfaces of the specimen and ring lie on the major axis of the diffractometer. Power for this ring rotation is brought in to the driver roller through a shaft and gear train from an induction motor at the rear of the unit. The gears can be disengaged when the ring rotation is not required.

In addition to the ring rotation mechanism, there is a synchronous clock drive at the rear of the unit that rocks the ring slowly about the conventional axis of the diffractometer through a friction clutch but independently of the normal diffractometer drive. The clutch permits rapid manual adjustment of crystal orientation. In order to avoid backlash in the rocking motion, the driving motor is opposed by a motor of lower torque, which is therefore forced to run backwards. A graduated circle (Fig. 125) is mounted on the tubular shaft supplying this rotation and permits the reading of the angular deviation between the crystal surface and the crystal lattice planes.

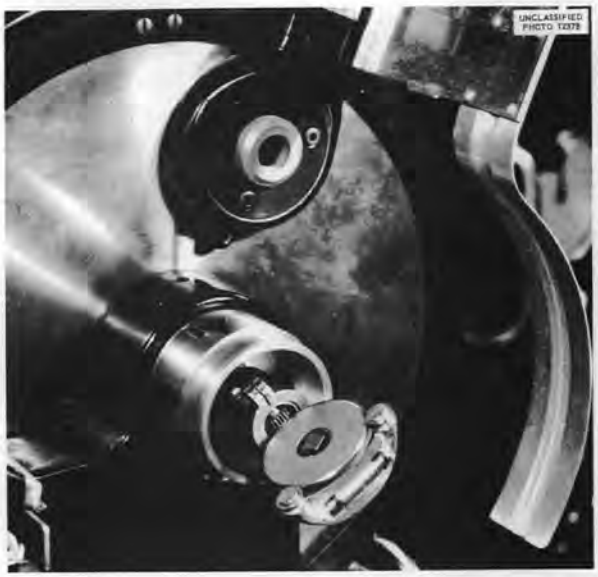

Fig. 124. Crystal-Mounting Ring with Specimen in Place.

The Fox Spinner in no way alters the original diffractometer, with the exception of a single $\frac{5}{32}$-in. hole drilled in the end of the bronze bearing, and it is a completely independent adapter for that instrument. It may be placed on, or removed from, the Norelco instrument (Fig. 126) in less than 5 min with complete ease of handling.

If the angle between the slip planes and pulling direction in, say, a copper single-crystal tensile specimen is desired, a simple orientation analysis is used. If the crystal is properly positioned in the adapter, the 2θ angle of the diffractometer is set at 144.7 deg in order to receive diffraction from the equivalent (420) planes. The crystal is automatically rocked and spun simultaneously,

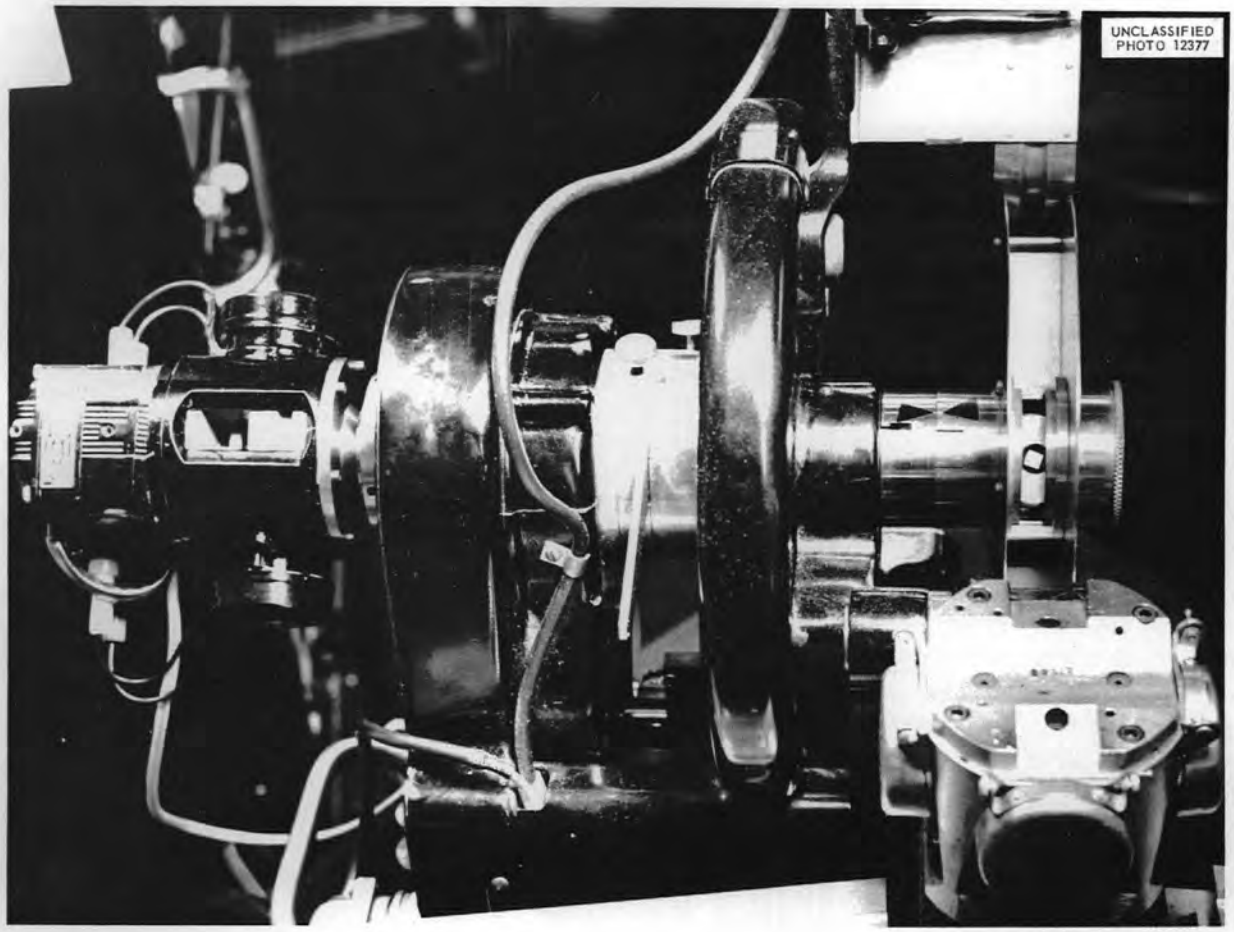

Fig. 125. Fox Spinner in Position on Norelco Machine.

with the crystal surface tilted initially at 72.35 deg, or $2\theta/2$, from its normal position. As a specific rule $2\theta/2$ is always the limiting angle of tilt, since any further increase in that angle would result in a blocking of the diffracted beam. The rocking and spinning motions result in a spiral search for the (420) reflections, as is shown on a portion of the standard stereographic net in Fig. 127. The angular traverse between corresponding points on the spiral is only 10 min of arc, sufficiently small so that all possible reflections can be located when normal diffractometer slits are used.

The stereographic plot in Fig. 127 shows that many planes other than the (420) will diffract as the crystal moves through a complete spiral, but, since the Geiger counter is set to receive reflection from only (420), these plane reflections alone will be recorded on the chart trace (Fig. 128); this trace shows (420) reflections appearing at tilt angles of 35, 34, and 26 deg. By plotting these angles as arcs in the standard stereographic projection, the normal to the crystal surface is located at their intersection. This normal can usually be found with an accuracy of $\pm\frac{1}{2}$ deg and thus locates the angle between the crystal surface and lattice plane with fair precision. The unique crystal orientation is then found by noting the exact spin position where the crystal diffracts, and this is usually done manually.

Any cubic crystal could be oriented in a similar manner. For example, if lead were to be studied, 2θ could be set at 123.3 deg and the equivalent (440) planes sought with an initial tilt of 61.6 deg. This technique is particularly useful in cold-worked crystals, where the Laue method fails.

UNCLASSIFIED
PHOTO 12379

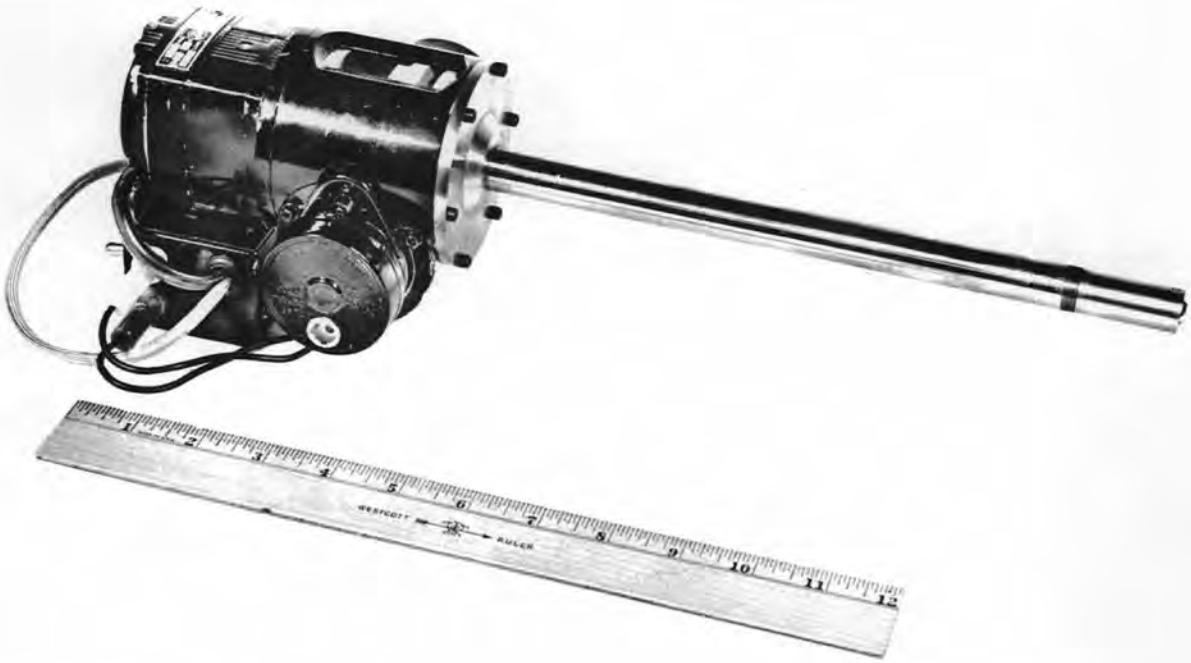

Fig. 126. Fox Spinner Removed from Norelco Machine.

If polycrystals are present in such a case, they can be detected and located by searching for (h00) reflections in the same manner as previously described, whereas etching methods might prove to be unfeasible.

Single-crystal studies of plastically deformed metals by standard x-ray methods are often hampered, since cold-work distortion results in a large reduction in peak intensities. Similarly, the distortion and disorder induced in some nucleon-bombarded single crystals makes normal x-ray measurements exceedingly difficult. It is in this type of study that the Fox Spinner is used most advantageously. A small x-ray exit slit 0.003 in. wide gives an essentially parallel beam of x-rays that strike the sample with an approximate 0.040-in. cross section, and the usual focusing conditions are then neglected.

Since the diffracting plane does not have to be coplanar with the crystal surface, many reflections having large Bragg angles can be measured. This, in turn, allows lattice parameter measurements to be made in large, randomly oriented single crystals with an accuracy of ±0.005%.

Qualitative rocking curves are obtained by first locating the desired reflection and then using the diffractometer in the normal manner. When quantitative analyses are desired, fixed-time counts are taken at Geiger-tube intervals of 0.025 deg, which is equivalent to moving the diffractometer a slit width of 0.003 in. Examples of some rocking curves that were made with this adapter are shown in Fig. 129. The curves are of the (420) reflections from a copper single-crystal tensile specimen of square cross section before and after tensile extension. This reflecting plane made an angle of 25 deg with the surface of the crystal. For purposes of graphic representation the peak intensities are normalized in this figure. A Laue back-reflection photograph (Fig. 130) of this same crystal after elongation clearly reveals the difficulty of making an analysis with the use of film techniques.

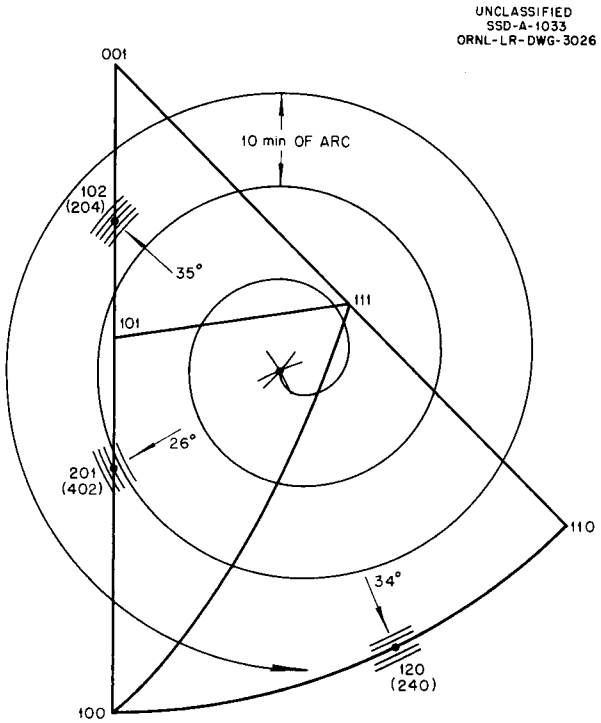

Fig. 127. Portion of Standard Stereographic Net for Cubic Crystals.

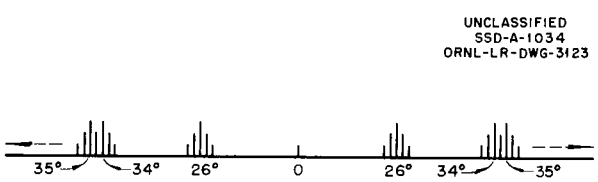

Fig. 128. Chart Trace for (420) Reflections.

The rocking-curve technique employing the Fox Spinner has required a cycle of manual operation for each Geiger-tube setting and was necessarily laborious. In order to minimize this manual manipulation, a reversible, synchronous rocking motor was substituted for the nonreversible driver previously described and is used in conjunction with a time circuit. As a result it is possible to increase the statistical accuracy by rocking in two directions, and the operation is made wholly automatic except for the original setting-up procedure.

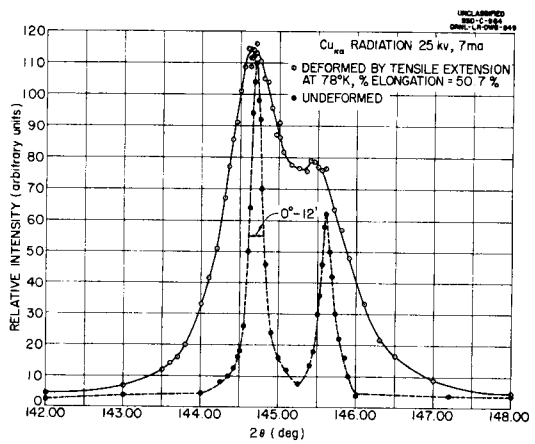

Fig. 129. Rocking Curves of (420) from a Copper Single Crystal Before and After Elongation.

SHIELDING FOR AN X-RAY DIFFRACTOMETER

G. E. Klein

The modified G-E diffractometer to be used for the examination of irradiated specimens was originally designed to be operated in one of the hot cells in the Solid State Building but is now set up in Room 67 of Building 3550.

Previous tests showed that samples measuring up to approximately 5 r on contact could be handled and that satisfactory x-ray diffraction patterns could be obtained therefrom.

A shield was fabricated to provide a minimum thickness of 2 in. of lead on all sides and on the top. Entrance ports and doors were included at appropriate positions to enable placement of the specimens in the holder, manipulation of the instrument, and any necessary servicing of the equipment, such as change of x-ray and proportional-counter tubes. The diffractometer is placed on a rigid steel frame, and solid concrete blocks built up to the height of the instrument base provide a foundation for the lead shield.

The shielding has been tested with a 10-mg radium source placed at the sample position, and

necessary lead has been added at appropriate spots so that adequate personnel protection within known limits is provided at various parts of the shielding.

Figure 131 shows the instrument resting on the steel frame before the shielding was added, while Fig. 132 is an over-all view of the lead shielding in place around the instrument.

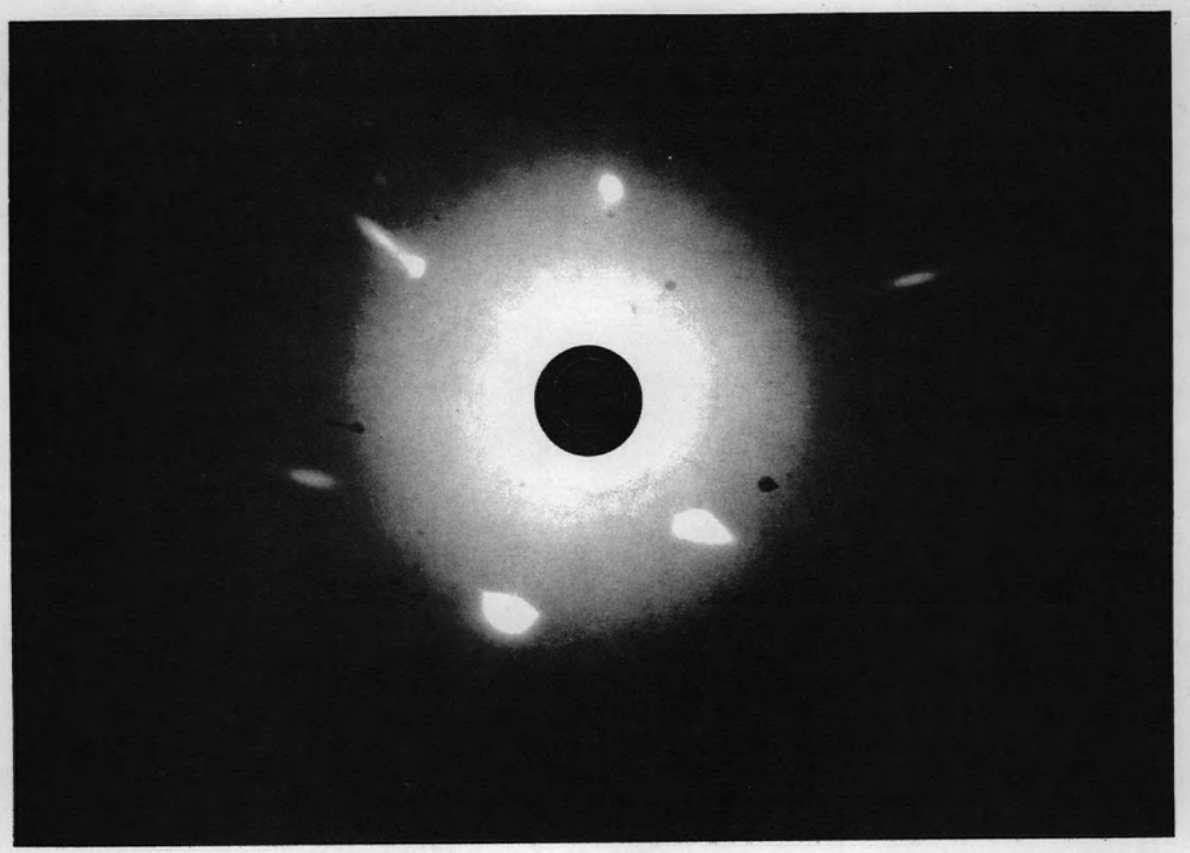

Fig. 130. Laue Back-Reflection Photograph of a Copper Single Crystal After Elongation.

UNCLASSIFIED
PHOTO 12757

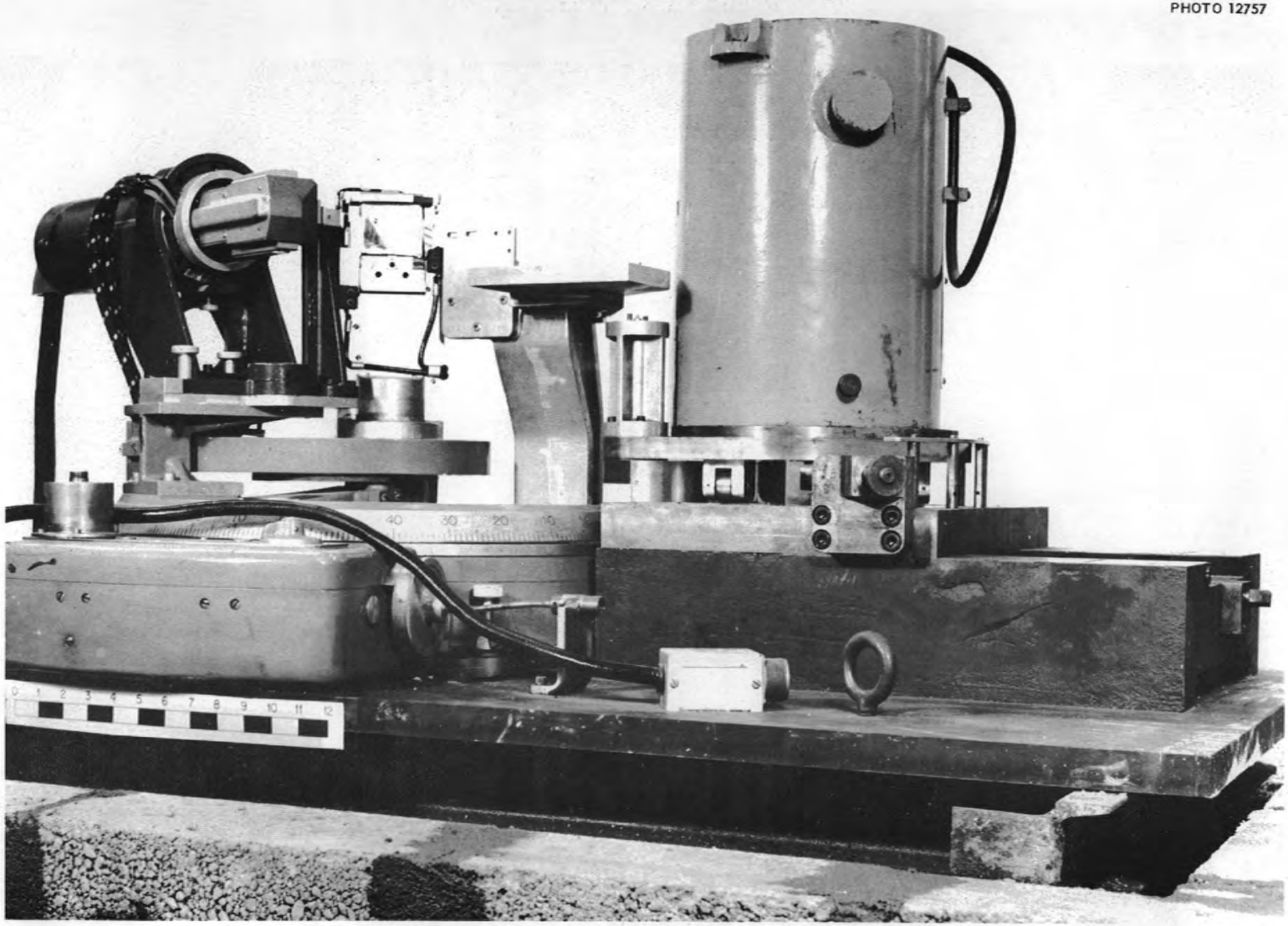

Fig. 131. G-E X-Ray Diffractometer.

Fig. 132. Shielded X-Ray Diffractometer.